# Spinal Cord Tissue Engineering Using Electrically Conductive Scaffolds

Daniel John Secker

Submitted in accordance with the requirements for the degree of
Doctor of Philosophy

The University of Leeds
Institute of Medical and Biological Engineering
School of Mechanical Engineering

September 2021

The candidate confirms that the work submitted is his/her own and that appropriate credit has been given where reference has been made to the work of others.

This copy has been supplied on the understanding that it is copyright material and that no quotation from the thesis may be published without proper acknowledgement.

The right of Daniel John Secker to be identified as Author of this work has been asserted by him in accordance with the Copyright, Designs and Patents Act 1988.

# Acknowledgements

To finish this PhD with the added layer of a global pandemic has undoubtedly been one of the most challenging times of my life and I have no doubt that I would never have made it without the support of those around me.

I'd like to thank everyone within my lab who has taken time to help me over the years, especially Sarah Myers for never being too busy to help and never getting frustrated answering questions I should really have known the answer to by now! Thanks to Phil Davies for being a friend and giving advice where it was needed, and for really making an effort to find me help elsewhere when he couldn't give it himself. On that note a big thanks to Lars Jeuken from the School of Biomedical Sciences who was so generous with his time and help when I needed to find an expert on electrical impedance, and for cycling to Uni on a snowy weekend to teach me how to use the equipment.

I'd like to thank everyone at the CReaTE group at the University of Otago for making me so welcome, my time on secondment will forever be one of my happiest memories and I'd particularly like to thank Khoon Lim for looking after me and giving guidance and to Tim Woodfield for offering me the secondment. On a similar note I'd also like to thank the Matsusaki group at Osaka University for the enjoyable time I had there, and in particular Michiya Matsusaki for offering me the secondment and being a great mentor whilst I was there and Hao Liu for being my tour guide to Japan!

I'd like to thank everyone in my cohort on the CDT program, to have a number of other people starting at the same time and going through the same trials and tribulations was so important, I know I have made some friends for life. I'd especially like to thank Ben and Jack for always being great drinking buddies and Trang for being a Rockstar and keeping my morale high at times when I didn't always think I'd make it. Also a thank you to Joanne Tipper and Claire Brockett for organising a great program which I think has really provided a lot of value for me.

Last but certainly not least I'd like to thank my supervisor Xuebin for his time and guidance throughout my project and for really making me feel that he cared. Also I would like to thank him for pushing me to take the opportunities to study abroad and taking time to set them up.

Outside of the PhD I would also like to thank my friends and family that have supported me when I've needed it. I'd like to thank my Mum and Dad for

# Abstract

Over 500,000 people suffer a spinal cord injury (SCI) every year worldwide, often causing significant loss in quality of life for SCI sufferers. Current clinical treatments focus on minimisation of the initial injury but there are limited options available for anabolic replacement of lost tissue.

Electrically conductive (EC) hydrogels have been investigated for SCI treatment. Despite success in stimulating increased axonal growth *in vivo*, few studies have combined EC hydrogels with stem cells to further spinal cord regeneration, despite identification of promising cell types.

This project developed an EC hydrogel for spinal cord tissue engineering applications, and tested the construct using both model neuronal cells and dental pulp stem cells (DPSCs). This was achieved through initial optimisation of crosslinking efficiency and Young's Modulus through crosslinker selection in a gelatin-norbornene (GelNOR) hydrogel. This hydrogel was then combined with EC gold nanorods (GNRs) to improve electrical conductivity, before being biologically tested using either normal human dermal fibroblasts (nHDFs) or DPSCs and finally with a model co-culture system, also developed in this project, of either cell type with PC12s.

The experiments found that the GelNOR hydrogel's physical properties were optimised at 10 wt% when crosslinked with dithiothreitol (DTT) at a 3:1 norbornene:thiol ratio. Physical properties of GelNOR were conserved whilst electrical conductivity was significantly increased at 0.5 mg/ml GNR concentration, and this resulted in improved neurite outgrowth from PC12s in co-culture with nHDFs in the EC hydrogel. DPSCs acted to increase PC12 proliferation in native GelNOR but were adversely affected by GNR presence in the final constructs.

Increased neurite extension in the EC vs native hydrogel shows the potential of GNR/GelNOR hybrid hydrogel for use in SCI repair, and the ability of DPSCs to improve proliferation of neural cells in GelNOR shows the potential of DPSCs and GelNOR for use in SCI repair.

# Table of Contents

# List of Tables

# List of Figures

# Chapter 1
# Introduction and Literature Review

## 1.1  Spinal Cord Injury

Every year over 500,000 people worldwide suffer a spinal cord injury (SCI), of which up to 90% are caused by some kind of trauma, the leading causes being motor vehicle accidents (47%), sports injuries (24%), falls (12%) and violence (7%) (Hulsebosch, 2002). The demographic with highest prevalence of SCI are males aged 18-32 years, with males in this age group more than four times more likely to suffer an SCI than their female counterparts, and in developed countries a second demographic of males and females over the age of 65 years is also seen, most likely due to an increasing aging population (B. B. Lee *et al.*, 2014).

The effects of SCI are highly variable with the level at which the SCI has occurred and the extent of the damage to the spinal cord. Whilst the most obvious effect is loss of somatic motor control over nerves below the level of the injury, there are wide-ranging implications for the autonomic nervous system as well, which can potentially have an even bigger impact on a patient's day to day life than the loss of movement. In a study analysing the treatment priorities of 681 SCI patients, (Anderson, 2004) found that for many patients it was the autonomic effects of their injury that were of biggest concern. Responses to Anderson's study showed that bowel/bladder control to some level is considered by many SCI patients to be more important to improve quality of life than regaining walking movement, as is regain of sexual function. Loss of bladder and bowel control can be significant even in patients with an SCI at a relatively high cervical level (Sayılır, Ersöz and Yalçın, 2013), and the loss of ability to fully empty the bladder can lead to future problems with urinary infections. Patients with an SCI above C5 are also at higher risk of long-term co-morbidities due to immune suppression, resulting from the disruption of communication between the brain stem and the spleen, causing abhorrent plasticity (Ueno *et al.*, 2016). Further co-morbidities include respiratory complications due to disconnection of the inter-costal muscles responsible for removal of secretions, neuropathic pain, pressure sores and osteoporosis related to immobility, loss of body temperature regulation, and more.

The high prevalence of SCI in young adults combined with less than 1% of patients achieving a full recovery by time of hospital discharge results in many SCI patients living with a long-term disability, which as discussed can be severe.  As a result, 20-30% of SCI patients show clinically significant signs of depression, and SCI patients are 2-5 times more likely to die prematurely (WHO, 2013).

Further to the human cost of SCI, the economic cost should also be considered. Due to the high levels of care needed, and the long-term nature of an SCI, in the UK alone the estimated overall cost of SCI related care to the NHS is £1 billion per annum (Spinal Research UK). The overall economic cost is likely much higher however, when a 60% unemployment rate for SCI patients is taken into account, combined with lost productivity for family who must act as part or full-time carers.

## 1.2  Structure and Function of the Spinal Cord

### 1.2.1  Macroscale

The spinal cord is part of the central nervous system (CNS), and it's primary function is to transmit information between the brain (also CNS) and the peripheral nervous system (PNS). This allows motor control of the body through impulses transmitted from the brain to the PNS, and for the brain to register sensory feedback through impulses transmitted from the PNS to the brain. Spinal cord tissue is highly anisotropic and is split into uni-directional ascending and descending tracts, with ascending tracts taking information from the PNS to the brain and descending tracts taking information from the brain to the PNS (Cramer and Darby, 2013).

At a high level, the spinal cord can be segmented into grey and white matter. Grey matter contains neuronal cells oriented along the length of the spinal cord, as well as supporting glial cells and capillaries. White matter surrounds the grey matter and is largely composed of axons running perpendicular to the neurons of the grey matter and supporting glial cells and capillaries (Watson and Kayalioglu, 2009).

The spinal cord is surrounded by the meninges, which act as a functional barrier and consists of three layers, as shown in Figure 1.1 (A), the pia mater (the innermost layer), arachnoid mater, and dura mater (outermost layer), with the space between the pia mater and arachnoid mater being filled with cerebrospinal fluid (CSF) (Cramer and Darby, 2013).
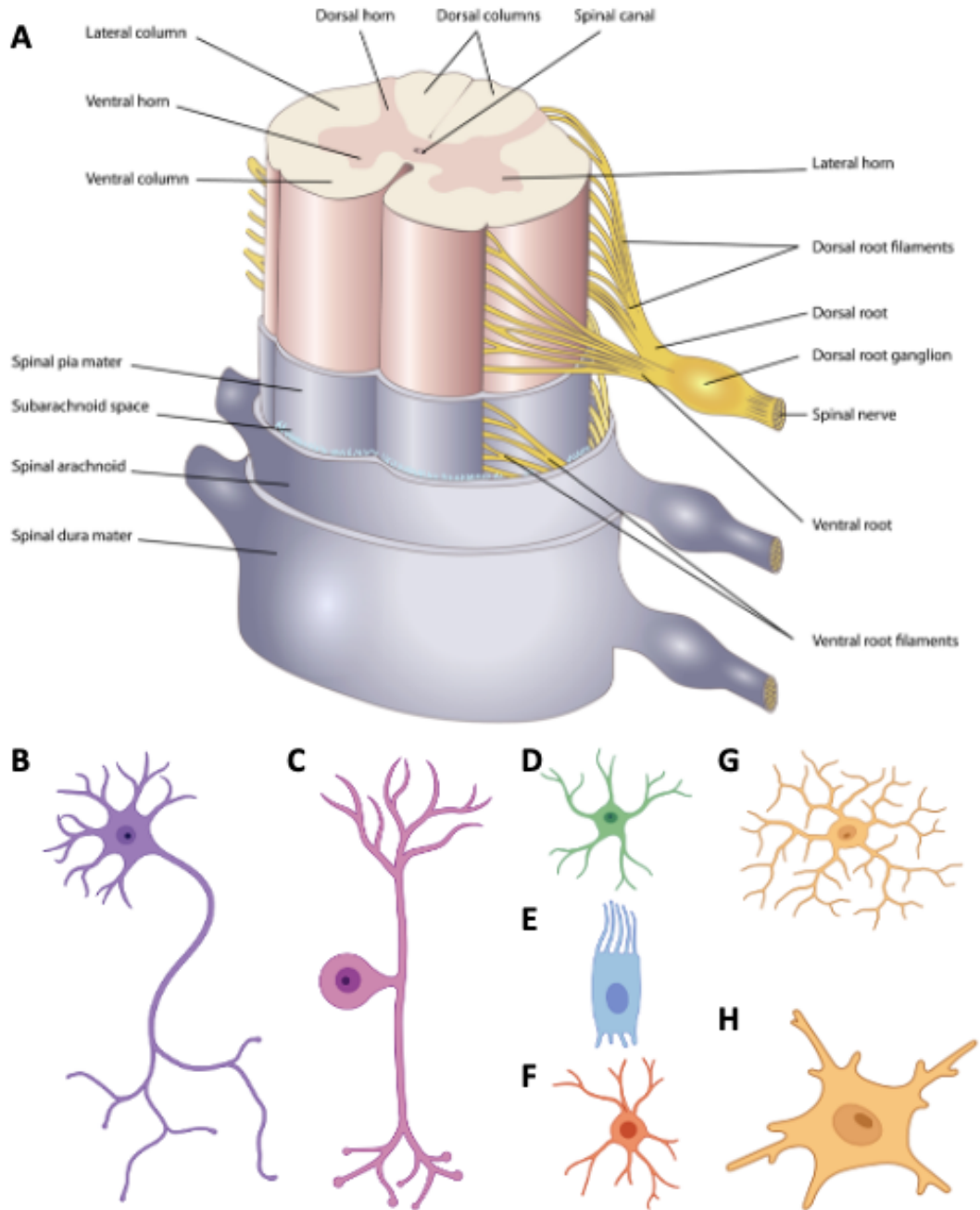
**Figure 1.1 - Macro and cell scale anatomy of the spinal cord.** (A) Macroscale anatomy of the spinal cord with cross section showing grey and white matter and meninges, and cells of the spinal cord including (B) motor neuron, (C) sensory neuron, (D) astrocyte, (E) ependymocyte, (F) oligodendrocyte, (G) 'steady-state' microglia, (H) 'active-state' microglia. Figure adapted and modified from BioRender and Shutterstock.

## 1.2.2 Microscale

At the cellular scale, the spinal cord primarily consists of neurons and supporting glia and extra-cellular matrix (ECM), which provides physical structure and support for cells.

### 1.2.2.1 Neurons

Neurons are an electrically excitable cell type that are able to receive electrical impulses through small projections called dendrites and conduct or generate their own electrical impulses along long processes called axons. There are three types of neuron in the spinal cord: motor neurons, which carry information from the brain and project to muscles and glands, sensory neurons which project to the brain and carry information from the PNS, and spinal interneurons, which connect other neurons within the spinal cord (Tortora and Derrickson, 2014).

Bundles of sensory neurons make up the ascending tracts which takes information from the PNS to the brain. These neurons, show in Figure 1.1 (B), are functionally unipolar and can be characterised as either unconscious or conscious, dependent on the tract that they are bundled into. Unconscious pathways are found in the spinocerebellar tracts and carry unconscious feedback from the muscles to the brain, whereas conscious pathways such as are found in the dorsal column-medial lemniscal (DCML) tract and spinothalamic tract are responsible for transmitting conscious signals such as touch, pressure, pain, and temperature (Tracy, 2015).

Unlike sensory neurons, motor neurons are multi-polar (Figure 1.1 (A)) and carry information from the brain and project to glands and skeletal, cardiac, and smooth muscle. Somatic motor neurons innervate skeletal muscle and visceral motor neurons relay information to the ganglionic neurons of the PNS, connecting with the autonomic nervous system to control smooth muscle, cardiac muscle, and glands (Stifani, 2014).

Spinal interneurons are also multi-polar and process information from sensory neurons and connect them to motor neurons to elicit an effector response (Fehlings *et al.*, 2020). Interneurons can be classified into local and propriospinal neurons, with local interneurons being responsible for reflexes and propriospinal neurons connecting different spinal segments. These neurons can also be classified as excitatory or inhibitory based on whether they release neurotransmitters such as glutamate or glycine (Sagner and Briscoe, 2019).

### 1.2.2.2 Glial cells

Around the neurons which are responsible for electrical impulse transmission, there are a number of types of supporting glial cells, which are responsible for maintainence and homeostasis of the spinal cord environment, supporting the primary functions of nervous transmission. Glial

cells in the CNS include ependmyocytes, astrocytes, oligodendrocytes, and microglia.

Ependymocytes, shown in Figure 1.1 (E) are found in the ependymal layer in the centre of the spinal cord. Ependymocytes produce and regulate cerebrospinal fluid (CSF), the clear and colourless liquid that provides nutrients, removes waste, and protects the CNS (Telano and Baker, 2018). As part of their role controlling the composition of CSF, ependymocytes modulate ion concentration and trophic and metabolic activity (Del Bigio, 2010).

Oligodendrocytes, shown in Figure 1.1 (F), are responsible for myelination in the CNS and have multiple long processes with specialised myelin extensions that wrap around axons and form internodes approx. 200 μm in length, separated by gaps of <1 μm known as nodes of Ranvier (Baumann and Pham-Dinh, 2001). The myelin sheath created by the oligodendrocytes allow increased conduction velocity of nervous impulses at lower energy requirements, with myelinated axons able to achieve conduction velocities more than an order of magnitude greater than unmyelinated axons (Salzer and Zalc, 2016).

Oligodendrocytes also perform a number of roles outside of myelination, though many of these are poorly understood. Though it is well accepted that oligodendrocytes play a role in supporting axonal health, largely through the provision of proteins such as proteolipid protein through myelin ensheathment, more recent evidence also suggests roles in energy provision via lactate shuttling and intra-axonal vesicle transport via exosomes (Philips and Rothstein, 2017).

Astrocytes, shown in Figure 1.1 (C), are a further type of supporting glial cell that form networks between themselves, neurons, and vasculature, to support the transmission of nervous impulses through the spinal cord (Sofroniew and Vinters, 2010). The most important roles of astrocytes is to support the functioning of synapses between neurons, nodes of Ranvier, and the vasculature.

Astrocyte processes enclose synapses, forming tripartite structures that control the fluid, ion, pH, and neurotransmitter concentration, all of which are essential for correct synapse functioning (Simard *et al.*, 2003). To exert this control, astrocytes interact with synapses through both contact mediated and secreted cues that alter the density of receptors, affecting the overall functioning of the neurotransmitter/receptor interaction. Similarly, astrocytes

interact with nodes of Ranvier through secretory mechanisms, such as the release of cell adhesion molecules that stabilise the node architecture (Serwanski, Jukkola and Nishiyama, 2017).

The final significant role of astrocytes is their interaction with the CNS blood supply. Astrocytes surround all blood vessels in the CNS and are able to control blood flow through the secretion of vasodilating or vasoconstrictive factors such as nitric oxide and arachidonic acid (Iadecola and Nedergaard, 2007). Through this interconnection between capillaries and energy consuming cells, astrocytes are able to control and distribute the supply of energy to the CNS, though the exact mechanisms through which they achieve this distribution is still not agreed upon in the literature (Bak and Walls, 2018).

Microglia are phagocytes that reside in the CNS and are responsible for immune function (Garaschuk and Verkhratsky, 2019). Microglia are homogenously distributed throughout the CNS and in the spinal cord are generally in one of either an 'activated' or 'steady' state. In a steady-state, during normal functioning of the CNS, microglia are highly branched, as shown in Figure 1.1 (F), and are able to sample their immediate environment through contacting other neuronal and glial cells and vasculature (Tremblay *et al.*, 2011). In steady state functioning, microglia are involved with a number of maintenance functions within the spinal cord such as secretion of neurotrophic factors such as BDNF to modulate neuronal cells and promote growth, and synaptic stripping, the process of removing redundant or damaged synapses through phagocytosis (Sierra *et al.*, 2010).

In response to injury, microglia enter an 'activated' state, during which their steady state branched processes retract into the cell body and are replaced with new processes that facilitate cell motility as shown in Figure 1.1 (F) (Parakalan *et al.*, 2012), allowing the microglia to move around the spinal cord environment and respond to foreign objects.

### 1.2.2.3 Extra-cellular Matrix

The ECM of the CNS is highly specialised and contains large amounts of proteoglycans and glycoproteins, which is different from the ECM of most tissues which contain more fibrillar collagens and fibronectin. This is likely the reason that CNS ECM has such a high water content and as a result is mechanically significantly weaker than that of other tissue (Bartlett, Choi and Phillips, 2016). There are three main regions of ECM in the spinal cord: the basement membrane around blood vessels; the condensed regions around

cell bodies, dendrites and axons known as perineuronal nets; and interstitial matrix around the functional aspects of the spinal cord (Lau *et al.*, 2013).

The basement membrane provides structural support, allowing cellular components to attach to the vasculature, and is mainly composed of type IV collagen with laminin and fibronectin attached, facilitating integrin mediated cellular adhesion (Sarrazin, Lamanna and Esko, 2011).

Perineuronal nets are involved in synaptic stabilisation and are largely composed of hyaluronan, chondroitin sulphate proteoglycans (CSPGs) and tenascin R (Kwok *et al.*, 2011). Tenascin is exclusive to the CNS ECM and is produced by oligodendrocytes and some neurons to aid perineuronal net formation (Burnside and Bradbury, 2014).

The interstitial matrix fills gaps between neurons and glial cells and is similarly composed to perineuronal nets, but with the addition of type IV collagen and laminin (Lau *et al.*, 2013), but with the difference that interstitial matrix is significantly less dense than that or perineuronal nets.

## 1.3 Pathophysiology of SCI

The initial traumatic SCI is generally the result of a contusive, compressive, or stretching injury (Perale *et al.*, 2011). This initial primary injury results in neurological damage caused by the ingress of the bony vertebrae into the spinal cord, and neurological cell death caused by mechanical and ischaemic insult is immediate. This initial injury also triggers a cascade of responses known as secondary injury.

### 1.3.1 Mechanisms of Secondary SCI

Secondary SCI occurs in the timeframe of minutes to weeks after the initial primary injury, and is characterised by ischemia, anoxia, free-radical formation, and excitotoxicity (Hulsebosch, 2002). Mechanical damage to the vasculature caused by the primary injury can cause haemorrhaging in the spinal cord and a breakdown of the blood/brain barrier, allowing ingress of inflammatory cells (Silva *et al.*, 2014) into the CNS. Reactive oxygen species (ROS) released by the inflammatory cells and other formed free radicals cause further cell death/damage through cell membrane peroxidation, resulting in loss of neuronal function. Though there is no doubt that these inflammatory cells are responsible for further neurological damage during the secondary phase, studies have also shown that inflammation plays an important role in neural tissue repair (Donnelly and Popovich, 2008), and that the difference between a destructive and constructive inflammatory

response to SCI may be only be the speed of its onset (Klusman and Schwab, 1997).

Further cell death is potentiated by the release of intracellular amino acids from damaged cells, resulting in excessive activation of glutamate receptors and further neuronal death due to this excitotoxicity (Park, Velumian and Fehlings, 2004). Apoptosis has also been identified as a major cause of cell death during secondary SCI, and occurs not only in neurons, but also in glial cells such as oligodendrocytes (Zhang *et al.*, 2012), which contributes to de-myelination of axons and further disruption of neural signals through the site of injury, even in pathways that are conserved. This triggering of neuronal and oligodendrial apoptosis may be related to upregulation of cell cycle proteins in neurons and glia as a result of SCI (Byrnes *et al.*, 2007).

As a result, secondary injury has the effect of actively increasing the extent of the damage caused by the initial mechanical insult, such that the damage caused during the secondary phase may even be greater than that caused by the initial injury. Further to this, alongside the described mechanisms of secondary SCI, other changes occur in the microenvironment around the injury site which act to impede any endogenous recovery through both chemical and physical means.

### 1.3.2  Molecular Inhibition of Axonal Growth

The mode of chemical inhibition is primarily through the presence of inhibitory molecules within the microenvironment, such as myelin-associated glycoprotein (MAG), oligodendrocyte myelin glycoprotein (OMgp), and Nogo-A (Filbin, 2003). These molecules are associated with myelin disruption/breakdown during both primary and secondary SCI, and when released into the spinal cord microenvironment have an inhibitory effect on axon growth. These myelin associated proteins share common receptors and act through the Rho pathway (Wang *et al.*, 2002), and ultimately its effector protein Rho-associated kinase (ROCK), which causes collapse of the neuronal growth-cone by targeting the actin and microtubule cytoskeleton, effectively suppressing neurite outgrowth (Monnier *et al.*, 2003).

### 1.3.3  The Glial Scar

The other way in which molecules in the injury microenvironment act to suppress neural repair is through formation of the glial scar which is composed largely of proteoglycans, the most well recognised of which are chondroitin sulphate proteoglycans (CSPGs), which are expressed by

reactive astrocytes after SCI (McKeon, Jurynec and Buck, 1999). This glial scar acts as a physical barrier to regeneration, stopping axons from sprouting and re-growing from the distal and proximal stumps into the site of injury, and is often cited as a key barrier to overcome in future SCI repair (Silver and Miller, 2004). Though the inhibitory effect of the glial scar on neural regeneration is well known, studies have also shown that in the acute phase of SCI, glial scarring also seems to play a role in limiting further damage after injury. This was evidenced by Sabelstrom and colleagues who showed significantly greater cavity formation after SCI when the glial scar was suppressed (Sabelstrom *et al.*, 2013).

The glial scar continues to grow and remodel after the time-period generally associated with secondary SCI has elapsed, and there still remains marked changes in the microenvironment post-SCI when compared with the non-pathological condition, which act to inhibit neural regeneration. This continued altered state is often referred to as the 'chronic phase' of SCI and is characterised by continued connective tissue deposition and glial scarring, white matter demyelination, and grey matter dissolution (Silva *et al.*, 2014). During this ongoing phase, SCI patients are also likely to develop chronic pain, with a study of 73 SCI patients by (Siddall *et al.*, 2003) finding that 83% of participants reported experiencing some kind of chronic pain at a 5-year follow up.

## 1.4  Current Clinical Treatments for SCI

Due to the time between injury and arrival at hospital, primary SCI is not a viable therapeutic target, and thus much of current treatment focuses on limiting further neurological damage during secondary SCI, and promoting functional recovery through neural plasticity.

### 1.4.1  Acute Surgical Interventions

The only surgical intervention commonly used in SCI patients is decompression, which aims to relieve pressure caused by ingress of hard tissue into the spinal cord during primary SCI by re-alignment of vertebrae that have moved during the initial injury, possibly combined with fixation (Brunette and Rockswold, 1987). The merits of decompression surgery have been the subject of much debate in recent years, and the literature on the subject is far from in agreement, this is likely due to the inconsistent nature of SCI and inconsistencies in the reported timing of the procedure. However, a review by (Fehlings and Perrin, 2005) found that more studies reported

early decompression to have a positive impact on recovery than reported no impact or negative impact. In recent years the implications of the timing of intervention have been more widely recognised, with a more recent meta-analysis by (Liu *et al.*, 2016) finding that SCI patients who underwent decompression surgery within 24 hours had significantly improved outcomes in terms of motor scores, neurological recovery rate, length of hospital stay, and reduction of complications, when compared to those who had to wait more than 24 hours.

## 1.4.2 Pharmacological Suppression of Secondary SCI

The use of pharmacological agents to limit secondary damage and support neurological recovery has long been identified as a possible way of treating SCI. Currently the drug most commonly prescribed for SCI treatment is methylprednisolone (MP), a corticosteroid that acts to decrease the inflammatory cycle by dampening the inflammatory cytokine cascade, acting to inhibit T-cell activation, decrease immune cell invasion into the CNS, and facilitating immune cell apoptosis (Sloka and Stefanelli, 2005). MP has however been the subject of much controversy as to its efficacy and possible dangerous side effects such as gastrointestinal bleeding, which lead to the American Association of Neurological Surgeons (AANS) to state that "*Treatment with methylprednisolone for either 24 or 48 hours is recommended as an option in the treatment of patients with acute spinal cord injuries that should be undertaken only with the knowledge that the evidence suggesting harmful side effects is more consistent than any suggestion of clinical benefit*" (AANS/CNS, 2002). A recent meta-analysis and systematic review by (Evaniew *et al.*, 2016) found that overall MP was not  associated with an improved long-term motor score recovery, but was significantly associated with side-effects such as gastrointestinal bleeding. The study did however suggest that short term-motor score may be improved when MP was administered within 8 hours of SCI, but stated that "*risk of bias and imprecision limit confidence in these findings*". Overall the authors concluded that their findings supported the current guidelines against routine use of MP.

Other possible pharmacological solutions to have been studied in large multi-centre clinical trials include monosialotetrahexosylganglioside (GM-1), thyrotropin-releasing hormone (TRH), and naloxone, of which GM-1 was not found to significantly improve primary outcome measure (Geisler *et al.*, 2001), and neither was naloxone (Bracken *et al.*, 1990). TRH was found to improve motor, sensory, and sunnybrook scores in incomplete SCI patients

only, however this finding was based on results for only 6 treated and 5 placebo patients at a 4-month follow-up (PITTS *et al.*, 1995).

### 1.4.3 Physical Therapy

The final way in which SCI patients are treated during the chronic phase of SCI is through physical therapy, which aims to maximise functional recovery through the use of neural plasticity in pathways that are conserved post-SCI. The process of neural plasticity refers to the remodelling of the CNS through neuronal re-organization, changes in activation patterns, synaptic rearrangements, and axonal sprouting (Silva *et al.*, 2014). The CNS is able to undergo extensive plasticity in response to stimuli such as learning, skill acquisition, and injury response, and was initially demonstrated in cats (Rossignol *et al.*, 1999) that were unable to support their own bodyweight post-SCI but were trained to walk on a treadmill. A recent study by (Garcia-Alias *et al.*, 2015) showed rats regaining skilled hand function lost upon severance of the corticospinal and rubrospinal tracts, by the compensatory remodelling of the reticulospinal tract, demonstrating the enormous malleability of the CNS, and in particular the reticulospinal pathways. These findings translate well in to human patients, with (Hicks *et al.*, 2005) finding that body-weight supported treadmill training three times a week for twelve weeks improved treadmill walking ability and subjective wellbeing of patients with incomplete SCI. As a result, locomotor training and physical therapy is now a standard for patients with incomplete SCI.

## 1.5 Novel Therapeutic Targets in SCI

As understanding of the pathophysiology of SCI and secondary SCI develops, so does the identification of potential targets for SCI treatment. By targeting specific aspects of secondary SCI, it is possible to reduce related death/damage of neural tissue, and to create a microenvironment conducive to neural repair and regrowth.

### 1.5.1 Reduction of Excitotoxicity

Excitotoxicity has been identified as a major cause of neuronal death immediately post-SCI due to a pathological influx of sodium ions. The use of sodium channel blockers such as mexiletine, phenytoin, and riluzole has been demonstrated to reduce the excitotoxic effect significantly and provide powerful neuroprotection in rat models of SCI (Ates *et al.*, 2007), however this study administered the treatment immediately after injury, a clinically unrealistic timescale. Questions about timing of treatment in the (Ates *et al.*,

2007) study have however been answered by (Grossman *et al.*, 2014), who demonstrated a significant increase in combined motor score in patients with cervical SCI when treated with riluzole in a phase I clinical trial, which also demonstrated its safety.

### 1.5.2 Modulation of the inflammatory response

One of the most significant possible targets in SCI treatment is the destructive inflammatory response triggered by SCI, the negative effects of which are well defined, resulting in the use of MP to treat SCI due to its anti-inflammatory effects. Though as discussed, the effect of MP in SCI treatment is controversial, a number of anti-inflammatory agents have been demonstrated to have neuroprotective properties post-SCI in animal models. The use of monoclonal antibodies, by (Mabon, Weaver and Dekaban, 2000) to block binding of β2 integrin on monocytes and macrophages to vascular adhesion molecule-1 (VCAM-1), and by (Bao *et al.*, 2004) against leukocyte integrin CD11d acted to reduce invasion of the respective immune cells into the CNS, thus reducing reactive oxygen/nitrogen species in the injury microenvironment and improving tissue preservation and neurological function. Further to this, (Arnold and Hagg, 2011) reported that treatment with anti-inflammatory minocycline 6 weeks post-SCI caused a significant improvement in locomotion in a mouse model of thoracic SCI, which then diminished a week after treatment termination. These findings also imply a role for inflammation, and thus anti-inflammatory treatment, in the chronic phase of SCI in which some aspect of the inflammatory response reduces neuronal connection through the injury site on an ongoing basis.

Non-steroidal anti-inflammatory drugs (NSAIDs) are already widely used in the clinic for pain relief and reduction of inflammation and one of these drugs, ibuprofen, has been identified as also having an inhibitory effect on RhoA, a known inhibitor of axonal re-growth post-SC (Fu, Hue and Li, 2007). Further studies have shown the ability of ibuprofen to reduce RhoA mediated inhibition of axonal sprouting in-vitro, and promote axonal re-growth in a rat contusion model, with subsequent behavioural and histological improvements (Wang *et al.*, 2009). This combination of anti-inflammatory action and Rho pathway inhibition identifies ibuprofen as a potentially powerful treatment post-SCI, however, the dosage used in these studies may be much higher than is thought clinically safe when converted to humans (Kwon *et al.*, 2011).

### 1.5.3 Suppression of Inhibitory Factors

Similarly to ibuprofen, other studies have sought to target the Rho-ROCK pathway as it is a point of convergence for a number of inhibitory factors, such as the previously discussed myelin-associated glycoproteins for which RhoA is an effector (Forgione and Fehlings, 2014). Studies of compounds that antagonise this pathway such as C3 transferase have seen long-distance axon regeneration and more rapid recovery of locomotion and forelimb-hindlimb co-ordination in mice post-SCI (Dergham *et al.*, 2002). Further to the success seen in animal studies, promising results have also been seen in phase I/IIa clinical trials treating SCI patients with a recombinant Rho protein antagonist BA-210 (Fehlings *et al.*, 2011).

A more easily accessible antagonist of myelin-associated axonal growth inhibitors is green tea. The polyphenols in green tea have been shown to be strong anti-oxidants, resulting in reduced oxidative stress and protection of spinal neurons (Zhao *et al.*, 2014). Further to this, epigallocatechin-3-gallate (EGCG), the active ingredient in green tea has been shown to prevent Nogo-A mediated neurite outgrowth inhibition and growth cone collapse, even at extremely low concentrations, which may be clinically significant as drinking green-tea results in small amounts of EGCG reaching the brain (Gundimeda *et al.*, 2015).

### 1.5.4 Inhibition of the Glial Scar

Some studies have sought to improve post-SCI recovery by targeting the physical barrier of the glial scar, with the hope that it's removal will allow a more permissive environment for axonal re-growth. Within the glial scar, CSPGs have been identified as inhibiting axonal growth by both physical and molecular mechanisms; physically the dense mesh of CSPGs and glia that make up the scar act to block axonal growth (Bradbury and Carter, 2011), and studies have also shown them to be potent molecular inhibitors of axonal growth, demonstrated by the preferential growth of chick DRG neurons on laminin stripes and their avoidance of stripes containing CSPGs in stripe assays (Snow *et al.*, 1990).

The enzyme chondroitinase ABC (ChABC) acts to separate the chondroitin sulphate GAG chains from the CSPG molecule (Yamagata *et al.*, 1968), preventing CSPG from interacting with matrix glycoproteins, and thus inhibiting the glial scar. In the previously described study by Garcia-Alias and colleagues (Garcia-Alias *et al.*, 2015), the authors successfully used ChABC to degrade CSPGs in the injury microenvironment and provide an

environment more permissive to neural re-growth. This study is perhaps not the best example however, as the ChABC animals also underwent physical therapy, which the control group did not. A number of other studies, however, have shown treatment with ChABC alone to be enough to improve recovery post-SCI, such as Tester and Howland (Tester and Howland, 2008), who found that ChABC treatment of thoracically hemisected cats produced accelerated recovery of skilled locomotion, and recovery of certain aspects of skilled locomotion to a greater than extent to in those not treated with ChABC.

### 1.5.5  Activation of Central Pattern Generators

The final therapeutic target currently under investigation in SCI repair that is worth considering, is the attempts to access those circuits below the SCI that are conserved post-SCI, but are inaccessible due to the inability of neuronal transmissions to pass through the site of injury. As previously described, these circuits may be accessed via means of neural plasticity, amplified through the use of physical therapy, and some studies have also sought to access these circuits by increasing activation through artificial means.

The use of the 5-hydroxytryptamine (5-HT) agonist quipazine was described by (Rossignol, 2000) in cats with large spinal lesions, as increasing the speed and regularity of walking, as well as the weight-bearing ability. Similarly, the use of epidural electrical stimulation by (Ichiyama *et al.*, 2005) in rats after complete spinal cord transection resulted in stepping motions that were dependent on sensory feedback of weightbearing. When combined with quipazine, the effect of epidural stimulation on bipedal stepping was increased further than with either quipazine or epidural stimulation alone (Ichiyama *et al.*, 2008). Both of these treatments clearly act to access central pattern generators (CPGs) which are present in the animal below the level of the SCI, as is particularly well evidenced by the complete transection model used in by Ichiyama (Ichiyama *et al.*, 2005, 2008). This raises the question of how well these findings will translate into humans, as though humans do also possess CPGs for actions such as walking (Danner *et al.*, 2015), due to the bipedal nature of human locomotion the brainstem is also required to maintain balance and posture (Takakusaki *et al.*, 2016), meaning rhythmic activity generated by CPGs at a spinal cord only level likely to be insufficient to achieve locomotion.

## 1.6  Cellular Therapies for SCI

### 1.6.1  Macrophages

As has been previously described, the immune response to SCI has both destructive and constructive effects, and thus there have been studies into the use macrophages to re-produce only the constructive parts of the immune response. Theory around the use of macrophages is conflicting, with Popovich and colleagues (Popovich *et al.*, 1999) showing that depletion of hematogeneous macrophages improved recovery in rat models of spinal-cord injury, agreeing with the need to suppress the host immune response during secondary SCI, whereas Schechter and co-workers (Shechter *et al.*, 2009) found that macrophages infiltrating the injury site played a key role in recovery through anti-inflammatory action in a mouse model of SCI. The reason for this conflicting evidence may be due to the distinct roles of macrophage sub-populations, with Kigerl et al (Kigerl *et al.*, 2009) showing two distinct sub-sets; the 'classical' pro-inflammatory M1, and the 'alternative' anti-inflammatory M2. The reason for the overall destructive nature of an unchecked host immune response to SCI is the much larger and more prolonged relative activation of M1 when compared to M2 macrophages. In their study, Kigerl showed that isolated M2 macrophages promoted axonal sprouting of dorsal root ganglion neurones over distances more than twice that allowed by M1 macrophages in-vitro (Kigerl *et al.*, 2009). Despite promising data around the use of macrophages in SCI, a multi-centre phase 2 clinical trial using an autologous incubated macrophage therapy to treat patients with acute, complete SCI, failed to show significant improvements in the primary outcome measure when compared to the control (Lammertse *et al.*, 2012).

### 1.6.2  Myelinating Cells

Due to the extensive de-myelination caused by SCI, and the resulting persistence of nerve fibres in an un-myelinated state, some studies have focused on the potential of glial cells to produce new myelin and restore conduction deficits (Hulsebosch, 2002).

Despite their usually residing in the peripheral nervous system (PNS) as opposed to the CNS, schwann cells (SCs) have been shown to invade the CNS upon SCI and assist in endogenous re-myelination and regeneration (Oudega and Xu, 2006). As a result, the use of SC transplants have been widely investigated for use in SCI repair, after their potential to guide axonal growth was demonstrated in tissue engineered peripheral nerve conduits

(Phillips *et al.*, 2005). Though a number of studies have used oligodendrocyte precursors (Li and Leung, 2015), the use of SCs as opposed to cell types native to the CNS is advantageous due to their relative ease of access in the PNS as opposed to CNS, and their ability to be readily expanded in in-vitro culture. Studies have shown transplanted SCs to improve neural repair and regain of function, such as by Takami and colleagues (Takami *et al.*, 2002), who found statistically significant improvements in both histological analysis of propriospinal and brainstem axon growth and improvement of hindlimb locomotor performance when compared to the control in a rat SCI model. Other innovative approaches have also been taken with SCs, such as by Kanno and colleagues (Kanno *et al.*, 2014), who genetically engineered SCs to secrete ChABC to suppress the glial scar and a bi-functional neurotrophin to promote new axonal growth, resulting in significant histological and functional improvements in a rat model of SCI. However in general, the improvements gained from SC transplant alone are not sufficient to cause regain of locomotor function (Kanno et al. 2015), and thus the role of transplanted SCs in SCI repair is likely to be to support other transplanted cell types, or as part of tissue engineered constructs. To this end, a much publicised study by Tabakow (Tabakow *et al.*, 2014), which used autologous sural nerve as a 'schwann cell bridge' in combination with autologous olfactory ensheathing cells to repair full SCI in a patient 21 months post injury, achieved a number of significant functional improvements such as recovery of sensation and partial recovery of voluntary movements in the lower extremities.

The olfactory ensheathing cells (OECs) used in Tabakow's study (Tabakow *et al.*, 2014) were expanded in culture after removal of one of the patients olfactory bulbs, which is fed by one of the most active sites of neurogenesis in adults, the sub-ventricular zone (Alvarez-Buylla and García-Verdugo, 2002). OECs have long been identified as having potential in SCI cell therapy, with the first clinical trials being carried out over a decade ago (Feron *et al.*, 2005). Since then, findings have been mixed as to the impact of OEC transplants, with some studies finding no significant neurological changes (Mackay-Sim *et al.*, 2008), and others finding modest neurological improvement (Tabakow *et al.*, 2013), however many of these studies acknowledge the experimental group size as being too small to make significant conclusions. A recent meta-analysis by (Watzlawick *et al.*, 2016) however, found an average of 19.2% increase in Basso, Beattie, and Bresnahan (BBB) score across 62 experiments comprising 1,164 animals, indicating the potential of OECs when used in an optimised protocol.

Interestingly this meta-analysis excluded any combination therapies and focused on treatments delivering OEC suspensions only, meaning the positive effect is likely to be underestimated as protocols such as those used by (Tabakow *et al.*, 2014) would be excluded.

### 1.6.3 Embryonic Stem Cells

Embryonic stem cells (ESCs) have been used extensively as a source of neural cell precursor, such as oligodendrocyte precursor cells (OPCs), due to the poor feasibility of using primary glia/neurons in cell related therapies due to issues around accessibility and ease of expansion in culture (Gordon, Amini and White, 2013). Implantation of mouse ESC derived neural precursors into a rat SCI model by McDonald and colleagues (McDonald *et al.*, 1999) showed these cells ability to survive and differentiate into glial cells (astrocytes, oligodendrocytes) and neurons, with concurrent functional improvements for the test rats. Further to this, Liu and colleagues (Liu *et al.*, 2000) demonstrated that ESC derived oligodendrocytes acted to myelinate axons in culture, but also to myelinate axons in myelin deficient mutant mice. This re-myelination activity of ESC derived oligodendrocytes was then reproduced in a rat SCI model by Kierstead et al (Keirstead *et al.*, 2005), but only when cells were transplanted during the acute phase of SCI. In 2009 American company Geron were given approval by the US regulator to commence clinical trials using hESC derived OPCs in SCI repair (Alper, 2009), but unfortunately the trial was abandoned after only a year after initiation despite encouraging preliminary results due to "capital insecurity and uncertain economic conditions" (Lukovic *et al.*, 2014). Further work by (Iwai *et al.*, 2015) has taken the use of ESC derived OPCs into a non-human primate model using contusive SCI in marmosets, and found significant improvements in motor functional recovery when compared to the control, but no further clinical trials have been initiated. The UK government has named regenerative medicine as one of its 'eight great technologies' (David Willets, 2013), in which the UK is perceived to be a potential world leader and will receive substantial government funding in the coming years, which perhaps will help to enable the initiation of further clinical trials by overcoming the problems cited in the Geron trial.

### 1.6.4 Induced Pluripotent Stem Cells

The reprogramming of fibroblast cells to an ESC like pluripotent state was first described by Takahashi and Yamanaka (Takahashi and Yamanaka, 2006), and since then the field of induced pluripotent stem cell (iPSC) research has grown exponentially. The reprogramming of adult cells into

pluripotency eliminates any issues around ease and ethics of access to ESCs, and subsequently iPSCs are now seen as the future pluripotent stem cell (PSC) of choice for many researchers. Initial concerns around the use of viral vectors to reprogram cells into pluripotency, and the use of potentially oncogenic genes such as c-Myc and Klf4 have been met by a number of alternative protocols removing the need for these elements, first achieved by Huangfu and colleagues (Huangfu *et al.*, 2008).

Despite their relatively recent discovery, iPSCs have already progressed into clinical trials using retinal pigment epithelial (iPSC-RPE) cells for treatment of age-related macular degeneration in Japan (Sayed, Liu and Wu, 2016), and though the trial was temporarily stalled due to a change in regulatory environment (Garber, 2015), progress in the field of SCI has been similarly rapid. Already studies have shown the ability of iPSCs to differentiate into OPCs and achieve re-myelination in-vitro and in-vivo in a similar fashion to ESCs in mouse SCI models (Kawabata *et al.*, 2016), and further to this iPSC derived neural precursors have been found to be safe and effective in promoting neural recovery in non-human primate models (Kobayashi *et al.*, 2012). These results, combined with improved accessibility and removal of ethical issues, suggest that iPSCs will almost certainly replace ESCs as a source of neural precursor cells for SCI repair in the future.

### 1.6.5 Neural Stem Cells

As well as derivation from a PSC source, neural stem cells (NSCs) also exist in the adult mammalian CNS in small quantities, and have also been used in SCI repair studies, these NSCs can be differentiated into neural precursor cells and then used as previously discussed. More often NSCs are derived from foetal CNS tissue and expanded due to obvious access issues with NSCs in adults. Reasons for potential preferred use of NSCs as opposed to ESCs include clear potential for differentiation into functional neurones and glia, and reduced propensity for tumour formation (Kim *et al.*, 2007), as well as ease of expansion in culture resulting in the ability to expand a therapeutically relevant population of cells from a much smaller amount of primary tissue when compared to ESCs (Okano *et al.*, 2003).

Transplanted NSCs, promoted to differentiate into neurons using a histone deacetylase inhibitor (HDACi), have been shown to produce dramatic improvements in hind limb function in a mouse model of SCI (Abematsu *et al.*, 2010). Further to this evidence for neuronal differentiation, other studies have successfully seen in-vivo differentiation of NSCs into astrocytes and oligodendrocyte, as well as neurons, in a non-human primate SCI model

(Iwanami *et al.*, 2005). NSCs have also reached clinical trials for SCI cell therapy in the form of foetal derived human NSCs, in chronic SCI from Neuralstem Inc, and in both cervical and thoracic acute SCI from Stem Cells Inc (Trounson and McDonald, 2015).

## 1.6.6 Mesenchymal Stem Cells

Though traditionally differentiation of mesenchymal stem cells (MSCs) has been thought to be limited to cells of osteogenic, chondrogenic, and adipogenic lineages, more recent studies have shown the ability of MSCs to differentiate across germ layers, and into neurons (Bae *et al.*, 2011). The nature of MSC derived neurons, and whether they are 'true' functional neurons or 'neuron-like' cells is the subject of much debate, and early studies that showed MSCs to take neuronal morphology and express neuronal markers were likely as a result of a stress response as opposed to true neuronal differentiation (Scuteri *et al.*, 2011). More recent studies have however shown functional differentiation to be possible in-vitro, such as MSCs differentiated to neurons by (Tropel *et al.*, 2006), who not only showed the expression of neuronal markers such as β3-tubulin, but also the functional characteristic of cytosolic calcium rise in response to neuronal activators. Despite the current work in-vitro, there is limited evidence for successful neural differentiation of MSCs in-vivo.

Though MSCs have seen success in animal models of SCI, it is generally due to non-neuronal replacement mechanisms, and it much more likely down to MSCs immunomodulatory properties (Ma *et al.*, 2014) allowing the creation of a more permissive environment for neural regeneration, as has been previously discussed. As an example, (Hofstetter *et al.*, 2002) found that the MSC derived neurons used in their study were unable to generate action potentials in-vitro and thus were not functionally useful, yet implantation of MSCs into a paraplegic rat model promoted host neural tissue survival, with concurrent functional improvements in gait. Upon histological analysis, the MSCs were found to be tightly associated with immature astrocytes which formed bundles bridging the epicenter of the injury. Interestingly, (Boido *et al.*, 2009) found that the immunomodulatory, non-neuronal replacement action of MSCs transplanted into a rat SCI model actually resulted in an improvement in functional recovery (as evidenced by grip test) that was greater than that in animals treated with ESC derived NSCs. This was despite the MSCs not expressing any neural markers, which the NSCs did, though it should be noted that due to wide variation the difference was not found to be significant. This evidence points to the

neuroprotective effect of the immunomodulatory MSC secretome as being the primary mode of action through which MSCs have potential in SCI cell therapy.

### 1.6.7 Dental Pulp Stem Cells

Dental pulp stem cells (DPSCs) have been investigated for use in SCI cell therapies, and have been shown to be suitable for promotion of SCI repair through numerous different mechanisms. DPSCs have been shown in multiple studies to be suitable for differentiation into neurons in-vitro (J.-H. Lee *et al.*, 2014; Osathanon *et al.*, 2014), and neuronally differentiated DPSCs have been confirmed to electro-physiologically active both in-vitro and in-vivo (Arthur *et al.*, 2008). Further to this, they have also been shown to be suitable for differentiation into glial cells, including schwann cells (Martens *et al.*, 2014), oligodendrocytes (Askari *et al.*, 2015), and astrocytes (Leong *et al.*, 2012). Interestingly, upon implantation into a rat contusion SCI model, a single culture of undifferentiated DPSCs has been shown to differentiate into neurons, astrocytes, and oligodendrocytes in-vivo (Taghipour *et al.*, 2012). The reason for this differentiation of a single culture into multiple different cell types may be explained by the work of Young and colleagues (Young *et al.*, 2016), who found significant clonal heterogeneity within a population of DPSCs recovered from a mouse incisor, and that within this population only cells with high nestin expression were suitable for differentiation into neurons or oligodendrocytes. DPSC implantation alone has also been shown to be enough to produce significant functional improvements in animal models of SCI; in rats as evidenced by significantly improved BBB scores (Nicola *et al.*, 2016), and in mice as evidenced by improved locomotion (de Almeida *et al.*, 2011).

Aside from the described ability of DPSCs to differentiate into neurons and supporting glia, they are also effective in supporting SCI recovery through non-cell replacement mechanisms. Similarly to MSCs, DPSCs are capable of suppressing inflammation, a key driver of secondary damage in SCI. This has been demonstrated by (Yamagata *et al.*, 2013) in a hypoxic/ischaemic stroke model in neonatal rats, in which the delivery of DPSCs or DPSC conditioned media acted to inhibit the expression of pro-inflammatory cytokines, and promote the expression of anti-inflammatory ones. Further to this, (Sakai *et al.*, 2012) found that as well as differentiating into oligodendrocytes, in a rat model of SCI transplanted DPSCs acted to inhibit neuronal and glial apoptosis (again a key driver of secondary damage in SCI), as evidenced by reduced staining of apoptotic markers. As well as

suppression of apoptosis in-vivo, (Sakai *et al.*, 2012) found that DPSC conditioned media suppressed the inhibitory effect of axonal growth inhibitors including CSPGs and MAG, as was evidenced by restoration of neurite outgrowth in neurons cultured on CSPG and MAG, which was not seen in neurons cultured in media conditioned by fibroblasts or MSCs.

The described results highlight DPSCs as being a particularly promising seed cell for use in cell based therapies for SCI, due to their ability to combat numerous different aspects of secondary SCI, whilst simultaneously being suitable for differentiation into a number of different neural cell types for neural regeneration through cell-replacement means.

### 1.6.8 Problems with Stem Cell Transplants in SCI

Though there is no doubt that cell therapies hold much potential in SCI repair, there are also a number of potential problems. With the use of PSCs, the ability to form a teratoma in-vivo is actually a defining characteristic, and as a result concerns have been raised about the oncogenic potential of PSC derived cells upon transplant (Bretzner *et al.*, 2011), as it would only take a small sub-population of cells not to be fully differentiated to potentially cause a teratoma upon implantation. Further to this, there has been much debate about the ethical issues surrounding extraction of ESCs and NSCs from embryonic and foetal tissue. Though these issues have been solved to an extent by the use of iPSCs, these cells have only been available for research for a relatively short time, and are subsequently less well defined.

Further to this it is a general problem that once stem cells have been implanted, there is limited control to specifically direct their ultimate cell fate. As a result, (Hofstetter *et al.*, 2005) demonstrated that stem cell implantation into a rat thoracic SCI had the potential to produce allodynia like responses, possibly due to the differentiation of implanted cells into sensory neurones.

## 1.7 Materials Based Approaches to SCI Treatment

As well as the biological approaches described, a number of studies have sought to use materials approaches to SCI treatment. Though these approaches are diverse, they generally use aligned polymer scaffolds to create a permissive environment and support axonal re-growth across the gap between distal ends of the spinal cord at the injury site.

### 1.7.1 Polymer Conduits

Nerve conduits have been used successfully to bridge gaps in damaged nerves in the peripheral nervous system (Pabari *et al.*, 2014), and as a result a number of studies have looked to bring the same theory into the central nervous system for SCI repair.

Early work in this area took the form of solid polymer constructs with channels running through them, such as the hollow silicone rubber tubes described by Borgens (Borgens, 1999). These scaffolds were often capable of supporting strong axonal growth through the internal channels, but were largely unsuccessful *in vivo* due to stress mismatches causing damage to the native tissue.

More modern imaginings of nerve guidance conduits take the form of bio-fabricated scaffolds made with techniques such as 3D printing to create complex 3D architectures (Jeong *et al.*, 2021). For example, the demonstration of Jiang and colleagues of a 3D printed collagen/silk fibroin scaffold that reduced glial scar formation in a rat transection model of SCI (Jiang *et al.*, 2020).

### 1.7.2 Electrospinning

One of the most promising areas of research using polymer constructs for SCI repair is that of electrospinning. Electrospinning uses voltage gradients between a polymer source and a grounded collector to and can produce a scaffold of aligned fibres with micrometre and nanometre diameters (Schaub *et al.*, 2016), and was first investigated for neural applications by Xu and colleagues (Xu *et al.*, 2004).

Since then, numerous studies have investigated electrospinning use in SCI repair and this wide use is likely driven by the wide range of FDA-approved polymers that are suitable for electrospinning, as well as being a highly tuneable system in terms of fibre size and alignment, making it suitable for use to meet a number of different approaches (Bhardwaj and Kundu, 2010). The ability of electrospinning to produce aligned constructs has been

leveraged by a number of researchers who have used them to promote aligned axon growth both *in vitro* and in rat models of SCI (Gelain *et al.*, 2010). This has more recently been taken further, and the ability of electrospun polymers to be loaded with proteins for controlled release has also been used in a number of studies to further direct the response of endogenous cells in response to SCI in rat models, through release of neurotrophic factors (Pan et al. 2019).

A significant drawback to electrospinning is the tendency of electrospun polymers to by hydrophobic thus decreasing cell attachment (Ikada, 1994), and as such successful electrospinning strategies often require further surface modifications of the spun fibres in order to manage this effect.

### 1.7.3  Hydrogels

Though both of the previously described materials approaches have both advantages and disadvantages, there is one key disadvantage to both of them. Though conduits and electrospun scaffolds are generally thought to be 3-dimensional scaffolds, in that they are not flat surfaces like a Petri dish, from a cellular perspective they still consist largely of 2D surfaces, just orientated or stacked in a different fashion.

The difference in behaviour of cells when cultured in 2D vs 3D is well known at this point, with a classic example being the tendency of human breast epithelial cells to mimic tumour cells in 2D culture but revert to normal growth behaviour when cultured in 3D (Petersen *et al.*, 1992). The change in behaviour between 2D and 3D culture is thought to be the result of changes in gene expression that rely on the way the cells interact with their environment. For example, in a 2D culture only half of the cell is able to interact with the culture scaffold, whilst the rest of the cell is exposed to the culture media and supplement molecules. This leads to highly polarized integrin binding and mechanotransduction not typical of cells in vivo, which effects the intracellular signalling experienced by the cell, which in turn affects the phenotypic fate of the cell (Gieni and Hendzel, 2008).

As previously suggested, though materials approaches such as the use of electrospun scaffolds and polymer channel conduits are 3D in terms of the space that they fill, from a cellular perspective many of these scaffolds still appear as 2D due to the small size of mammalian cells. This means that despite the scaffold being '3D', they do not avoid the problem of errant cell behaviour caused by 2D culture, which is a problem when using these scaffolds for *in vitro* modelling of native cell responses to the scaffold.

Hydrogels are a class of material in which polymer chains are dissolved into liquid and then triggered to form networks that encapsulate the liquid inside them (Ahmed, 2015), forming solid gels. These gels can be used to support cell culture in a way that is more 'truly' 3D on a cellular level, in that all surfaces of the cell are inside the gel, and they are not just attached via one surface.

The types of polymer chains and methods to trigger gelation are highly diverse, but hydrogels can be broadly split into the two categories of organic and inorganic. Organic hydrogels use naturally occurring polymers to form highly bioactive gels, which can be thought of as 'promotional' due to having a number of bioactive domains that can actively promote cellular activity such as the RGDS amino acid sequence. Inorganic, or synthetic, hydrogels on the other hand do not possess these same bioactive domains and thus cannot direct cellular behaviour in the same way as organic gels and in this way can be thought of as only 'permissive', but as a trade off they are highly tailorable (Klotz *et al.*, 2016).

Due to the trade-off between the tendency of organic gels to be biocompatible and bioactive through possession of specific domains but give poor control over mechanical characteristics, and the ability of synthetic gels to be highly tailorable but have low bioactivity, hybrid gels are generally thought to combine the best of both (Zhu and Marchant, 2014). These types of gels will often use an organic backbone consisting of a natural polymer like collagen or gelatin, and look to tailor the resulting gel through the addition of inorganic side chains, such as methacrylate groups, to improve control over physical aspects (Klotz *et al.*, 2016).

As an example, gelatin is an attractive organic polymer for use in hybrid hydrogels due to its biocompatibility, degradability, its low cost, and its ease of manipulation (Lai and Li, 2010). Further, it retains the bioactive domains present in base collagen whilst presenting lower antigenicity due to heat denaturation (Van den Steen *et al.*, 2002). Gelatin can easily be functionalised with synthetic side chains via a number of methods allowing gelatin based hydrogels to have diverse chemistries and different crosslinking methods in the final gel (Greene and Lin, 2015), the most common of which is likely gelatin methacryloyl (GelMA) which is crosslinked via a chain growth reaction.

A number of approaches using a-cellular hydrogels to treat SCI have been described in the literature. These approaches rely on the endogenous cell response to populate the hydrogel scaffold, and typically have used

topographical cues similar to the ones provided by conduits, such as the use of pre-formed multi-channel gels by Dumont and colleagues (Dumont *et al.*, 2019). Dumont showed increased axonal infiltration using these topographical cues in a rat hemi-section model, which was also found by Sun et al in a similar construct and hemi-section model, alongside increased endogenous stem cell recruitment (Sun *et al.*, 2019). Though these pre-formed hydrogels have shown promise for SCI repair, the need to preform gels in order to design in channels for axonal growth is at odds with the irregular geometry and stress sensitivity of a spinal cord lesion and thus the need for preformation is a barrier to use in clinical applications (Hlavac, Kasper and Schmidt, 2020). Instead, injectable hydrogels are likely to be the preferred solution for treatment of SCI due to their ability to form to the shape of the cavity which they are injected into. These hydrogels can be suitable as a vehicle for loading with various therapeutics intended to direct endogenous cellular activity post-implantation (Song *et al.*, 2019).

## 1.8  Tissue Engineering

Thus far the use of cell therapies and the use of biomaterials for treatment of SCI has been separately discussed. Tissue engineering is a multi-disciplinary research field that combines cells, biomaterials, and bioactive molecules such as cytokines and growth factors to direct cell behaviour (de Isla *et al.*, 2010), and thus would combine aspects of the previous sections together into tissue engineering strategies. A number of tissue engineering approaches have been described in the literature for treatment of SCI.

### 1.8.1  Tissue Engineering Approaches to SCI

A common problem with cell therapies in the central nervous system is the tendency of implanted cells not to persist at the target site and for stem cells the differentiation behaviour is not controlled after implantation (Vismara *et al.*, 2017). These problems can be solved to an extent through the use of materials scaffolds, that the cells are seeded onto, which will remain in place at the implantation site and thus make the seeded cells more likely to remain in place too. Further, these biomaterials can be functionalised with small molecules such as growth factors that will control stem cell behaviour post-implantation (Hlavac, Kasper and Schmidt, 2020).

Polymeric materials such as the electrospun scaffolds described in previous sections have been implanted in combination with cells in tissue engineering approaches to treat SCI, such as the adipose derived stem cells on an Emu

oil (EO)-loaded PCL/collagen nanofiber scaffold used by Netaji (Nejati *et al.*, 2020). These approaches have seen success but the previously described disadvantages of these solid materials remain, alongside the fact that these materials are by necessity pre-formed and cannot fit to an irregularly shaped SCI cavity in the same way that hydrogels can.

Cell laden hydrogels have been used extensively in tissue engineering approaches to SCI treatment and it has also been demonstrated that hydrogels containing natural components are able to illicit positive cellular responses (Hlavac, Kasper and Schmidt, 2020) *in vivo*. A number of the cell types previously described for SCI cell therapy have also been used in combination with hydrogel systems for delivery in tissue engineering approaches. Stem cells have been used, such as the iPSC derived neural progenitors used by Fuhrmann in combination with methylcellulose based hydrogel functionalised with RGD peptide to improve maturation of the cells *in vitro* (Führmann *et al.*, 2016). Immunomodulatory approaches have also been taken such as by Hong and colleagues who achieved improved functional recovery in a rat model of SCI using macrophages encapsulated in a Imidazole-poly (organophosphazenes) hydrogel (Hong *et al.*, 2017).

## 1.8.2 Electrically Conductive Scaffolds in Tissue Engineering Applications

A number of tissues in the body are electrically active, and thus it would make sense that a tissue engineered construct aiming to replicate that tissue would need to accommodate that electrical activity. Electrically conductive scaffolds have been used in tissue engineering approaches targeting electrically active tissues such as cardiac muscle patches (Navaei *et al.*, 2016), but have also been used in tissues that are not electrically active such as bone and cartilage (Balint, Cassidy and Cartmell, 2014).

There are a number of strategies for increasing the electrical conductivity of tissue engineering scaffolds and increased electrical conductivity has been demonstrated across a range of scaffold types, such as the use of doping of electrospun polymer with electrically conductive (+)-camphor-10-sulfonic acid (HCSA) as shown by Zhang (Zhang and Rutledge, 2012).

Focusing on the hydrogel context, there are two general approaches to increase electrical conductivity; to fabricate the hydrogel out of polymer with electrically conductive structure or side chains, or to incorporate electrically conductive particles into the hydrogel to improve construct conductivity (Min, Patel and Koh, 2018a). Though the approach of producing the base

hydrogel from electrically conductive polymers is generally thought to be more cell friendly and reproducible as problems related to nanoparticle cytotoxicity and distribution are removed, the use of nanoparticles is still generally preferred (Min, Patel and Koh, 2018a). This is due to the flexibility that nanoparticle incorporation offers by allowing the use of any base hydrogel rather than limiting to those that are already electrically conductive. Both of the described approaches have previously been taken by researchers working in the field of tissue engineering for SCI repair (L. Zhou *et al.*, 2018a; Zhang *et al.*, 2020).

Electrically conductive hydrogels have been used in tissue engineering across a range of tissues including skin, muscle, cardiac, and bone tissue, as well as in bioelectronics and drug delivery (Athukorala *et al.*, 2021)

### 1.8.3 Electrically Conductive Hydrogels in SCI Repair

Further to the tissues previously described, electrically conductive hydrogels have also been used in studies into SCI repair.

Xu and colleagues saw significantly improved locomotion in a rat model of SCI and accelerated differentiation of NSCs *in vitro* using a hyaluronic acid-graft-dopamine hydrogel matrix with increased conductivity due to incorporation of polydopamine modified germanium phosphide nanosheets. This study was particularly interesting as germanium phosphide is highly conductive but also biodegradable, meaning that it would not persist after hydrogel degradation in the same was as carbon or metallic nanoparticles (Xu *et al.*, 2021). Similarly, Zhou and colleagues found that by increasing tannic acid concentration, and thus electrical conductivity, in their hydrogels, they were also able to accelerate the differentiation of NSCs in-vitro and also found increased recruitment of endogenous NSCs after implantation *in vivo* (L. Zhou *et al.*, 2018a).

Use of these types of gel in the literature is largely as pure biomaterials, with few studies using these hydrogels as carriers for cells in tissue engineering approaches during *in vivo* studies, and instead opting to test with cells *in vitro* before implanting a-cellular gels into their animal models. Though much of the literature concerning the use of electrically conductive hydrogels in SCI repair has been within the last 5 years, the various successes of studies to this point identifies electrically conductive hydrogels as a promising method for treatment of SCI.

## 1.9  Summary and Project Aims

Based on the literature review, this project will seek to develop an electrically conductive scaffold for use in tissue engineering applications aimed at treatment of SCI. The scaffold will be based on a natural/synthetic hybrid hydrogel and will seek to use DPSCs as the chosen cell type.

The project will have two broad aims: firstly, the creation of an electrically conductive hydrogel scaffold, and secondly, the biological testing of this electrically conductive hydrogel scaffold, both in terms of its effect on model neural cells and its effect on DPSCs.

These aims will be achieved through completion of the following objectives:

- Selection and optimisation of a hydrogel and initiation system
- Translation of the selected hydrogel into an electrically conductive hydrogel through addition of electrically conductive components
- Creation of a 3D model neural cell system for testing
- Transfer of the created model system into the electrically conductive hydrogel for final testing
- Culture of DPSCs in electrically conductive hydrogel

# Chapter 2
# General Materials and Methods

## 2.1 Materials

### 2.1.1 Equipment

The following table documents the various pieces of equipment used in this project.

**Table 2.1 - List of equipment used herein, including supplier information**

| Equipment and Model | Supplier |
|---|---|
| Confocal Laser Scanning Microscope, SP8 | Leica, DE |
| Freeze drier, Alpha 1-2 Ldplus | Christ, DE |
| ImageJ Software | NIH, USA |
| Light unit, Omnicure S1000 | Excelitas, US |
| Modular Compact Rotational Rheometer, MCR302 | Anton Paar, AU |
| Plate reader, Varioskan Flash | Fisher Scientific, USA |
| Potentiostat, Metrohm Autolab B.V | Metrohm Autolab, GER |
| RStudio Software | RStudio |
| Scanning Electron Microscope, SU8230 | Hitachi, JP |
| Sputter Coater, Agar Auto | Agar Scientific, USA |
| Transmission Electron Microscope, FEI Titan3 Themis 300 | Fisher Scientific, USA |
| Ultracentrifuge, Avanti J26XP | Beckman Coulter, USA |
| Uni-axial compression testing rig, Criterion Model C45 | MTS, USA |

### 2.1.2 Antibodies

The following table documents the various antibodies used in this project.

**Table 2.2 - List of antibodies used herein, including supplier information**

| Antibody | Supplier |
|---|---|
| Chicken anti-rabbit Alexa Fluor 488 (A-21441) | Fisher Scientific |
| Goat anti-mouse Alexa Fluor 647 (A-21235) | Fisher Scientific |
| Mouse anti-CD31 IgG (VMA00321) | Bio Rad Laboratories, UK |
| Polyclonal rabbit anti-beta III Tubulin IgG (ab18207) | Abcam, UK |
| Rhodamine-Phalloidin (R415) | Invitrogen, USA |

## 2.1.3 Chemicals

The following table documents the various chemicals used in this project.

**Table 2.3 - List of chemicals used herein, including supplier information**

| Chemicals and reagents | Supplier |
|---|---|
| alamarBlue reagent | Bio-Rad Laboratories, UK |
| CellTracker Green™ | Fisher Scientific, USA |
| DAPI (4,6-diamidino-2-phenylindole) | Sigma Aldrich, UK |
| Dimethyl sulfoxide (DMSO) | Fisher Scientific, USA |
| Di-thiothreitol (DTT) | Sigma Aldrich, UK |
| DMEM Cell Culture Medium | Lonza, UK |
| EGM -2MV Cell Culture Medium and supplements | Lonza, UK |
| Fibrinogen from human plasma (F3879) | Merck, USA |
| Foetal Bovine Serum | Sigma Aldrich, UK |
| Gold (III) chloride trihydrate (HAuCl4) | Sigma Aldrich, UK |
| Hexadecyltrimethylammonium bromide (CTAB) | Sigma Aldrich, UK |
| Horse serum, heat-deactivated | Sigma Aldrich, UK |
| L-ascorbic acid | Sigma Aldrich, UK |
| L-Glutamine | Sigma Aldrich, UK |
| L-Glutamine, 200 mM | Sigma Aldrich, UK |
| LIVE/DEAD assay | Invitrogen, USA |
| Neutral buffered formalin, 10% | Sigma Aldrich, UK |
| Penicillin/Streptomycin | Sigma Aldrich, UK |
| Penicillin-streptomycin, 5000 U ml-1 | Sigma Aldrich, UK |
| Phosphate Buffered Saline (PBS) | Lonza, UK |
| Poly Ethylene Glycol-4SH | Sigma Aldrich, UK |
| Poly Ethylene Glycol-8SH | Sigma Aldrich, UK |
| Recombinant Human β-NGF | Bio-Legend, USA |
| RPMI 1640 Cell Culture Medium | Lonza, UK |
| Silver nitrate (AgNO3) | Sigma Aldrich, UK |
| Sodium Azide | Sigma Aldrich, UK |
| Sodium borohydride (NaBH4) | Sigma Aldrich, UK |
| Sodium Persulphate (SPS) | Sigma Aldrich, UK |
| Thrombin from human plasma (10602400001) | Merck, USA |
| Tris(2,2-bipyridyl)dichlororuthenium(II) hexahydrate | Sigma Aldrich, UK |
| Triton X-100 | Sigma Aldrich, UK |
| Trypan Blue | Fisher Scientific, USA |
| Trypsin/EDTA | Lonza, UK |
| α-MEM Cell Culture Medium | Lonza, UK |

### 2.1.4  Consumables

The following table documents the various consumables used in this project.

**Table 2.4 - List of consumables used herein, including supplier information**

| Consumable | Supplier |
|---|---|
| Histology cassettes | Fisher Scientific, USA |
| Indium tin oxide coated glass slides, surface resistivity 15-25 Ω/sq | Merck, US |
| TEM grids, Ultra-Thin Carbon on LC on 300 mesh Copper | EM Resolutions, UK |

## 2.2  Methods

### 2.2.1  Synthesis of Gelatin Norbornene

Gelatin-Norbornene (GelNOR) macromer was synthesised by partner research group, the Christchurch Regenerative Medicine and Tissue Engineering (CReaTE) Group, at the University of Otago, New Zealand, and was received freeze-dried. GelNOR is synthesised by reacting gelatin with carbic anhydride in order to graft norbornene rings onto the gelatin backbone.

The CReaTE group also characterised the degree of functionalisation (DOF) (i.e. the percentage of amine groups replaced with norbornene groups on the gelatin backbone) of each batch of GelNOR macromer to allow calculation of the moles of norbornene per mole of GelNOR.

## 2.2.2 Mass Loss and Swelling Studies

The soluble fraction and mass swelling ratio of a batch of hydrogel discs was determined using mass loss and swelling studies.

Hydrogel discs were weighed immediately post fabrication ($m_{initial}$). After weighing, half of the gels were immediately frozen in a -80 °C freezer. The remaining half of the gels were transferred to histology cassettes and swollen for 24 hours in 1 x PBS + 0.1% sodium azide.

After 24 hours the swollen gels were removed from PBS, blotted to remove excess liquid, and weighed again ($m_{swollen}$). Once weighed, these gels were also frozen in a -80 °C freezer. After 24 hours of freezing, all gels (both swollen and unswollen, now frozen) were transferred to a freeze-drier, and freeze-dried for 48 hours.

Post freeze drying, the gels were weighed a final time ($m_{dry\ t=0}$ for gels frozen without swelling, and $m_{dry}$ for gels frozen after swelling). The collected weights were then used to determine the gel's soluble fractions and swelling ratios, based on equations previously described in the literature (Mwangi and Ofner, 2004), (Deiber *et al.*, 2009), and (Martinez-Lopez *et al.*, 2011).

$$Mass\ Swelling\ Ratio = \frac{m_{swollen}}{m_{dry}}$$

$$Soluble\ Fraction = \frac{m_{initial.dry} - m_{dry}}{m_{initial.dry}}$$

where

$$m_{initial.dry} = m_{initial} \times Actual\ Macromer\ Fraction$$

$$Actual\ Macromer\ Fraction = \frac{m_{dry\ t=0}}{m_{initial}}$$

The gels which were frozen immediately after initial weighing, without swelling, were used to calculate Actual Macromer Fraction, and this value was then used to calculate the Soluble Fraction using the gels which had been swollen.

### 2.2.3 Gold Nanorod Synthesis

GNRs were fabricated using a seed-mediated growth method adapted from Nikoobakht and El-Sayed (Nikoobakht and El-Sayed*, 2003), which involved adding gold nanosphere 'seeds' to a growth solution.

#### 2.2.3.1 Preparation of Growth Solution

Hexadecyltrimethylammonium bromide (CTAB) (20 ml at 0.2 M) was warmed to 25 °C. Silver nitrate ($AgNO_3$) (1.12 ml at 0.004 M) was added to the CTAB slowly, under gentle stirring. Gold (III) chloride trihydrate ($HAuCl_4$) (20 ml at 0.001 M) was pre-warmed to 25 °C and added to the solution under gentle stirring, creating a deep yellow solution. After 60 seconds of mixing, L-ascorbic acid (280 µl at 0.0788 M) was added dropwise under fast stirring, causing the solution to turn colourless. After the addition of the L-ascorbic acid, the whole solution was warmed to 30 °C.

#### 2.2.3.2 Preparation of Seed Solution

CTAB (5 ml at 0.2 M) was warmed to 25 °C. $HAuCl_4$ (5 ml at 0.0005 M) was pre-warmed to 25 °C and added to the CTAB solution under gentle stirring, creating a deep yellow solution. To the stirred solution, ice-cold sodium borohydride ($NaBH_4$) (600 µl at 0.01 M) was added all at once under vigorous stirring, and was continued to be stirred vigorously for two minutes. After two minutes, stirring was turned off and the solution was kept at 25 °C until use.

#### 2.2.3.3 Seeding of Growth Solution

Once the growth solution was warmed to 30 °C, 48 µl of seed solution was added to the growth solution under stirring. After one minute the stirring was discontinued, and the static solution was left for 16 hours at 30 °C to allow GNR growth.

#### 2.2.3.4 Processing of Fabricated GNRs

After 16 hours, the GNR solution was processed and stored using a method adapted from Navaei and colleagues (Navaei *et al.*, 2016). The GNR solution was transferred into two 50 ml tubes, weighted equally using DIW, and centrifuged at 12,000 rpm for 10 minutes in an ultra-centrifuge, temperature controlled at 20 °C. The supernatant from each tube was removed, and transferred into a third 50 ml tube, which was re-spun, before having the supernatant discarded. The resulting cell pellets for each of the three tubes were resuspended in 0.5 ml of 0.001 M CTAB, and each transferred into separate 2 ml Eppendorf tubes. Each 50 ml tube was rinsed

with a further 0.5 ml of 0.001 M CTAB, which was then transferred into the respective Eppendorf tube to ensure that no GNRs were left in the initial tubes. The Eppendorf tubes were then spun again at 12,000 rpm for 10 minutes in a centrifuge, temperature controlled at 20 °C, and the supernatant discarded. Each GNR pellet was re-suspended in 1 ml of 0.001 M CTAB, and spun again at 12,000 rpm for 10 minutes. The supernatant was discarded, and each GNR pellet was re-suspended in 0.5 ml 0.001 M CTAB, and all three solutions were combined in a single Eppendorf.

### 2.2.3.5  Storage of GNRs

GNRs were stored in 0.001M CTAB at 4 °C until use.

### 2.2.4 General Cell Culture

All incubation was performed at 37 $^o$C and at 5% $CO_2$ unless otherwise stated. All centrifugation steps were performed at room temperature. All percentages described are (v/v) unless stated otherwise.

### 2.2.4.1 Resurrection of Cells from Liquid Nitrogen

A vial containing the target cells was removed from liquid nitrogen and thawed quickly in a 37 $^o$C water bath. The cell solution was then transferred to a universal tube filled with 8 ml of pre-warmed media. The vial was then rinsed with a further 1 ml of pre-warmed media, which was added to the universal tube, and the universal was centrifuged at 1,200 rpm for 5 minutes. Post centrifugation, the supernatant was removed and the cell pellet was re-suspended in 1 ml of media, which was then transferred into a T75 cell culture flask containing 11 ml of pre-warmed media, and the universal was rinsed with a further 1 ml of media which was also transferred into the T75 flask. The cell-culture flask was then transferred to an incubator.

### 2.2.4.2 Passaging and Maintenance

Cells were monitored and passaged at 80% confluence. Media was removed and discarded, and the culture surface was washed twice with 5 ml of PBS to remove any remaining serum. To detach the cells trypsin/EDTA was then added (1.5 ml for T75 and 3.5 ml for T175 flasks) and the flask was returned to the incubator for 10 minutes. After 10 minutes the flask was tapped firmly to aid cell detachment, and fresh media was transferred into the flask to neutralise the trypsin/EDTA (4.5 ml for T75 and 11.5 ml for T175 flasks). The suspension was then transferred to a sterile universal and centrifuged at 1,200 rpm for 5 minutes, the supernatant was discarded, and the pellet was resuspended in 1 ml of fresh media. The cells were then counted as described in section 2.2.4.3, and re-seeded at a density of 1 million cells per T75 flask, or 2 million cells per T175.

### 2.2.4.3 Cell Counting

Cell counting was performed using trypan blue. Trypan blue is a dark blue cell impermeable dye and thus when mixed with a cell suspension live cells with in-tact cell membranes will not be permeable to the blue dye, and so should be counted, but dead cells with compromised membranes will be permeable to the dye, and so should not be counted.

Cells were first trypsinised, centrifuged, and re-suspended as described in section 2.2.4.2. After re-suspension, 25 µl of cell solution was mixed with 25

μl of trypan blue dye in an Eppendorf tube, and 20 μl of the resulting solution was transferred to a haemocytometer for counting. The total number of cells in the four outer grids were counted and the concentration of cells in solution was determined using the following equation:

$$Concentration \ (cells.ml^{-1}) = \frac{Total \ Cell \ Count}{4} \times 2 \times 10,000$$

### 2.2.4.4  Culture of DPCSs

DPSCs were sourced from Lonza Bioscience and were provided from the supplier with a certificate of analysis that confirmed the cell population expressed the CD105, CD166, CD29, CD90, and CD73 cell surface markers, and did not express CD34, CD45, and CD133.

DPSCs were cultured in α-MEM media supplemented with 10% FBS, 1% P/S and 1% L-glutamine. The DPSCs were cultured in adherent fashion in T75 and T175 tissue culture flasks, and were passaged and maintained as described in section 2.2.4.2.

### 2.2.4.5  Culture of HFFs and nHDFs

Human foreskin fibroblasts (HFFs) and normal human dermal fibroblasts (nHDFs) are the same cell type, with the distinction between the two being that HFFs are sourced from a juvenile donor and nHDFs from an adult.

HFFs were sourced from the CReaTE group at the University of Otago, and nHDFs were sourced from Promocell, catalogue number (C-12352).

Both HFFs and nHDFs were cultured in DMEM media supplemented with 10% FBS and 1% P/S. The HFFs and nHDFs were cultured in adherent fashion in T75 and T175 tissue culture flasks, and were passaged and maintained as described in section 2.2.4.2.

### 2.2.4.6  Culture of HUVEC Cells

Human umbilical vein endothelial cells (HUVECs) were sourced from the Matsusaki group in the department of applied chemistry at Osaka University.

HUVECs were cultured in EGM -2MV media supplemented with 5% FBS, 0.1% rhEGF, 0.1% R$^3$-IGF-1, 0.4% rhFGF-B, 0.1% GA-1000, 0.04% hydrocortisone, 0.1% VEGF, and 0.1% ascorbic acid. The HUVECs were cultured in adherent fashion in T75 and T175 tissue culture flasks, and were passaged and maintained as described in section 2.2.4.2.

### 2.2.4.7 Coating of Tissue Culture Flasks with Fibronectin

Fibronectin was received as 0.2 mg/ml solution, and was further diluted in PBS without calcium or magnesium to a concentration of 20 ng/ml. This solution was then pipetted onto the culture surface of a T75 tissue culture flask, with 1.5 ml being used to cover the whole surface, and left to dry in a laminar flow hood for 1 hour. After an hour the excess fibronectin was removed by aspiration and the coated flasks were either used or stored at 4 $^{o}$C until use.

### 2.2.4.8 Culture of PC-12 Cells

The PC-12 cell line is derived from a rat pheochromocytoma and is commonly used in neural models because PC12 cells exhibit a number of features of mature dopaminergic neurons (Wang *et al.*, 2015). PC12s were sourced from the European Collection of Authenticated Cell Cultures (ECACC, ref: 92090409) and were cultured in RPMI 1640 media, supplemented with 10% deactivated horse serum, 5% FBS, 1% P/S, and 1% L-glutamine.

PC12s were cultured in semi-adherent culture (i.e. a mixture of adherent and suspended cells) on T75 tissue culture flasks that had been pre-coated with fibronectin as described in section 2.2.4.7. During culture, media was changed twice weekly. During media changes, old media was removed and transferred to a universal tube and replaced with fresh media. The old media was then centrifuged at 1,200 rpm for 5 minutes, the supernatant was removed, and the cell pellet was resuspended in 1 ml of fresh media and added back to the cell culture flask.

During passaging, media was removed and transferred to a universal tube. The culture surface was then washed twice with 5 ml of PBS to remove any remaining serum and was replaced with 1.5 ml of trypsin/EDTA. The flask was then returned to the incubator for 10 minutes. After 10 minutes the flask was tapped firmly to aid cell detachment, and 11.5 ml of fresh media was transferred into the flask to neutralise the trypsin/EDTA. The media was then transferred into a second universal tube, and both universal tubes were centrifuged at 1,200 rpm for 5 minutes before the supernatant was removed and each cell pellet was resuspended in 1 ml of fresh media. These two cell suspensions were then combined, counted, and re-seeded into fibronectin coated T75 flasks at a density of 1 million cells per T75 flask.

## 2.2.4.9  Cryopreservation of Cultured Cells

Cells were trypsinised and counted as described in section 2.2.4.3. Freezing media was prepared, consisting 10% DMSO, 40% FBS, and 50% complete cell culture medium for the cell type to be frozen. A volume of cell suspension required for 1 million cells was then centrifuged at 1,200 rpm for 5 minutes and the supernatant discarded. The cell pellet was then re-suspended in 1 ml of freezing media and immediately transferred to a labelled cryovial. This cryovial was then immediately transferred to a Mr Frosty freezing container which was immediately placed in a -80 $^o$C freezer, where it remained overnight, before the frozen cryovials were transferred to liquid nitrogen storage.

## 2.2.5 Biochemical Assays

All biochemical assays were performed on cells encapsulated in hydrogels in 3D.

### 2.2.5.1 LIVE/DEAD Assay

Cell viability was assessed using a Life Technologies LIVE/DEAD assay kit, consisting of calcein and ethidium homodimer. Calcein stains live cells, as after it is transported into the cell intracellular esterases remove calcein's acetomethoxy group, meaning the calcein is trapped inside the cell and fluoresces green. Dead cells do not show esterase activity and thus are not stained. Ethidium homodimer is a cell-impermeant molecule that can only move into cells with a compromised cell membrane (i.e. dead cells but not live cells) and will fluoresce strongly red when bound to DNA, staining the nuclei of dead cells (Sanfilippo *et al.*, 2011).

On the day of the assay, samples were removed from the cell culture media and placed in an empty 24-well plate, where they were washed twice with PBS for 5 minutes per wash. Samples were then submerged in LIVE/DEAD stain solution for 20 minutes on a rocker table, in a light tight container. The stain solution was then removed and samples were washed twice in PBS, for 5 minutes per wash. Samples were then kept submerged in PBS, in a light-tight container, until imaging.

Images of the stained cells were analysed using ImageJ software to determine percentage viability.

$$Cell\ Viability = \frac{live\ cell\ count}{total\ cell\ count} \times 100$$

### 2.2.5.2 Alamar Blue Assay

Alamar blue is an assay to measure the overall metabolism of a cell population. The resazurin in the alamar blue stain (blue, low fluorescence) is reduced to resorufin (pink, high fluorescence) by enzymes involved in cellular metabolism. As a result the reduction of the alamarBlue stain by a cell population will be directly related to the metabolic activity of that cell population (Rampersad, 2012).

On the day of the assay, 'alamar blue assay medium' was made up, which consisted of 90% complete cell culture medium and 10% alamarBlue stain solution by volume. The resulting solution is photosensitive and thus was

handled in low-light conditions. Low-light handling of any solutions containing alamar blue stain solution was continued throughout the assay. For the experimental wells, the cell-culture medium was replaced with 500 µl of alamar blue assay medium. At the same time, three empty wells are also filled with alamar blue assay medium to act as a reference. All wells were then incubated for 16 hours at 37 °C and 5% $CO_2$ in a standard incubator.

Post incubation the alamar blue assay medium was removed from the cell culture plate, and for each of the experimental and reference wells, 100 µl of assay medium was transferred into each of three wells of a 96-well plate. This 96 well-plate was then loaded into a plate reader, and the absorbance of each well was read at both 570 nm and 600 nm. The percentage reduction of alamar blue is then determined using the following equation:

$$\% \, Reduction \, of \, Alamar \, Blue = \frac{(O2 \, \times \, A1) - (O1 \, \times \, A2) \, \times \, 100}{(R1 \, \times \, N2) - (R2 \, \times \, N1)}$$

Where:

O1 = Molar extinction co-efficient of oxidized alamarBlue at 570 nm
R1 = Molar extinction co-efficient of reduced alamarBlue at 570 nm
O2 = Molar extinction co-efficient of oxidized alamarBlue at 600 nm
R2 = Molar extinction co-efficient of reduced alamarBlue at 600 nm
A1 = Absorbance of test wells at 570 nm
A2 = Absorbance of test wells at 600 nm
N1 = Absorbance of reference wells at 570 nm
N2 = Absorbance of reference wells at 600 nm

**Table 2.5 – Molar extinction co-efficient of alamarBlue at different wavelengths**

| Wavelength | Reduced (R) | Oxidized (O) |
|:---:|:---:|:---:|
| 540 nm | 104395 | 47619 |
| 570 nm | 155677 | 80586 |
| 600 nm | 14652 | 117216 |
| 630 nm | 5494 | 34798 |

# Chapter 3
## Optimisation and Characterisation of a GelNOR Hydrogel Scaffold

## 3.1 Introduction and Aims

As previously described, GelMA is a synthetically functionalised natural polymer that can be crosslinked via photo-polymerisation in a chain growth reaction. Chain growth crosslinking occurs through the growth of kinetic chains, in which an initial radical forms an active centre on a monomer molecule, which then propagates through other surrounding monomer molecules, adding one monomer molecule at a time to form a new polymer which is one repeat unit longer and with a new active centre, ready to add a further monomer molecule. In light initiated systems, this reaction is largely controlled by the intensity and duration of the energy input, with greater energy driving the growth of longer chains and thus more highly crosslinked polymers (Lim *et al.*, 2016).

Though hydrogels such as GelMA, that are crosslinked via chain growth reactions, have seen extensive use in tissue engineering applications (Klotz *et al.*, 2016) there are a number of drawbacks to this method of crosslinking. Firstly, the random nature of chain-growth reactions often result in highly heterogeneous networks, as the crosslinking chains are not uniform in length, and can propagate differently dependent on the local availability of reaction substrate (Shih and Lin, 2012). Secondly, chain growth photo-polymerisation has been shown to yield high initial radical concentrations, which is harmful to cells that are encapsulated in the hydrogel (Lin, Sawicki and Metters, 2008). This second disadvantage may be even more significant when UV-light photo-initiation is used to initiate crosslinking, as UV-light is known to be harmful to cells and cause genetic and chromosomal instability (Dahle, Kvam and Stokke, 2005).

A number of the described disadvantages of chain-growth polymerisation can be overcome by instead using step-growth gelation, of which 'click-chemistry' is a common type. In step-growth polymerisations, consecutive reaction steps cause an increase in macromolecules of high molecular weight, and within this reaction type, click reactions have high selectivity, quantitative yields, mild reaction conditions, absence of by-product, and inertness towards other functional groups. (Billiet, Fournier and Du Prez, 2009). In the context of crosslinking reactions, 'click' reactions are favourable due to the control they offer, and for cell supporting hydrogels, for

the mild reaction conditions they are able to be realised in. The high levels of control are due to the high specificity of the reaction, allowing a crosslinking molecule to be selected that will only react with the required part of the hydrogel backbone, with the crosslinking molecule acting as the bridge and thus being consistent in every crosslink. The ability to crosslink in mild reaction conditions is due to the relatively low energy required to support the reaction between a single point on a crosslinker molecule and the hydrogel backbone, as compared to a chain growth reaction which relies on continued and significant energy input to drive growth of the kinetic chains.

To this end, Fairanks and colleagues (Fairbanks, Schwartz, Halevi, *et al.*, 2009) developed a step-growth polymerization scheme based on the click reaction between norbornene and thiol (Figure 3.1).
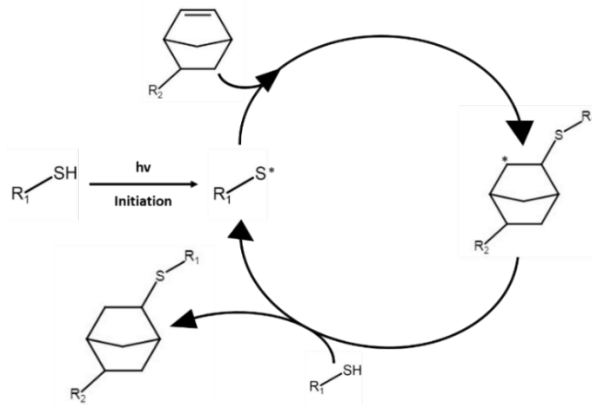


**Figure 3.1 - Radical Mediated Thiol-Norbornene Reaction Scheme.** Free radical, generated by removing proton from thiol group, attacks norbornene double bond to bind thiol-norbornene. Free radical on norbornene ring then propagates reaction by removing proton from a further thiol group.

This system overcomes the described disadvantages of chain growth polymerisation whilst retaining the advantages of photochemistry, as the crosslinking reaction is both light and radical mediated. The thiol-norbornene photo-click system has been demonstrated to produce significantly lower levels of radicals during light irradiation, and to be significantly less damaging to natural proteins (McCall and Anseth, 2012). Further, the nature of click chemistry means that the crosslinks will be more homogenous than in random chain growth polymerisation, due to the molecular bridge between two thiol-norbornene links being the same for each crosslink when using the same crosslinking molecule, instead of relying on the growth of kinetic chains. Thiol–norbornene based hydrogels have also been shown to be highly biocompatible for biomedical applications (Lin, Ki and Shih, 2015)

One of the advantages of gelatin as a natural base polymer from which to make natural/synthetic hydrogels, is the relative ease with which side groups of varying characteristics can be grafted onto its 'backbone' (Klotz *et al.*, 2016). Gelatin-Norbornene (GelNOR) is synthesised by reacting carbic anhydride with gelatin's amine side groups to form amide-linked norbornene side chains. GelNOR can then be crosslinked in a step-growth polymerisation by reacting these amide-linked norbornene side chains with the thiol groups on a multi-functional thiol crosslinking agent, in a thiol-norbornene photo-click reaction as shown in Figure 3.2 (Greene and Lin, 2015).
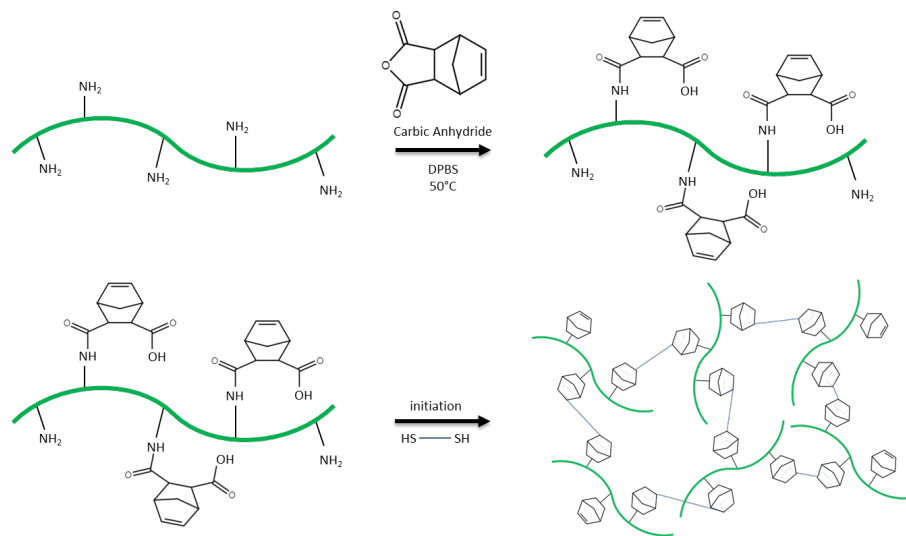


**Figure 3.2 – Fabrication and Crosslinking of GelNOR.** (Above) Norbornene functionalised side chains are grafted onto gelatin's amine side groups using carbic anhydride, forming GelNOR. (Below) Crosslinking is achieved via radical mediated click reaction with a multi-functional thiol crosslinker.

Further to the described advantages of step-growth polymerisation using thiol-norbornene chemistry, the nature of the photo-click system also allows for variation with chosen crosslinking molecule. As previously described, GelNOR can theoretically be crosslinked using any multi-functional thiol molecule, in which the thiol groups on the crosslinker react with the norbornene groups of GelNOR, and the body of the crosslinking molecule forms the crosslinking bridge. In this way, it is obvious that the selection of crosslinking molecule will have a significant impact on the physical properties of the resulting hydrogel, as has been demonstrated by (Mũnoz *et al.*, 2014). Further to this, crosslinking of thiol-norbornene systems occurs most efficiently at a stochiometric ratio (Fairbanks, Schwartz, Halevi, *et al.*, 2009). This suggests a possibility for further variation of hydrogel properties

based on the thiol to norbornene ratio in the reaction mixture, as well as the actual crosslinking molecule chosen, in that deliberately choosing thiol to norbornene ratios either side of stochiometric will produce different gel characteristics.

Though step-growth through the thiol-norbornene photo-click system overcomes the described problems associated with chain growth polymerisation, namely the initial build-up of high concentrations of damaging free-radicals and the growth of heterogeneous networks, photo-crosslinking of GelNOR has only been described in the literature using UV-light. When GelNOR was initially described by Munoz and colleagues (Mũnoz *et al.*, 2014), crosslinking was initiated using lithium acylphosphinate (LAP), though Irgacure 2959 (i2959) has also been used since (Tigner *et al.*, 2020). Both LAP and i2959 are a Norish type I photo-cleaved initiators, and are used in combination with UV-light. LAP has seen increased interest in recent years due to its absorbance/cleavage curve meaning it can generate enough radical for successful gelation at a more cytocompatible wavelength of 365nm, rather than the 320 nm typically used with i2959 (Occhetta *et al.*, 2015), though at 365 nm this wavelength is still in the UV range of the spectrum. Despite this, the comparison performed by Tigner and colleagues (Tigner *et al.*, 2020) did not find significant differences in cell viability between LAP and i2959. This may have been due to the decision to irradiate both LAP and i2959 samples at 365 nm, a more cell friendly wavelength than the 320 nm often used with i2959. Although both 320 nm and 365 nm are UV-A wavelengths, 320 nm is on the boundary of being UV-B, which has been shown to be 5-fold more damaging to cells in terms of DNA mutagenesis (Dahle *et al.*, 2005), and thus even though the i2959 required a longer time at higher light intensity to cure effectively at 365 nm, the more cytocompatible light wavelength meant that i2959 performed similarly to LAP in terms of cell viability. Alternatively it may be that the NIH 3T3 fibroblasts used, being a relatively hardy cell line, were less effected by the cytotoxic effects of UV-light irradiation than other more fragile cell types may be.

Though the drawbacks of UV-light initiation are well recognised, effective options for visible-light initiated systems are currently limited. Though a number of visible light systems have been demonstrated for use with the thiol-norbornene click system, such as Eosin-Y (Shih and Lin, 2013), these visible light initiation systems are usually Norish type II, non-cleavage type, systems and have lower initiation efficiency than their type I, cleavage type,

UV-initiated counterparts (Lin, Ki and Shih, 2015). As a result, no visible light systems have been used to initiate crosslinking of GelNOR in the literature.

A new Norish type II initiation system, combining a ruthenium complex (tris-bipyridyl-ruthenium (II) hexahydrate) and sodium persulphate (SPS) co-initiator, was recently demonstrated for photo-initiation of GelMA crosslinking using visible-light by Lim and colleagues (Lim *et al.*, 2016), with the stated purpose of reducing oxygen inhibition. As part of this work, Lim also demonstrated the Ruthenium/SPS system to have initiating efficiency comparable to i2959 in a GelMA, chain growth system. The success of this visible-light system in generating enough radical for crosslinking of GelMA via chain-growth polymerisation, which is generally photo-initiated using i2959 or LAP in combination with UV-light, identifies this system as possibly also being suitable for step-growth polymerisation of GelNOR as it is similarly radical dependent, and has also been previously demonstrated to be crosslinked by both i2959 and LAP.

The aims of this chapter are to validate the previously described visible light system for use with GelNOR and to optimise crosslinker selection and concentration. This will be achieved through the following objectives:

1. Validate the use of Ruthenium/Sodium Persulphate system previously used in chain growth crosslinking of GelMA hydrogels (Lim *et al.*, 2016) for use in 'photo-click' crosslinking of GelNOR hydrogels
2. Optimise the crosslinker selection, crosslinker concentration, and wt% of GelNOR hydrogel, in order to tailor the physical properties of the hydrogel for spinal cord tissue engineering applications
3. Analyse the viability and behaviour of cells encapsulated in the optimised hydrogel system

## 3.2 Methods

### 3.2.1 Validation of Visible-Light System for use in GelNOR

In order to test the novel ability of the Ruthenium/SPS initiation system to initiate crosslinking in GelNOR hydrogel, a light exposure time-sweep was performed to test crosslinking efficiency at different light exposure durations. The initiator concentrations used were 10 mM SPS and 1 mM Ruthenium, as previously described by Lim and colleagues (Lim *et al.*, 2016). The concentration of DTT crosslinker used was 0.043 M, corresponding to a 1:6 norbornene:thiol (NOR:SH) ratio in the final solution of 10 wt% GelNOR.

GelNOR macromer was fabricated by collaborating research group, the Christchurch Regenerative Medicine and Tissue Engineering (CReaTE) group at the University of Otago, and was received freeze-dried.

### 3.2.2 Preparation of Hydrogel Solution

GelNOR macromer was dissolved in PBS, heated to 37 °C , at 20 wt%. Once dissolved, 200 µl GelNOR solution was transferred to an Eppendorf tube and maintained at 37 °C, and 187 µl PBS was added, followed by 43 µl of 0.5 M DTT, and the solution was vortexed for 5 seconds.

Once vortexed, 10 µl of 0.5 M SPS was added to the very bottom of the Eppendorf tube, with care taken not to mix the SPS into the hydrogel solution, followed by the addition of 10 µl of 0.05 M Ruthenium to the very surface of the gel, once again being careful not to mix during addition. The whole solution was then vortexed for 10 seconds and immediately aliquoted into 30 µl disc moulds.

### 3.2.3 Time-sweep Initiation

Hydrogel discs were cured using an Omnicure S1000 visible light unit, providing 30 mW/cm$^2$ light at wavelength 400-450 nm. Irradiation times were 15, 30, 60, 90, 120, 180, 300, 450, 600, and 900 seconds. Immediately after gelation, gels were removed from the moulds and analysed.

### 3.2.4 Comparison of Crosslinker and GelNOR wt%

In order to optimise the GelNOR hydrogel scaffold, a range of crosslinking molecules, crosslinker concentrations, and gel wt% were used to fabricate GelNOR hydrogels, which were then physically characterised.

### 3.2.5 Fabrication of GelNOR Scaffolds

GelNOR hydrogel solutions were prepared as described in section 3.2.2, but using different crosslinking molecules and concentrations. Crosslinker concentration was defined by the molar ratio of norbornene to thiol in the sample. These crosslinking molecules and concentrations are detailed in Table 3.1:

**Table 3.1 – Summary of hydrogel compositions for fabrication of GelNOR hydrogels of varying wt%, crosslinking molecule, and crosslinker concentration.** All values given, except for NOR:SH ratios, are in µl.

(a)

| NOR:SH | DTT crosslinked 10 wt% | | | | |
|---|---|---|---|---|---|
| | 20 wt% GelNOR | PBS | 0.5 M DTT | 0.5 M SPS | 0.05 M Ru |
| 1:1 | 250 | 223 | 7 | 10 | 10 |
| 1:2 | 250 | 216 | 14 | 10 | 10 |
| 1:3 | 250 | 208.5 | 21.5 | 10 | 10 |
| 1:6 | 250 | 187 | 43 | 10 | 10 |
| 1:12 | 250 | 144 | 86 | 10 | 10 |

(b)

| NOR:SH | PEG-4SH crosslinked 10 wt% | | | | |
|---|---|---|---|---|---|
| | 20 wt% GelNOR | PBS | 0.125 M PEG-4SH | 0.5 M SPS | 0.05 M Ru |
| 1:1 | 250 | 215.7 | 14.3 | 10 | 10 |
| 1:2 | 250 | 201.4 | 28.6 | 10 | 10 |
| 1:3 | 250 | 187.4 | 42.8 | 10 | 10 |
| 1:6 | 250 | 144.2 | 85.8 | 10 | 10 |
| 1:12 | 250 | 58.4 | 171.6 | 10 | 10 |

(c)

| NOR:SH | PEG-8SH crosslinked 10 wt% | | | | |
|---|---|---|---|---|---|
| | 20 wt% GelNOR | PBS | 0.05 M PEG-8SH | 0.5 M SPS | 0.05 M Ru |
| 1:1 | 250 | 212 | 18 | 10 | 10 |
| 1:2 | 250 | 194.2 | 35.8 | 10 | 10 |
| 1:3 | 250 | 176.4 | 53.6 | 10 | 10 |
| 1:6 | 250 | 123 | 107 | 10 | 10 |
| 1:12 | 250 | 16 | 214 | 10 | 10 |

(d)

| NOR:SH | DTT crosslinked 5 wt% | | | | |
|---|---|---|---|---|---|
| | 10 wt% GelNOR | PBS | 0.5 M DTT | 0.5 M SPS | 0.05 M Ru |
| 1:1 | 250 | 226.5 | 3.5 | 10 | 10 |
| 1:2 | 250 | 223 | 7 | 10 | 10 |
| 1:3 | 250 | 219.5 | 10.8 | 10 | 10 |
| 1:6 | 250 | 208.5 | 21.5 | 10 | 10 |
| 1:12 | 250 | 187 | 43 | 10 | 10 |

(e)

| NOR:SH | PEG-4SH crosslinked 5 wt% | | | | |
|---|---|---|---|---|---|
| | 10 wt% GelNOR | PBS | 0.125 M PEG-4SH | 0.5 M SPS | 0.05 M Ru |
| 1:1 | 250 | 224.8 | 7.2 | 10 | 10 |
| 1:2 | 250 | 215.7 | 14.3 | 10 | 10 |
| 1:3 | 250 | 208.6 | 21.4 | 10 | 10 |
| 1:6 | 250 | 187.1 | 43 | 10 | 10 |
| 1:12 | 250 | 144.2 | 85.8 | 10 | 10 |

(f)

| NOR:SH | PEG-8SH crosslinked 5 wt% | | | | |
|---|---|---|---|---|---|
| | 10 wt% GelNOR | PBS | 0.05 M PEG-8SH | 0.5 M SPS | 0.05 M Ru |
| 1:1 | 250 | 221 | 9 | 10 | 10 |
| 1:2 | 250 | 212.1 | 17.9 | 10 | 10 |
| 1:3 | 250 | 203.2 | 26.8 | 10 | 10 |
| 1:6 | 250 | 176.5 | 53.5 | 10 | 10 |
| 1:12 | 250 | 123 | 107 | 10 | 10 |

(g)

| DTT crosslinked 2.5 wt% | | | | | |
|---|---|---|---|---|---|
| NOR:SH | 5 wt% GelNOR | PBS | 0.5 M DTT | 0.5 M SPS | 0.05 M Ru |
| 1:1 | 250 | 228.25 | 1.75 | 10 | 10 |
| 1:2 | 250 | 226.5 | 3.5 | 10 | 10 |
| 1:3 | 250 | 224.6 | 5.4 | 10 | 10 |
| 1:6 | 250 | 219.25 | 10.75 | 10 | 10 |
| 1:12 | 250 | 208.5 | 21.5 | 10 | 10 |

(h)

| PEG-4SH crosslinked 2.5 wt% | | | | | |
|---|---|---|---|---|---|
| NOR:SH | 5 wt% GelNOR | PBS | 0.125M PEG-4SH | 0.5 M SPS | 0.05 M Ru |
| 1:1 | 250 | 226.4 | 3.6 | 10 | 10 |
| 1:2 | 250 | 222.8 | 7.2 | 10 | 10 |
| 1:3 | 250 | 219.8 | 10.2 | 10 | 10 |
| 1:6 | 250 | 208.5 | 21.5 | 10 | 10 |
| 1:12 | 250 | 187.1 | 42.9 | 10 | 10 |

(i)

| PEG-8SH crosslinked 2.5 wt% | | | | | |
|---|---|---|---|---|---|
| NOR:SH | 5 wt% GelNOR | PBS | 0.05M PEG-8SH | 0.5 M SPS | 0.05 M Ru |
| 1:1 | 250 | 225.5 | 4.5 | 10 | 10 |
| 1:2 | 250 | 221.05 | 8.95 | 10 | 10 |
| 1:3 | 250 | 216.6 | 13.4 | 10 | 10 |
| 1:6 | 250 | 203.25 | 26.75 | 10 | 10 |
| 1:12 | 250 | 176.5 | 53.5 | 10 | 10 |

Hydrogel discs were cured using an Omnicure S1000 visible light unit, providing 30 mW/cm$^2$ light at wavelength 400-450 nm, for 3 minutes.

### 3.2.6 Mass Loss and Swelling Studies

The soluble fraction and swelling ratio of fabricated hydrogels was determined through the use of mass loss and swelling studies, as described in section 2.2.2.

### 3.2.7 Uni-Axial Compression Testing

The mechanical properties of the fabricated hydrogels were determined through uni-axial compression testing, using an MTS Criterion, Model 42.

Immediately after fabrication, hydrogel samples were swollen in 1 x PBS + 0.1% sodium azide for 24 hours. Sample height was then determined by placing the sample on a microscope slide and using callipers to determine

the height of the slide and the sample. The height of the slide was then subtracted to give the height of the sample. Samples were then imaged using a light microscope, and the images were analysed using ImageJ software to determine the sample surface area.

Samples were then loaded onto the lower testing head of the testing rig, and the head was lowered to an appropriate point above the sample. The pre-load phase was then initiated, in which the upper testing head was lowered towards the sample at a rate of 0.01 mm/s until the upper head made contact with the sample (determined as when a force exceeding the 0.015 N pre-load limit was registered). This phase was developed through an iterative process, during which samples were repeatedly tested with an increasing pre-load limit until the limit was sufficient for the machine to reproducibly detect the sample out of any 'noise' that was present, with minimal errors. This method ensured that the lowest feasible pre-load limit was chosen, ensuring that the test started from as close to the true 'zero strain' as possible.

Once the upper testing head had contacted the sample, the pre-strain phase was then initiated, in which the sample was compressed at a speed of 0.01 mm/s to 5% strain, before dwelling for 30 seconds. The use of a dwell period was chosen to allow the sample to equilibrate to the test conditions before starting the main test phase, improving reproducibility.

After the 30 second dwell the test phase was started, in which the sample was compressed to 80% strain at a speed of 0.01 mm/s. This slow speed was chosen in order to be slow enough to remove any effect of strain rate on the measured modulus.

### 3.2.8  3D Culture of Human Foreskin Fibroblasts in Optimised GelNOR Hydrogel

In order to test the effect of different wt% and DTT concentrations on cell viability and behaviour, a population of human foreskin fibroblasts (HFFs) were cultured in 5 wt% and 10 wt% GelNOR hydrogel, crosslinked with DTT at a range of NOR:SH concentrations.

#### 3.2.8.1  Preparation of GelNOR Macromer

GelNOR macromer was weighed in a sterile manner, and dissolved in sterile PBS at 37 °C.

#### 3.2.8.2  Preparation of Crosslinker and Initiators

DTT was dissolved in PBS, as were SPS and Ruthenium. Each solution was then sterile filtered through a 0.2 μm syringe filter.

#### 3.2.8.3  Cell Culture

HFFs were cultured as outlined in section 2.2.4.5

#### 3.2.8.4  Preparation of HFFs

Passage 16 – 22 HFFs were trypsinised and counted as described in section 2.2.4.3. An amount of cell stock solution was then transferred to a 10 ml falcon tube, such that the number of cells in the volume of medium corresponded to a cell concentration of 5 million cells/ml in the final hydrogel. Cells were then pelleted via centrifugation at 1,200 rpm for 5 minutes, and the medium removed.

The cell pellet was then re-suspended in sterile GelNOR solution.

#### 3.2.8.5  Encapsulation and 3D Culture of HFFs

The HFF laden GelNOR was used to prepare hydrogel solutions as described in section 3.2.2, which were then pipetted into silicone disc moulds, and crosslinked using using an Omnicure S1000 visible light unit, providing 30 mW/cm$^2$ light at wavelength 400-450 nm, for 3 minutes.

The HFFs were encapsulated in 5 wt% and 10 wt% GelNOR, crosslinked with DTT at a range of NOR:SH ratios, as described in Table 3.1 part (a) and (d).

Post-fabrication, cell encapsulated hydrogels were immediately submerged in complete DMEM medium and incubated at 37 °C. Media was changed after 24 hours, and then every subsequent 48 hours.

### 3.2.9 Analysis of Cell Viability and Behaviour

Cells encapsulated in GelNOR hydrogels were analysed at day 1, 7, 14, and 21.

### 3.2.9.1 LIVE/DEAD Assay

Viability of HFFs was analysed using LIVE/DEAD assay was performed as described in section 2.2.5.1.

### 3.2.9.2 Alamar Blue Assay

Metabolic activity of HFFs was analysed using alamar blue assay was performed as described in section 2.2.5.2.

### 3.2.9.3 Morphology Analysis

In order to semi-quantitatively analyse cellular morphology, LIVE/DEAD images were analysed using ImageJ's particle counting function, and the average 'circularity' scores of the cells from each image were used to compare the extent to which cells had taken a 'spread' or 'rounded' morphology.

### 3.2.10 Statistical Analysis

When comparing performance of a number of gels at the same wt% and crosslinker but a range of different NOR:SH ratios, a one-way ANOVA was used with post-hoc Tukey test.

When comparing gels of the same NOR:SH ratio or wt% but different crosslinker, when comparing only two crosslinkers an independent two-tailed t-test was used, or if comparing more than two crosslinkers a one-way ANOVA was used with post-hoc Tukey test.

When comparing performance of only two gels of the same NOR:SH ratio but of different wt%, when comparing only two wt% an independent two-tailed t-test was used, or if comparing more than two wt% a one-way ANOVA was used with post-hoc Tukey test.

All statistical analysis was performed using the 'rstats' package in RStudio.

All data is presented as mean ± standard deviation.

Repeats are presented as (n = x, y) where x is the number of replicates performed within an experiment, and y is the number of times the experiment was performed.

## 3.3 Results

### 3.3.1 Validation of Ruthenium/SPS Initiation System for use with GelNOR

The Ruthenium/SPS visible-light initiation system has previously been described for use in GelMA, but has not previously been used with GelNOR. As such, the ability of the visible-light system to initiate gelation of GelNOR hydrogel must be validated before further use.

### 3.3.2 Time-sweep Visible-light Irradiation

Suitability of the visible-light initiation system for use in crosslinking of GelNOR hydrogel was first analysed using a light irradiation time-sweep.

The results from the time-sweep indicate that the gel achieves maximum crosslinking efficiency rapidly, with the first time-point of 15 seconds achieving a soluble fraction of 11.94% (Figure 3.3). No subsequent irradiation time achieved a statistically significantly lower soluble fraction than this first time-point. The only timepoint that was significantly different to any others was the 5 minute irradiation time, which had a soluble fraction that was significantly lower than that of the 2 minute and 15 minute timepoints ($p < 0.05$ for both, one-way ANOVA with post-hoc Tukey test).
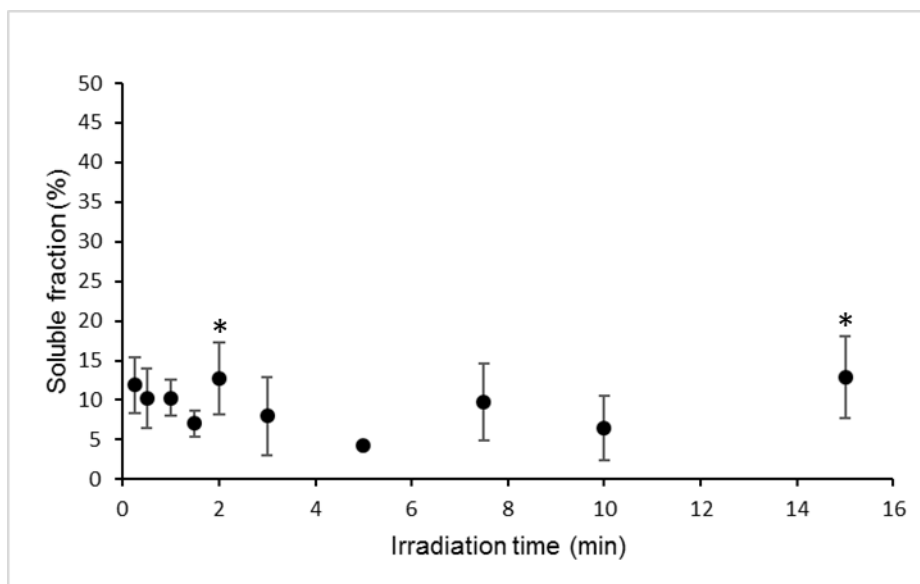


**Figure 3.3 – GelNOR photo-initiation time-sweep.** Soluble fraction of 10 wt% GelNOR hydrogels, crosslinked with DTT at 1:6 NOR:SH ratio, initiated with Ruthenium/SPS visible light initiation system at a range of irradiation times. * $p < 0.05$ vs. 5 minutes. (n=5, 3 at all irradiation times).

### 3.3.3 Analysis of the Effect of Crosslinker Selection and wt% on Hydrogel Properties

In order to optimise the choice of crosslinking molecule, norbornene to thiol ratio (NOR:SH), and hydrogel wt%, GelNOR hydrogels were fabricated and characterised at a range of wt% and using a range of crosslinking molecules and concentrations. The crosslinkers compared were all multi-functional thiol molecules, of which DTT is bi-functional, PEG-4SH is tetra-functional, and PEG-8SH is octa-functional.

When used to crosslink GelNOR hydrogel, gels crosslinked with DTT and PEG-8SH did not gel at 2.5 wt%. It was also not possible to crosslink 10 wt% gels with PEG-8SH, as the PEG-8SH was precipitated out of solution during mixing.

#### 3.3.3.1 Analysis of Soluble Fraction and Swelling Ratio

The soluble fraction and mass swelling ratio of the gels was analysed through mass loss and swelling studies. Soluble fraction denotes the proportion of macromer that is lost during swelling, due to it not being effectively crosslinked. In this way, soluble fraction can be used to measure the crosslinking efficiency of a gelation reaction. The mass swelling ratio is a measure of the amount of liquid taken up by the hydrogel network, and this can be used as a measure of how 'loose' the hydrogel network is after reaching equilibrium swelling.

For gels crosslinked with DTT, a bell-curve trend in crosslinking efficiency was observed from 1:1 to 1:12 NOR:SH ratio (Figure 3.4), with the 1:1 gels and 1:12 gels having significantly greater soluble fractions than those at 1:2 – 1:6, at both 5 and 10 wt% (p<0.0001 for all described cases, if the failure to gel of the 5 wt%, 1:12 gel is taken on the same terms as a 100% soluble fraction). For the 5 wt% gels this curve was more pronounced, with the 51.1% soluble fraction of the 1:2 NOR:SH ratio gel being more than 3 times greater than the 13.2% of the 1:3 gel, and more than 5 times greater than the 9.9% of the 1:6 gel. The soluble fractions of the 1:3 and 1:6 gels, however, were not significantly different from each other at either 5 or 10 wt%. Though the soluble fraction of the 1:2 NOR:SH gel at 10 wt% was similarly higher than the 1:3 and 1:6 gels (7.4% vs 3.1% and 3.9% respectively), the differences between the 1:2, 1:3 and 1:6 gels were not statistically significant at this wt%. The effect of wt% on the soluble fraction was also evident, with the 5 wt% gels having statistically significantly higher

soluble fractions than the 10 wt% gels, at all NOR:SH ratios except 1:6 (Welch's t-tests).
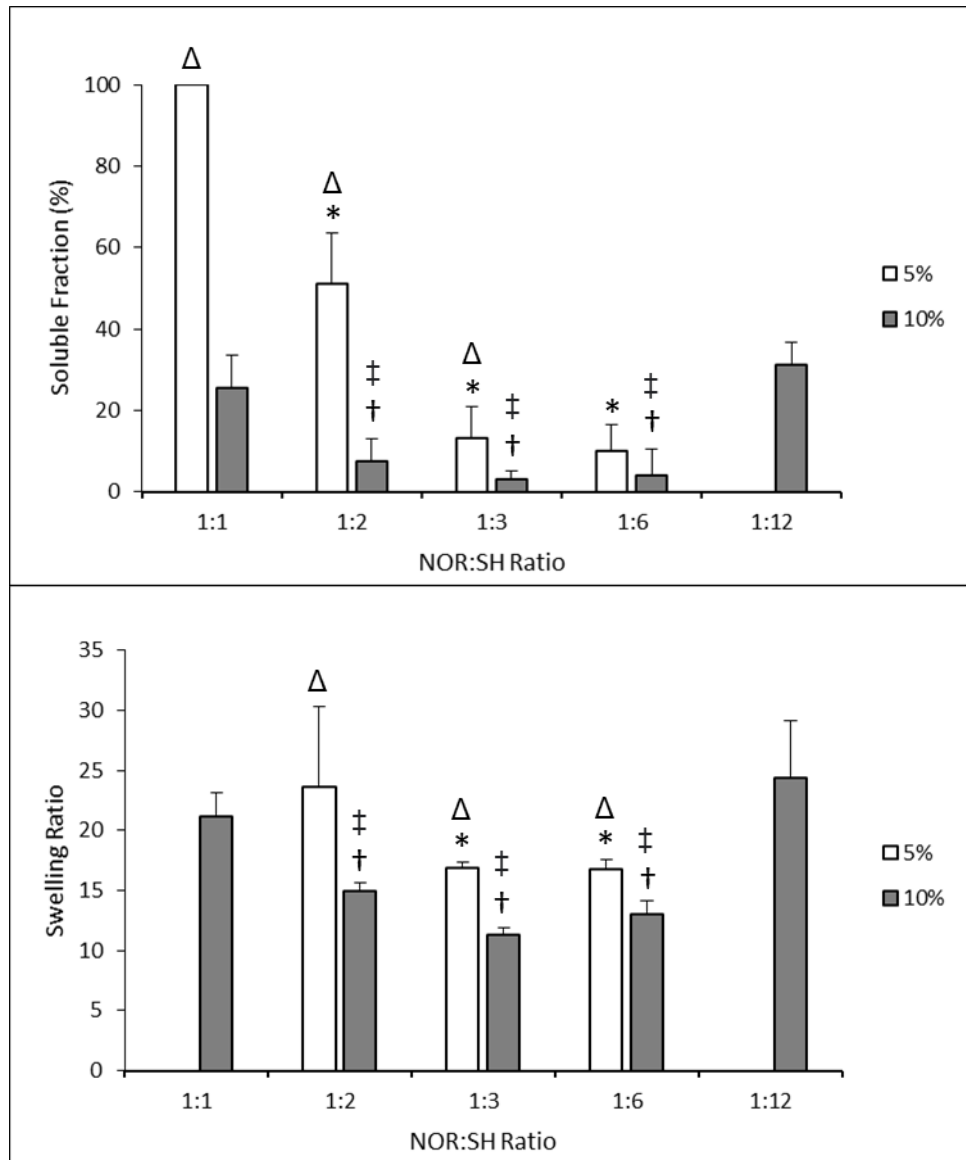


**Figure 3.4 – Soluble fraction and swelling ratio of 5 and 10 wt% GelNOR hydrogels crosslinked with DTT at a range of NOR:SH ratios.** The soluble fraction data (above) is incomplete for 5 wt% GelNOR, as the 1:12 NOR:SH gel failed to gel. Similarly, the swelling ratio data is incomplete for 5 wt% GelNOR, as the 1:1 NOR:SH gel had 100% soluble fraction and the 1:12 NOR:SH gel failed to gel, meaning the full mass loss and swelling study could not be carried out on these gels. Significance levels for soluble fraction: * $p < 0.05$ vs. 1:1 gels at 5 wt%, † $p < 0.05$ vs. 1:1 gels at 10 wt%, ‡ $p < 0.05$ vs. 1:12 gels at 10 wt%, Δ $p < 0.05$ vs. 10 wt% at matched NOR:SH ratio. Significance levels for swelling ratio: * $p < 0.05$ vs. 1:2 gels at 5 wt%; † $p < 0.05$ vs. 1:1 gels at 10 wt%, ‡ $p < 0.05$ vs. 1:12 at 10 wt%, Δ $p < 0.05$ vs. 10 wt% at matched NOR:SH ratio. (n=5, 3).

Both the gel wt% and the crosslinker NOR:SH ratio also had an effect on the mass swelling ratio of the gels, with the 5 wt% gels having statistically significantly higher swelling ratios than the corresponding NOR:SH ratios at 10 wt% gel. Further, gels at 5 wt% 1:2 NOR:SH had a statistically significantly higher swelling ratio than the 1:3 and 1:6 gels at the same wt% ($p<0.05$ for both, one-way ANOVA with post-hoc Tukey test), though the 1:3 and 1:6 gels were not significantly different from each other. This trend approximately matches that observed for soluble fraction. For the 10 wt% gels, the swelling ratio followed a similar trend to the soluble fraction, with the 1:1 and 1:12 gels having significantly higher swelling ratio than the 1:2 – 1:6 gels, but the swelling ratios of the 1:2, 1:3, and 1:6 gels were not significantly different to each other (one-way ANOVA).

The described bell curve trend in crosslinking efficiency was also seen in the 10 wt% gels when crosslinked with PEG-4SH (Figure 3.5 & Figure 3.6). Although both 1:1 and 1:12 NOR:SH gels had elevated soluble fractions, only the 1:12 achieved statistical significance, which it did against 1:2, 1:3 ($p<0.05$), and 1:6 ($p<0.01$), but not 1:1. The soluble fraction of the 1:1, 1:2, 1:3, and 1:6 gels were not significantly different from each other (one-way ANOVA).

The swelling ratio of the 10 wt% gels crosslinked with PEG-4SH followed a similar trend to the soluble fractions. However, although the 1:12 NOR:SH gels had a significantly higher soluble fraction than all the other ratios tested, they did not have a significantly higher swelling ratio. The swelling ratio of the 1:12 gels was significantly greater than that of the 1:6 gels ($p<0.001$), but was not significantly greater than the 1:2 and 1:3 gels, and was actually significantly lower than that of the 1:1 gels ($p<0.01$), despite the soluble fraction being significantly greater. The correlation between soluble fraction and swelling ratio was in keeping with the trend seen for gels crosslinked with DTT, but the unexpectedly low swelling ratio of the 1:12 NOR:SH gel was not.

The bell curve trend in crosslinking efficiency at different NOR:SH ratios, seen in GelNOR crosslinked with DTT and PEG-4SH at 10 wt%, was not seen in GelNOR gels crosslinked with PEG-4SH below 10 wt%. At 5 wt% both the 1:1 and 1:2 NOR:SH gels had a significantly higher soluble fraction than the 1:3 and 1:6 NOR:SH gels, but where the 1:12 gel had increased soluble fraction with DTT crosslinking, and 10 wt% PEG-4SH crosslinked gels, at 5 wt% the soluble fraction of the PEG-4SH crosslinked 1:3, 1:6, and 1:12 NOR:SH gels were not significantly different to each other. Similarly,

where the swelling ratio increased in the 1:12 NOR:SH gels with DTT crosslinking, and 10 wt% PEG-4SH crosslinked gels, for the 5 wt% the swelling ratio decreased continuously as the NOR:SH ratio increased.
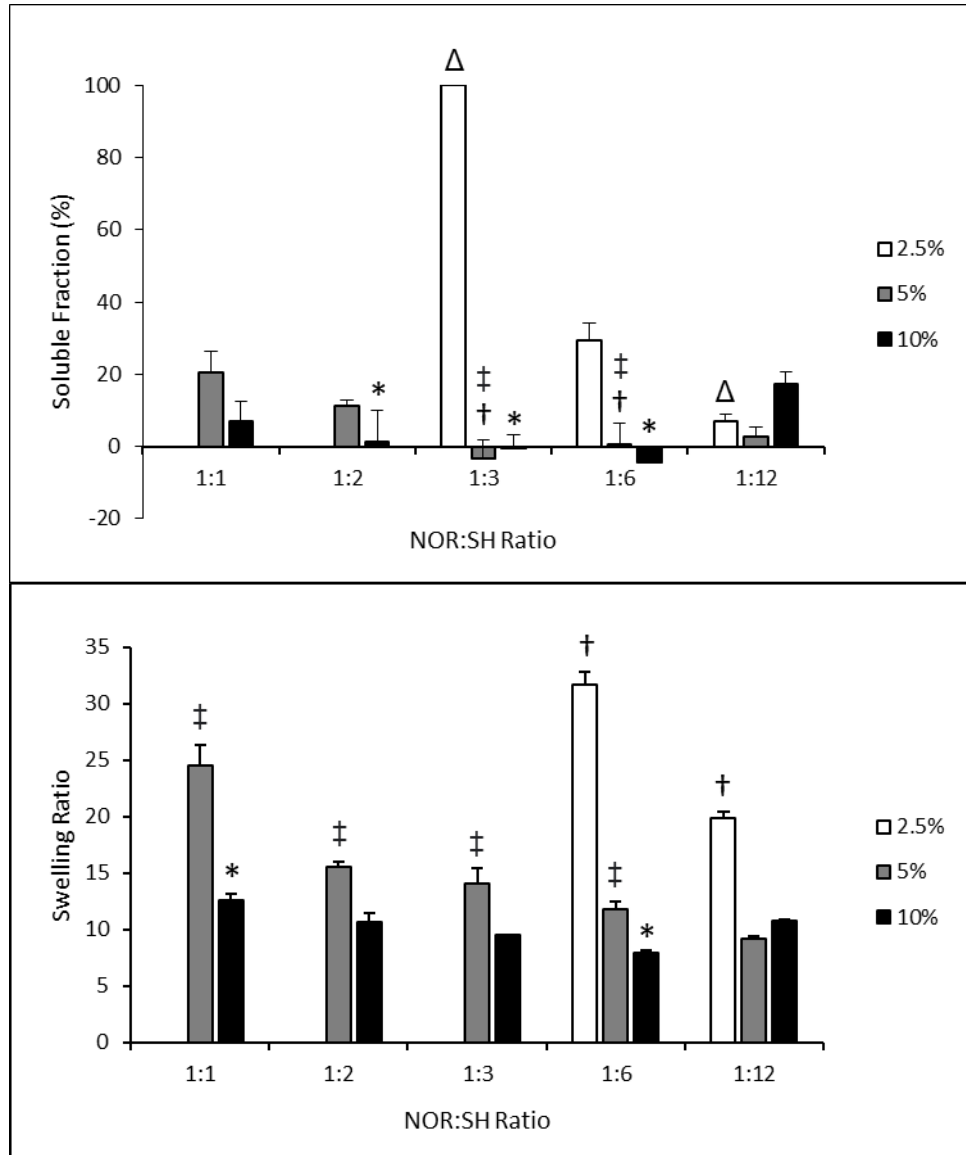


**Figure 3.5 – Soluble fraction and swelling ratio of 2.5, 5, and 10 wt% GelNOR hydrogels crosslinked with PEG-4SH at a range of NOR:SH ratios.** The soluble fraction data (above) is incomplete for 2.5 wt% GelNOR, as the 1:1 and 1:2 NOR:SH gels failed to gel. Similarly, the swelling ratio data (below) is incomplete for 2.5 wt% GelNOR, as the 1:3 NOR:SH gel had 100% soluble fraction and the 1:1 and 1:2 NOR:SH gels failed to gel, meaning the full mass loss and swelling study could not be carried out on these gels. Significance levels for soluble fraction: * $p < 0.05$ vs. 1:12 gels at 10 wt%, † $p < 0.05$ vs. 1:1 gels at 5 wt%, ‡ $p < 0.05$ vs. 1:2 gels at 5 wt%, Δ $p < 0.05$ vs. 1:6 gels at 2.5 wt%. Significance levels for swelling ratio: * $p < 0.05$ vs. 1:12 gels at 10 wt%, † $p < 0.05$ vs. 5 wt% gels at matched NOR:SH ratio, ‡ $p < 0.05$ vs. 10 wt% gels at matched NOR:SH ratio. (n=5, 3).
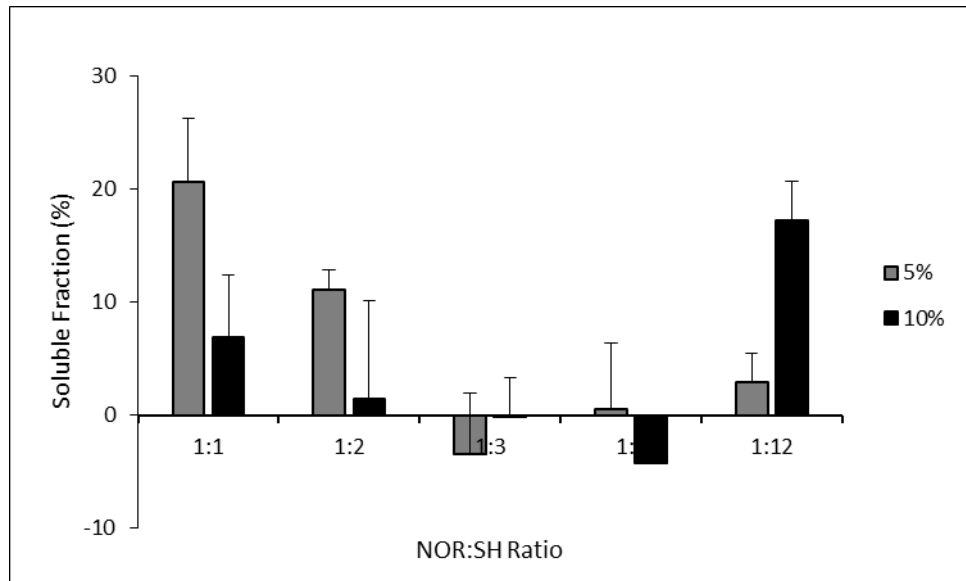
**Figure 3.6 – Soluble fraction and swelling ratio of 5 and 10 wt% GelNOR hydrogels crosslinked with PEG-4SH at a range of NOR:SH ratios.** This is a repeat of the soluble fraction data in Figure 3.5, but with the 2.5 wt% data removed to allow improved visualisation of the 5 and 10 wt% trends. (n=5, 3).

The PEG-4SH crosslinked 1:12 NOR:SH ratio gels were the only one of the tested crosslinkers and NOR:SH ratios where the 5 wt% gel had a statistically significantly lower soluble fraction and swelling ratio than the 10 wt% gel ($p < 0.001$ and $p < 0.01$, respectively). This was also seen with the 2.5 wt% gel, which also had a significantly lower soluble fraction than the 10 wt% gel ($p < 0.01$), but still had a higher swelling ratio than both the 5 and 10 wt% gels ($p < 0.0001$).

The 2.5 wt% gels followed a different trend in soluble fraction to all other gels tested, in that the 1:12 NOR:SH gels had significantly lower soluble fraction than the 1:6 gels ($p < 0.0001$), which in turn had a significantly lower soluble fraction than the 1:3 gels ($p < 0.0001$). Though it is difficult to describe a trend from only two results, it can also be noted that the swelling ratio of the 2.5 wt% gels crosslinked with PEG-4SH decreased significantly from 1:6 to 1:12 NOR:SH ($p < 0.0001$), in keeping with the behaviour of the 5 wt% gels, rather than the 10 wt% gels.

Similarly to the DTT crosslinked gels, reduction in the wt% of the PEG-4SH crosslinked gels resulted in an increased swelling ratio. With the 2.5 wt% gels having a higher swelling ratio than the 5 wt% gels at all NOR:SH ratios tested, and the 5 wt% gels having a higher swelling ratio than the 10 wt%

gels at all NOR:SH ratios tested, except the 1:12 NOR:SH ratio as previously described.

As previously described, 10 wt% GelNOR gels crosslinked with DTT and PEG-4SH showed the same bell curve trend in crosslinking efficiency with variation of NOR:SH ratio, but the use of PEG-4SH rather than DTT did cause some changes. Though soluble fraction was not significantly different between the 1:2, 1:3, and 1:6 gels, the soluble fraction of the PEG-4SH crosslinked gels was significantly lower than that of the DTT crosslinked gels at both 1:1 and 1:12 NOR:SH ($p < 0.01$, Welch's t-test) (Figure 3.7). Further, the swelling ratio of the PEG-4SH crosslinked gels was significantly lower than that of the DTT crosslinked gels at all NOR:SH ratios tested.
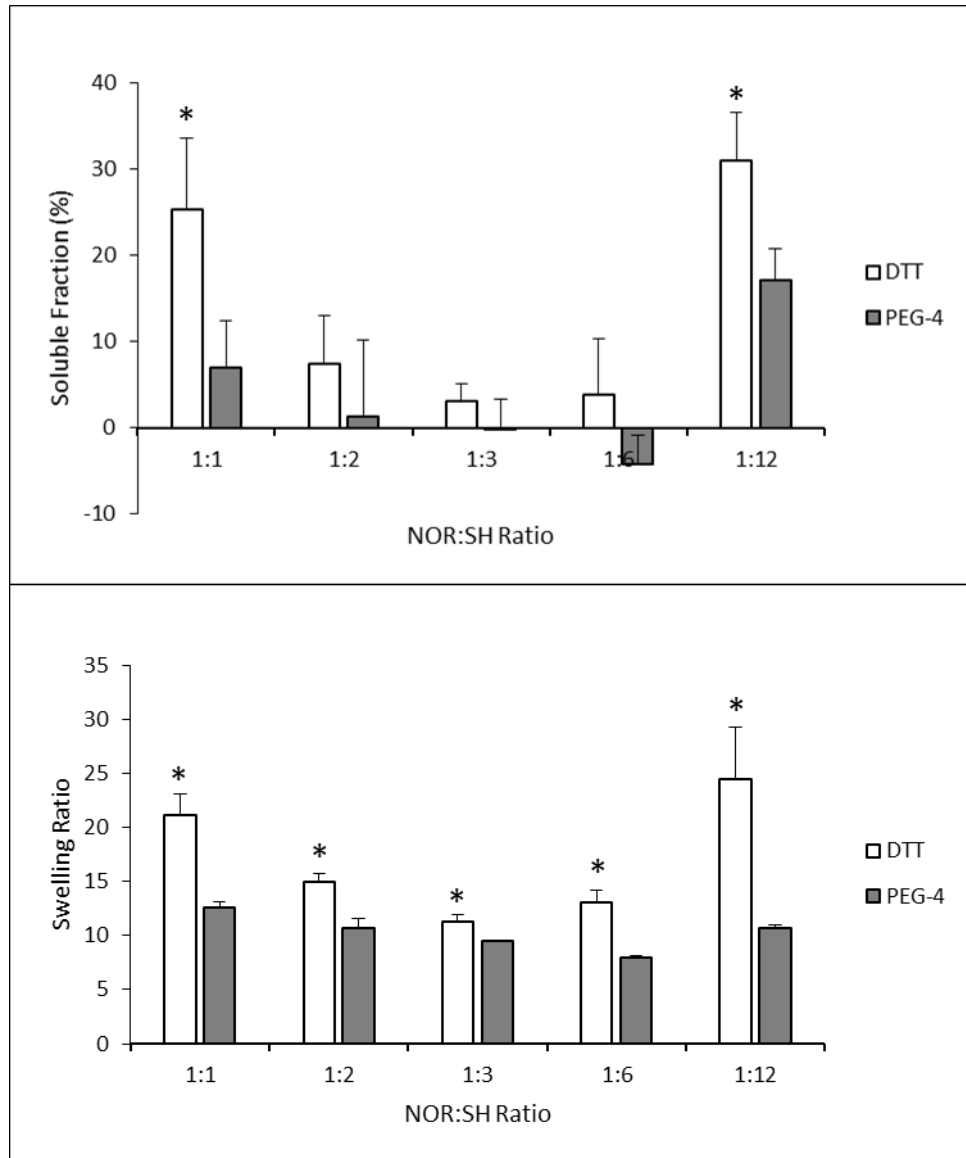
**Figure 3.7 – Soluble fraction and swelling ratio of 10 wt% GelNOR hydrogels crosslinked with DTT and PEG-4SH at a range of NOR:SH ratios.** Significance levels for soluble fraction: * $p < 0.05$ vs. PEG-4SH crosslinked gels at matched NOR:SH ratio. Significance levels for swelling ratio: * $p < 0.05$ vs. PEG-4SH crosslinked gels at matched NOR:SH ratio. (n=5, 3).

The effect of crosslinker selection on soluble fraction is greater at lower wt%, demonstrated by PEG-4SH crosslinked gels achieving significantly lower soluble fraction than those crosslinked with DTT at all NOR:SH ratios except 1:6 in 5 wt% gels (Figure 3.8). The PEG-8SH gels also exhibited a significantly lower soluble fraction than the DTT crosslinked gels for all ratios except 1:3, but the soluble fractions were not significantly different between PEG-4SH and PEG-8SH crosslinked 5 wt% gels, except at 1:2 NOR:SH ratio at which the PEG-4SH was lower ($p < 0.001$).

The selection of crosslinker was also shown to have an impact on the swelling ratio of the 5 wt% gels, with the swelling ratios of both the PEG-4SH and PEG-8SH crosslinked gels being significantly lower than those of DTT crosslinked gels at all measured NOR:SH ratios. The swelling ratios of the PEG-8SH crosslinked gels were also significantly lower than those of the PEG-4SH crosslinked gels at 1:1 ($p<0.05$), 1:2 ($p<0.01$), 1:3 ($p<0.001$), and 1:6 ($p<0.0001$) NOR:SH, but not at 1:12.

A similar trend was seen in the soluble fraction between PEG-4SH and PEG-8SH crosslinked gels at 5 wt%, in that the soluble fraction similarly does not increase to 1:12 NOR:SH, as it does for DTT crosslinked gels, and like PEG-4SH crosslinked gels, the soluble fraction of the 1:12 NOR:SH ratio PEG-8SH crosslinked gel was not significantly different to the 1:3 and 1:6 gels. Similarly to the PEG-4SH gels, the swelling ratios of the PEG-8SH gels also decreased sequentially from 1:1 to 1:6 NOR:SH ratio, but then increased from 1:6 to 1:12, though this increase just misses being statistically significant.
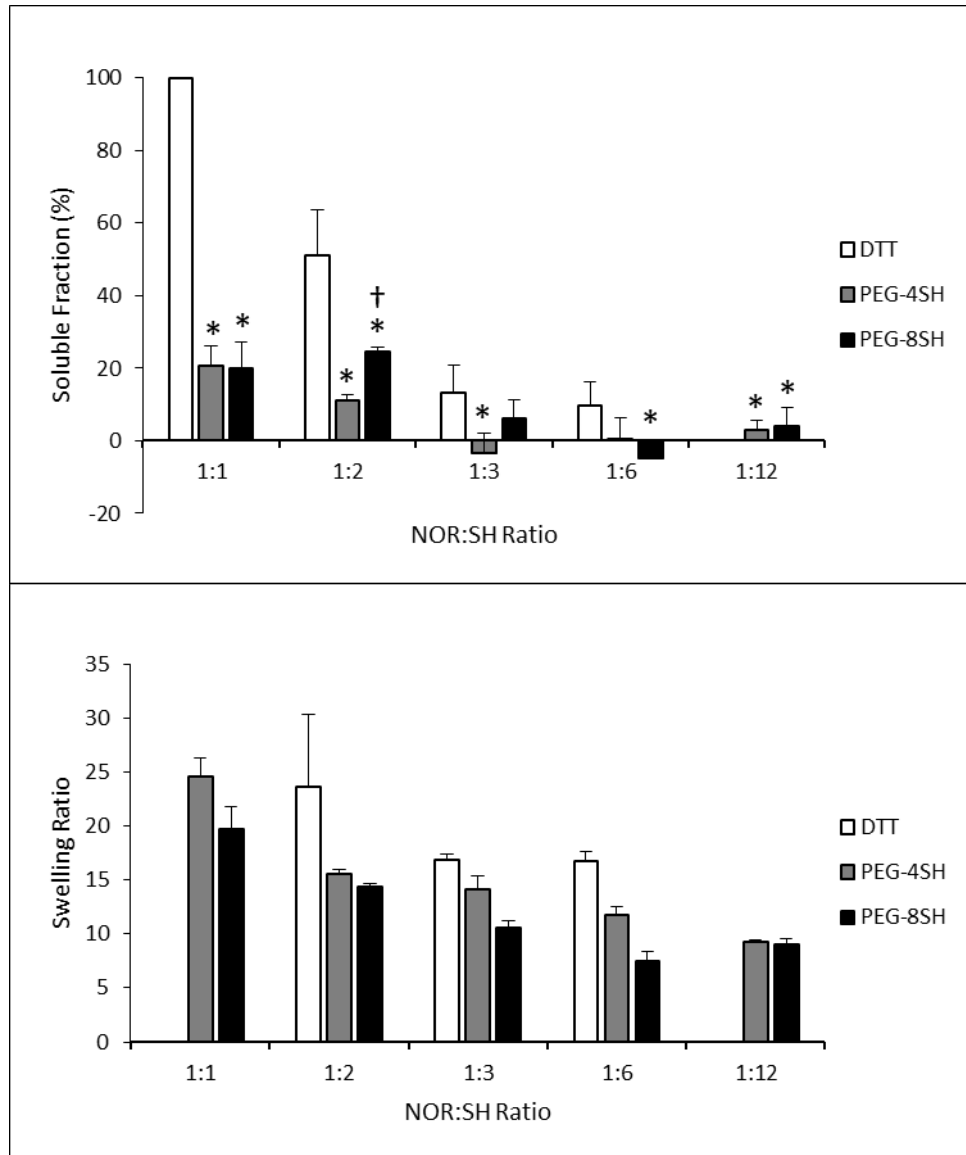
**Figure 3.8 – Soluble fraction and swelling ratio of 5 wt% GelNOR hydrogels crosslinked with DTT, PEG-4SH, and PEG-8SH at a range of NOR:SH ratios.** Significance levels for soluble fraction: * $p < 0.05$ vs. DTT crosslinked gels at matched NOR:SH ratio, † $p < 0.05$ vs. PEG-4SH gels at 1:2 NOR:SH ratio. (n=5, 2).

### 3.3.3.2  Analysis of Mechanical Properties

Data from the MTS Criterion was converted from displacement and force into strain and stress, respectively. The data was then used to plot a graph of stress vs strain, and the gradient of the line was analysed to determine the material's Young's Modulus. The 10-15% strain region was identified as the best choice for providing consistently linear data, identified by the $R^2$ value closest to 100 across all tested samples, though it is unavoidable that the $R^2$ value will vary to some degree between samples. Young's Modulus data from this strain region was used to compare mechanical properties of tested samples.

The trend in Young's Moduli of 10 wt% GelNOR, crosslinked with DTT at different NOR:SH ratios, approximately corresponds to the inverse of the swelling ratios in Figure 3.4, resulting in a bell curve around the 1:3 NOR:SH gel. Comparison with 10 wt% GelMA also shows the GelNOR hydrogel, crosslinked with DTT at all tested NOR:SH ratios, to be much weaker than GelMA at the same wt% (Figure 3.9).
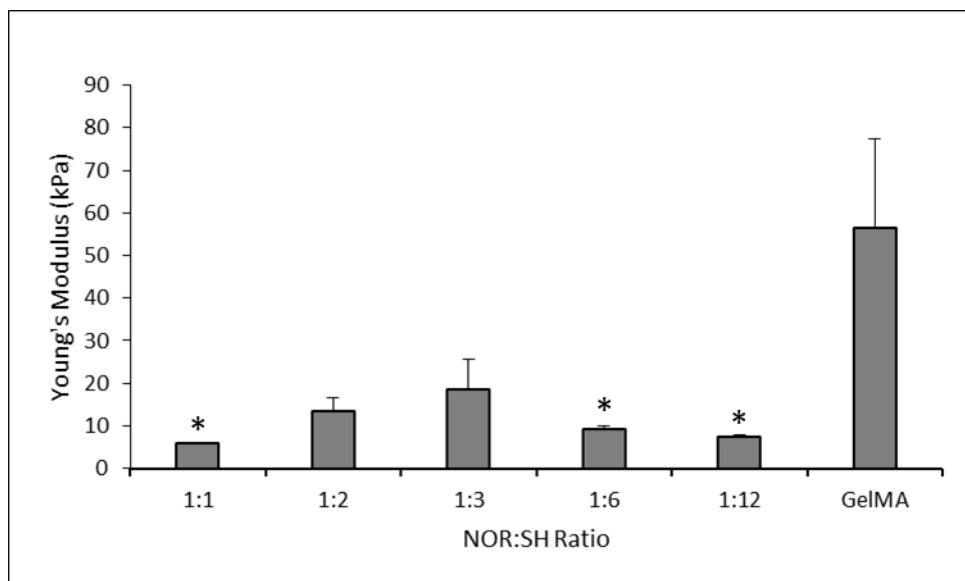


**Figure 3.9 – Young's Moduli of 10 wt% GelNOR hydrogels crosslinked with DTT at a range of NOR:SH ratios.** Samples are shown in comparison to 10 wt% GelMA for reference. * $p < 0.05$ vs. 1:3 NOR:SH. (n=4, 2).

Though the soluble fraction for 10 wt% GelNOR gels were not significantly different between 1:2, 1:3 and 1:6 gels, the swelling ratio of the 1:3 gel was significantly lower than that of both the 1:2 and 1:6 gel. The 1:3 NOR:SH gels had a significantly greater Young's modulus than that of the 1:1 (p<0.01), 1:6 (p<0.05), and 1:12 (p<0.05) NOR:SH gels (one-way ANOVA

with post-hoc Tukey test), but also had a significantly lower Young's modulus than the 10 wt% GelMA comparison (p<0.01, Welch's t-test).

In contrast to the 10 wt% gels, at 5 wt% the 1:6 NOR:SH gels had a significantly greater Young's Modulus than the 1:3 gel (p<0.01, Welch's t-test) (Figure 3.10). This is despite no significant difference being observed in soluble fraction or swelling ratio between the 1:3 and 1:6 gels (Figure 3.4). The 1:2 NOR:SH gel had significantly higher soluble fraction and swelling ratio than the 1:3 and 1:6 gels, and was also the weakest of the analysed gels, such that it was significantly affected by background 'noise' during compressive testing and was thus untestable.
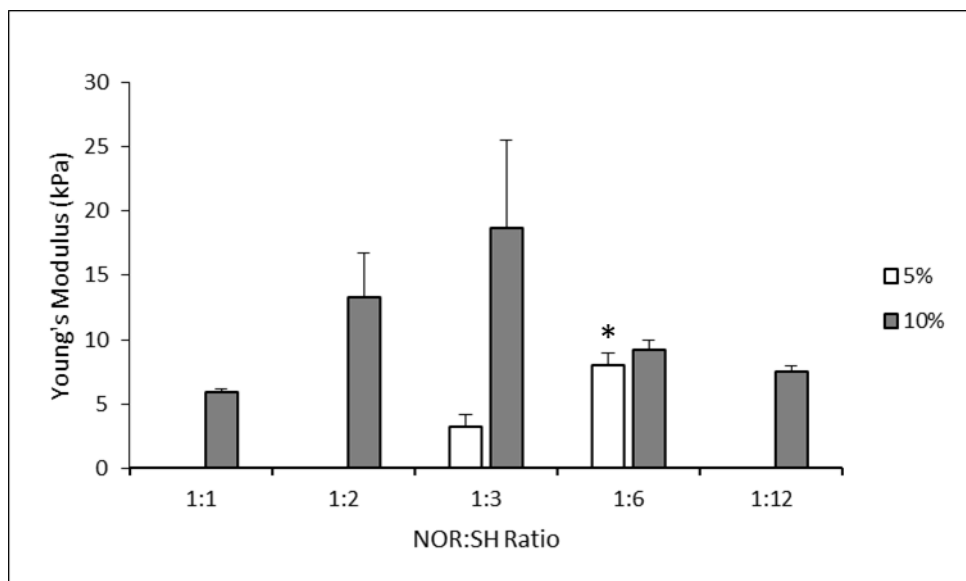


**Figure 3.10 – Young's Moduli of 5 and 10 wt% GelNOR hydrogels crosslinked with DTT at a range of NOR:SH ratios.** Data is incomplete for 5 wt% as 1:1 and 1:12 NOR:SH gels had 100% soluble fraction thus did not gel, and the 1:2 NOR:SH gels were so weak as to be untestable with this method. * p<0.05 vs. 1:3 NOR:SH 5 wt%. (n=4, 2).

The described increase in Young's Modulus in the 1:6 NOR:SH gels at 5 wt% is such that the Young's Modulus (7.99 kPa) was not significantly lower than the corresponding 10 wt% gels (9.20 kPa). This is despite the 5 wt% gels having significantly greater swelling ratio.

The described correlation with swelling ratio was not seen for 5 wt% PEG-4SH crosslinked gels (Figure 3.11). Instead, there was no significant difference between the Young's Moduli of the 1:1, 1:2, and 1:3 NOR:SH gels, despite the significant differences seen in swelling ratio. The Young's Modulus of the 1:6 NOR:SH gels (123 kPa) was an order of magnitude

greater than that of the 1:3 gels (11.8 kPa), and the 1:12 gel was significantly stiffer again (p<0.0001), with a Young's Modulus of 182 kPa.

The difference in Young's Modulus between the 2.5 wt% and 5 wt% gels was significant at both 1:6 and 1:12 NOR:SH (p<0.0001 and p<0.001 respectively, Welch's t-tests), with the 5 wt% gel being approximately 10 times stiffer at 1:6 NOR:SH, and approximately 5 times stiffer at 1:12. As with the crosslinking efficiency, the Young's Modulus was greater in the 2.5 wt% gels crosslinked with PEG-4SH at 1:12 NOR:SH than at 1:6, though the difference did not achieve statistical significance. This follows the trend seen in 5 wt% PEG-4SH crosslinked gels of being stiffer at higher NOR:SH ratios.

When compared to the 10 wt% GelMA gels, the 5 wt% PEG-4SH crosslinked GelNOR gels were weaker than 10 wt% GelMA at 1:1 – 1:3 ratios (p<0.01 for all), but stiffer at both 1:6 (p<0.001) and 1:12 (p<0.0001) NOR:SH, respectively (Welch's t-tests).
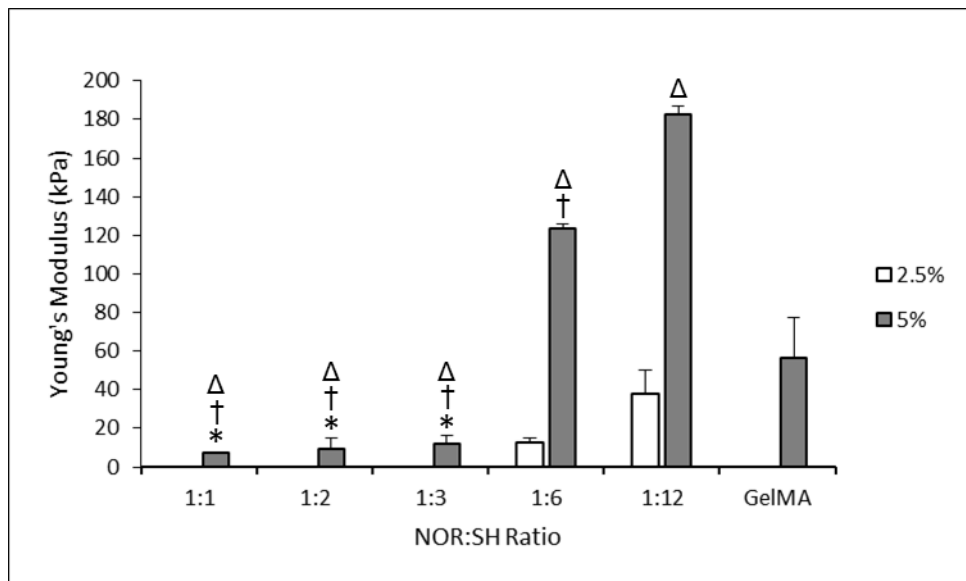


**Figure 3.11 - Young's Moduli of 2.5 and 5 wt% GelNOR hydrogels crosslinked with PEG-4SH at a range of NOR:SH ratios.** Data is incomplete for 2.5 wt% as the 1:1 and 1:2 NOR:SH gels did not gel, and the 1:3 NOR:SH gels had 100% soluble fraction. Data is shown in comparison to 10 wt% GelMA for reference. Significance levels * p<0.05 vs. 1:6 NOR:SH,† p<0.05 vs. 1:12 NOR:SH, Δ p<0.05 vs. 10 wt% GelMA. (n=5, 2).

The effect of crosslinker selection and concentration on the mechanical properties of the resulting GelNOR gels was significant (Figure 3.12). Though there was no significant difference in Young's Modulus between PEG-4SH and PEG-8SH crosslinked 5 wt% gels at 1:1 or 1:12 NOR:SH, PEG-8SH crosslinked gels were significantly stiffer than PEG-4SH gels at

1:2 NOR:SH (p<0.01, Welch's t-test). At 1:3 NOR:SH, the PEG-8SH crosslinked gels were more than 6 times stiffer than the PEG-4SH crosslinked gels and more than 15 times stiffer than the DTT crosslinked gels (p<0.0001, one-way ANOVA with post-hoc Tukey test). The PEG-8SH crosslinked gels were also more than double the stiffness of the PEG-4SH crosslinked gels (p<0.001) and more than 34 times stiffer than the DTT crosslinked gels, at 1:6 NOR:SH (p<0.0001). Similarly, the PEG-4SH crosslinked gels were more than 15 times stiffer than DTT crosslinked at 1:6 NOR:SH (p<0.01), but there was no significant difference in stiffness between DTT and PEG-4SH crosslinking at 1:3 NOR:SH.

The overall trend in stiffness followed by the PEG-8SH gels with increasing NOR:SH ratio was not the same as that followed by the PEG-4SH gels. Where the Young's Modulus of the PEG-4SH gels did not increase significantly from 1:1 to 1:2 to 1:3 NOR:SH (7.08 to 9.31 to 11.8kPa), the Young's Modulus of the PEG-8SH crosslinked gels increased substantially from 1:1 to 1:2 to 1:3 NOR:SH (8.00 to 30.30kPa to 80.155kPa), though these increases were only statistically significant between 1:1 and 1:3 NOR:SH (p<0.01). Further, where the Young's Modulus of the PEG-4SH crosslinked gels increased significantly from 1:6 to 1:12 NOR:SH, it decreased significantly in gels crosslinked with PEG-8SH (p<0.001), such that the Young's Moduli of gels crosslinked with PEG-4SH and PEG-8SH were not significantly different at 1:12 NOR:SH.
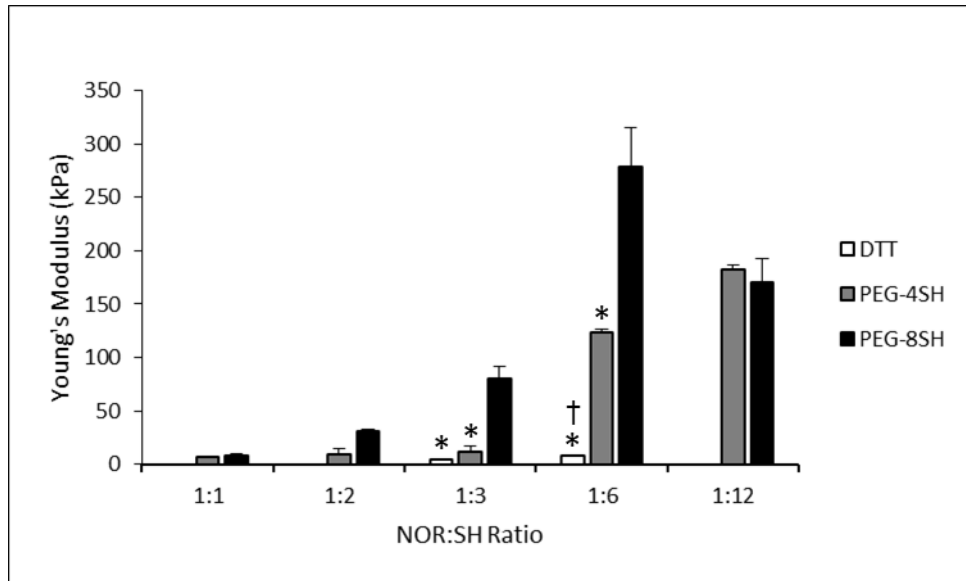
**Figure 3.12 – Young's Moduli of 5 wt% GelNOR hydrogels crosslinked with DTT, PEG-4SH, or PEG-8SH at a range of NOR:SH ratios.** Data is incomplete for 5 wt% gels crosslinked with DTT as the 1:1 and 1:12 NOR:SH gels had 100% soluble fraction thus did not gel, and the 1:2 NOR:SH gels were so weak as to be untestable with this method. Significance levels * $p < 0.05$ vs. PEG-8SH, † $p < 0.05$ vs. PEG-4SH. (n=4, 2).

### 3.3.4 Analysis of cells encapsulated in GelNOR Hydrogel Scaffolds

Passage 16 – 21 HFF cells were encapsulated in GelNOR hydrogels crosslinked with DTT at a range of NOR:SH ratios, at 5 and 10 wt%.

At 5 wt%, the 1:2 NOR:SH gels degraded rapidly in culture and the 1:1 and 1:12 gels failed to gel. The 1:3 and 1:6 NOR:SH gels remained intact until the day 7 time-point, but were degraded before the day 14 time-point. At 10 wt% the 1:12 NOR:SH gels dissolved within the first 24 hours, and the 1:1 gels were degraded before the day 14 time-point.

### 3.3.4.1 Analysis of Cell Viability

Cell viability was initially analysed through LIVE/DEAD staining. Encapsulated cells were stained with Propidium Iodide (red, dead) and Calcein AM (green, live) before being imaged using a fluorescence microscope and apotome. Examples of resulting images are given in Figure 3.13.
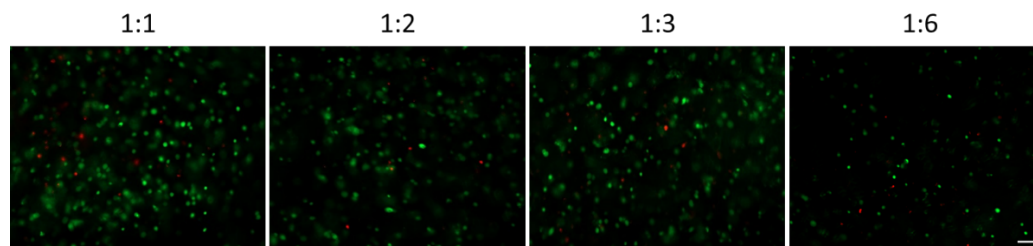


**Figure 3.13 – HFFs encapsulated in 10 wt% GelNOR, crosslinked with DTT at a range of NOR:SH ratios, and stained with Calcein AM (green, live) and propidium iodide (red, dead) for LIVE/DEAD assay, 1 day post encapsulation.** (Scale bar = 100 µm)

In order to analyse viability quantitatively, the fluorescence microscope images were analysed using ImageJ. Cell counts were performed of both live and dead cells, and these results were then expressed as percentage cell viability, as shown in Figure 3.14.

When HFFs were encapsulated in 10 wt% GelNOR, LIVE/DEAD assay showed no significant variation in cell viability at the day 1 time point between different NOR:SH ratios (one-way ANOVA). As time in culture increased, there was a general trend of decreasing viability from day 1 to day 21 in both the 1:2 and 1:3 NOR:SH gels, though none of the observed changes in viability were statistically significant.

In the 1:6 NOR:SH gels, cell viability increased from day 1 to day 7, and then plateaued from day 7 to day 21.However, none of the observed viabilities were significantly different from each other at any assay time point. The 1:1 NOR:SH gels disintegrated between the day 7 and day 14 assay time points, and the 1:12 NOR:SH gels failed to gel when loaded with cells.
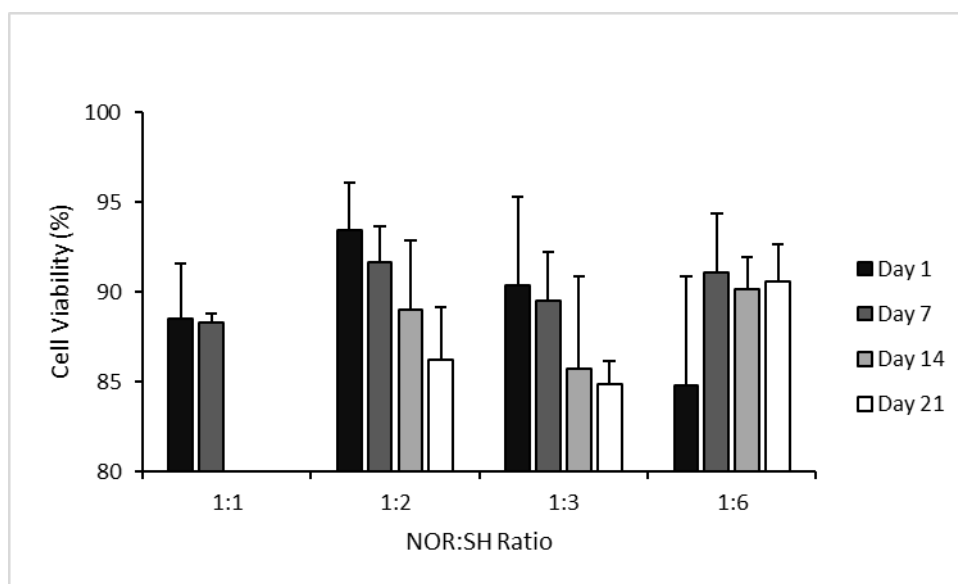


**Figure 3.14 – Viability of HFFs cultured in GelNOR hydrogels, crosslinked with DTT at a range of NOR:SH ratios at 10 wt%, across a range of timepoints.** (n=3, 3).

HFFs were also encapsulated in 5 wt% GelNOR at a range of NOR:SH ratios and viability evaluated (Figure 3.15). The samples failed to gel at both 1:1 and 1:12 NOR:SH, and 1:2 NOR:SH gels disintegrated between the day 1 and day 7 time-points, so only the 1:3 and 1:6 NOR:SH gels were evaluable, though even the gels in these two groups disintegrated before the day 14 time-point.

At the day 1 time-point, there was no significant difference in the observed viabilities of cells encapsulated in 5 wt% GelNOR crosslinked with DTT at 1:3 and 1:6 NOR:SH ratio. Though the viabilities observed in both the 1:3 and 1:6 NOR:SH ratio gels decreased between day 1 and day 7, only the decrease seen in the 1:3 NOR:SH gel, from 93.4% to 80.9%, was statistically significant ($p < 0.05$, Welch's t-test). At the day 7 time-point there was no significant in cellular viability between the 1:3 and 1:6 NOR:SH ratio gels.
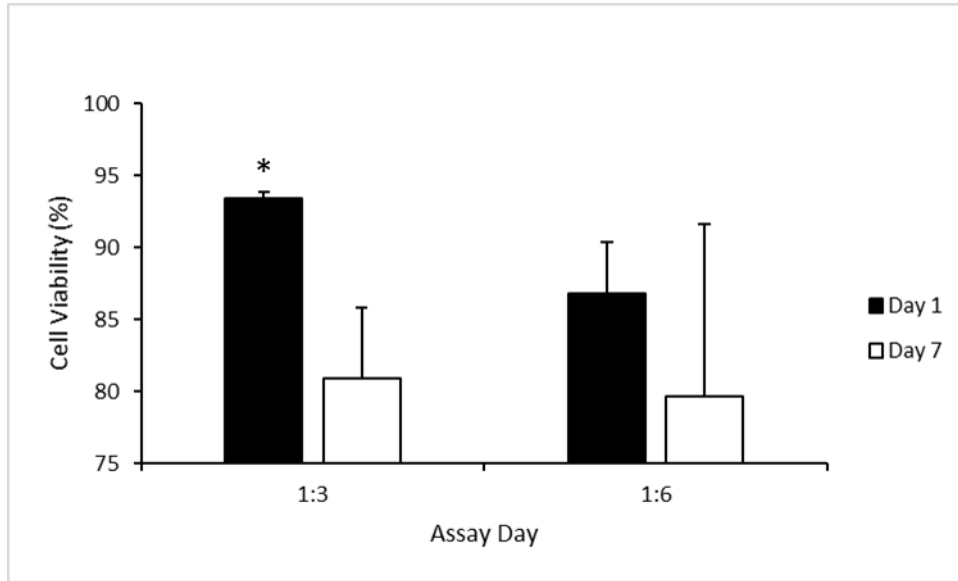
**Figure 3.15 – Viability of HFFs cultured in GelNOR hydrogels, crosslinked with DTT at 1:3 and 1:6 NOR:SH ratios at 5 wt%, at day 1 and day 7 timepoints.** Significance levels * $p < 0.05$ vs. Day 7. (n=3, 3).

Comparisons in cell viability between 5 wt% and 10 wt% gels were made for gels crosslinked at 1:3 and 1:6 NOR:SH ratio only (Figure 3.16). Comparison showed that there were no significant differences in observed cell viability between 5 wt% and 10 wt% gels, at the same NOR:SH ratio, at either the day 1 or day 7 time point.
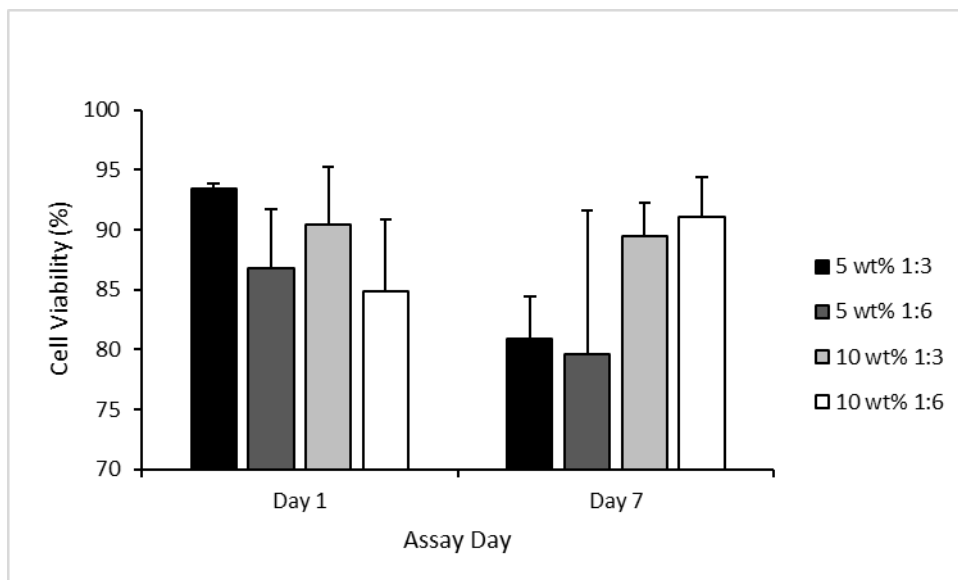


**Figure 3.16 – Comparison of viabilities of HFFs cultured in GelNOR hydrogels, crosslinked with DTT at 1:3 and 1:6 NOR:SH ratio and at 5 wt% and 10 wt%, at day 1 and day 7 timepoints.** (n=3, 3).

Further to the described LIVE/DEAD assays, cell viability was also analysed using an alamarBlue cellular metabolism assay. AlamarBlue is reduced by enzymes involved in cellular metabolism, resulting in a colour change and thus a change in light absorbance, allowing observation and comparison of the overall metabolic activity of a cell population.

AlamarBlue assay clearly showed an increase in HFF population cellular metabolism at each time-point for 10 wt% gels at all NOR:SH ratios (Figure 3.17). At day 1, there was no significant difference in alamarBlue stain reduction between any of the tested NOR:SH ratios (one-way ANOVA). Similarly, there were no significant differences in alamarBlue stain reduction between any of the tested NOR:SH ratios at day 7 or 14. At day 21, alamarBlue stain reduction was greatest in the 1:2 NOR:SH ratio gel, and was significantly greater than that seen in the 1:6 NOR:SH gel ($p < 0.01$, Welch's t-test). AlamarBlue reduction by cells cultured in the 1:2 NOR:SH gels was also greater than that in the 1:3 NOR:SH gel, but was not statistically significantly so, and stain reduction in the 1:3 NOR:SH gel was greater than in the 1:6 NOR:SH gel, but again this was not statistically significant.
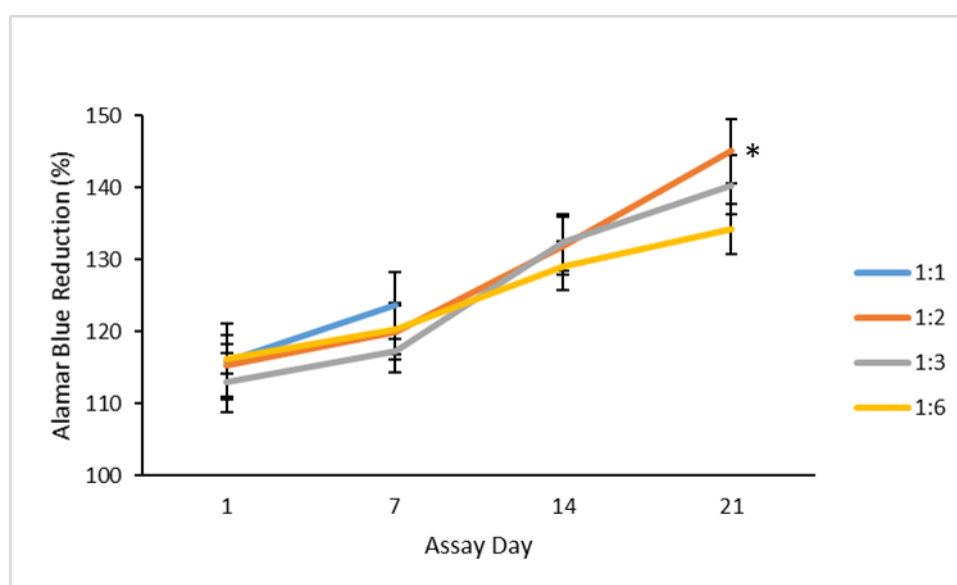


**Figure 3.17 – Results of alamarBlue assay on HFFs encapsulated in 10 wt% GelNOR hydrogel, crosslinked with DTT at a range of NOR:SH ratios, across a 21-day culture period.** Significance levels *$p < 0.05$ vs. 1:6 NOR:SH. (n=3, 3).

Comparisons in alamarBlue stain reduction between 5 wt% and 10 wt% gels were able to be made for gels crosslinked at 1:3 and 1:6 NOR:SH ratio at the day 1 and day 7 timepoints (Figure 3.18). At the day 1 timepoint, there

was no significant difference in alamarBlue stain reduction between 5 wt% gels crosslinked at 1:3 and 1:6 NOR:SH ratio. However, at both the 1:3 and 1:6 NOR:SH ratio, alamarBlue stain reduction by cells encapsulated in 5 wt% gels was significantly greater than that in the 10 wt% gels of corresponding NOR:SH ratio ($p < 0.05$ and $p < 0.01$ respectively, Welch's t-test). The difference in alamarBlue stain reduction between 5 and 10 wt% gels of corresponding NOR:SH ratio is even more pronounced at the day 7 timepoint, at both the 1:3 ($p < 0.0001$) and 1:6 ($p < 0.001$) NOR:SH ratios. At the day 7 timepoint, alamarBlue stain reduction was also significantly greater for cells cultured in the 1:6 NOR:SH ratio gel compared to the 1:3 NOR:SH ratio, at 5 wt% ($p < 0.01$, Welch's t-test).
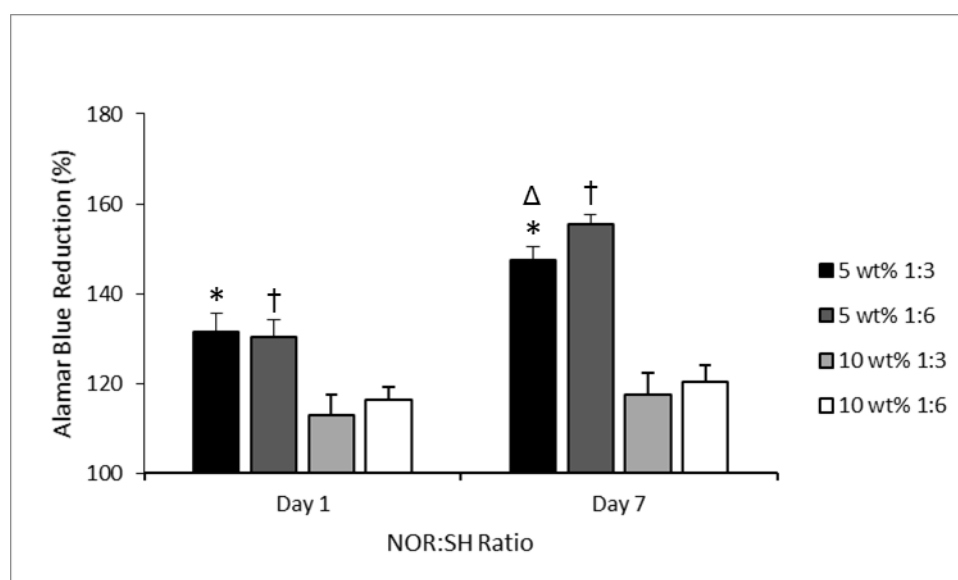


**Figure 3.18 – Comparison of alamarBlue reduction by HFFs cultured in GelNOR hydrogels, crosslinked with DTT at 1:3 and 1:6 NOR:SH ratio and at 5 wt% and 10 wt%, at day 1 and day 7 timepoints.** Significance levels *$p < 0.05$ vs. 10 wt% 1:3, † $p < 0.05$ vs. 10 wt% 1:6, Δ $p < 0.05$ vs. 5 wt% 1:6. (n=3, 3).

A final consideration that was made when analysing cellular viability was the presence of 'dual labelling' during the LIVE/DEAD assay. Dual labelling occurs when cells take up both the 'live' Calcein AM stain and the 'dead' propidium iodide stain. Typically, live cells are impermeable to propidium iodide, but it is possible for damaged cells to become 'leaky', allowing ingress of propidium iodide despite the cell still being alive.

There was little evidence of dual labelling at the day 1 timepoint, where, none was observed in cells in the 1:2 NOR:SH gels, and only a small number of dual labelled cells was observed in 1:3 and 1:6 NOR:SH gels

(Figure 3.19). There was increased dual labelling at the day 7 timepoint, with some evidence now visible at the 1:2 NOR:SH ratio, extensive dual labelling at 1:3 NOR:SH, and at 1:6 NOR:SH was observed where the numbers of dual labelled cells appeared to outnumber the number of 'single labelled' cells, although this was not objectively quantified. At 21 days in culture, there was no obvious dual labelling in the 1:2 and 1:3 NOR:SH gels, and though there were occasional dual labelled cells visible in the 1:6 NOR:SH gels, the level has decreased dramatically.
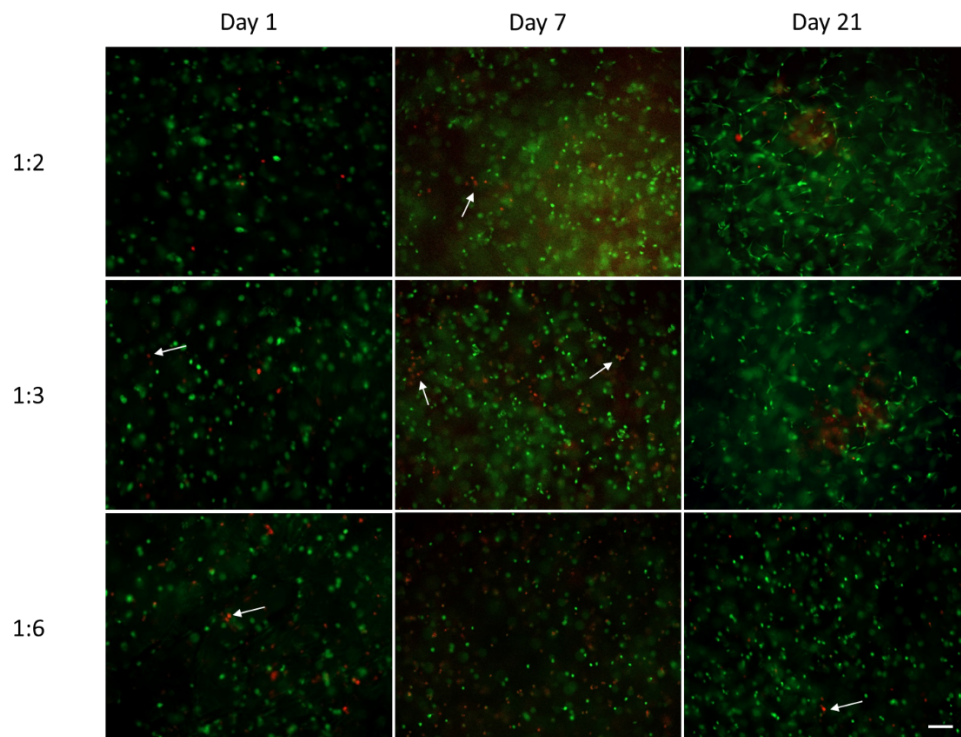


**Figure 3.19 – Viability of HFFs encapsulated in 10 wt% GelNOR, crosslinked with DTT at a range of NOR:SH ratios.** The cells were stained with Calcein AM (green, live) and propidium iodide (red, dead) according to the LIVE/DEAD assay, 1, 7, and 21 days post encapsulation. Arrows indicate evidence of 'dual labelling', none were added to the 1:6 NOR:SH, Day 7, image due to the high prevalence of dual labelling. (Scale bar = 100 µm)

### 3.3.4.2 Analysis of Cellular Behaviour

In order to analyse the behaviour of cells encapsulated in the GelNOR hydrogels, cellular morphology was analysed through staining with Calcein AM and rhodamine-phalloidin, and observation using fluorescence microscopy and light-microscopy.

Observation of morphology via Calcein AM staining showed that for 10 wt% gels crosslinked with DTT, at the initial day 1 timepoint cells encapsulated at all NOR:SH ratios were very rounded (Figure 3.20). At 1:1, 1:2 and 1:3 NOR:SH ratio, cells became progressively more spread as time in culture increased. At day 14 and day 21, cells encapsulated in 1:2 and 1:3 gels were highly elongated, exhibiting a fibroblastic morphology. In contrast, cells encapsulated at 1:6 NOR:SH maintained the rounded morphology seen at the day 1 timepoint throughout the 21 days in culture.
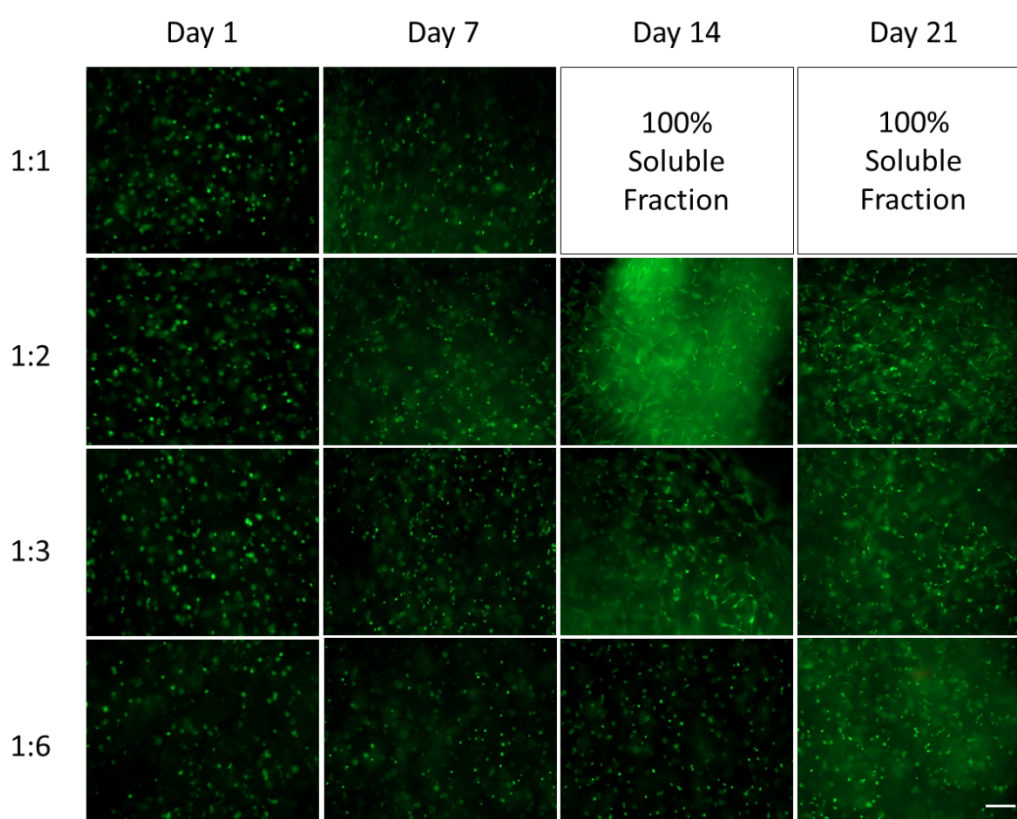


**Figure 3.20 – Fluorescence microscopy images of HFFs encapsulated in 10 wt% GelNOR, crosslinked with DTT at a range of NOR:SH ratios, taken over 21 days in culture.** Cells are stained using Calcein AM (green). (Scale bar = 100 μm)

In order to analyse cellular morphology quantitatively the Calcein AM images were processed using ImageJ, allowing each stained cell to be given a 'circularity' score, with a perfect circle being scored '1' and a perfect line

being scored '0'. This allows comparison of the average circularity score, as demonstrated in Figure 3.21.
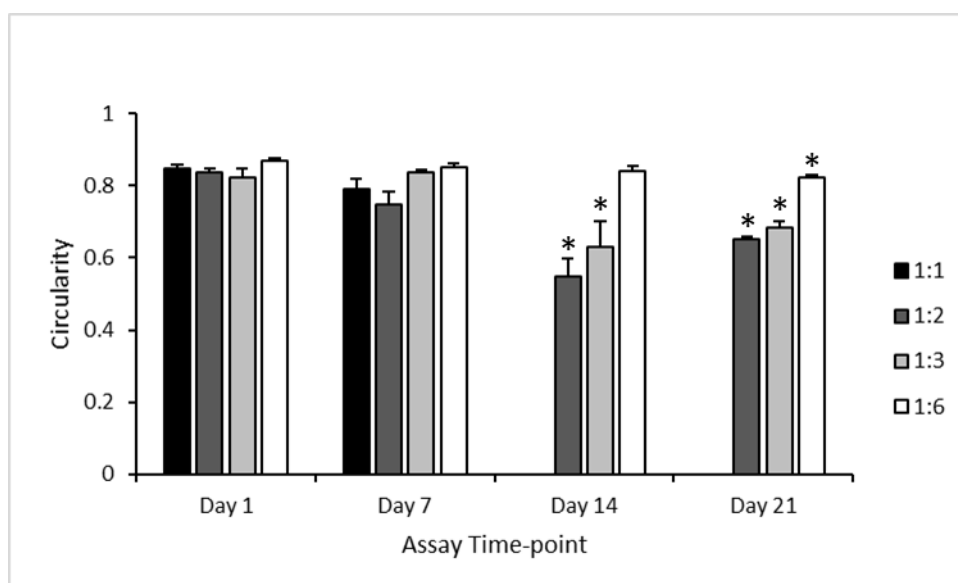


**Figure 3.21 – Circularity scores for HFFs encapsulated in 10 wt% GelNOR, crosslinked with DTT at a range of NOR:SH ratios, at a range of time points taken over 21 days in culture.** Significance levels * $p<0.05$ vs. Day 1 at the corresponding NOR:SH ratio. (n=3, 3).

Cells encapsulated in 10 wt% gels at 1:2 and 1:3 NOR:SH became less rounded and more fibroblastic over time in culture, evidenced by a drop in circularity score from 0.83 to 0.65 and 0.82 to 0.69, respectively. At 1:3 NOR:SH, HFF circularity was significantly lower at both the day 14 and day 21 time points when compared to the day 1 time point ($p<0.05$, one-way ANOVA with post-hoc Tukey test), and the same is true at 1:2 NOR:SH ratio ($p<0.01$ at day 21 and $p<0.0001$ at day 14, one-way ANOVA with post-hoc Tukey test).

Conversely, the drop in circularity score from day 1 to day 21 in 1:6 NOR:SH gels, 0.87 to 0.82, was much lower than that seen in the 1:2 and 1:3 NOR:SH gels. Though this drop is still statistically significant ($p<0.01$, one-way ANOVA with post-hoc Tukey test), the day 21 circularity score for 1:6 NOR:SH gels was still higher than the day 1 score for the 1:3 NOR:SH gels. Interestingly, for all NOR:SH ratios tested the drop in circularity is between day 1 and 7 was not statistically significant, and for 1:3 NOR:SH ratio gels the circularity actually increased over this time period.

At day 1, the circularity score of the 1:6 NOR:SH ratio gels was significantly higher than both the 1:2 and 1:3 gels ($p<0.05$ and $p<0.01$ respectively, one-

way ANOVA with post-hoc Tukey test). At day 7, the circularity score of the 1:2 NOR:SH gels was significantly lower than both the 1:3 and 1:6 NOR:SH gels ($p<0.05$ and $p<0.01$ respectively, one-way ANOVA with post-hoc Tukey test), though the circularity scores of cells encapsulated in 1:3 and 1:6 NOR:SH gels are not significantly different to each other. This indicates that cells encapsulated in 1:2 NOR:SH gels were able to 'spread' more quickly than those in 1:3 and 1:6 NOR:SH gels. By day 14, the circularity scores of cells encapsulated in 1:2 and 1:3 NOR:SH gels were both significantly lower than those in 1:6 NOR:SH gels ($p<0.01$ and $p<0.05$ respectively, one-way ANOVA with post-hoc Tukey test), and the same was true at the day 21 time point ($p<0.0001$ for both, one-way ANOVA with post-hoc Tukey test).

When encapsulated at 5 wt%, because the gels were only evaluable at the day 1 and day 7 time-point, the progression in cellular morphology was less obvious over the shorter timescale. Though the time in culture was only a third of that achieved with the 10 wt% gels, the same shift towards a fibroblastic morphology was evident over time in culture (Figure 3.22).
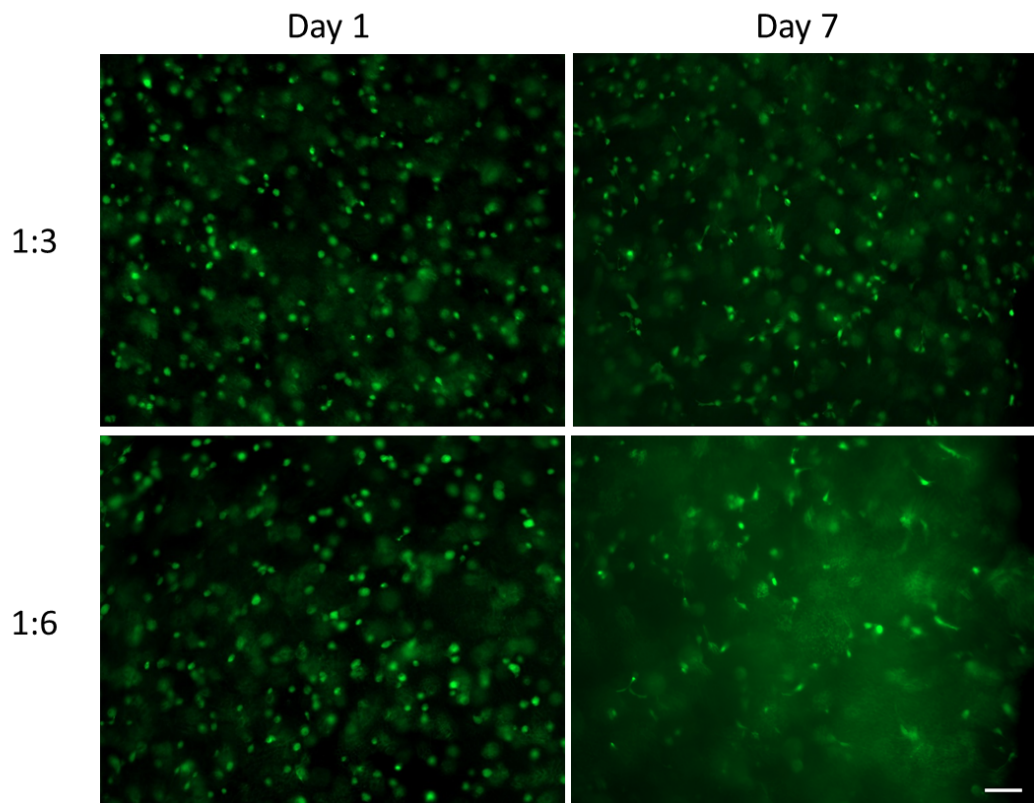


**Figure 3.22 – Circularity scores for HFFs encapsulated in 5 wt% GelNOR, crosslinked with DTT at a range of NOR:SH ratios, after 1 and 7 days in culture.** (Scale bar = 100 µm)

It is again possible to support qualitative observation with quantitative data derived from image processing using ImageJ (Figure 3.23). At 5 wt%, the circularity scores of the cells in the 1:3 and 1:6 NOR:SH gels were not significantly different from each other (Welch's t-test), and though circularity scores decreased from day 1 to day 7 at both NOR:SH ratios, this was not significant.

At day 1, the circularity scores of cells encapsulated in 5 wt% GelNOR were not significantly different from those encapsulated in 10 wt% GelNOR at the corresponding NOR:SH ratio. At day 7, however, circularity scores were significantly lower for 5 wt% gels than 10 wt% gels at both the 1:3 and 1:6 NOR:SH ratio ($p < 0.05$ for both, Welch's t-test).
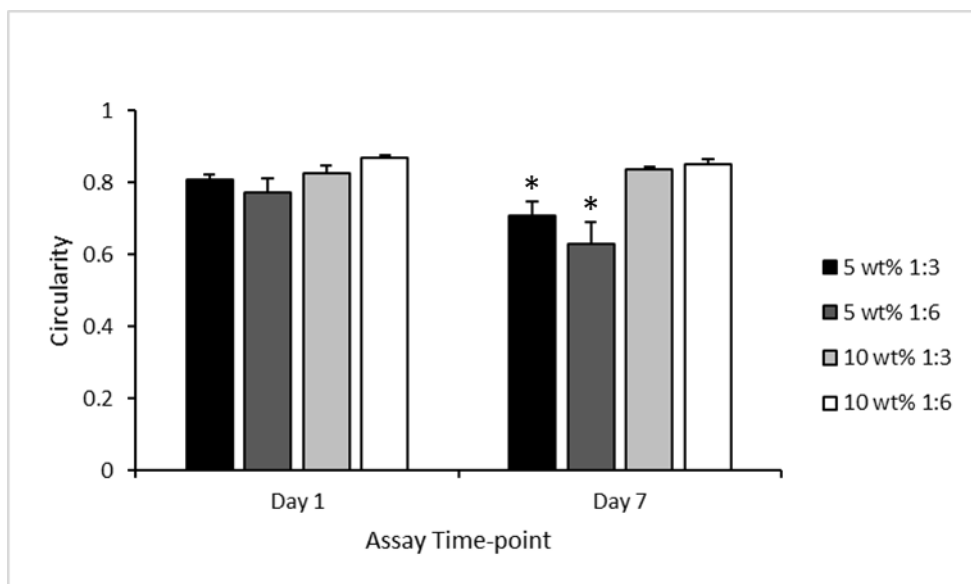


**Figure 3.23 - Circularity scores for HFFs encapsulated in 5 and 10 wt% GelNOR, crosslinked with DTT at a range 1:3 and 1:6 NOR:SH ratios, after 1 and 7 days in culture.** Significance levels * $p < 0.05$ vs. 10 wt% at the corresponding NOR:SH ratio. (n=3, 3).

Cell morphology was also investigated through staining the cells with rhodamine-phalloidin, an F-Actin probe. Though it was possible to use images for 5 wt% gels at both the day 1 and 7 timepoint, and for 10 wt% gels at the day 1 time-point, after these timepoints the rhodamine-phalloidin staining did not produce evaluable images.

When comparing the day 1 and day 7 timepoints for cells encapsulated in GelNOR at 10 wt% (Figure 3.24), it can be seen that there was little F-Actin activity at the day 1 timepoint, but this increased between the day 1 and 7 timepoints for both the 1:3 and 1:6 NOR:SH gels. In terms of comparison between NOR:SH ratios, there was greater F-Actin activity in the 1:3

NOR:SH gels than in the 1:6 NOR:SH gels, at both the day 1 and day 7 timepoints, but the cells themselves remained rounded and morphologically similar at both ratios.
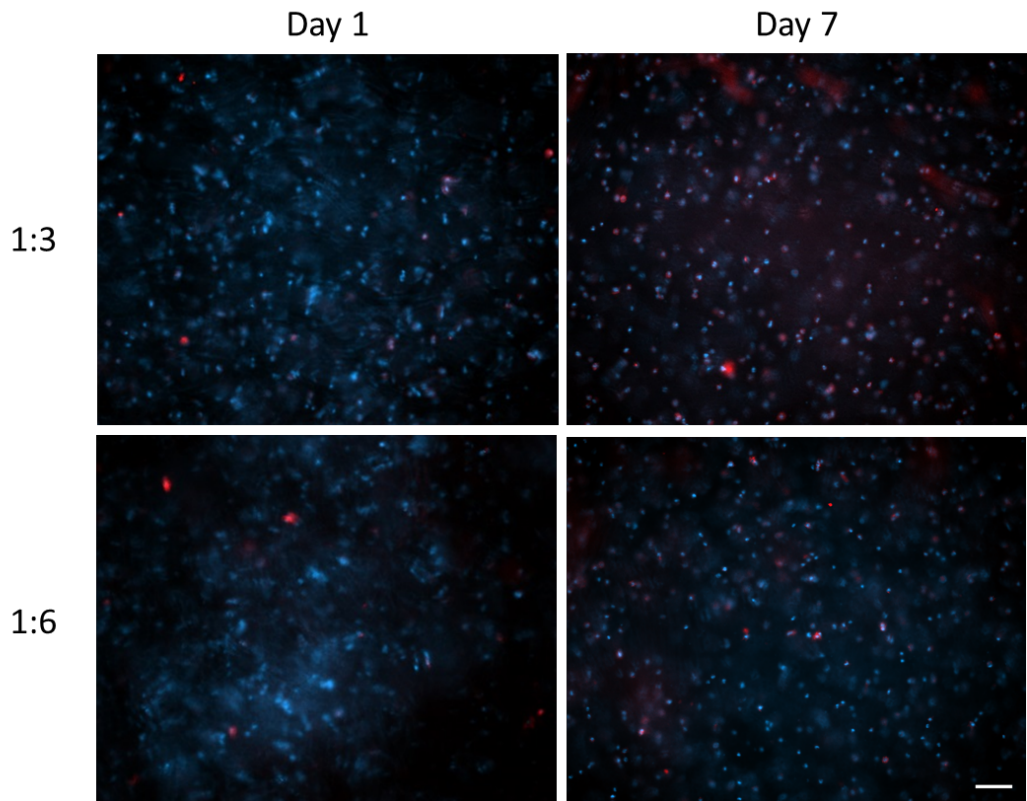


**Figure 3.24 – Comparison of HFFs, stained with rhodamine-phalloidin (F-Actin, red) and DAPI (nucleus, blue), encapsulated 10 wt% GelNOR crosslinked with DTT at 1:3 and 1:6 NOR:SH ratio, after 1 and 7 days in culture.** (Scale bar = 100 µm)

When comparing the day 1 and day 7 timepoints for cells encapsulated in GelNOR at 5 wt%, there was an increase in the F-Actin activity; however, the increase appears to be more significant and is accompanied by significant morphological changes (Figure 3.25). At day 7, the HFFs encapsulated in 5 wt% gels exhibited elongated morphologies and interconnected cell networks at both 1:3 and 1:6 NOR:SH. HFFs encapsulated in 10 wt% did not exhibit these characteristics at this timepoint, for either NOR:SH ratio.

When comparing the F-Actin activity of HFFs encapsulated in 5 and 10 wt% gels at the day 1 timepoint, HFFs encapsulated in 5 wt% gels had higher F-Actin activity than those encapsulated at 10 wt%, at all NOR:SH ratios. This earlier F-Actin activity may be an indicator of the more significant morphological changes to come at the next timepoint.
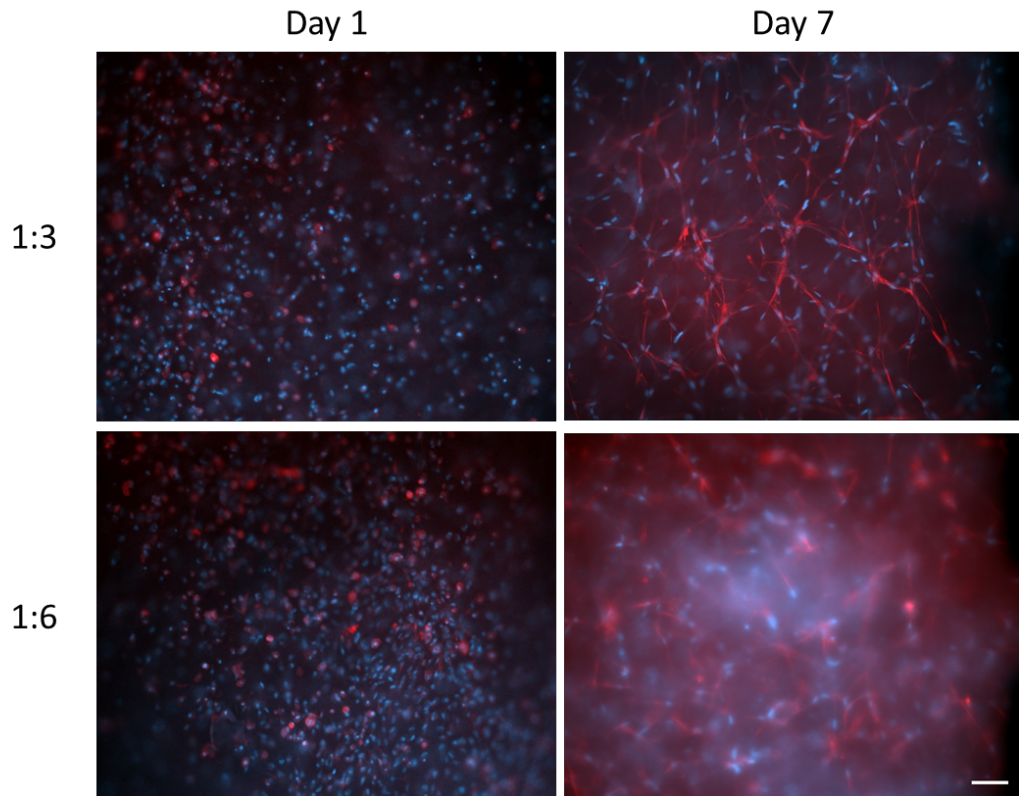
**Figure 3.25 - Comparison of HFFs, stained with rhodamine-phalloidin (F-Actin, red) and DAPI (nucleus, blue), encapsulated in 5 wt% GelNOR crosslinked with DTT at 1:3 and 1:6 NOR:SH ratio, after 1 and 7 days in culture.** (Scale bar = 100 µm)

Ideally further morphological observation would have been possible through the rhodamine-phalloidin staining. However, because this was not possible at later timepoints, the rhodamine-phalloidin staining assays were supplemented with light microscopy imaging at the final timepoints of each gel.

For HFFs encapsulated in 10 wt% gels, the morphology of the encapsulated cells corresponded to that seen when stained with Calcein AM, in which HFFs encapsulated in 1:3 NOR:SH gels were able to take an elongated, fibroblastic morphology, but those encapsulated in 1:6 NOR:SH gels were not able to spread and remained rounded (Figure 3.26).
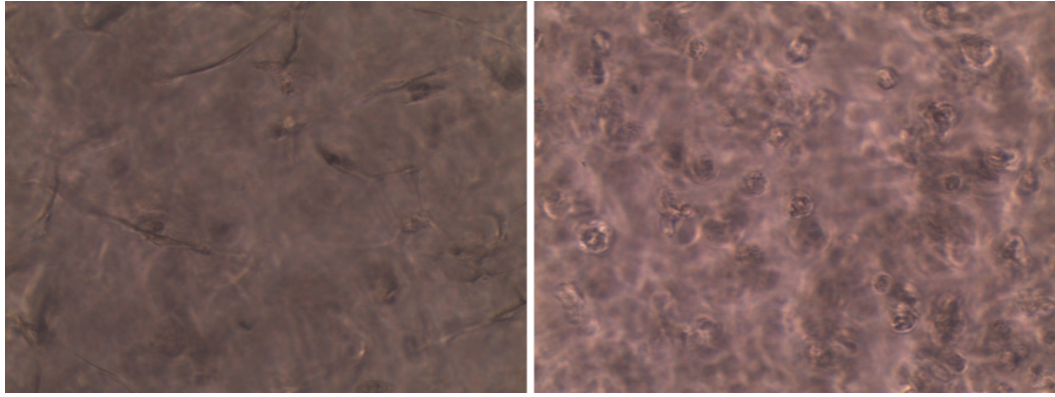
**Figure 3.26 – Light microscopy images of HFFs encapsulated in 10 wt% GelNOR, crosslinked with DTT at 1:3 (left) and 1:6 (right) NOR:SH ratio, after 21 days in culture.** (x20 magnification)

For HFFs encapsulated in 5 wt% gels, at both 1:3 and 1:6 NOR:SH ratio the HFFs were observed to spread extensively and formed interconnected cell networks (Figure 3.27). This corresponds well with the rhodamine-phalloidin staining assay at day 7, but did not correspond with images taken at the same timepoint staining with only Calcein AM.
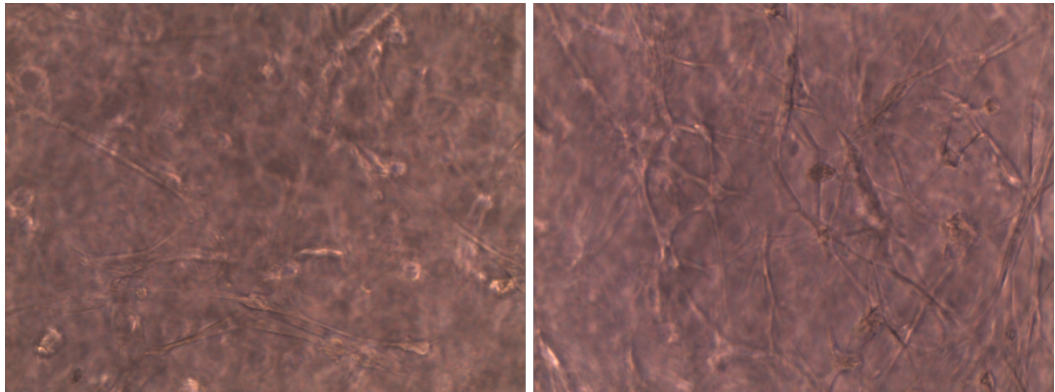


**Figure 3.27 – Light microscopy images of HFFs encapsulated in 5 wt% GelNOR, crosslinked with DTT at 1:3 (left) and 1:6 (right) NOR:SH ratio, after 7 days in culture.** (x20 magnification)

## 3.4  Discussion

The objectives of this chapter were to; validate the visible light initiation system described by Lim and colleagues (Lim *et al.*, 2016) for use with GelNOR hydrogels, to optimise the physical characteristics of GelNOR hydrogels for use in spinal cord tissue engineering applications, and to test the viability and behaviour of cells cultured in optimised hydrogels.

### 3.4.1  Validation of Visible-Light System for use with GelNOR

The Ruthenium/SPS visible light initiation system was effective for initiation of gelation of GelNOR hydrogels. This was evidenced by the high crosslinking efficiencies achieved at all tested irradiation times in the time sweep testing of crosslinking efficiency (Figure 3.3). The achieved soluble fraction at the 15 minute irradiation time (12.9% ± 5.23) is comparable to that that achieved by Lim and colleagues (Lim *et al.*, 2016) when using the same irradiation time and intensity with GelMA (10.6% ± 3.9), demonstrating the system's effectiveness.

Though the soluble fraction achieved for GelNOR at the 15 minute time-point is comparable to that achieved with GelMA in the literature, it should also be noted that for GelNOR hydrogels, the soluble fraction achieved at the 15 minute timepoint is not significantly different to that achieved at the 15 second timepoint (11.9% ± 3.53). A number of irradiation times between the 15 second and 15 minute timepoint achieve lower soluble fractions, though most of these are not statistically significantly so. The only timepoint to achieve a statistically significantly lower soluble fraction than any other timepoint is the 5 minute timepoint, however, as the soluble fraction then rises again at the 7.5, 10, and 15 minute timepoints it is likely that the statistically significant p score at the 5 minute timepoint is a type I error.

The rapid gelation observed, in which the GelNOR hydrogel achieves full crosslinking within 15 seconds, is due to the step-growth gelation system of the GelNOR, and this rapid time to achieve full crosslinking agrees well with other thiol-ene hydrogel systems described in the literature (Lin, Raza and Shih, 2011), though possibly not with the original work on GelNOR performed by Munoz and colleagues (Mũnoz *et al.*, 2014). In their publication a rapid onset of gelation was noted (within 12 seconds), but it was judged that complete gelation was not achieved until approximately 300 seconds, which is in contrast to the complete gelation achieved at 15 seconds in the experiments observed in this chapter. Though Munoz used in-situ rheometry to judge the complete gelation time, through observation of

the time taken to reach a plateau in the measured G' value, and thus the comparison with soluble fraction achieved in the time sweep irradiation experiment is not like-for-like, the results are still conflicting. If the gelation reaction was not complete until 300 seconds in the performed experiments then a decrease in soluble fraction to the 300 second timepoint with a subsequent plateau would be expected, and this was not observed.

The difference in observations can be reconciled by considering the possibility that the chain growth reaction continues post light-irradiation. As can be seen from Figure 3.1, once the initial radical is generated by the initiation system, the thiol-norbornene reaction is self-renewing, and thus it is possible that once the light irradiation has initiated the crosslinking reaction, once removed from the light source the reaction continues to completion in the dark.

This would mean that, for the 15 second timepoint, at the point when irradiation had finished and the sample was removed from the light source and kept in the dark, the crosslinking was incomplete, but the reaction continued whilst the sample is kept in the dark, and was complete by the time the sample was transferred to the -80 °C freezer, which would be more than 5 minutes from light-irradiation. Because the in-situ rheometry time-sweep used by Munoz analyses the same sample with continuing light irradiation, as opposed to light irradiating multiple samples for different exposure times with subsequent rheometric testing, it is not possible to confirm this possibility with the available information. Though other experiments, not included in this chapter, showed that gels can be crosslinked to 16.4% ± 2.55 by 5 minutes exposure to ambient light, gels were kept in light free conditions before and after irradiation, and weighed in low light conditions for an extra exposure time of less than one minute of low ambient light, so it is unlikely that experimental error was introduced by gels being significantly further crosslinked by ambient light. It should also be noted that all gels that were prepared and not light-irradiated, instead being kept in the dark as a negative control, failed to gel.

Future work to answer this question may therefore take the form of an in-situ rheometry time sweep, in which the light source is turned off after 15 seconds but the rheometric testing continues to analyse any continued gel response post-irradiation. If the gel does continue to cure post-irradiation then this would raise an interesting possibility of a tailorable gel delivery system consisting of an initial high dose irradiation, and immediate injection/delivery of the solution before gelation.

Alternatively, the other differences between the gels tested in the time-sweep experiment and by Munoz are that Munoz used a lower gel wt% and LAP based light initiation system (Mũnoz *et al.*, 2014). The crosslinking molecule was the same, at comparable NOR:SH ratio, as was the degree of functionalisation of the GelNOR macromer. The GelNOR wt% could have had an effect, as at 5 wt% there are effectively half the functional norbornene groups available for crosslinking in the same volume of sample, further work to test the effect of wt% would be to repeat the visible light time sweep performed in this chapter using 5 wt% GelNOR instead of 10 wt%. Alternatively, the use of an LAP based type I initiation system instead of a Ruthenium/SPS based type II system may have had an effect on the rate of radical generation during light irradiation, and thus the rate at which the gel cured, however, it would be more likely for the type I system to generate more radical more quickly, and thus cure the gel faster. Further work to investigate the difference between the two systems could either focus purely on the rate of radical generation of each system during light irradiation, or could measure this indirectly through comparative time-sweep analysis of the two systems via either soluble fraction or G' through rheometry.

### 3.4.2 Optimisation of Physical Characteristics

In order to optimise the physical characteristics of the GelNOR hydrogels for use in spinal cord tissue engineering applications, a number of aspects must be taken into account. The primary physical considerations are the stiffness of the construct as a whole, as this will be pivotal to its interaction with native tissue on a whole tissue level, and the cellular level gel microstructure, as this will determine the behaviour of cells encapsulated within the construct. Tissue level construct stiffness was measured using compressive uniaxial testing to determine the Young's Modulus of the gel. Mass swelling ratio at equilibrium was used to analyse the cellular level microstructure, as this gives a measure of the amount of water absorbed by the macromer at equilibrium, and is thus a measure of the 'tightness' of the polymer network which is directly correlated with network mesh size and porosity. Further to this, gels must achieve a high enough crosslinking efficiency to ensure the production of stable, reproducible, homogenous gels. This was measured by using mass loss and swelling studies to determine the gels' soluble fraction. During this chapter, the effect on the physical characteristics of the formed gel caused by variations in the crosslinker selection, norbornene to thiol ratio, and gel wt% were analysed, with the intention to use these three variables to tailor the physical properties of the gel to the desired application.

The effect of each of these aspects on the physical properties of thiol-ene click hydrogels (Lin, Raza and Shih, 2011), as well as specifically GelNOR (Mũnoz *et al.*, 2014; Greene and Lin, 2015) have previously been analysed to some extent, though previous work has not simultaneously analysed all of these aspects to the extent of experiments performed in this chapter. Further, the effect of these aspects on gel physical properties has largely been considered in terms of G' value, with some consideration also for mass swelling ratio.

Initial work in this chapter focused on the soluble fraction and mass swelling ratio of GelNOR gels with varying wt%, norbornene to thiol ratio, and crosslinker functionality. This was then followed by mechanical characterisation through compressive uni-axial testing, giving the compressive Young's Modulus, rather than the Storage Modulus (G') analysed by others. This means that absolute values for mechanical testing will not be directly comparable with previously published data, but comparison of trends is still possible.

Mass loss and swelling studies showed that the soluble fraction follows a stochiometric pattern with increasing NOR:SH ratio, agreeing with previously published data from development of the thiol-norbornene photo-click system (Fairbanks, Schwartz, Bowman, *et al.*, 2009), and further work by Munoz (Mũnoz *et al.*, 2014), though previous publications tested G' rather than soluble fraction. Where previous publications have only analysed NOR:SH variation at constant wt%, or wt% variation at constant NOR:SH ratio, the experiments in this chapter were able to analyse both simultaneously by taking a more extensive approach. In this way, it is possible to see that the nature of the stochiometric ratio with variable NOR:SH ratio changes with wt%. Though GelNOR crosslinked with PEG-4SH at varying NOR:SH ratio shows a stochiometric pattern with maximum crosslinking efficiency around 1:3 and 1:6 NOR:SH at both 5 and 10 wt%, the soluble fractions above and below the stochiometric ratio are different for each wt%. At 10 wt% the 1:12 NOR:SH ratio has significantly higher soluble fraction than the other tested ratios, whereas the soluble fraction at 1:1 NOR:SH ratio is only slightly elevated compared to 1:2 – 1:6 NOR:SH, and is not significantly greater than the 1:2 ratio. Conversely at 5 wt% the opposite is true, with the soluble fraction being significantly higher at 1:1 than at the other tested NOR:SH ratios, and with soluble fraction at 1:12 NOR:SH not being significantly greater than at the stochiometric ratio, and actually lower even than at 1:2 NOR:SH.

None of the previously published work has tested the effect of variable NOR:SH ratio on PEG-8SH crosslinked gels, and it is interesting to note that PEG-8SH crosslinked GelNOR does not show a stochiometric trend in soluble fraction at the NOR:SH ratios tested. Instead there is no significant difference in soluble fraction between gels crosslinked at 1:3 – 1:12 NOR:SH ratio, and soluble fraction is actually lower at 1:12 then 1:3 NOR:SH. The absence of a rise in soluble fraction to the 1:12 NOR:SH ratio in PEG-8SH gels is likely due to the reduction in the absolute number of molecules of crosslinker used, as using the NOR:SH ratio as opposed to concentration adjusts for crosslinker functionality. This means that for the same NOR:SH ratio, the number of crosslinker molecules used in PEG-4SH crosslinked gels is half that used in PEG-8SH gels, and in DTT crosslinked is a quarter of that used in PEG-8SH crosslinked gels. This means that the effect that causes the rise in soluble fraction at higher NOR:SH ratios, in which an over-abundance of thiol molecules limits the number of successful crosslinks due to competition for norbornene binding sites, is less pronounced in crosslinkers with greater functionality. This is supported by the observation that soluble fraction for gels crosslinked with DTT (which only has two thiol groups as opposed to eight in PEG-8SH, and therefore has four times the number of molecules at the same NOR:SH ratio) is highest at 1:12 NOR:SH at both 5 and 10 wt%.

Soluble fraction was generally higher at lower wt% for NOR:SH outside the optimum stochiometric ratio, but was not significantly different at the optimum 1:3 and 1:6 NOR:SH ratio. Interestingly, at the same wt% the PEG crosslinked gels achieved lower soluble fractions at all NOR:SH ratios including the optimum stochiometric ratio. This is likely due to PEG crosslinked gels having less homopolymerisation. Homopolymerisation, or cyclisation, is when a crosslinking molecule forms multiple successful connections, but with the same strand of macromer rather than two separate strands of macromer, therefore not successfully forming a crosslink. This is less likely when PEG-4 or 8 is used as the crosslinker, as if two arms connect with norbornene rings on the same macromer strand, there are still two arms available for successful crosslinking. Conversely, if DTT forms connections with two norbornene rings on the same macromer strand, it does not have further thiol groups available for crosslinking.

The mass swelling ratios observed during testing followed the same trends as the soluble fractions for varying NOR:SH ratios. This is likely due to the soluble fraction and swelling ratio having a cause and effect relationship. At

a set gel wt%, the number of norbornene binding sites available for potential crosslinking is the same at all NOR:SH ratios, and thus the soluble fraction determines the number of crosslinks formed. At lower soluble fractions there will be a greater number of crosslinks formed, and thus the network will be tighter and swell less, resulting in a lower mass swelling ratio. At higher soluble fractions, with less crosslinks formed, the network will be looser and thus able to swell to a greater extent.

When comparing between wt%, mass swelling ratio was always greater at lower wt%, even when soluble fraction was equal or lower than at the higher wt%. This is because at a lower wt% there are less norbornene binding sites available for crosslink formation, and so even at an equal soluble fraction less crosslinks will be formed, resulting in a looser network and thus greater swelling.

Interestingly, the trend in mass swelling ratio between different crosslinkers does not follow the pattern predicted by Munoz (Mũnoz *et al.*, 2014) that, "*To increase the degree of gelatin hydrogel swelling while maintaining the high cross-linking efficiency, one could use multi-arm (e.g. PEG4SH or PEG8SH) cross-linkers with higher molecular weights. This approach should increase hydrogel swelling due to the extended cross-linker chain length in between the gelatin chains*". In fact, the opposite was true, and mass swelling ratio was highest when using DTT (the lowest molecular weight crosslinker), and lowest when using PEG-8SH (the highest molecular weight crosslinker). This is likely due the effect of having more thiol groups centred around the same point in crosslinkers with greater functionalisation, making the polymer network tighter, outweighing the described effect of longer chain lengths in molecules with higher molecular weight. An alternative explanation for this trend is that there may be an effect on the mass loss and swelling data caused by the higher molecular weight. This can be observed in the raw mass loss and swelling data, in that although there is no significant difference in the initial weight ($m_{initial}$) between gels crosslinked with DTT, PEG-4SH, and PEG-8SH (e.g. at 5 wt%, 1:6 NOR:SH, DTT = 0.0236 ± 0.00151, PEG-4SH = 0.02588 ± 0.00068, and PEG-8SH = 0.02514 ± 0.00125), significant differences can be seen in the dry weights of unswollen gels ($m_{dry\ t=0}$)  (DTT = 0.00186 ± 0.0001, PEG-4SH = 0.00238 ± 0.00011, and PEG-8SH = 0.00256 ± 0.00019). From this it can be seen that the mass of crosslinker added in initially heavier in PEG crosslinked gels than in DTT crosslinked, potentially skewing mass swelling ratio. However, this possibility seems unlikely as the differences in mass between PEG-4SH and PEG-8SH

at $m_{dry\ t=0}$ are not statistically significant, but a number of the differences in mass swelling ratio are. When it is considered the exact same mass of PEG-4SH and PEG-8SH will have been used in gels with equal NOR:SH ratios, due to PEG-8SH being double the molecular weight but also double the functionality, the effect of crosslinker mass on mass swelling ratio is effectively controlled for. This means the difference in swelling ratio must have been due to effects caused by different degrees of functionality.

Trends in swelling ratio were also good predictors of trends in mechanical stiffness of the gels, and this relationship between stiffness and network structure in hydrogels is well recognised (Cha *et al.*, 2011). The relationship between stiffness and mass swelling ratio, when used for comparison however, is only applicable between NOR:SH ratios and wt%, but not between crosslinkers. For example, at 1:6 NOR:SH ratio, 5 wt% gels crosslinked with PEG-4SH and 10 wt% gels crosslinked with DTT have similar mass swelling ratio (11.8 and 13.0 respectively), but have Young's Moduli that are an order of magnitude different (123kPa and 9.20 kPa respectively). This means that, though the network 'tightness' does correlate with mechanical stiffness, the crosslinker selection has a much greater impact. The observed difference between the stiffness of gels with comparable soluble fractions and mass swelling ratios but different crosslinkers is most likely due to the higher molecular weight of the PEG crosslinker making PEG crosslinked gels more dense. Trends in swelling ratio and stiffness are consistent between wt%, and the rising stiffness with wt% is consistent with the literature for DTT crosslinked GelNOR (Mũnoz *et al.*, 2014), and results can be said to be consistent with (Greene and Lin, 2015) for PEG-4SH gels, though the scale of the difference in stiffness between wt% is much greater in the results of these experiments than for (Greene and Lin, 2015), though this is likely due to the testing of Youngs Modulus via uni-axial compression rather than Storage Modulus via rheology.

Where the results of these experiments disagreed with the literature with regards to physical stiffness, is that Munoz (Mũnoz *et al.*, 2014) stated that the stochiometric ratio of NOR:SH is consistent between DTT and PEG-4SH crosslinked gels is consistent when adjusted for crosslinker functionality. It should be noted however that this is not shown in the publication's results figures. The results of uni-axial compressive testing performed in these experiments found that the Young's Modulus did not trend stoichiometrically with NOR:SH ratio at the NOR:SH ratios tested. This may have been

different at 10 wt% or at 5 wt% with continuing increase in NOR:SH ratio, and these possibilities could be the subject of future supplementary work.

Interestingly, the Young's Modulus falls from 1:6 to 1:12 NOR:SH in PEG-8SH crosslinked gels, but rises in PEG-4SH crosslinked gels, and this is reflected in a rise in swelling ratio for PEG-8SH crosslinked gels but a fall in PEG-4SH crosslinked. This is despite consistent soluble fraction between 1:6 and 1:12 for both PEG-4SH and PEG-8SH. This shows a possibility that for PEG crosslinked gels the Young's Modulus doesn't just rely on successful formation of crosslinks, but also on the number of successful crosslinks on single crosslinking molecules. The consistent soluble fraction shows that PEG-8SH is forming as many crosslinks at both 1:6 and 1:12 NOR:SH, but the fact this is accompanied by rising swelling ratio suggests that these crosslinks are not as focused round a single point. In other words, PEG-8SH molecules are able to form connections using, for example, five to eight of their eight arms at 1:6 NOR:SH, but only two to four of their eight arms at 1:12 NOR:SH, which is why the swelling ratios of PEG-4SH and PEG-8SH gels are very similar at 1:12 NOR:SH ratio (9.22 and 9.05 respectively), but significantly different at 1:6 NOR:SH (11.8 and 7.49 respectively).

When considering materials based treatments for SCI, it is important to match the stiffness of spinal cord as closely as possible, as mechanical mismatches between implants and bodily tissues can be detrimental to native tissue. This is a concept that is well accepted after years of medical implant therapies in the clinic (Carnicer-Lombarte *et al.*, 2019), and has also been shown in more a more limited way with materials based SCI treatment strategies to this point (Straley, Foo and Heilshorn, 2010). It is for this reason that it is likely the ideal hydrogel mechanical properties will be very similar to native tissue or slightly weaker, as when the stiffness of two adjacent materials (or material and tissue) are mismatched, it is generally the less stiff that will be damaged (Shi *et al.*, 2013). It should also be considered that the optimised GelNOR composition will be loaded with electrically conductive nanoparticles in the next chapter, which previous studies have shown is likely to increase stiffness (Navaei *et al.*, 2016).

In terms of optimisation of the physical properties of the hydrogels for spinal cord tissue engineering, the mechanical properties of spinal cord reported in the literature vary widely. This variation is due to differences in characterisation methods (e.g. rheological, compressive, tensile), and within each method, differences in strain amplitude, strain rate, and chosen strain

region to use data from. Further to this, there is wide variation in the species from which spinal cord is taken, including human, porcine, canine, feline, and rodent, and the storage conditions and speed from extraction to testing.

The testing performed by (Karimi, Shojaei and Tehrani, 2017) appears to be the most relevant for comparison. This is because the characterisation method used is uni-axial compressive testing on fresh human tissue, and using comparable test protocols. The protocol is a static test at low strain speed, with (Karimi, Shojaei and Tehrani, 2017) using a displacement speed of 5mm/min (approx. 0.08mm/s), which, though faster than the 0.01mm/s used in this chapter, was also deliberately chosen to be slow enough to minimise any viscoelastic effects caused by higher strain speeds.

Characterisation of human spinal cord by (Karimi, Shojaei and Tehrani, 2017) resulted in a Young's Modulus of 40.12 kPa. The tested gels which most closely matched this Young's Modulus for each crosslinker were the 2.5 wt%, 1:12 NOR:SH, PEG-4SH crosslinked gels (37.6 kPa), 5 wt%, 1:2 NOR:SH, PEG-8SH crosslinked gels (30.3 kPa), and 10 wt%, 1:3 NOR:SH crosslinked gels (18.6 kPa).

The gels chosen to take forward to cell culture were the DTT crosslinked gels, as these were consistently below the required Young's Modulus for all tested wt% and NOR:SH ratios, allowing comparison of these different factors in cell culture. Further to this, the ability to use a higher wt% means a higher amount of gelatin in the gels, thus providing a greater number of bioactive domains for cellular attachment. The PEG-4SH and PEG-8SH were too stiff at the majority of tested wt% and NOR:SH ratio combinations, and of the tested wt% and NOR:SH ratios combinations that were below the required Young's Modulus, a number had soluble fractions above 15%, and so were judged to be unsuitable to take forward.

### 3.4.3  3D Cell-Culture in Optimised Hydrogels

Initial cell viability testing of HFFs encapsulated in DTT crosslinked GelNOR showed good cell viability at all tested wt% and NOR:SH ratio combinations. Cell viabilities were slightly lower than those reported by Munoz of 97% and 91% at 4 and 8 wt% respectively (though the NOR:SH ratio is not detailed), as compared to a high of 93.4% for 1:2 NOR:SH ratio gels and a low of 84.8% in 1:6 NOR:SH ratio gels at 10 wt% (Mũnoz et al., 2014). In keeping with Munoz, cell viabilities were higher at lower wt% gels for all NOR:SH ratios tested. This demonstrates the visible-light initiation system to achieve comparable viabilities to LAP for cells encapsulated in GelNOR gels, further

proving its validity. These figures are also comparable to the approx. 90% viability achieved by Lim and colleagues (Lim *et al.*, 2016) when testing the Ruthenium/SPS visible-light system with GelMA. Interestingly, though (Lim *et al.*, 2016) found that the viability was significantly improved with the Ru/SPS visible-light system over the i2959 UV-based initiation system when using GelMA, and Munoz (Mũnoz *et al.*, 2014) found significantly improved cell viabilities when using GelNOR over GelMA with an LAP initiation system, the combination of GelNOR and the Ru/SPS visible-light initiation system described in this chapter did not achieve improved viabilities over either of the previously described publications, and in fact on average was slightly lower. This may be due to the >90% viabilities in both of the previously named studies being difficult to improve on. It is particularly unexpected that the viabilities achieved by the step-growth GelNOR system used in this chapter were lower on average than the chain-growth GelMA system used by (Lim *et al.*, 2016). This may be due to the use of the extremely hardy MCF-7 cell line by Lim (Lim *et al.*, 2016) as opposed to HFFs in this study, and in subsequent viability experiments using MSCs (Lim *et al.*, 2016) achieved lower viabilities with the same system. The fact that Munoz (Mũnoz *et al.*, 2014) achieved comparable or better cell viabilities using LAP + UV-light than were achieved in this chapter using Ru/SPS + visible-light suggests that the step-growth vs chain-growth comparison is much more significant for cell viability than the UV vs visible-light comparison.

The NOR:SH ratio at which the gels were crosslinked does appear to have an impact on initial cell viability, with the 1:6 NOR:SH 10 wt% gels, the highest DTT concentration used, having the lowest initial viability and the 1:3 NOR:SH 5 wt% gels, the lowest DTT concentration used, having the highest. This is also supported by the 5 wt% gels having higher viabilities than the 10 wt% gels at the same NOR:SH ratio, as the 10 wt% gels will have double the DTT concentration used in the 5 wt% gels. The data does not confirm a clear relationship however, as viability does not reliably decrease in a linear fashion with increasing DTT concentration, and none of the differences between NOR:SH ratios are statistically significant.

The viabilities of cells encapsulated in all tested gels decrease with time in culture, with the exception of the 1:6 NOR:SH 10 wt% gels. This trend is unexpected, as logically cells would be damaged during the encapsulation process, leading to a lower viability at the day 1 timepoint, before recovering and proliferating over time to continually increase viability. There would be a

possibility of cell viability decreasing at the final timepoint if the cell population grew so large that the hydrogel scaffold was no longer able to support sufficient nutrient transport, but this would certainly not be expected as early as the day 7 timepoint. Conversely, the viability trend over time in culture seen in the 1:6 NOR:SH ratio 10 wt% gels, of a low initial viability that recovers with time in culture, is more expected, and is likely due to the high DTT concentration causing the lowest initial viability at day 1. Again, none of the differences between timepoints are statistically significant for any of the tested gels, and so this may be an artefact.

The calcein stain used in the LIVE/DEAD assay was also used to assess cell morphology both qualitatively, and quantitatively using Image J. From the observed images and data, a general trend could be observed in which HFFs encapsulated in gels with lower Young's Modulus and higher mass swelling ratio were able to elongate earlier and to a greater extent. This is due to these properties corresponding with a looser polymer network, allowing the cells more room at a cellular level to elongate. The only exception to this trend was the morphologies observed in HFFs encapsulated in the 1:6 NOR:SH 10 wt% gels. Though, at 10 wt%, the 1:3 NOR:SH ratio gel has a higher Young's Modulus and a lower swelling ratio, meaning that it is stiffer and has tighter network structure, than the 1:6 gel, the encapsulated HFFs take an elongated morphology in the 1:3 but not the 1:6 NOR:SH gel. This is unexpected, as the HFFs are able to elongate earlier and to a greater extend in 1:1 and 1:2 NOR:SH ratio gels than in the 1:3, and to a much greater extent in the 5 wt% than in the 10 wt% gels. Following the same trend, at 10 wt% the HFFs encapsulated in the 1:6 NOR:SH ratio gels should elongate in the same manner as those in the 1:2 NOR:SH gels (i.e. faster and earlier than the 1:3 NOR:SH) due to the stochiometric properties of the Young's Modulus and mass swelling ratio around the 1:3 NOR:SH ratio. Instead, the HFFs encapsulated in the 1:6 NOR:SH gel at 10 wt% remain rounded throughout the full 21 days in culture.

The most likely explanation for this unexpected behaviour is that the DTT concentration in the 10 wt%, 1:6 NOR:SH gel is twice that in the 1:3 NOR:SH gel, and three times that in the 1:2 NOR:SH gel. DTT is a reductant which can damage cells through reduction of disulphide bonds in the cell membrane (Konigsberg, 1972), and thus at high concentrations can be cytotoxic. Though the result was not statistically significant, the viability of HFFs encapsulated in 1:6 NOR:SH gels was lower than those encapsulated

in other gels at 10 wt% after 1 day in culture. Further, there was much more extensive dual labelling at day 7 in the 10 wt% 1:6 NOR:SH gels than in any other, demonstrating that the cells that did survive the initial DTT exposure were less healthy than in other gels. Despite extensive dual labelling being observed at day 7, there was relatively little at day 1. This is likely because the cells were so badly damaged that there was not enough esterase activity to convert Calcein AM dye to fluorescent calcein, and thus the cells that were dual labelled at day 7 were only identified as 'dead' at day 1. This also explains the low cell viability that jumps to day 7.

Though the alamar blue data at day 1 shows population cell metabolism of the HFFs encapsulated in the 1:6 NOR:SH gels to not be significantly different from any of the other NOR:SH ratios at 10 wt%, by the day 21 timepoint it is significantly lower than HFFs in the 1:2 NOR:SH ratio and also lower than in 1:3 NOR:SH. That the alamar blue reduction value is much lower at day 21 in the 1:6 NOR:SH gels than the other tested values does point to the initial damage being greater for these cells, and thus recovery being more impaired. It should however be noted that the alamar blue assay analyses a full cell population, and because it was not paired with a DNA quantification assay results should not be considered on a per cell basis. In this way, that HFFs encapsulated in the 1:6 NOR:SH 10 wt% gel have lowest cellular metabolism at day 21 could be either due to a change in metabolism per cell at constant population size, or an change in population size at constant metabolism. Either could be due to DTT related damage at the time of encapsulation, and could explain why 1:6 NOR:SH 10 wt% gel have lowest cellular metabolism at day 21 despite having the highest viability.

Alternatively, instead of the explanation that both low population cell metabolism and lack of cell elongation are caused by damage from DTT in the encapsulation process, it is possible that the low cellular metabolism is caused by the lack of cell elongation. HFFs are anchorage dependent cells (Peehl and Stanbridge, 1981), and thus cell proliferation and phenotype modulation depends on integrin-mediated cellular interaction with integrin-binding molecules, and other molecules, present on the cell growth substrate (Merten, 2015). In the absence of cellular elongation, the lower number of such integrin mediated cellular adhesions to the hydrogel substrate may have meant that the HFFs in the 1:6 NOR:SH gel were less metabolically active and/or proliferated less. This explanation is also supported by the comparison between the 1:3 NOR:SH 10 wt% gel and the 1:6 NOR:SH 5

wt% gel, both of which were exposed to the same DTT concentration during encapsulation, in which the HFFs in the 5 wt% gel show significantly greater metabolism at both day 1 and 7. The significantly increased metabolism at day 1, when the cell population number should have been close to identical, particularly shows the link between the cell morphology and metabolism, as cells were significantly less round in the 5 wt% gels compared to the 10 wt%.

A possible drawback to the methodology of using calcein staining to analyse cellular morphology is that calcein only stains the cell body. Calcein stains cells when intracellular esterases convert Calcein AM dye to fluorescent calcein through acetoxymethyl ester hydrolysis (Neri *et al.*, 2001). Because of this, only the cell cytoplasm in the main body of the cell is stained, and not any elongating processes. The weakness of this method can be seen when comparing images of calcein stained cells to those of rhodamine-phalloidin stained cells, in which the F-Actin of the elongating parts of the cells are stained, and to light microscope images, for example in by comparing Figure 3.22, Figure 3.25, and Figure 3.27. The effect seems to be a delay in when the elongation is seen in the calcein imaging, which doesn't pick up the initial elongating processes, but does show when the cell body elongates to fit the new cell shape. Unfortunately rhodamine-phalloidin imaging in 10 wt% gels after day 7 was not possible and the returned images were extremely poor. This may be due to deposition of extra-cellular matrix components by the HFFs after day 7 as the cells elongate and become more metabolically active, as secretion of connective tissues and fibrosis is a well-known biological role of fibroblast cells (Kendall and Feghali-Bostwick, 2014). The combination of protein deposition by HFFs and the use of a fluorescence microscope equipped with apotome rather than confocal microscope in this chapter likely contributed to the difficulty in imaging rhodamine-phalloidin stained cells.

A further weakness of using image processing to semi-quantitatively analyse qualitative images is the heterogeneity of images. Though a standard ImageJ automated process was used in order to remove any variation that would have been seen through manual image thresholding, the original images themselves are taken manually by an operator, and thus variation cannot be avoided.

Though these are weaknesses in using calcein staining for morphological assessment, it is consistent with the method used by Munoz and colleagues (Mũnoz *et al.*, 2014). The earlier and greater elongation seen in lower wt% gels is consistent with cell morphology seen in GelNOR encapsulated MSCs

by (Mũnoz *et al.*, 2014), who did not use cell culture to compare different NOR:SH ratios, but did compare different wt%. Though performing analysis of cellular morphology using images of calcein stained cells is consistent with the method used by (Mũnoz *et al.*, 2014), the two methods differ in that the experiments in this chapter measured 'circularity', whereas (Mũnoz *et al.*, 2014) analysed cell length. Circularity was chosen rather than cell length because cell length does not implicitly measure cellular morphology, for example a cell that has swollen but remain rounded may measure the same 'length' as a cell that has not swollen but has elongated. Where these two cells may score similarly for length, they would be differentiated for circularity. Further, the use of a fluorescence microscope equipped with apotome rather than confocal microscope in this chapter means that calcein images include cells in the foreground, background, and focal plane, which would have an effect on their measured length. Blurring of cells not in the focal plane may cause a tendency towards circularity, but this is still preferable to a size measurement.

Interestingly, the previously described observation that cell elongation in calcein stained images seem to be delayed was not seen in the study by (Mũnoz *et al.*, 2014). In contrast, (Mũnoz *et al.*, 2014), observes significant cell elongation as early as day 2 in calcein images, whereas in the experiments in this chapter significant elongation isn't observed qualitatively in calcein images for 5 wt% gels at day 7, despite the light microscope images and rhodamine-phalloidin staining clearly showing the cells are elongated. The differences are minor between the two studies, with (Mũnoz *et al.*, 2014) using MSCs rather than HFFs and 4 wt% rather than 5 wt% GelNOR, but these differences do not clearly explain the difference in observations.

Though the experiments in this chapter did not use PEG-crosslinked gels for cell culture, previous examples in the literature of PEG-crosslinked GelNOR gels tend to show cells remaining rounded rather than elongating (Greene and Lin, 2015; Truong *et al.*, 2016). This supports the decision to use DTT rather than PEG-4SH or PEG-8SH to crosslink GelNOR gels for cell culture.

## 3.5  Conclusions

The aims of this chapter were threefold; to validate the Ruthenium/SPS visible-light initiation system for use with step growth GelNOR hydrogel, to optimise the physical properties of the GelNOR hydrogel for use in this project, and to test the effect of these physical characteristics on the behaviour of cells encapsulated in the hydrogel.

The results of the experiments in this chapter confirmed that the Ruthenium/SPS visible-light initiation system is suitable for use with step growth GelNOR hydrogels. The results also showed that the physical characteristics of gels crosslinked with DTT were the most closely aligned with the target physical characteristics. Further, results of cell encapsulation experiments showed that optimum NOR:SH ratio for DTT crosslinking is 1:2 or 1:3 in 10 wt% gels and 1:3 or 1:6 in 5 wt% gels. The results of this chapter suggest that, as observed by cellular behaviour, the 5 wt% gels produce the ideal physical characteristics in terms of network microstructure, but the 10 wt% gels produce full gel physical stiffness closest to native tissue. For this reason, further investigation into the effect of gold nanorod encapsulation on physical properties is necessary in the next chapter before final gel selection.

On reflection, it is possible that there may have been a quicker route to the end goal, which was selection of an optimum crosslinking molecule and concentration, for the experiments in this chapter. As an example, if a decision had been taken to have a cut-off, above which a soluble fraction was deemed unacceptably high, then it would have been possible not to take so many different crosslinker/concentration combinations through to the uni-axial testing phase, reducing the amount of work that was done. Similarly, once it had been identified that DTT crosslinked gels at 1:1, 1:2, and 1:12 NOR:SH ratio had poor crosslinking efficiency and mechanical properties, the decision could have been made only to take the 1:3 and 1:6 NOR:SH gels into the final cell culture, again more than halving the amount of work done. Conversely, it could also be argued that a strength of this work, and something that sets it apart from previous studies, is that a wider range of different crosslinkers and ratios were used than have been investigated previously. As such, it is worth acknowledging that although this exhaustive method had weaknesses in terms of the time taken and extra work created to get to the final goal, the extra work and thoroughness was potentially also a strength.

# Chapter 4
## Development of GelNOR/GNR Hybrid Hydrogels for Spinal Cord Tissue Engineering

## 4.1 Introduction and Aims

As previously described, hydrogels have been identified as having potential for use in tissue engineering strategies for spinal cord injury repair (Perale *et al.*, 2011). Further, electrically conductive scaffolds have been widely investigated for their potential in tissue engineering applications and have received attention from researchers working on the regeneration of electrically active tissues such as cardiac tissue (Navaei *et al.*, 2016) and peripheral nerve (Das *et al.*, 2015a), as well as for the regeneration of tissues that are not electrically active in-vivo such as bone and cartilage (Jacob *et al.*, 2018). As the spinal cord is electrically active, treatment of SCI has also been identified as a possible target for this kind of tissue engineering approach.

A number of recent studies have investigated the use of electrically conductive scaffolds to treat SCI in animal models. These studies found that scaffolds with enhanced electrical conductivity improved both functional and histological outcomes when used to treat SCI, compared to less conductive native materials (Shu *et al.*, 2019). Further, the nature of electrically conductive scaffolds identifies them as possibly having use in combination therapies alongside spinal cord electrical stimulation therapies such as those described in section 1.5.5.

As previously discussed in Chapter 1, there are two general approaches to increasing electrical conductivity of hydrogels: to fabricate the hydrogel out of polymer with electrically conductive structure or side chains, or to incorporate electrically conductive particles into the hydrogel to improve construct conductivity. The use of nanoparticles is still generally preferred due to the flexibility that nanoparticle incorporation offers by allowing the use of any base hydrogel rather than limiting to those that are already electrically conductive (Min et al. 2018). Both of the described approaches have previously been taken by researchers working in the field of tissue engineering for SCI repair (L. Zhou *et al.*, 2018a; Zhang *et al.*, 2020).

The nanoparticles that have been used in electrically conductive hydrogels are varied, but are generally either metallic in nature, such as gold or silver, or carbon-based, such as graphene or carbon nanotubes (Min, Patel and

Koh, 2018b). As well as the material that the particles are made from, there is also shape to consider, as at a nanoscale the electrical behaviour of particles can be highly shape dependant. An example of this is the higher electrical conductivity of gold nanorods (GNRs) as opposed to gold nanospheres (GNSs) (Yoshida and Toshima, 2014), due to the effect of shape on surface plasmonic forces (Cao, Sun and Grattan, 2014). There is also a range of other shapes to consider such as nanowires and nanoplates, each with their own specific characteristics.

GNRs are an ideal nanoparticle for incorporation into electrically conductive tissue engineering scaffolds. This is because, further than their previously described superior electrical conductivity, they are cytocompatible (Sebastián *et al.*, 2012), diverse in their possible surface chemistries (Burrows *et al.*, 2016), and highly tuneable using a well-established and relatively low complexity method which generates a high yield of GNRs (Nikoobakht and El-Sayed*, 2003).

Gold nanoparticles have been used to improve neurite outgrowth in PC12 cells during 2D culture (Park *et al.*, 2009), as well as for tissue engineering of peripheral nerve (Das et al. 2015) in 3D, but in both cases nanospheres were used rather than nanorods. Though GNRs have been used for the fabrication of electrically conductive hydrogels for 3D tissue engineering (Navaei *et al.*, 2017), there are currently no studies using GNR loaded hydrogels for spinal cord tissue engineering or 3D neuronal culture.

The aim of this chapter is to develop an electrically conductive hydrogel based on the addition of GNRs to the previously optimised GelNOR hydrogel. This will be achieved through the following objectives:

1. Optimise the fabrication, storage, and encapsulation of gold nanorods for reproducible dispersion in the GelNOR hydrogel optimised in the previous chapter.
2. Determine the effect of GNR encapsulation on the physical and electrical properties of GelNOR hydrogels.
3. Select GNR/GelNOR hybrid hydrogel for final electrically conductive hydrogel cell culture experiments.

## 4.2 Methods

### 4.2.1 GNR Fabrication

GNRs were fabricated as described in section 2.2.3.

#### 4.2.1.1 Storage of GNRs

GNRs were characterised by methods described in section 4.2.2, and stored in 0.001M CTAB at 4 °C until use.

### 4.2.2 GNR Characterisation

#### 4.2.2.1 UV-Visible Spectrophotometry

Immediately after processing, three wells of a 96-well plate were filled with 100 μl of GNR suspension, and a fourth well was filled with 100 μl of the storage solution (0.001 M CTAB) as a reference well. The 96-well plate was then transferred to a plate reader for absorbance analysis.

The absorbance of each well was measured at 2 nm increments from 380 nm to 1050 nm inclusive, and the absorbance at each wavelength of the reference well was subtracted from the corresponding absorbance for the three wells containing GNR solutions.

#### 4.2.2.2 Transmission Electron Microscopy

Support for Transmission Electron Microscopy (TEM) was provided by Leeds Electron Microscopy and Spectroscopy Centre (LEMAS).

GNRs were fabricated as described in section 2.2.3 and 10 μl of the resulting GNR solution was then added to 90 μl of DIW for a one in ten dilution. From the dilute solution, 5 μl was pipetted onto a carbon film coated copper TEM grid, resting on filter paper.

GNR micrographs were obtained using an FEI Titan3 Themis 300 TEM. For each batch, the size of 200 particles was measured using ImageJ software in order to obtain the average size and the size distribution.

In addition, energy-dispersive X-ray spectroscopy (EDX-TEM) was used to confirm that GNRs were in fact gold, and selected area electron diffraction (SAED) was performed to acquire images of diffraction patterns to analyse the GNRs' crystal structure. Diffraction pattern images were processed using Gatan Microscopy Suite software to measure the pattern's d-spacings. The results were checked against the XPert reference database in order to identify the GNR crystal structure.

### 4.2.3  Fabrication of GelNOR/GNR Hybrid Hydrogels

GelNOR/GNR hybrid gels were fabricated at 10 wt% GelNOR and crosslinked with DTT at a 1:3 NOR:SH ratio using the SPS/Ruthenium visible light initiation system previously described. Gels were made in 150 µl batches and crosslinked in 30 µl disc moulds of 5 mm diameter and 1 mm depth.

#### 4.2.3.1  Preparation of GelNOR Solution

GelNOR macromer was dissolved in PBS, heated to 37 °C , at 20 wt%. Once dissolved, 75 µl GelNOR solution was transferred to an Eppendorf tube, 62.5 µl of PBS was added, and the solution was vortexed for 5 seconds and kept at 37 °C.

#### 4.2.3.2  Preparation of GNRs

GNRs were fabricated as described in section 2.2.3.

An appropriate amount of GNR stock solution for the desired final GNR concentration was transferred to an Eppendorf tube and spun at 12,000 rpm for 10 minutes in an ultra-centrifuge, temperature controlled at 20 °C, and the supernatant discarded.

#### 4.2.3.3  Fabrication of GelNOR/GNR Hybrid Hydrogel Solution

The GNR pellet was resuspended in the GelNOR solution and mixed thoroughly by pipetting at vortexing. The GelNOR/GNR solution was then sonicated for 10 minutes at 37 °C in a sonic bath and vortexed thoroughly again to homogenise GNR dispersion within the gel.

Once the GelNOR/GNR hybrid gel had been homogenised, 6.45 µl of 0.5 M DTT was added and the solution was vortexed for 5 seconds. Once vortexed, 3 µl of 0.5 M SPS was added to the very bottom of the Eppendorf tube, with care taken not to mix the SPS into the hydrogel solution, followed by the addition of 3 µl of 0.05 M Ruthenium to the very surface of the solution, once again being careful not to mix during addition. The whole solution was then vortexed for 10 seconds and immediately aliquoted into 30 µl disc moulds.

#### 4.2.3.4  Initiation of Gelation

Hydrogel discs were cured using an Omnicure S1000 visible light unit, providing 30 mW/cm2 light at wavelength 400-450 nm. Samples were irradiated for 5 minutes before being turned over and irradiated for a further 5 minutes.

### 4.2.4  Optimisation of Sonication Protocol

Sonication testing was performed in order to determine the effect that using sonication to homogenise GNR dispersion in GelNOR hydrogel had on the integrity of the GNRs.

#### 4.2.4.1  Fabrication of GelNOR/GNR Hybrid Hydrogel Solution

GelNOR/GNR hybrid hydrogel solution was fabricated as described in section 4.2.3.3, at a concentration of 0.25 mg/ml. For sonication testing a 500 µl batch size was used in a 1 ml Eppendorf tube.

#### 4.2.4.2  Fabrication of GelNOR Hydrogel Solution

A 500 µl solution of 10 wt% GelNOR was fabricated for use in a reference well. This solution was fabricated as described in section 3.2.2.

#### 4.2.4.3  UV-Visible Spectrophotometry

Three wells of a 96-well plate were filled with 100 µl of GelNOR/GNR hybrid solution, and a fourth well was filled with 100 µl of 10 wt% GelNOR as a reference well. The 96-well plate was then transferred to a plate reader for absorbance analysis, which was kept at 37 °C throughout.

The absorbance of each well was measured at 2 nm increments from 380 nm to 1050 nm inclusive, and the absorbance at each wavelength of the reference well was subtracted from the corresponding absorbance for the three wells containing GNR solutions. This initial reading was designated t=0.

The pure GelNOR and GelNOR/GNR solutions were then transferred from the 96-well plate back into their respective Eppendorf tubes, which were submerged in a sonic bath and sonicated at 37 °C.

Samples were removed from the sonic bath and UV-visible spectrophotometric analysis was performed at 10 minute intervals up to and including 60 minutes.

### 4.2.5 Comparison of GNR Storage Solution for Final GNR Dispersion

In order to determine the effect that CTAB concentration in the storage solution had on the formation of GNR aggregates, and subsequent GNR dispersion in GelNOR, GNRs dispersed in 10 wt% GelNOR were analysed after processing and storage using DIW and 0.001 M CTAB.

#### 4.2.5.1 Preparation of GNRs using 0.001M CTAB

GNRs were fabricated as described in section 2.2.3 and used immediately post-fabrication to avoid any pre-aggregation of GNRs during storage.

UV-Visible spectrophotometry was then performed as described in section 4.2.2.1, and GNR solution was adjusted to 0.5 mg/ml through centrifugation at 12,000 rpm for 10 minutes and re-suspension in 0.001 M CTAB.

UV-Visible spectrophotometry was then repeated in order to give an initial absorbance spectrum of GNRs suspended in 0.001M CTAB at 0.5 mg/ml.

#### 4.2.5.2 Preparation of GNRs using De-Ionised Water

GNRs were fabricated as described in section 2.2.3 and used immediately post-fabrication to avoid any pre-aggregation of GNRs during storage.

GNR solution was adjusted to 0.5 mg/ml through centrifugation at 12,000 rpm for 10 minutes and re-suspension in de-ionised water (DIW) and UV-Visible spectrophotometry was performed in order to give an initial absorbance spectrum of GNRs suspended in DIW at 0.5 mg/ml.

#### 4.2.5.3 Fabrication of GelNOR/GNR Hybrid Hydrogel Solutions

GelNOR/GNR hybrid hydrogel solution was fabricated as described in section 4.2.3.3, using GNRs prepared in either DIW or 0.001 M CTAB, at a concentration of at 0.5 mg/ml.

#### 4.2.5.4 UV-Visible Spectrophotometry

UV-Visible spectrophotometry was performed as described in section 4.2.2.1, with 10 wt% GelNOR being used as the reference well.

#### 4.2.5.5 Transmission Electron Microscopy

TEM grids were prepared by pipetting 5 µl onto a TEM grid placed on absorptive filter paper. After addition of the hydrogel, the TEM grid was moved to a glass slide and irradiated using an Omnicure S1000 visible light unit, providing 30 mW/cm2 light at wavelength 400-450 nm for 3 minutes.

Imaging was then performed using a FEI Titan3 Themis 300 TEM.

### 4.2.6  Characterisation of GelNOR/GNR Hybrid Hydrogels

### 4.2.6.1  Scanning Electron Microscopy

Samples were fabricated as described in section 4.2.3, at GNR concentrations of 0.0, 0.5, 1.0, and 1.5 mg/ml. Samples were then swollen overnight in PBS + 0.1% Sodium Azide before being frozen at -80 °C for 24 hours. Frozen samples were then freeze-dried for 48 hours.

Post freeze-drying, samples were sectioned longitudinally using a surgical scalpel and mounted on SEM stubs, before being sputter coated with a 5 nm layer of gold in a sputter coater.

Samples were then imaged in a scanning electron microscope (SEM) operating in secondary electron mode at a range of accelerating voltages.

SEM micrographs were analysed using ImageJ software in order to measure pore sizes.

### 4.2.6.2  Mass Swelling Ratio Analysis

Hydrogels fabricated for SEM analysis as described in section 4.2.6.1 were also weighed immediately after fabrication, after swelling, and after freeze-drying.

The mass swelling ratio was then calculated as described in section 2.2.2.

### 4.2.6.3  Rheological Characterisation

Samples were fabricated as described in section 4.2.3, at GNR concentrations of 0.0, 0.5, 1.0, and 1.5 mg/ml, and swollen overnight in PBS + 0.1% Sodium Azide. Samples were then characterised using a rheometer.

**Amplitude Sweep**

Amplitude sweeps were performed on the base GelNOR hydrogel at 10 wt% in order to determine the sample's linear viscoelastic region (LVR). The protocol consisted of an amplitude sweep from 0.1 – 100% shear strain at a frequency of 10 rad/s.

The LVR was then determined from the resulting data and an appropriate amplitude was taken forward into further frequency sweep testing, which was used for materials characterisation.

**Frequency Sweep**

The characterisation protocol was a frequency sweep from 0.1 – 100 rad/s at an amplitude of 5% shear strain. The rheometer stage was temperature controlled at 25 °C, and an 8 mm geometry was used for testing, at a working gap of 0.8 mm.

### 4.2.6.4  Electrical Impedance Spectroscopy

ITO slides with resistance 15-25 Ω/sq were cut into squares of approximately 20 x 20 mm using a diamond cutter. A silicon mould was then placed on the ITO coated surface.

GelNOR/GNR hybrid solution was then prepared as described in section 4.2.3.1 and pipetted into a single mould placed on the ITO slide. A second ITO slide was then placed on top of the silicon mould to 'sandwich' the hybrid hydrogel, with hydrogel solution contacting the ITO surfaces of both slides.

The hybrid hydrogel was then cured between the ITO slides as described in section 4.2.3.4.

The ITO/silicone spacer/hydrogel construct was then connected to a Metrohm Autolab B.V potentiostat, running Nova 1.10 software. Connections were made using crocodile clips, with reference and counter electrodes connected in series on one crocodile clip and the sensing and working electrodes connected in series on the other. The test procedure was then started.

The test procedure involved an AC frequency sweep from 100,000 – 0.1 Hz at an amplitude of -0.1 – 0.1 V.

Samples were housed inside a faraday cage during testing in order to minimise background electrical noise.

### 4.2.7  Statistical Analysis

All statistical analysis was performed using the 'rstats' package in RStudio, and used one-way ANOVA or Welch's t-test as described.

All data is presented as mean ± standard deviation.

Repeats are presented as (n = x, y) where x is the number of replicates performed within an experiment, and y is the number of times the experiment was performed.

## 4.3  Results

### 4.3.1  Analysis of Fabricated GNRs

Fabricated GNRs were analysed through TEM and UV-Visible Spectrophotometry. These techniques were chosen because they are the techniques most commonly used by commercial providers to supply GNR characterisation data, and results are given in Figure 4.1.
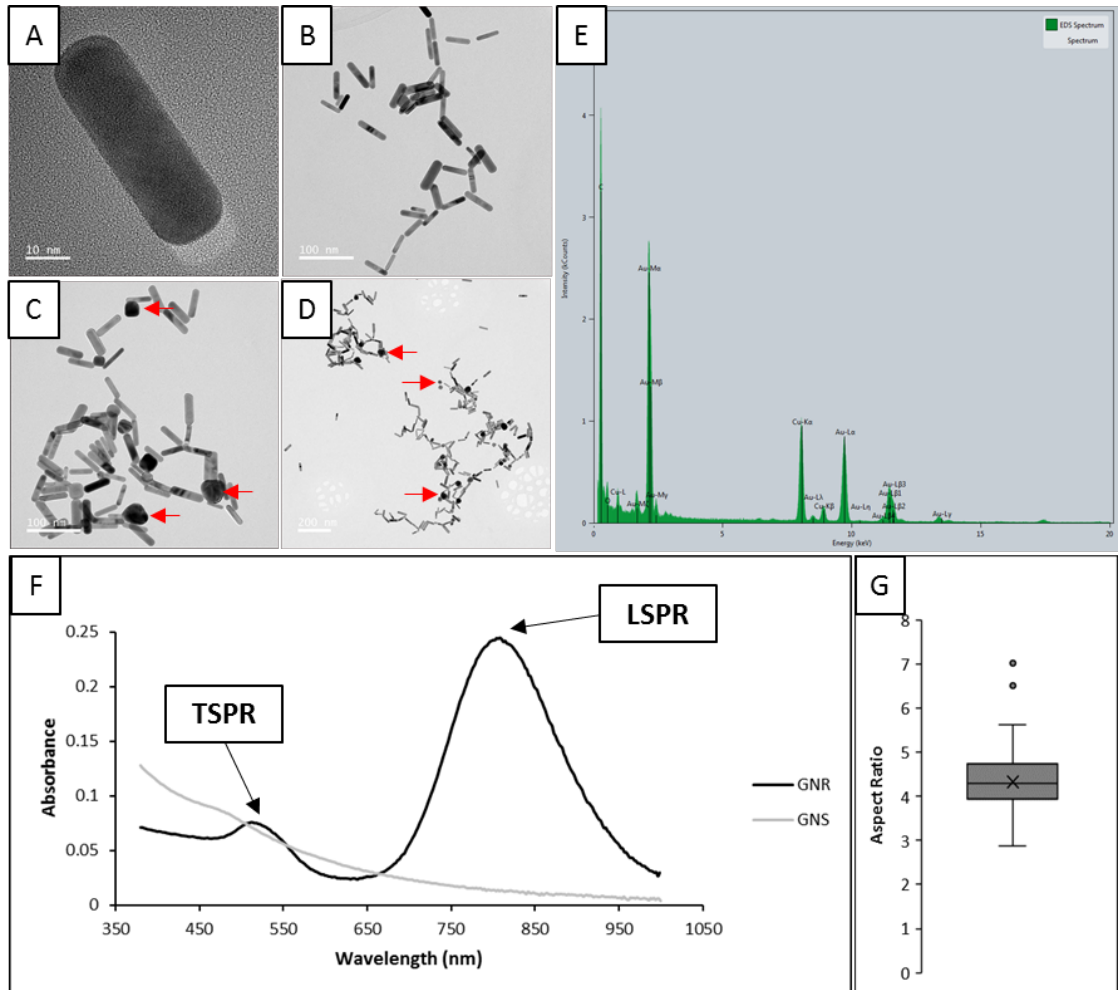


**Figure 4.1 – Characterisation of GNRs.** (A) TEM micrograph of individual and (B, C, D) multiple GNRs, with red arrows indicating presence of non-rod shaped amorphous gold. (E) EDX results confirming GNRs are composed of gold. (F) Example UV-visible spectrophotometry results for gold nanospheres (GNS) in seed solution and final fabricated GNRs, with transverse surface plasmonic resonance (TSPR) and lateral surface plasmonic resonance (LSPR) peaks at 514 nm and 810 nm respectively. (G) Box and whisker plot showing aspect ratios of fabricated nanorods.

TEM of the fabricated nanorods showed the successful formation of nanorod shapes of mean length of 49.6 nm ± 8.15, mean width of 11.7 nm ± 2.64, and mean aspect ratio of 4.33 ± 0.64. Of the observed particles, 88.13% ±

2.06 of observed particles were nanorod shaped (Figure 4.1 A-D), and 11.87% ± 2.06 were amorphous. TEM-EDX analysis showed that the nanorods observed were in fact gold, as evidenced by peaks at characteristic energy levels, once the carbon film and copper TEM grid was accounted for (Figure 4.1 E).

UV-Visible spectrophotometry showed a shape characteristic of gold nanorods (Henson *et al.*, 2018), with mean lateral and transverse peaks of 812 nm ± 21.6 and 509 nm ± 2.77 respectively across all measured batches (Figure 4.1 F&G).

The nanorod crystal structure was also analysed using high-resolution TEM (HR-TEM) and selected area electron diffraction (TEM-SAED) as detailed in Figure 4.2.
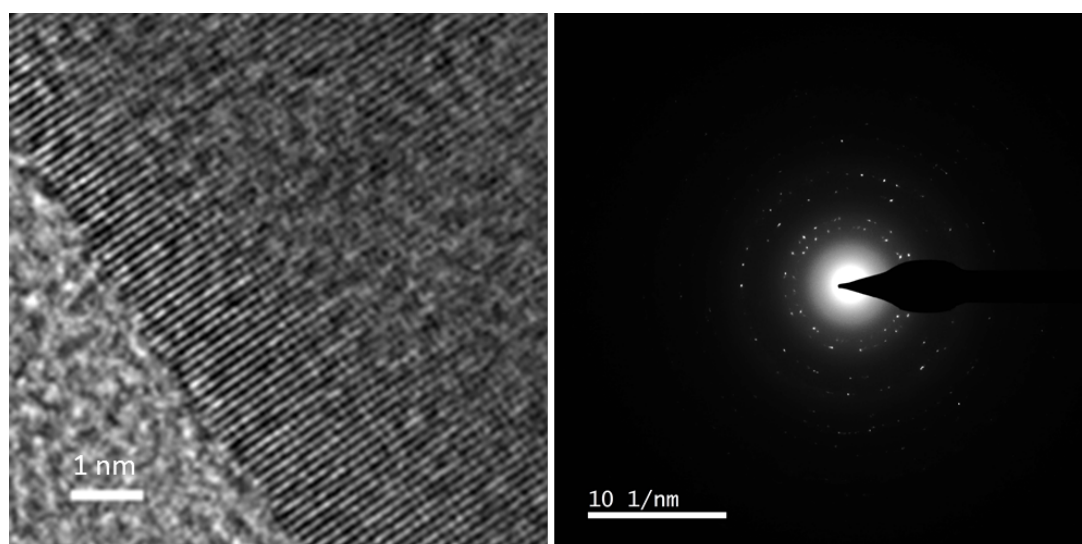


**Figure 4.2 – HR-TEM (left) and TEM-SAED diffraction pattern (right) of GNRs.**

HR-TEM imaging showed a polycrystalline structure and this was confirmed through TEM-SAED analysis, which showed a Debye-Scherrer ring pattern characteristic of polycrystalline gold. The patterns observed through TEM-SAED were indexed using the XPert database according to (111), (200), (220), and (311) lattice planes, indicating face centred cubic (fcc) gold on the basis of d-spacings of 2.39 Å, 2.08 Å, 1.48 Å, and 1.22 Å respectively.

## 4.3.2 Analysis of GNR dispersion in Hybrid Hydrogels

One of the key methods for GNR dispersion in hydrogel used in the literature is sonication (Navaei *et al.*, 2016). In order to test the ability of the fabricated GNRs to withstand sonication dispersal, GNRs were suspended in GNR hydrogel and sonicated for 60 minutes. UV-Visible Spectrophotometry was performed every 10 minutes to analyse GNR stability, and absorbance spectra are illustrated in Figure 4.3.
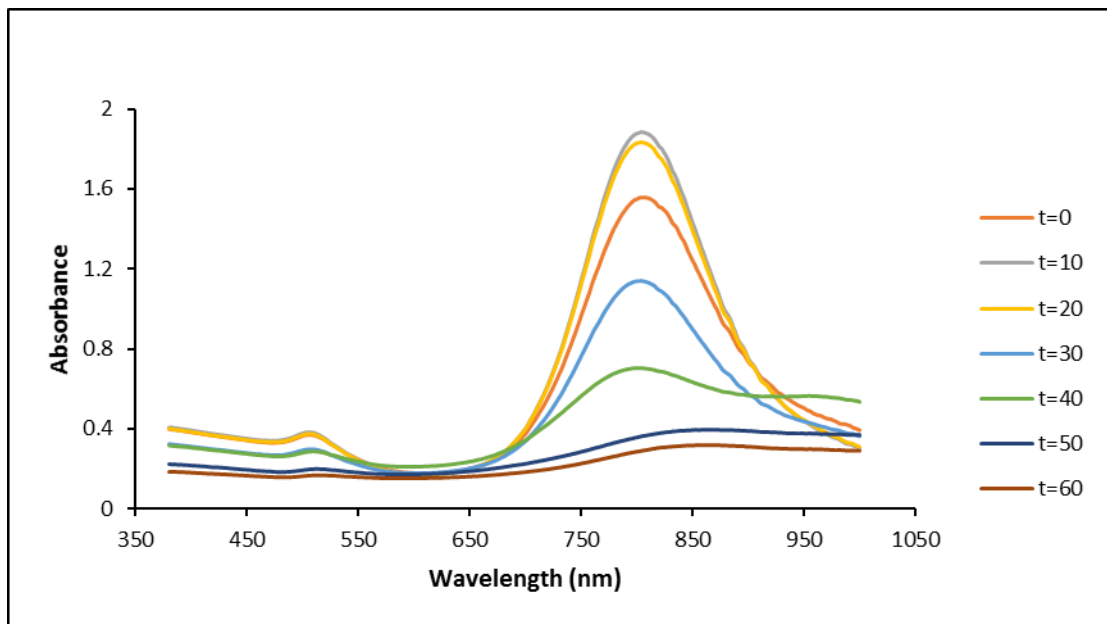


**Figure 4.3 – Sonication testing of GNRs.** GNRs were sonicated for 60 minutes and analysed with UV-visible spectrophotometry every 10 minutes during sonication. (n=3, 2).

The results of sonication testing show clearly that GNRs are degraded by sonication, and that a significant drop in lateral plasmonic peak absorbance is seen as early as 30 minutes. After the 30 minute point, the lateral peak loses all shape, followed by the transverse peak. This is clear evidence of the GNRs breaking down.

At the initial reading before sonication (t=0), evidence of aggregation can be seen in the 'shoulder' of the curve after the lateral plasmonic peak. This shoulder is observed when comparing the shape of the t=0 and the t=10 curves, in which the tail of the lateral peak at t=0 crosses the tail of the t=10 lateral peak, despite the t=0 peak having lower absorbance and the depth of the trough between transverse and lateral peaks being equal between the timepoints. The crossing of the post lateral peak tails is due to the absorbance being higher for t=0 at the highest wavelengths measured but

lower at the lateral peak (p<0.01, one-way ANOVA with post-hoc Tukey test), resulting in a 'shoulder' in which the high end of the lateral peak does not drop to an equal level to the low end of the lateral peak. This shoulder is indicative of aggregation (Henson *et al.*, 2018).

This shoulder is lessened at t=10, as evidence by the higher absorbance reading at the lateral peak and lower absorbance at the highest end of the spectrum. This shows a clear de-aggregation effect of the sonication. Further, the curves at t=10 and t=20 are equal, and the absorbance at their lateral peaks is not significantly different (one-way ANOVA).

At t=30, the absorbance at both the transverse and lateral peaks is significantly lower than at t=20 (p<0.001, one-way ANOVA with post-hoc Tukey test). Further, there is a perceptible decrease in peak symmetry. This can be shown by measuring the distance from the peak wavelength (i.e. 'centre' of the peak) to each side of the peak at an absorbance equal to half the peak absorbance. For t=20, the ratio between the distance to the low side of the peak and the high side of the peak is 1.25, and that increases to 1.32 for t=30. The curve at t=30 also has a shoulder at the highest end of the spectrum that causes the lateral peak tail to cross the tail of t=20. This combination of increased asymmetry and post-peak shoulder suggests increasing polydispersity of size and aspect ratio of the measured GNRs (Henson *et al.*, 2018), caused by the GNRs breaking down.

The observed 'shoulder' at t=30 increases so much at t=40 that it is barely a shoulder anymore and is better described as a continuation of the peak. This is true to such an extent that it isn't possible to analyse the symmetry of the peak at half the peak absorbance because the absorbance of the post-peak tail never decreases this far. The complete loss of peak shape at t ≥40 indicates loss of shape fidelity for the GNRs, and whereas at t=30 there was increasing dispersity of sizes and aspect ratios, now there is an increasing dispersity of shapes. It is however worth noting, that the lateral peak absorbance wavelength doesn't shift more than 4 nm from the lowest to highest wavelength measure for samples from t=0 to t=40, and is not significantly different at any timepoint (one-way ANOVA).

At t=50 and t=60 the transverse peak also collapses and though the general shape follows that at t=40, the GNRs are too far degraded to obtain any information from their absorbance spectra.

After establishing that the fabricated GNRs could only be sonicated for a maximum of 20 minutes before starting to break down, and that maximum

dispersion from sonication was achieved at 10 minutes, this sonication time was taken forward for further experiments.

The next step was to determine the most suitable 'carrier' suspension solution for the GNRs before re-suspension into GelNOR. Though previous studies using hydrogel suspended GNRs for cell culture applications are limited, some have used DIW as the carrier solution (Navaei *et al.*, 2016). DIW is an ideal carrier solution due to its high biocompatibility but was disregarded as a storage solution for this project due to problems with aggregation over repeated centrifuge and resuspension cycles. It is possible however that by processing GNRs through the repeated centrifuge and resuspension cycles using 0.001M CTAB and then performing the final resuspension with DIW, it is possible to avoid GNR aggregation whilst also minimising the amount of cytotoxic CTAB taken into the final hydrogel.

The homogeneity of GNR dispersion when carried in DIW vs 0.001 M CTAB prior to resuspension, is shown in Figure 4.4.
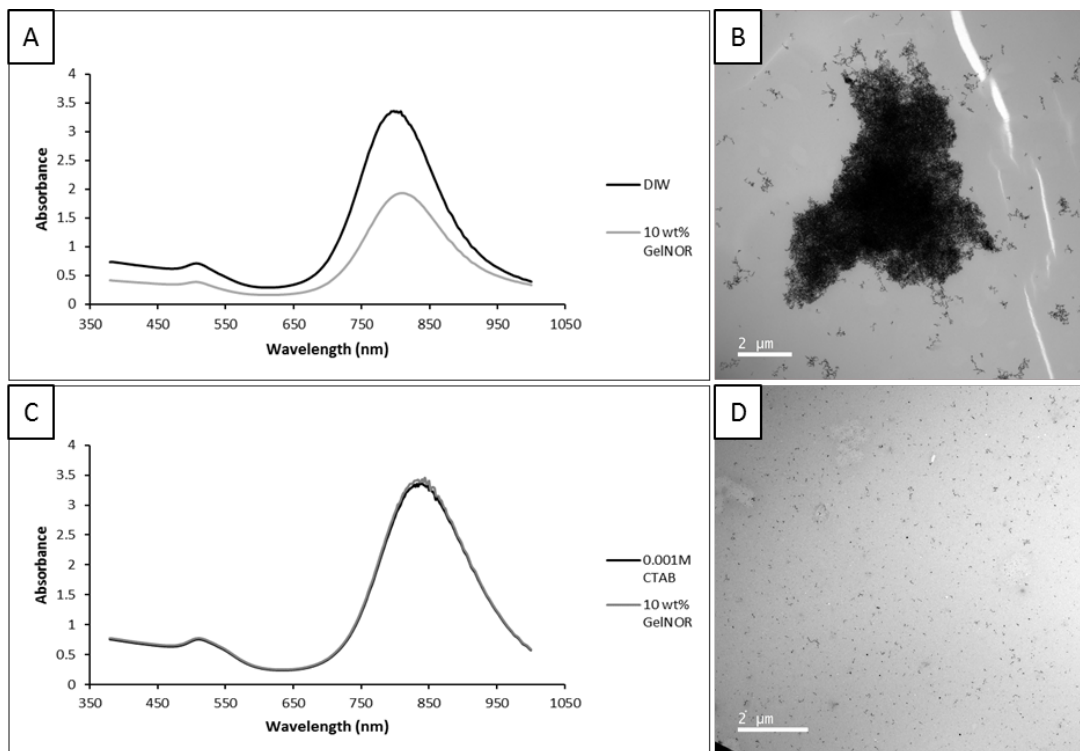


**Figure 4.4 – Comparison of GNR dispersion in GelNOR when prepared with different storage solutions.** (A) UV-Visible absorbance spectrum of GNRs suspended in DIW and subsequently in 10 wt% GelNOR at 0.5 mg/ml, (B) showing clear evidence of aggregation. (C) UV-Visible absorbance spectrum of GNRs suspended in 0.001M CTAB and subsequently in 10 wt% GelNOR at 0.5 mg/ml, (B) showing aggregate free, homogenous GNR dispersion. (n=3, 2)

From the observed results, it can be seen that GNRs carried in DIW were far more prone to aggregation than those carried in 0.001 M CTAB, and that storage in DIW for even a single centrifuge and resuspension cycle had a significant impact on GNR dispersion homogeneity when transferred into 10 wt% GelNOR. This is immediately obvious qualitatively from the TEM micrographs of the two samples, but is also backed up quantitatively by the UV-visible absorbance spectra. The absorbance at both the transverse and lateral peaks drops significantly after dispersion in 10 wt% GelNOR when GNRs are carried in DIW before suspension ($p < 0.01$ and $p < 0.001$ respectively, Welch's t-test). Further, the UV-visible absorbance spectrum for GNRs post-suspension in 10 wt% GelNOR has a noticeable shoulder after the lateral peak, as evidenced by an approximately equal absorbance at the highest measured wavelength (1000 nm), despite the GelNOR suspended GNRs having significantly lower lateral peak and trough between peaks. This shoulder can be taken as further evidence of aggregation (Henson *et al.*, 2018).

Conversely, when GNRs were carried in 0.001 M CTAB before re-suspension in 10 wt% GelNOR, the UV-visible absorbance spectra of the GNRs before and after re-suspension in 10 wt% GelNOR are almost identical. There is also a small amount of 'noise' on the lateral peak, which is enhanced after re-suspension in 10 wt% GelNOR. One possible reason is a small amount of the reaction solution persisting in the storage solution which isn't present in the pure 0.001 M CTAB solution used to blank the absorbance spectra, causing unexpected noise. This is then enhanced after re-suspension by the accidental addition of CTAB to the GNR/GelNOR hybrid gel during re-suspension, which isn't present in the pure 10 wt% GelNOR solution used to blank the GNR/GelNOR spectrum. Alternatively, it is possible that at high absorbance values such as the approximately 3.5 seen in this case the resolution between absorbances drops and thus the reading is more prone to producing 'noise'. Though it isn't clear what the cause is, it does not affect the overall shape of the curve or the observed absorbances.

### 4.3.3 Analysis of Physical Characteristics of Hybrid Hydrogels

### 4.3.3.1 Microstructure Analysis

In order to analyse the effect of GNR incorporation on the hydrogel network microstructure, cross sections of freeze-dried 10 wt% GelNOR hydrogels were imaged using SEM after incorporation of GNRs at a range of concentrations. An example of a hydrogel cross-section is given in Figure 4.5.
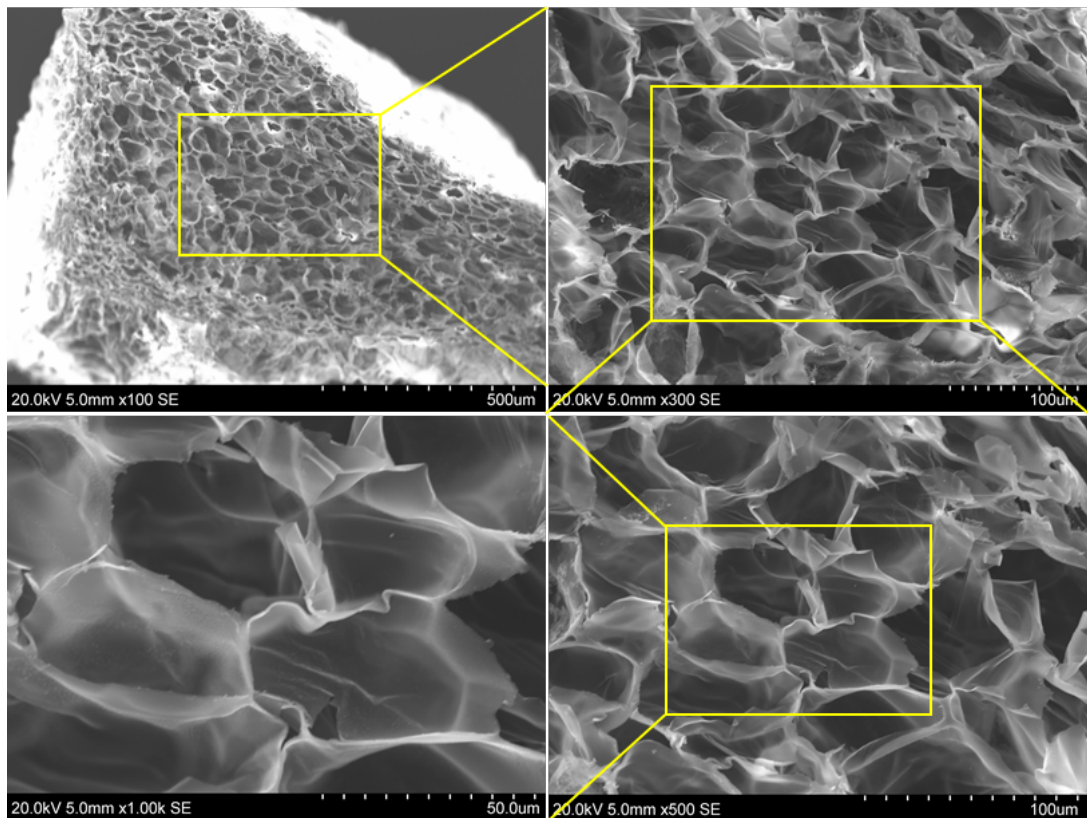


**Figure 4.5 – SEM micrographs of 10 wt% GelNOR disc cross-sections at increasing magnifications.** Yellow boxes signify the section of each image which is shown in the next higher magnification image.

The SEM micrographs show that there is a range of pore sizes present in the hydrogel cross-section, and that pore size and shape is potentially influenced by proximity to the edges of the gel. Due to this, SEM micrographs were taken in the centre of the gel as pore sizes are less influenced by edge effects in this region.

Micrographs were taken of multiple samples at each concentration and the pore sizes in the resulting images were analysed manually using ImageJ software. Images and pore sizes are given in Figure 4.6.
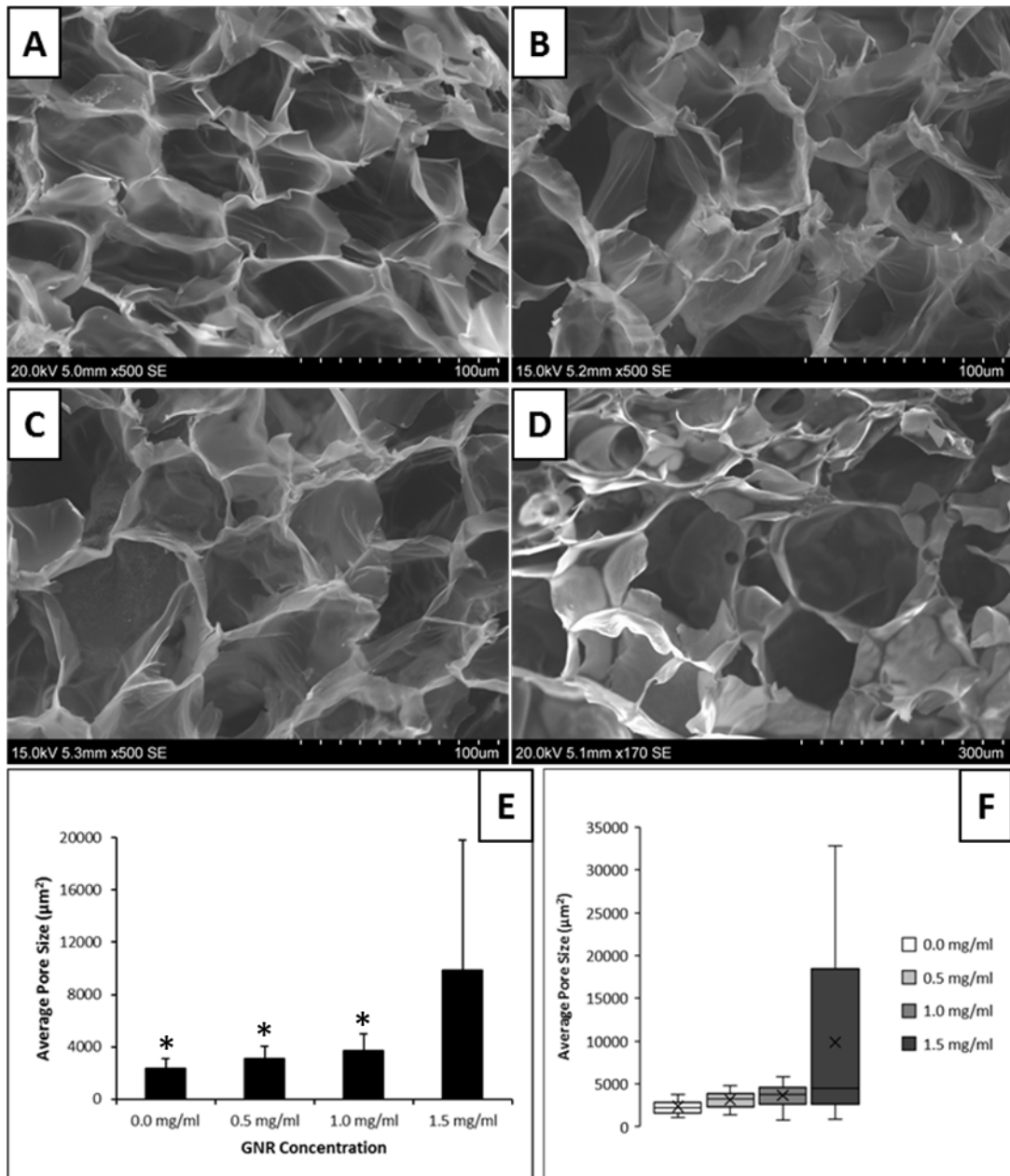
**Figure 4.6 – Comparison of pore size and network microstructure of 10 wt% GelNOR/GNR hybrid hydrogels at a range of GNR concentrations.** SEM micrographs of hydrogel cross-sections at (A) 0.0 mg/ml, (B) 0.5 mg/ml, (C) 1.0 mg/ml, and (D) 1.5 mg/ml (note change in scale). Corresponding pore sizes as determined by ImageJ analysis are expressed as (E) mean with error bars showing standard deviation and (F) box and whisker plots of full data set. Significance levels * $p < 0.05$ vs. 1.5 mg/ml. (n ≥ 50, 2).

From Figure 4.6 it can be seen qualitatively that the hybrid hydrogels retain similar microstructures as GNRs increase up to 1.0 mg/ml. As the GNR concentration increases to 1.5 mg/ml, however, a marked change in the microstructure is seen as the pore sizes become much larger and more variable. This observation is reflected in the qualitative analysis of pore size,

in which the 1.5 mg/ml hybrid hydrogel has an average pore size that is significantly larger than the 0.0, 0.5, and 1.0 mg/ml hybrid gels (Figure 4.6E; $p < 0.01$, $p < 0.01$, and $p < 0.05$ respectively, one-way ANOVA with post-hoc Tukey test). The average pore size increases to a lesser extent from 0.0 mg/ml to 0.5 mg/ml and 0.5 mg/ml and 1.0 mg/ml, though these increases were not statistically significant. Further to this, it can be seen from the supporting box and whisker pots (Figure 4.6F) that the range of sizes is increased in the 1.5 mg/ml gels, with the maximum pore size in the 1.5 mg/ml being 36.9 times larger than the minimum, compared to 3.40, 3.50, and 7.28 in the 0.0, 0.5, and 1.0 mg/ml gels, respectively. This is reflected in the differences in mean and median pore size at each GNR concentration, with the difference being 6.64%, 4.45% and 1.12% for 0.0, 0.5, and 1.0 mg/ml, respectively, but 121% in the 1.5 mg/ml. This indicates a relatively small number of extremely large pores pulling the average pore size up in the 1.5 mg/ml gels as compared to a relatively normal distribution of pore sizes in the lower GNR concentration gels.

EDX was not performed during SEM analysis as the samples were sputter coated with gold. This decision was taken because EDX had already been performed on GNRs suspended in GelNOR hydrogel during TEM analysis as described in previous figures and the objective of SEM analysis was to image the cross-sectional microstructure. Thus repeating EDX with SEM was deemed unnecessary and so the decision was taken to sputter coat with gold rather than using carbon coating which would have allowed EDX analysis.

Mass loss and swelling measurements were also taken on the samples prior to SEM, with results described in Figure 4.7.
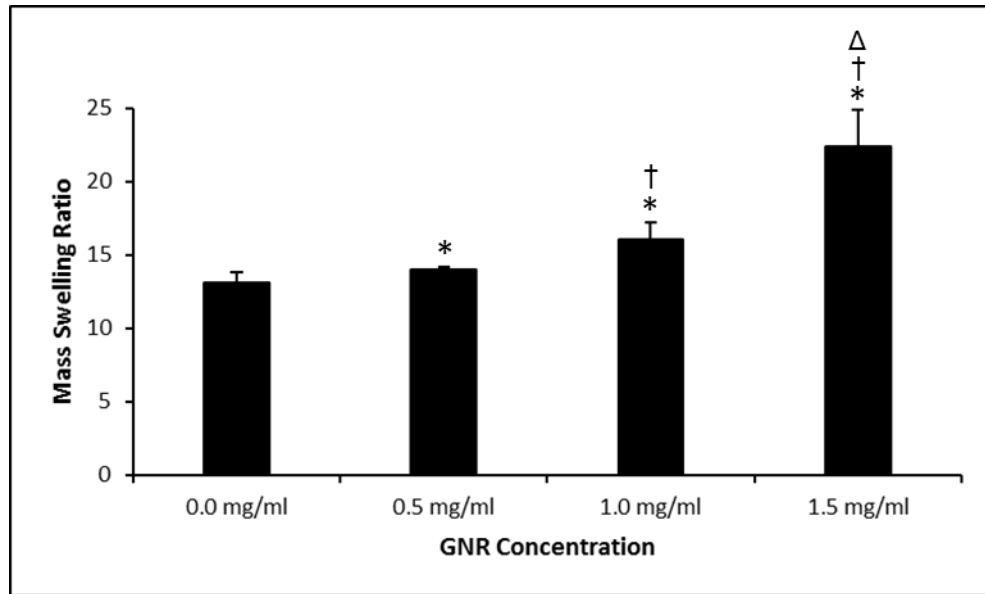
**Figure 4.7 – Mass swelling ratios of 10 wt% GelNOR/GNR hybrid hydrogels at a range of GNR concentrations.** Significance levels * $p < 0.05$ vs. 0.0 mg/ml; † $p < 0.05$ vs. 0.5 mg/ml; Δ $p < 0.05$ vs. 1.0 mg/ml. (n=4, 2).

The mass loss and swelling data shows a trend of increasing mass swelling ratio with increasing GNR concentration. There is a small but statistically significant increase from a swelling ratio of 13.1 at 0.0 mg/ml to 14.0 at 0.5 mg/ml ($p < 0.05$, one-way ANOVA with post-hoc Tukey test). At 1.0 mg/ml, the swelling ratio of 16.1 is significantly higher than at both 0.0 and 0.5 mg/ml ($p < 0.001$ for both, one-way ANOVA with post-hoc Tukey test), but significantly lower than at 1.5 mg/ml. The swelling ratio of 22.4 seen at 1.5 mg/ml is significantly greater than all other measured concentrations ($p < 0.001$ for each, one-way ANOVA with post-hoc Tukey test).

### 4.3.3.2 Mechanical Characterisation

The effect of GNR incorporation on hydrogel mechanical properties was then analysed through rheological testing Figure 4.8.
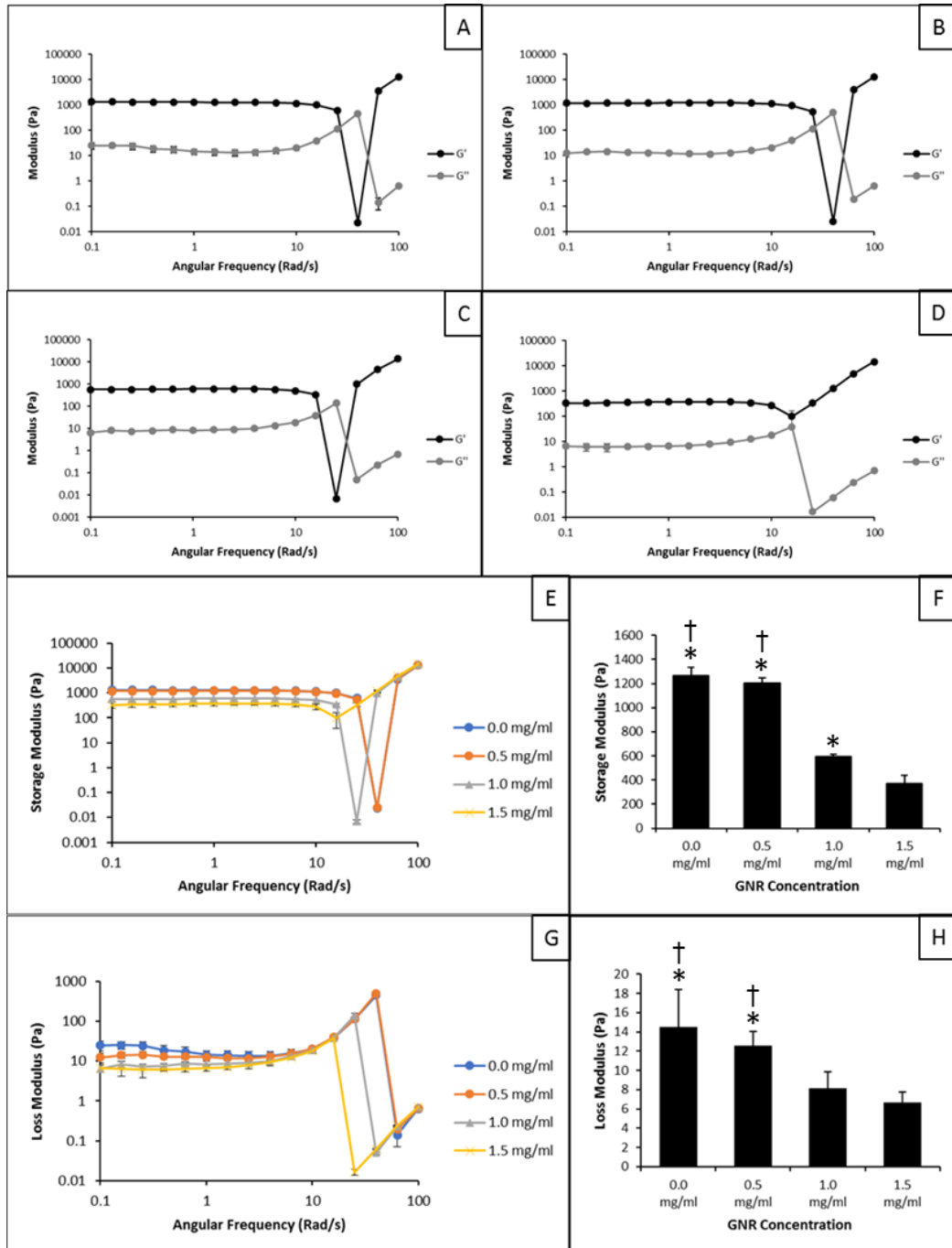


**Figure 4.8 – Rheological characterisation of 10 wt% GelNOR/GNR hybrid hydrogels at a range of GNR concentrations.** Combined storage (G') and loss (G'') moduli across full frequency sweep for 10 wt% GelNOR with GNR concentrations of (A) 0.0 mg/ml, (B) 0.5 mg/ml, (C) 1.0 mg/ml, and (D) 1.5 mg/ml. (E) Combined storage moduli of all tested concentrations across full frequency sweep and (F) at 1 Rad/s. (G) Combined loss moduli of all tested concentrations across full frequency sweep and (H) at 1 rad/s. Significance levels * $p < 0.05$ vs. 1.5 mg/ml; † $p < 0.05$ vs. 1.0 mg/ml. (n=4, 2).

Rheological testing produced an unexpected trend, in which the hybrid hydrogels became weaker with higher concentrations of GNRs. All tested concentrations had a similar profile across the frequency sweep for both storage and loss moduli. Both storage and loss moduli initially plateaued across the lower frequencies, before gradually starting to converge between approximately 6 and 15 rad/s.

There was then a sudden and large drop in storage modulus in the 0.0, 0.5, and 1.0 mg/ml gels whilst the loss modulus continued to increase, resulting in a crossover point in which the loss modulus becomes greater than the storage modulus (Figure 4.8A – C). There was then an immediate recovery of storage modulus to a modulus higher than before the sudden drop and a corresponding sudden and large drop in the loss modulus. Both storage and loss moduli then increased in an approximately linear fashion at the high-frequency end of the frequency sweep.

The 1.5 mg/ml gels, conversely, do not consistently show the same 'crossover point and recovery' behaviour (Figure 4.8D). Instead, in some samples the storage and loss moduli crossover but in others they do not (data for individual samples not shown). This resulted in the average storage modulus at the crossover frequency (15.8 rad/s) not crossing the average loss modulus at the same frequency. After this point the loss modulus dropped suddenly in the same way that it did in all other measured GNR concentrations, before increasing in an approximately linear fashion at the highest frequencies measured. The storage modulus also increased in an approximately linear fashion after the lowest point at 15.8 rad/s, as seen in all other measured GNR concentrations.

As well as the shape of the graphs, there is also the absolute value of the moduli to consider. The pure GelNOR hydrogel and the hybrid hydrogel with GNRs encapsulated at 0.5 mg/ml matched closely across the frequency sweep, and were not significantly different at the 1 rad/s comparison frequency for either G' or G'' (Figure 4.8F and H). The frequency of 1 rad/s was taken as a point for comparison due to its position as being in the centre of the linear plateau for both the storage and loss moduli. As the GNR concentration increased to 1.0 mg/ml, the storage modulus decreased significantly in comparison to both 0.0 and 0.5 mg/ml at the 1 rad/s comparison frequency (Figure 4.8F; $p<0.001$, one way ANOVA with post-hoc Tukey test), and the loss modulus also drops significantly in comparison to the 0.0 mg/ml gel ($p<0.05$, one way ANOVA with post-hoc Tukey test) but not in comparison to the 0.5 mg/ml gel. Further to this, the previously

described crossover and recovery point happens at lower frequency of 25.1 rad/s rather than the 39.8 rad/s seen in the 0.0 and 0.5 mg/ml gels.

Both the storage and loss moduli drop again as the GNR concentration increases to 1.5 mg/ml, with the storage modulus of 370 Pa at the 1 rad/s comparison point being significantly lower than that at 0.0, 0.5, and 1.0 mg/ml (p<0.001 for all, one way ANOVA with post-hoc Tukey test). The loss modulus of 6.70 Pa at 1 rad/s is also significantly lower than at 0.0 and 0.5 mg/ml (p<0.01 and p<0.05 respectively, one way ANOVA with post-hoc Tukey test), but is not significantly different to that at 1.0 mg/ml.

A further insight into the material behaviour can be derived by considering the loss factor (G'' / G').  The loss factor over the course of the frequency sweep is shown in Figure 4.9.
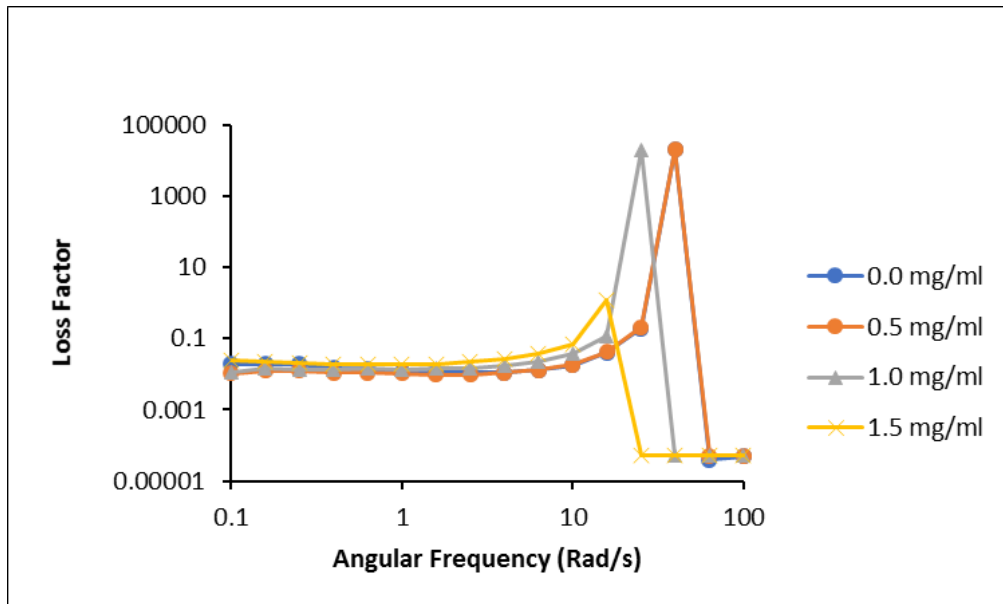


**Figure 4.9 – Loss factor of 10 wt% GelNOR at 0.0 – 1.5 mg/ml GNR concentration, across a frequency sweep of 0.1 – 100 Hz.** (n=4, 2).

Figure 4.9 shows a relatively stable loss factor across the lower frequencies, from 0.1 – 10 Hz, for all GNR concentrations. This is followed by a large single point increase, happening at different points between for each GNR concentration, between the measurement points of 15.8 and 39.8 Hz. Potentially the most significant data points, however, are those after the single point maximum for which the loss factor is extremely close to 0.

### 4.3.3.3  Electrical Characterisation

The effect of GNR incorporation on the hydrogel's electrical conductivity was measured using EIS. The full results are shown in Figure 4.10.
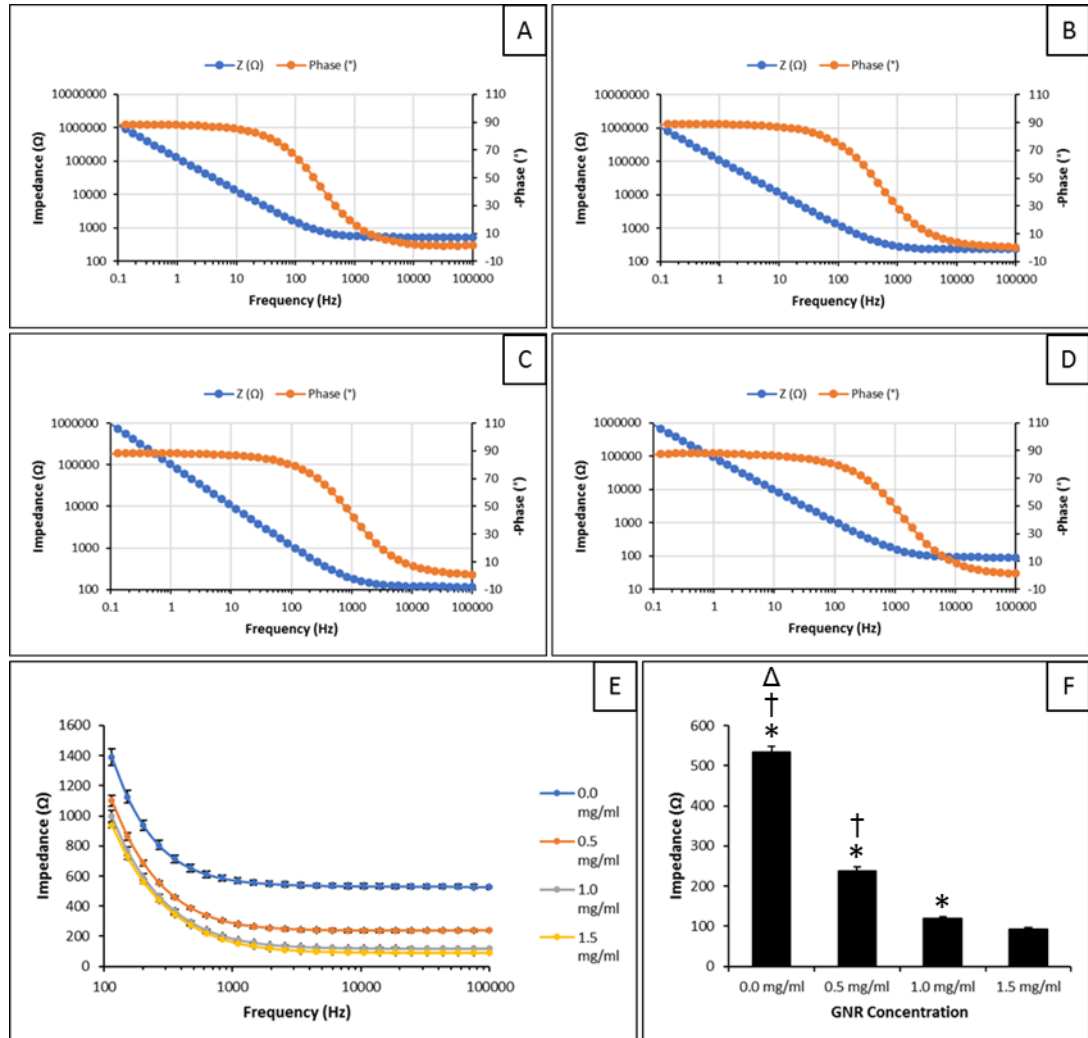


**Figure 4.10 – EIS characterisation of 10 wt% GelNOR/GNR hybrid hydrogels at a range of GNR concentrations.** Bode plots showing absolute impedance and phase angle across full frequency sweep for 10 wt% GelNOR with GNR concentrations of (A) 0.0 mg/ml, (B) 0.5 mg/ml, (C) 1.0 mg/ml, and (D) 1.5 mg/ml. (E) Combined 'half' Bode plot comparing impedance values only of all measured GNR concentrations between 100 - 100,000 Hz and (F) chart showing comparative impedance at 10,000 Hz. Significance levels * $p<0.05$ vs. 1.5 mg/ml; † $p<0.05$ vs. 1.0 mg/ml; Δ $p<0.05$ vs. 0.5 mg/ml. (n=4, 2).

Figure 4.10 shows that the impedance and phase angle behave similarly across the frequency sweep for all measured GNR concentrations This is evidenced by the consistent shape of the Bode plots for gels at all GNR concentrations (Figure 4.10A – D). Also consistent across all GNR

concentrations was the tendency of the system capacitance to dominate below a frequency of approximately 1000 Hz. For this reason, it was decided to compare the impedance of the respective gels at frequencies above 1000 Hz, and specifically have a single point comparison at 10,000 Hz in the linear plateau region of the plot.

Comparison of gel impedance at these frequencies showed a sharp drop in impedance between the pure GelNOR and the 0.5 mg/ml GNR hybrid gel, followed by a smaller drop between the 0.5 and 1.0 mg/ml gels, and a drop between 1.0 and 1.5 mg/ml that was smaller still (Figure 4.10F).

When these data were compared at 10,000 Hz, however, the difference in impedance between each gel was statistically significant due to very tight reproducibility ($p < 0.001$ for all gel comparisons except between 1.0 – 1.5 mg/ml, for which $p < 0.05$, one-way ANOVA with post-hoc Tukey test).

This comparison of absolute impedance at a single frequency does not take into account the full electrical characteristics of the Bode plot, however, and so this comparison was further supplemented with a comparison of the admittance. This admittance plot was then used to calculate resistance for statistical comparison between GNR concentration, and the results are shown in Figure 4.11.
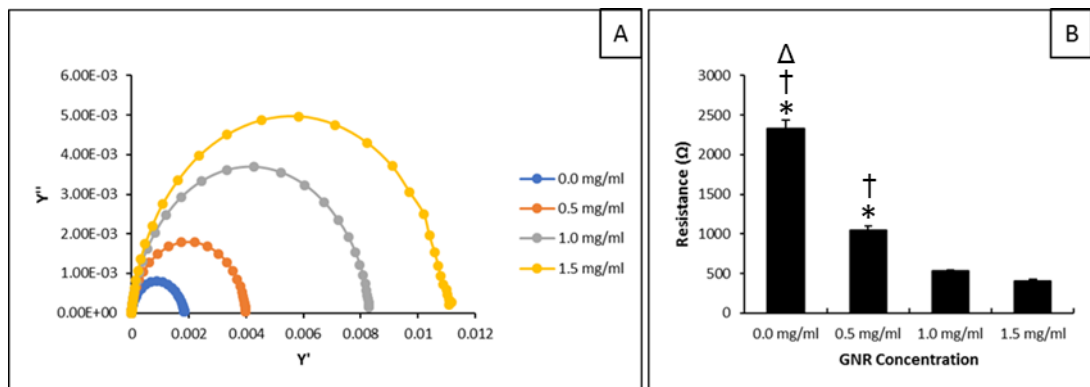


**Figure 4.11 – Admittance and resistance of 10 wt% GelNOR/GNR hybrid hydrogels at a range of GNR concentrations.** (A) Admittance plots comparing hybrid hydrogels at all measured concentrations. (B) Resistance of samples derived from admittance plots. Significance levels * $p < 0.05$ vs. 1.5 mg/ml; † $p < 0.05$ vs. 1.0 mg/ml; Δ $p < 0.05$ vs. 0.5 mg/ml. (n=4, 2).

By the increasing size of the characteristic admittance semi-circles, the admittance increases significantly with each increase in GNR concentration (Figure 4.11A). When this data was translated into resistance, a similar trend was seen to the trend in absolute impedance described in Figure 4.10.The

differences between all gels were statistically significant except for between 1.0 and 1.5 mg/ml, for which the difference in resistance was not significantly different (Figure 4.11B; $p < 0.001$ for all others, one-way ANOVA with post-hoc Tukey test).

## 4.4 Discussion

### 4.4.1 Fabrication of GNRs and Reproducible Encapsulation in GelNOR Hydrogels

The produced nanorods matched well with those described by Nikoobakht and El-Sayed (Nikoobakht and El-Sayed*, 2003), who were the first to describe CTAB-capped GNR fabrication by the seed-mediated growth method used in this project. The observed lateral peak wavelength of 812 nm matches well with the lateral peak of GNRs fabricated using the highest $AgNO_3$ concentration used by Nikoobakht and El-Sayed, which was the same concentration used in this chapter. This lateral peak also corresponded well with the 810 nm reported by Navaei and colleagues (Navaei *et al.*, 2016) who used the same synthesis protocol, though they interestingly saw a significantly lower average aspect ratio of 3.15 as opposed to the 4.33 seen here or the 4.5 seen by (Nikoobakht and El-Sayed*, 2003). It is certainly unexpected for two batches of GNRs with such similar UV-visible absorbance spectra to have such significantly different aspect ratios, but one explanation may be that (Navaei *et al.*, 2016) included non-nanorod shaped particles in their shape analysis, but they were excluded from the shape analysis in this chapter. Though one of the advantages of using this CTAB-capped seed-mediated growth method is the low fraction of non-nanorod shapes produced (approx. 12% in the synthesis in this chapter), it does still produce enough of a fraction to have an impact on the measured average aspect ratio if all these particles are counted as having an aspect ratio of approximately 1.

Higher aspect ratio GNRs are theoretically more electrically conductive (Yoshida and Toshima, 2014), but to achieve an aspect ratio significantly higher than that observed in the GNR fabrication described in this chapter would require a more complex binary (dual) surfactant synthesis (Nikoobakht and El-Sayed*, 2003). The added complexity of this option was considered unnecessary for the requirements of this project. Similarly, a further synthesis step to remove spherical particles and improve GNR shape fidelity, such as the use of multiple centrifugation steps (Sharma, Park and Srinivasarao, 2009), gravimetric sedimentation (Khanal and Zubarev, 2008), or depletion forces (Park, Koerner and Vaia, 2010), was also considered, but ultimately deemed unnecessary.

Batches of synthesised GNRs with high shape fidelity will generally form tighter pellets when purified through centrifugation. These tighter pellets will

be much more difficult to break apart due to the high depletion forces caused by the monodisperse nature of the initial GNR colloid, meaning that when the GNRs are forced together by centrifugation such that there is no space for CTAB micelles between the GNRs, they will gain a net osmotic pressure keeping the GNRs together (Wei, Bai and Fan, 2019). This was reflected anecdotally during protocol development, in which GNRs fabricated by the protocol described by Nikoobakht and El-Sayed (Nikoobakht and El-Sayed*, 2003) allowed immediate re-suspension of the GNR pellet in GelNOR by pipetting supplemented by short time sonication, but the same centrifugation protocol applied to commercially purchased nanorods of the same peak wavelengths took up to an hour of sonication and pipette mixing to break the GNR pellet apart. This is most likely due to the highly monodisperse nature of commercially purchased nanorods, and this effect was seen whether the initial carrier solution was 0.001 M CTAB or DIW.

The long sonication times required for resuspension of size and shape purified nanorods more closely match the 1 hour used by Navaei (Navaei *et al.*, 2016). The sonication testing in this chapter indicated significant destruction of nanorods at the 30-minute time-point, and similarly commercial nanorod providers suggest 'between 15 seconds and 1 minute combined with vortexing to break up aggregates' though this is not specific to resuspension in hydrogel solutions after centrifugation. The difference between the 1 hour of sonication used by Navaei to re-suspend GNRs and the destruction within 30 minutes seen in these experiments is significant, considering the same GNR synthesis protocol was used. The protocol described by Navaei (Navaei *et al.*, 2016) does not mention a purification step, and the transverse to lateral peak absorbance ratio of approximately 1:2 indicates a high rate of shape impurities (Henson *et al.*, 2018). The supplementary TEM images also show a range of GNR shapes and sizes, as well as the presence of non-nanorod shaped gold spheres, and so the GNRs used by (Navaei *et al.*, 2016) do not appear to be highly monodisperse.

The TEM-SAED analysis performed in this chapter shows that the synthesised GNRs had a face-centred cubic (FCC) crystal structure. This was as expected, as gold usually crystallises to FCC as it is gold's lowest free-energy structure (Han *et al.*, 2020). Because FCC is the most thermodynamically stable structure for wet-synthesised gold nanorods (Lu *et al.*, 2021), the GNRs synthesised in this chapter should not have been unusually unstable and prone to destruction by sonication. Other more tightly

packed structures have been achieved in the literature (Fan *et al.*, 2020) which may be more resistant to break down by sonication, but these crystal structures are difficult to synthesise and thus it is unlikely that Navaei (Navaei *et al.*, 2016) formed none-FCC GNRs when using the standard protocol from Nikoobakht and El-Sayed (Nikoobakht and El-Sayed*, 2003).

Despite the long sonication times used by Navaei (Navaei *et al.*, 2016), the TEM images of GNR loaded GelMA hydrogels do appear to show GNRs that have not been destroyed by the sonication, and are not significantly aggregated, however, the TEM images are taken from a single small area of their gel and do not have enough clarity at lower magnification to identify potential aggregation in the wider gel. The TEM images are also supplemented with UV-visible absorbance spectra, but again these spectra are potentially incomplete with respect to allowing identification of GNR behaviour in the whole gel.

Though absolute absorbance values from UV-visible spectra are highly dependent on aspects of the measuring set-up, such as optical path length, and so are not appropriate to compare, other descriptors of the data are available for comparison. As an example, the previously described transverse to lateral peak absorbance ratio of 1:2 seen by Navaei and colleagues (Navaei *et al.*, 2016) is lower than the 1:3 seen in this chapter, and the approx. 1:3.5 seen by Nikoobakht and El-Sayed (Nikoobakht and El-Sayed*, 2003) and this lower ratio may be evidence of shape impurities (Henson *et al.*, 2018). This may be indicative of GNR aggregation when suspended in the hydrogel, or possibly indicative of a GNR sample showing high rates of shape impurities (Henson *et al.*, 2018). It would also possible to see further indicators of GNR behaviour by observing the shape of the lateral plasmonic peak of the spectra, but Navaei and colleagues did not show this as part of their results, and instead stopped the absorbance spectra at about 820 nm, directly after the lateral peak. As a result the UV-visible absorbance spectra supplied by Navaei gives limited information on GNR behaviour (Navaei *et al.*, 2016).

Despite the potentially incomplete absorbance spectra, TEM images show complete GNRs are present in the final hydrogel, as previously described. This means that the GNRs do survive the elongated sonication, and thus the difference in observed sonication tolerance must be due to some other experimental factor, such as a protective effect conferred by the GelMA hydrogel solution being greater than that of GelNOR, or the use of significantly weaker sonication. Interestingly, a number of publications using

GNRs resuspended in other types of hydrogels do not mention sonication to improve dispersion at all (Bermúdez-Jiménez *et al.*, 2019; Turner, Og and Murphy, 2020; Wickramasinghe *et al.*, 2020), and the effect of sonication on de-aggregation of GNRs post-resuspension in this chapter was significant but relatively small.

It could also be that the difference in sonication tolerance was due to the use of DIW as an initial carrier solution difference in the GNR packing during centrifugation caused by the substitution of 0.001 M CTAB for DIW (Navaei *et al.*, 2016). It may be that the absence of CTAB acts to decrease electrostatic repulsion between the GNRs after centrifugation, and this is reflected in the higher rate of aggregation seen during the comparison of CTAB and DIW as carrier solution before GNR resuspension in GelNOR in this chapter. However, this use of DIW resulted in the presence of small clusters of GNR aggregation throughout the gel alongside successfully resuspended GNRs, and not the kind of tight GNR pellet that was seen with high shape fidelity commercial GNRs which needed 1 hour of sonication to resuspend. It therefore seems unlikely that the use of DIW rather than 0.001 M CTAB is the cause of the different behaviour.

As previously described, DIW is a preferable GNR carrier solution compared to 0.001 M CTAB due to its higher cytocompatibility, and as such DIW and CTAB were compared for use as carrier solution prior to resuspension of GNRs in GelNOR. It was initially hoped that GNRs would retain their surface chemistry to enough of an extent that CTAB coating effect would still be strong enough to discourage aggregation through electrostatic repulsion (Wei, Bai and Fan, 2019), but the free CTAB in solution would be minimised as this is potentially the greatest cause of cytotoxicity (Alkilany *et al.*, 2009). The formation of significant GNR aggregates when DIW was used rather than CTAB resulted in the selection of CTAB as the carrier solution for the rest of the experiments in this chapter, rather than DIW. Though CTAB is mildly cytotoxic as a GNR capping agent (Huff *et al.*, 2007), it is not to such an extent that cytocompatibility considerations inhibit the use of CTAB-capped GNRs for cell culture applications (Mehtala *et al.*, 2014). The citrate-capped synthesis method developed by Jana and colleagues (Jana, Gearheart and Murphy, 2001), on which the Nikoobakht and El-Sayed (Nikoobakht and El-Sayed*, 2003) method was based, was considered as an alternative but not pursued due to a number of disadvantages such as the low GNR yield. Another approach would have been to minimise the effect of the CTAB capping post-synthesis by methods such as surfactant

exchange (Mehtala *et al.*, 2014) or the addition of functional groups to the surface CTAB to minimise toxicity (Wan *et al.*, 2015), but again this was not pursued due to the added complication being judged to be unnecessary when CTAB-capped GNRs are widely used in other cell-culture applications.

The finally optimised GNR incorporation protocol produced gels with minimal GNR aggregated which were well dispersed throughout the gel. It should be noted however that UV-visible absorption spectra did not take into account any effect of the addition of initiators or the act of gelation, and though the TEM images showed minimal aggregation these were taken of very thin samples by necessity. A further additional technique may also have been useful to see the distribution of GNRs in 3D throughout the whole gel such as MicroCT, or by fluorescently tagging the GNRs and imaging the hybrid gels using a confocal microscope.

### 4.4.2  Effect of GNR Encapsulation on the Physical Properties of GelNOR Hydrogels

The cross-sectional microstructure of the gels was qualitatively similar at GNR concentrations of 1.0 mg/ml and below, and this was reflected quantitatively in the lack of significant difference in measured pore size across these concentrations. There was a significant departure from this both quantitatively and qualitatively at 1.5 mg/ml, where the shape and size fidelity of the observed pores is lost completely. Anecdotally, based on the integrity of the gels after fabrication, it was expected that the 1.5 mg/ml hybrid gels would have 100% soluble fraction after swelling, and it was surprising that these gels survived to be tested. This may go some way to explaining the observed loss of microstructure in the 1.5 mg/ml gels.

Though this technique of SEM imaging freeze-dried hydrogel cross-sections is used in the literature to describe hydrogel microstructures (Navaei *et al.*, 2016), it is important to understand exactly what is being shown. The porous texture created by freeze-drying of the hydrogel is actually a product of ice-grain formation during the freezing process, these ice-grains pushing the polymer chains into the inter-granular space, which form a porous network once the ice has been sublimed during freeze-drying (Grenier *et al.*, 2019). As such, the initial structure of the polymer network in the hydrogel is just one contributing factor to the final porous structure after freeze-drying, and factors such as the rate of freezing will possibly have a more significant impact (Kang, Tabata and Ikada, 1999; O'Brien *et al.*, 2004). This final structure, therefore, should not be taken as entirely representative of the

initial structure, and this information should instead be used for comparison between experimental groups based on the assumption that other factors (such as freezing rate, freeze-drying temperature and pressure etc) are controlled for and consistent between groups. As an example, the average mesh size calculated for 10 wt% GelNOR hydrogels crosslinked with DTT at 1:3 NOR:SH ratio was approximately 36 nm when analysed through mass loss and swelling in Chapter 3, which is several orders of magnitude smaller than the average ice grain size of approximately 55 µm measured through ImageJ analysis of SEM cross-section of 0.0 mg/ml gels in this chapter. This magnitude of discrepancy in the calculated mesh size and observed pore size is typical of that observed in the literature (Grenier *et al.*, 2019).

The described mode of action for pore formation being dependent on ice-grain formation dynamics potentially explains the loss of homogenous microstructure at 1.5 mg/ml whilst a degree of homogeneity is retained at lower GNR concentrations. Ice-grain formation is driven by nucleation and growth mechanisms, but is also constrained by interactions between the nanoscale polymer network and the growing ice crystals (Grenier *et al.*, 2019). Tighter polymer networks will therefore start to have an impact on ice-grain growth at a lower ice-grain size than looser networks. Similarly, more homogenous polymer networks will result in more homogenous ice-grain sizes.

Looser polymer networks, past a certain point, may also allow for multiple nucleation sites within a single network pore, resulting in multiple smaller ice-grains in a space otherwise taken by a single large ice-grain, further increasing size variability compared to polymer networks tighter than this point. Very loose polymer networks will also have significantly less ability to constrain crystal growth and will result in occasional outsize ice-grains as well. This explains the extreme size variability and the observation of a pore size range for 1.5 mg/ml gels that spans from sizes smaller than the smallest pore sizes to significantly larger than the largest pore sizes seen in the lower GNR concentration hybrid gels.

As previously mentioned, the extent to which the cross-sectional pore sizes after freeze-drying are a representation of the native polymer network is debateable. This is further highlighted by the fact that there are significant differences in the mass swelling ratios, an indicator of polymer network tightness, between GNR concentrations that do not have significant differences in mean pore size as measured by SEM. That the significant differences observed in mass swelling ratios were not always reflected in

pore size by SEM indicates that the SEM structure may not necessarily reflect differences in wet network structure. Further to this, the cross-section SEM method will see variation in pore size based on the part of the pore that is sectioned (whether the section goes through the widest point or a narrower point), in which pores of exactly the same size could be measured as being different sizes dependant on the part of the pore the section crosses. Because of this, it is difficult to know how much pore size variation to attribute to true variation, and how much is as a result of the section placement.

The differences in mass swelling ratio may also be indicative of low crosslinking efficiency and thus high soluble fractions lost during swelling, as this relationship was explored in the discussion of Chapter 3. Ideally a further full mass loss and swelling study would have been performed to analyse soluble fractions, but these studies are relatively sample intensive and thus were not carried out due to the expense of the GNRs.

As long as the limitations of this technique are acknowledged, and in particular with regard to comparison of absolute pore sizes with values in the literature, then this technique can be used as the basis for comparison between different hydrogels as part of the same experiments. This technique is also useful for comparing observed trends with trends observed in the literature. During similar characterisation experiments Navaei actually saw slightly decreased pore size and swelling ratio in GNR/GelMA hybrid gels at higher GNR concentrations, observations which conflict with the results of the experiments in this chapter (Navaei *et al.*, 2016). This inconsistency in observed properties was also seen during rheological testing.

The apparent loss of microstructure at 1.5 mg/ml as shown in the SEM micrographs corresponds to a significant loss of mechanical strength during rheological testing at the same GNR concentration. This is because the hydrogel microstructure is so badly compromised that it does not resist deformation to the same extent as the more ordered microstructure does in the lower GNR concentration gels. Interestingly however, there is also a significant drop in G' at the 1.0 mg/ml GNR concentration despite the retention of the microstructure as assessed by SEM, though both the 1.0 and 1.5 mg/ml hybrid gels have significantly increased swelling ratios when compared to the 0.0 and 0.5 mg/ml gels. The increase in swelling ratio generally indicates a 'looser' hydrogel polymer network, resulting in lower mechanical stiffness.

The overall trend in mechanical strength was a reduction in both G' and G''
as GNR concentration increased. This was unexpected as it was initially
predicted that loading the GelNOR hydrogels with GNRs would increase the
mechanical stiffness and result in increased G'. This is what was seen by
Navaei (Navaei *et al.*, 2016) when testing hybrid GelMA/GNR hydrogels at
the same GNR concentrations, using GNRs fabricated using the same
method as described by Nikoobakht and El-Sayed (Nikoobakht and El-
Sayed*, 2003), where Young's Modulus increased with GNR concentration
rather than decreased as seen in these experiments.

The first consideration when reconciling the different trends observed in
mechanical stiffness between these experiments and those in the literature
(Navaei *et al.*, 2016) is the difference in characterisation techniques. Whilst
these experiments use rheological characterisation, Navaei used atomic
force microscopy (AFM) (Navaei *et al.*, 2016). AFM is a surface based
technique that involves measuring the material's surface resistance to
indentation, allowing analysis of force vs displacement to give Young's
Modulus (Yoo *et al.*, 2014). In this way, AFM only measures the mechanical
properties at the surface of the gel (the maximum indentation depth used by
Navaei was 4 µm), whereas rheological testing analyses the properties of
the whole construct. This nano-scale indentation head also makes AFM
much more sensitive to local microscale variations in mechanical stiffness,
such as those caused by the presence of clusters of metal nanoparticles.
This type of microscale variation is potentially evident from cross sectional
AFM diagrams in which Navaei saw very high and very low Young's
Modulus measured micrometres apart (Navaei *et al.*, 2016).

AFM may have been chosen by Navaei rather than a technique that
analyses full construct properties because of their use of a 150 µm thick
construct. Though rheology has been used for polymer films in this thickness
range (Schawe, Possart and Krogh, 2016) there is little in the literature
describing rheological testing of hydrogels at this thickness. As a result AFM
may have been chosen due to limited other options.

Whilst the use of 150 µm thick constructs limits the range of possible
mechanical characterisation techniques, it does have the considerable
advantage of reducing the light absorbance through the construct of the
suspended GNRs. The light absorbance of GNRs will have a knock-on effect
on the efficiency of a crosslinking system that relies on either visible or UV
light, and by reducing the construct thickness to 150 µm the disruption of
crosslinking is kept to a minimum. Whilst it was initially hoped that due to the

step-growth polymerisation system used in GelNOR hydrogels (rather than chain growth in GelMA), and the equal performance at low curing times in terms of Young's Modulus and soluble fraction seen in Chapter 3, that the effect of GNR light absorbance would be minimised. Based on the results of the rheological testing and the SEM cross sections however, it seems that the GNRs have had a significant effect to disrupt the crosslinking, as evidenced by the significant reductions in G' at higher GNR concentrations, and the apparent loss of microstructure at the highest GNR concentration of 1.5 mg/ml. Further, the relatively small, but statistically significant, increases in swelling ratio may be an indicator of increased soluble fraction and thus reduced crosslinking efficiency as this relationship has previously been described in Chapter 3, however this is difficult to say for sure without full mass loss and swelling studies. As a result, it is impossible to say for sure whether the drop in modulus at higher GNR concentrations is due to a reduction in crosslinking efficiency or some other influence that the GNR concentration has on the hydrogel microstructure.

A further consideration as to the negative effect the suspended GNRs may have on light penetration is the wavelength of the light used. This project used a visible light system with wavelength of 400 – 450 nm, but Navaei actually used an unusually high wavelength range of 360 – 480 nm for the normally UV-light initiated i2959 (Navaei *et al.*, 2016). To account for this unusually high wavelength, Navaei used an extremely high irradiation intensity of 800 mW/cm$^2$ (assuming that is what was meant by 800 mW) and increased the irradiation time with GNR concentration to account for potential absorption. This inconsistent irradiation time may in fact partially account for the tighter network and higher modulus in the higher GNR concentration gels, as longer irradiation times would be expected to produce stiffer gels in chain growth hydrogels such as the GelMA used by Navaei (Lim *et al.*, 2016).

As well as analysing the rheology moduli for comparison of mechanical properties between GNR concentrations at a single frequency, there is also the behaviour of the gels across the full frequency sweep to consider.

As previously described, the general trend for all GNR concentrations analysed with rheological testing was for G' and G'' to plateau across the lower frequencies and start to converge with increasing frequency before sharply crossing over and recovering. After the crossover point the G' then recovers but the G'' sees a large drop off, after which point both G' and G'' increase to the final frequency point.

Initially this behaviour appears to be a breaking of network microstructure and the gel yielding, resulting in a phase shift from gel to sol-gel, before an immediate recovery. This is a particularly unusual behaviour, and further examination of the loss factor across the frequency sweep helps to explain the observed data.

The sudden spike and then drop in loss factor, at the crossover point, to a value so close to zero is an indicator that this is likely an artefact. Although a more elastic response may be expected at higher frequencies, a loss factor this close to zero means that the hydrogel is behaving almost perfectly elastically, which is very unlikely. Further discussion with the rheometer manufacturer suggests that this is an artefact of the chosen measuring system rather than a true behaviour of the material.

It is likely that the artefact seen is due to a problem inherent with the measuring system used. When operating a rheometer at high frequencies, larger diameter geometries are generally preferred. This is because the shear strain percentage is taken relative to the working gap, meaning that for a 5% shear strain and an 800 µm working gap, the circular rotation will equal 40 µm at the geometry circumference. This means that for an 8 mm diameter geometry the rheometer drive shaft must rotate 0.57 degrees, but for a 25 mm diameter geometry the drive shaft must only rotate 0.18 degrees. This means that the geometry must move approximately 315% the rotation to achieve the same shear strain when using an 8 mm geometry as compared to a 25 mm geometry.

At the higher frequencies this extra rotation becomes a problem because the combination of the frequency and the distance the drive shaft must move mean that the adjustment and measurement speed required to achieve these constraints is outside the system's capability.

The fact that the artefact behaviour happens at lower frequency for weaker gels (and becomes less pronounced in very weak gels) suggests that there is some role played by the sample material characteristics in deciding the point at which the required test constraints move outside of the measurement system capability. Ultimately, however, the artefact is caused by a limitation of the chosen measurement geometry.

To keep the maximum speed within the capability of the rheometer would require the use of a 25 or 50 mm geometry rather than the chosen 8 mm geometry. However, these larger geometries would require a corresponding higher sample volume, which due to the nature of the GNR/GelNOR hybrid

hydrogels makes geometries of this size unsuitable. As an example, optimisation experiments carried out with the 25 mm geometry required between 10 – 20 times larger sample volume per test, making the use of GNRs at the concentrations tested in these experiments financially unfeasible.

An alternative method of reducing the distance of travel for the rheometer is to decrease the working gap used, as this is the dimension that the shear stain percentage is taken relative to. This would create a different problem however, in that it would increase the initial axial loading on the sample before the test starts. This would act to compress the material and increase the density of the hydrogel polymer network being tested, so increasing the materials stiffness and resulting in measurement of higher characteristic moduli. The sample is already compressed to 20% axial strain (800 µm from a 1 mm mould), before swelling is taken into account, in order to ensure no empty space is left under the rheometer head. This working gap was chosen as a balance between a larger gap which would axially compress the sample less but exacerbate the previously described problem with large shear displacement, and a smaller gap which would reduce the required shear displacement but increase compression and correspondingly cause an increase in measured moduli.

A possible source of error in this method, however, is the different swelling ratios of the hybrid hydrogels between the different GNR concentrations. Those with higher swelling ratios will undergo a larger percentage of axial compression when loaded into the rheometer at the same working gap. Though these differences are likely to be relatively small (in the order of a few percent), the use of a set working gap distance will cause some artificial inflation of the G' values in samples with greater swelling ratios. An alternative method to set the working gap would be to measure the height of each sample and set the rheometer working gap to a value equal to, for example, 10% compression, which would ensure an equal compression of each sample in terms of percentage strain. The trade-off with this method is that the different working gap distance will result in an inconsistent shear displacement during testing.

The use of a fixed 800 µm working gap from a 1 mm mould is consistent with the sample loading approach of Munoz (Mũnoz *et al.*, 2014) when rheologically characterising GelNOR hydrogels, but with the difference that Munoz punched 8 mm diameter holes out of a larger hydrogel sheet, an approach which would be unsuitable for GNR/GelNOR hybrid hydrogels for

the reasons previously described. Though Munoz also used an 8 mm diameter geometry, they used amplitude sweeps rather than frequency sweeps and compared their samples in the LVER. Despite these two different approaches, the when the G' for 5 wt% gels was tested (data not shown) the 330 +- 23 Pa observed was a reasonable match for the 429 +- 10 Pa seen for GelNOR rheological testing by Munoz (Mũnoz *et al.*, 2014). This is likely because at the actual comparison point, the shear strain and frequency will have been very similar or equal, as Munoz (Mũnoz *et al.*, 2014) performed the amplitude sweep between 0.1 – 5% and the frequency sweep used in these experiments was performed at 5% amplitude. Though Munoz (Mũnoz *et al.*, 2014) don't detail what frequency their amplitude sweep was performed at, the G' measured in the experiments in this chapter was very stable across the frequency sweep between 0.1 – 10 rad/s.

The results at the higher end of the frequency sweep would have provided novel data on the behaviour of GelNOR hydrogels and GNR/GelNOR hybrid hydrogels, as to whether they behaved in Newtonian or non-Newtonian fashion. Previous high frequency rheological characterisation of gelatin hydrogels has mainly focused on their liquid or physical gel form due to their potential for application as bio-inks in 3D bioprinting (Tigner *et al.*, 2020). To date there is little in the literature as to the high frequency behaviour of chemically crosslinked forms of gelatin hydrogels. Though this data would have been novel and interesting, it is not pivotal to the progression of this project and comparison at 1 rad/s can be used as part of a decision on which GNR concentration to take forward.

### 4.4.3 Effect of GNR Encapsulation on the Electrical Properties of GelNOR Hydrogels

In line with what was expected, the electrical impedance of the hybrid hydrogels decreased with increasing GNR concentration.

The decision to compare impedance at higher frequencies (above 100Hz with single point comparison at 10,000 Hz) was taken because of the tendency for capacitance to dominate at lower frequencies, as evidenced by the phase angle rising and remaining at 90 degrees, and the constant increase in resistance with decreasing frequency. The capacitance behaviour was likely as a result of double layer capacitance due to the gels being made with PBS, which has a high salt content, and double layer capacitance can also have an extra resistive effect (Lück and Latz, 2019). Because the goal of the EIS testing was to determine the impedance and/or resistance of the gel to electrical current, this testing was concerned with electron transfer through the gel and no other behaviour. As a result, though the capacitance behaviour may have been interesting to analyse for different applications, efforts were made to reduce the impact of capacitance on the data and this also included using admittance plots to find absolute resistance in a way that was independent of any capacitance.

A similar approach was also taken by Navaei, who only compared impedance at frequencies above 20 Hz (Navaei *et al.*, 2016). A similar trend was seen by Navaei at lower frequencies, in that impedance increased exponentially with decreasing frequency below approximately 500 Hz, and may explain the decision not to continue the impedance spectrum any lower than 20 Hz. Though this rise is likely also due to capacitance behaviour, Navaei do not also show phase angle and so this cannot be stated for sure.

Though Navaei did not detail the results of any statistical analyses used to compare impedance data (instead taking all GNR concentrations through to cell culture), the EIS results did follow a similar trend, in that impedance decreased with increasing GNR concentration. Interestingly, Navaei saw a much smaller drop in impedance than was seen in these experiments between the 0.0 and 0.5 mg/ml GNR concentrations. In the EIS experiments in this chapter, the largest drop in impedance was seen between the 0.0 and 0.5 mg/ml concentrations. This was also followed for Navaei by much larger drops between 0.5 and 1.0 mg/ml and 1.0 and 1.5 mg/ml than the impedance drops that were seen in the experiments in this chapter (Navaei *et al.*, 2016).

This difference in the rate of impedance drop between each GNR concentration is not readily explainable, and the differences in the absolute measured impedance values are also very noteworthy. At 10,000 Hz, a point where the impedance spectra of both the GelMA tested by Navaei and the GelNOR tested in this chapter are in a plateau, the impedance of approximately 1800 Ω seen in GelMA is more than three times larger than the 533 Ω seen in GelNOR. This is despite the use of samples that were 150 µm thick with diameter of approximately 10 mm, as opposed to the thickness of 1 mm and diameter of 5 mm used in this chapter which would logically result in higher resistance based on construct shape alone.

There are a number of possible explanations for the discrepancy in measured values between Navaei and the experiments in this chapter, and include aspects of the experimental set up as well as true differences in the measured gels.

Firstly, the EIS set-up used by Navaei was not described in detail, *"For impedance analysis, hydrogel constructs were located between two indium tin oxide (ITO) coated glass slides (Sigma-Aldrich) with an AC bias sweeping (Agilent 4284A LCR meter) from 20 Hz to 1 MHz"* (Navaei *et al.*, 2016). This means that there may have been a number of differences in EIS set-up between Navaei and the work in this chapter. One possible example is the surface resistivity of the ITO slides. The experiments in this chapter used the lowest available surface resistivity ITO slides and deliberately minimised the distance between the ITO-crocodile clip interface and the tested hydrogel. If (Navaei *et al.*, 2016) used higher resistance ITO and larger distances between the EIS machine interface and the measured samples, this could have had an effect on the measured impedance. Similarly, the quality of connections used between the ITO and the EIS equipment may have made a difference. Though both of these aspects would likely have had an effect, it is unlikely that they would account for the large gap in measured impedances alone.

Possibly the largest difference in experimental set-up is the type of equipment used. Whereas the experiments in this chapter used a potentiostat, Navaei used an LCR meter. Though both of these instruments are similar in that they measure the same things – inductance, capacitance, and resistance, there are also fundamental differences in the way that these instruments analyse overall impedance. Further to this, Navaei don't detail the potential that their impedance measurements are performed at, and use

of an amplitude significantly different to the ± 0.1 V used in these experiments may have had a significant effect on measured impedance.

This difference in equipment and possible differences in used potentials are the experimental factors most likely to cause significant differences in measured impedance between Navaei and the experiments in this chapter.

Alternative options for measuring hydrogel impedance used widely in the literature are the 4-point probe method (Kaklamani *et al.*, 2018) and techniques such as electrostatic force microscopy (EFM) and scanning surface potential microscopy (SSPM) which use atomic force microscopes (Tararam *et al.*, 2017). These options were considered but decided against in favour of EIS, due to the ability of EIS to measure the full construct, as opposed to the measurement of surface properties provided by 4-point probe, EFM and SSPM.

The alternative explanation to differences in the experimental set-up is the possibility that GelNOR is three times less electrically impeding than GelMA, despite the previously mentioned differences in sample shape. This is made less likely however, by the findings of Shin and colleagues who saw resistance of approx. 750 $\Omega$ in the high frequency plateau part of their EIS spectrum of pure GelMA hydrogel (Shin *et al.*, 2013). This value was achieved using sample thickness equal to Navaei, though Shin and colleagues do not detail their sample diameter, test potential, or EIS equipment (Shin *et al.*, 2013; Navaei *et al.*, 2016). Further to this, Shin also saw a similar increase in resistance due to capacitance at lower frequencies, but the frequency this increase begins at is much higher than for either Navaei or the experiments in this chapter. It is also worth noting the large error bars in Navaei's data for the 0.0 -1.0 mg/ml hybrid gels and the lack of any statistical comparison making their results less reliable, as well as an unexplained drop in impedance at the high end of the frequency spectrum for the 0.0 and 0.5 mg/ml hybrid gels but not 1.0 or 1.5 mg/ml (Navaei *et al.*, 2016), which is also absent for Shin (Shin *et al.*, 2013).

There is currently nothing in the literature analysing the electrical properties of GelNOR hydrogels, so there are currently no available reference values to compare against.

### 4.4.4  Selection of GNR/GelNOR for Electrical Stimulation Cell Culture Experiments

At the highest GNR concentration of 1.5 mg/ml, despite being the most electrically conductive option the gel microstructure is severely compromised by the GNR addition and this is reflected in the greatest loss of microstructure and mechanical strength. A similar loss of mechanical strength is also seen at the 1.0 mg/ml GNR concentration. This is not completely reflected by the microstructure analysis, in which the pore size and swelling ratio is slightly increased compared to the native gel, but is comparable. On the basis of the significant loss of mechanical strength alone, however, the 1.0 and 1.5 mg/ml hybrid GNR/GelNOR gels were discounted from being taken forward to cell culture as this was taken to indicate that, at these high concentrations, the GNR addition disrupted the formation of the hydrogel microstructure. This decision was further supported by the 0.5 mg/ml GNR/GelNOR hybrid gels experiencing no significant loss of mechanical properties whilst still being significantly more electrically conductive than the GelNOR hydrogel alone.

## 4.5 Conclusions

The aims of this chapter were threefold: to optimise a GNR fabrication, storage, and encapsulation protocol that would allow reproducible dispersion of GNRs in GelNOR hydrogel, to determine the effect of GNR encapsulation on the physical properties of GelNOR hydrogels, and to select a GNR/GelNOR hybrid hydrogel to take into final cell culture experiments.

This experiments in this chapter allowed the successful development of a protocol for reproducible homogenous suspension of GNRs in GelNOR hydrogel, and determined that CTAB capped self-fabricated GNRs performed better for this application than commercially purchased citrate capped GNRs. Further, the characterisation experiments carried out in this chapter allowed selection of a final GNR/GelNOR hybrid hydrogel to take into the final cell culture experiments. The 0.5 mg/ml GNR concentration was selected on the basis of improved electrical properties with minimal disruption of physical characteristics and performance.

## Chapter 5
## Development of a 3D Co-Culture System

## 5.1 Introduction and Aims

The field of tissue engineering is highly diverse, and spans across a number of different treatment areas. It is also highly multidisciplinary but can generally be thought to contain three key aspects: the use of regenerative cells, the use of a materials scaffold to support the cells, and the use of bioactive molecules such as cytokines and growth factors to direct the cells in formation of the desired tissue (de Isla *et al.*, 2010).

With respect to bioactive molecules, there are a number of different approaches to directing cells with bioactive molecules for tissue engineering applications. Though the most commonly used method of stimulating cells with bioactive molecules *in-vitro* is via supplementation of the cell culture medium, there are pitfalls to this method. Whereas *in-vitro* it is easy to replenish the levels of target bioactive molecules with each media change, this is not possible *in-vivo*. Approaches to delivery of the desired molecules in a similar intermittent manner *in-vivo* may be achieved by oral delivery, however this delivery route is less targeted to the implant site (Xu *et al.*, 2020). As well as this, a weakness of intermittent supplementation both *in vitro* and *in vivo* is a difficulty maintaining the concentration of the bioactive molecule in the therapeutic window, rather than having concentrations too high immediately after delivery and too low in the period leading up to replenishment (Sood and Panchagnula, 2003). An example of this is shown in Figure 5.1.
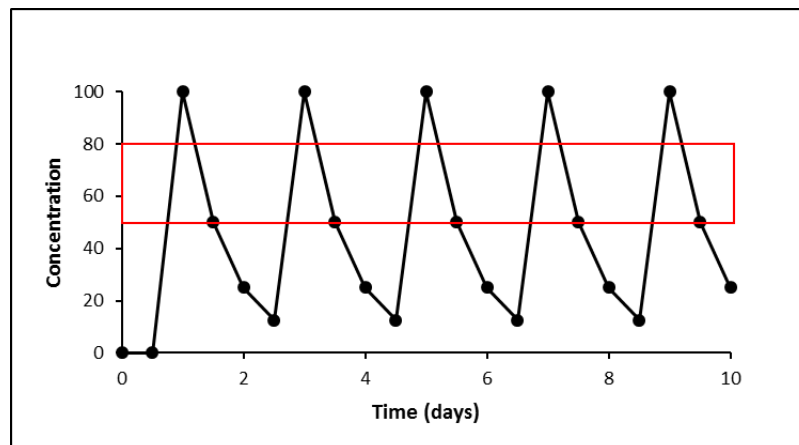


**Figure 5.1 – Example of rise and fall through therapeutic window (red) of bioactive molecule concentration during degradation and intermittent replenishment of a bioactive molecule.**

In order to overcome the described problems with keeping bioactive molecule concentrations in the target range, a number of alternative approaches to bioactive molecule supplementation have been described. These approaches instead use controlled release strategies to keep the desired bioactive molecules at the target concentration without the need for active replenishment. These strategies often involve the controlled release of bioactive molecules from specially designed smart materials, such as polymers with drug compounds covalently bonded, which are released as the polymer degrades (Rashidi *et al.*, 2010). In this way, tissue engineering strategies can be designed by combining two of the three previously described aspects of tissue engineering, in this case bioactive molecules and materials.

An alternative to this approach is to combine the bioactive molecule aspect of tissue engineering with the cellular aspect, and use one cell type to control the behaviour of another cell type in co-culture. In this approach, the bioactive molecules secreted by one cell type directs the behaviour of another cell type, such as the use of fibroblast cells to stimulate HUVEC cells to form capillary networks through the secretion of VEGF and bFGF (Nishiguchi *et al.*, 2014). This approach also raises the possibility of using cells in the tissue engineering construct, not to create the desired tissue themselves, but to direct the endogenous cellular response after implantation. This may be a particularly useful approach in SCI repair due to the multi-faceted response required to treat SCI (Yamamoto *et al.*, 2014) and the number of different cell types and complex structures that make up the central nervous system. Further to this is the relatively poor availability of neural precursor cells such as NSCs for transplantation (Zhang *et al.*, 2016), and the fact that primary neurons are difficult to expand to therapeutically relevant populations in culture due to mature neurons not undergoing cell division (Gordon, Amini and White, 2013), even if a suitable source can be found. For these reasons, instead of implanting a tissue engineering construct containing numerous different cell types that aims to closely replicate the native tissue structure, it may be better to implant a single cell type that is able to direct the cellular response of multiple different cell types at the injury site.

As well as *in-vivo* applications, this approach may also be advantageous *in-vitro* when creating models of the spinal cord, central nervous system, or the blood brain barrier, where again there are numerous different cell types to consider.

The PC12 cell line is derived from a rat pheochromocytoma and is commonly used in neural models because they exhibit a number of features of mature dopaminergic neurons (Wang *et al.*, 2015). The popularity of the PC12 cell line is largely due to its versatility and ease of culture (Wiatrak *et al.*, 2020). Further to this, the fact that the PC12 cell line has been used extensively in various areas of neurobiology research means that it is well characterised, with a large amount of background knowledge on their proliferation and differentiation (Wiatrak *et al.*, 2020).

Stimulation of neurite outgrowth in PC12 cells has previously been demonstrated using a number of different bioactive molecules, most commonly neurotrophic factors such as NGF (Greene and Tischler, 1976). As well as neurotrophic factors other molecules such as bFGF (Rydel and Greene, 1987) have also been used, and it is this particular molecule that identifies PC12 cells as being possibly suitable for differentiation stimulated by nHDF cells, which as previously described, secrete bFGF *in-vitro*. Though it has not previously been described in the literature, this would identify nHDFs as a possible readily available cell type to co-culture with PC12 cells for *in-vitro* studies requiring neurite outgrowth, with the previously described advantages of stimulating neurite outgrowth through co-culture rather than media supplementation with growth factors. Further, the ability of nHDF cells to also stimulate capillary formation in HUVEC cells (Costa-Almeida *et al.*, 2015) may mean that nHDFs would be a suitable cell type to stimulate both capillary formation in HUVECs and neurite outgrowth in PC12s simultaneously. Stimulation of differentiation in both PC12 and HUVEC cells simultaneously through co-culture has not been previously described in the literature, and would be a novel approach that would contribute towards modelling of the blood brain barrier (BBB). Co-culture may also be a particularly effective way to differentiate PC12s due to the relatively fast half-life of both bFGF and NGF (Wu *et al.*, 2018).

A number of studies that have previously used 3D co-culture with nHDFs to stimulate differentiation in HUVEC cells, such as that demonstrated by Naka and colleagues (Naka *et al.*, 2020), have used fibrin hydrogels. These hydrogels are based on the reaction between thrombin and fibrinogen, in which thrombin cleaves fibrinopeptide A from within the fibrinogen Aα-chains to produce fibrin (Mosesson, 2005). The produced fibrin monomer then self-associates to form insoluble fibrin hydrogel (Shirwaiker, Purser and Wysk, 2014). These gels are highly tuneable through manipulation of fibrinogen and thrombin concentrations and can also incorporate different bioactive

peptides and growth factors to alter hydrogel functionality (Ahmed, Dare and Hincke, 2008).

Though the end goal of this project was to use the hybrid GNR hydrogels based on GelNOR that were developed in the previous chapters, a decision was made to use fibrin hydrogels for the development of the co-culture in this chapter as a stepping stone between previously published work and the final goal of this project.

The aim of this chapter is to investigate the potential of nHDFs to stimulate differentiation of PC12s in 3D co-culture using fibrin hydrogels. This is to be achieved through completion of the following objectives:

1. Test the ability of nHDFs to stimulate neuronal differentiation in PC-12 cells in 3D co-culture, using fibrin hydrogels.
2. Optimise 3D co-culture conditions .
3. Test the ability of nHDFs to stimulate simultaneous neuronal differentiation in PC-12 cells and capillary formation in HUVEC cells in 3D co-culture.

## 5.2 Methods

### 5.2.1 Cell Culture

HUVEC, nHDF, and PC12 cells were recovered from cryostorage as detailed in section 2.2.4.1. HUVEC cells were then cultured as described in section 2.2.4.6 and nHDFs as in section 2.2.4.5. PC12s were cultured as in section 2.2.4.8, with the exception that the culture media used was the same complete DMEM as used for the nHDF cells.

The HUVECs used in the experiments described in this chapter were used between passage 6-8, the PC12s between passage 3-6, and the nHDFs between passage 10-12.

### 5.2.2 Fluorescent Labelling of Live Cells Using CMFDA

CellTracker Green™ CMFDA (5-chloromethylfluorescein diacetate) is a cell-tracing dye. CMFDA is non-fluorescent and passes freely through the cell membrane, upon which the CMFDA is activated by intracellular enzymes and fluoresces. CMFDA's chloromethyl group then reacts with thiol-containing proteins inside the cell, meaning that the fluorescent probe is unable to leave and 'tags' the cell (Lulevich *et al.*, 2009). This fluorescent probe is then passed to daughter cells but cannot be passed to adjacent cells in a population.

Cells were labelled with CellTracker Green™ approximately 16 hours before being used in experiments. CellTracker Green™ was dissolved in DMSO to a concentration of 10mM, before being diluted to a 10 µM working solution using cell culture media. For HUVEC cells the working solution dilution was performed using EGM without FBS.

The tissue culture flasks containing HUVECs were taken out of the incubator and the media was removed. The cells were then washed once with PBS and the CellTracker Green™ working solution was added. The HUVECs were then incubated in the CellTracker Green™ working solution for 30 minutes at 37 °C. After 30 minutes the CellTracker Green™ solution was removed and replaced with fresh complete EGM, and the cells were incubated at 37 °C until use.

### 5.2.3 Fibrin Hydrogel Preparation

Fibrinogen powder was dissolved in DMEM medium containing 1% Pen/Strep but no FBS at a concentration of 20 mg/ml.

Thrombin powder was dissolved in DMEM medium containing 1% Pen/Strep but no FBS at a concentration of 10 units/ml.

Sterile pre-homogenised collagen microfibres were prepared as described by Naka and colleagues (Naka *et al.*, 2020) and were received pre-prepared from the Matsusaki Group. These collagen microfibres were dissolved in in DMEM medium at a concentration of 15 mg/ml.

### 5.2.4  nHDF and HUVEC Co-Culture

Initially, the ability of nHDFs to stimulate tube formation in HUVEC cells in nHDF/HUVEC co-culture, as described by Costa-Almeida and colleagues (Costa-Almeida *et al.*, 2015), was tested. The day before the experiment the HUVECs were labelled with CellTracker Green™ Green as described in section 5.2.2.

On the day of the experiment HUVEC and nHDF cells were trypsinised and counted as described in section 2.2.4.3. Appropriate numbers of each cell type to give a seeding density of 5 million cells/ml and a HUVEC:nHDF ratio of 1:2 were combined and centrifuged at 1,200 rpm for 5 mins. The supernatant was then removed and the pellet resuspended in thrombin solution which was kept in the incubator at 37 °C until use.

Separately, 10 μl of collagen microfibre solution was combined with 10 μl of fibrinogen solution. This was then added to 10 μl of thrombin/cell solution and rapidly mixed before being pipetted onto a 35 mm Petri dish in a single 'drop'. This drop was then left untouched for 5 minutes before being transferred to an incubator at 37 °C for a further hour.

After an hour, the resulting gels were then immersed in culture media composed of equal parts complete DMEM and complete EGM as described in sections 2.2.4.5 and 2.2.4.6, and media was changed every 2 days throughout the experiment. The HUVECs were visualised through confocal microscopy, with CellTracker Green™ imaging on day 0, 4, 8, and 12, and CD31 staining, as described in section 5.2.7, and imaging on day 7 and 14.

### 5.2.5  nHDF and PC12 Co-Culture

The ability of nHDFs to stimulate differentiation in PC12 cells was tested in an nHDF/PC12 co-culture model.

On the day of the experiment PC12 and nHDF cells were trypsinised and counted as described in section 2.2.4.3. Appropriate numbers of each cell type to give a seeding density of 5 million cells/ml and nHDF:PC12 ratios of 1:1 or 2:1 were combined and centrifuged at 1,200 rpm for 5 mins. The

supernatant was then removed and the pellet resuspended in thrombin solution which was kept in the incubator at 37 °C until use.

Separately, 10 µl of collagen microfibre solution was combined with 10 µl of fibrinogen solution. This was then added to 10 µl of thrombin and cell solution and rapidly mixed before being pipetted onto a 35 mm Petri dish in a single 'drop'. This drop was then left untouched for 5 minutes before being transferred to an incubator at 37 °C for a further hour.

PC12 only gels were also prepared to act as negative controls and show that it was indeed the action of the nHDFs that stimulated PC12 differentiation.

The resulting gels were then immersed in complete DMEM culture media as described in section 2.2.4.5, and media was changed every 2 days throughout the experiment. The PC12s were visualised through confocal microscopy and β-III Tubulin staining as described in section 5.2.8 on day 7 and 14.

## 5.2.6  nHDF and PC12 and HUVEC Co-Culture

The ability of nHDFs to stimulate differentiation of both HUVEC and PC12 cells simultaneously at a range of cell densities was tested in an nHDF/HUVEC/PC12 co-culture model.

On the day of the experiment PC12, HUVEC and nHDF cells were trypsinised and counted as described in section 2.2.4.3. Appropriate numbers of each cell type to give a seeding density of 5 million cells/ml and nHDF:HUVEC:PC12 ratios of 1:0.5:1, 1:0.5:0.5 or 1:0.5:0.1 were combined and centrifuged at 1,200 rpm for 5 mins. The supernatant was then removed and the pellet resuspended in thrombin solution which was kept in the incubator at 37 °C until use.

Separately, 10 µl of collagen microfibre solution was combined with 10 µl of fibrinogen solution. This was then added to 10 µl of thrombin and cell solution and rapidly mixed before being pipetted onto a 35 mm Petri dish in a single 'drop'. This drop was then left untouched for 5 minutes before being transferred to an incubator at 37 °C for a further hour.

Gels containing HUVECs and PC12s at a ratio of 1:1 without nHDFs were also fabricated to act as negative controls and show that it was indeed the action of the nHDFs that stimulated HUVEC and PC12 differentiation.

The resulting gels were then immersed in culture media composed of equal parts complete DMEM and complete EGM as described in sections 2.2.4.5 and 2.2.4.6, and media was changed every 2 days throughout the

experiment. The PC12s and HUVECs were visualised through confocal microscopy and combined CD31 and β-III Tubulin staining as described in section 5.2.9 on day 7 and 14. For one group of gels at nHDF:HUVEC:PC12 ratio of 1:0.5:0.5, NGF was also added to the culture media at a concentration of 100 ng/ml to act as a positive control for PC12 differentiation.

Gels containing nHDF/HUVECs only at a ratio of 2:1 were also fabricated and stained using the combined CD31 and β-III Tubulin staining method described in section 5.2.9 to act as a negative control to the β-III Tubulin stain.

### 5.2.7  CD31 Immunostaining

On the assay day, gels were removed from the incubator and culture media was removed. The gels were then washed twice in PBS before being fixed in paraformaldehyde phosphate buffer solution (PFA) for 15 minutes. The PFA was then removed and the gels were washed twice with PBS before being detached from the culture surface. The gels were then submerged in in PBS with 0.2% v/v Triton-X and left for two hours. The PBS with Triton-X was then removed and the gels were washed twice with PBS before being submerged in PBS with 1% w/v bovine serum albumin (BSA-PBS) and left for a further 1 hour. The BSA-PBS was then removed and the gels were washed twice with PBS. The primary antibody was then added, which was a solution of mouse anti-CD31 (10 µg/ml) in BSA-PBS, and the gels were incubated for 16 hours at 4 °C.

The primary antibody solution was then removed and the gels were washed twice in PBS. The secondary antibody solution was then added, this solution contained both goat-anti-mouse Alexa Fluor 647 (20 µg/ml) and Hoescht nuclear stain (1 µg/ml), in BSA-PBS. The gels were left submerged in secondary antibody stain solution for 2 hours at 4 °C. The stain solution was then removed, the gels were washed twice in PBS, then submerged in PBS and placed on a rocker table for 2 hours.

After 2 hours the PBS was replaced with fresh PBS, and the gels were imaged using a confocal microscope.

### 5.2.8  β-III Tubulin Immunostaining

On the assay day, gels were removed from the incubator and culture media was removed. The gels were then washed twice in PBS before being fixed in paraformaldehyde phosphate buffer solution (PFA) for 15 minutes. The PFA was then removed and the gels were washed twice with PBS before being

detached from the culture surface. The gels were then submerged in in PBS with 0.2% v/v Triton-X and left for two hours. The PBS with Triton-X was then removed and the gels were washed twice with PBS before being submerged in 1% w/v BSA-PBS and left for a further 1 hour. The BSA-PBS was then removed and the gels were washed twice with PBS. The primary antibody was then added, which was a solution of rabbit anti-β-III tubulin (5 μg/ml) in BSA-PBS, and the gels were incubated for 16 hours at 4 °C.

The primary antibody solution was then removed and the gels were washed twice in PBS. The secondary antibody solution was then added, this solution contained both chicken-anti-rabbit Alexa Fluor 488 (10 μg/ml) and Hoescht nuclear stain (1 μg/ml), in BSA-PBS. The gels were left submerged in secondary antibody stain solution for 2 hours at 4 °C. The stain solution was then removed, the gels were washed twice in PBS, then submerged in PBS and placed on a rocker table for 2 hours.

After 2 hours the PBS was replaced with fresh PBS, and the gels were imaged using a confocal microscope.

## 5.2.9 Combined CD31 and β-III Tubulin Immunostaining

On the assay day, gels were removed from the incubator and culture media was removed. The gels were then washed twice in PBS before being fixed in paraformaldehyde phosphate buffer solution (PFA) for 15 minutes. The PFA was then removed and the gels were washed twice with PBS before being detached from the culture surface. The gels were then submerged in in PBS with 0.2% v/v Triton-X and left for two hours. The PBS with Triton-X was then removed and the gels were washed twice with PBS before being submerged in 1% w/v BSA-PBS and left for a further 1 hour. The BSA-PBS was then removed and the gels were washed twice with PBS. The primary antibody solution was then added, which was a solution containing both mouse-anti-CD31 (10 μg/ml) and rabbit-anti-β-III tubulin (5 μg/ml) in BSA-PBS, and the gels were incubated for 16 hours at 4 °C.

The primary antibody solution was then removed and the gels were washed twice in PBS. The secondary antibody solution was then added, this solution contained goat-anti-mouse Alexa Fluor 647 (20 μg/ml), chicken-anti-rabbit Alexa Fluor 488 (10 μg/ml), and Hoescht nuclear stain (1 μg/ml), in BSA-PBS. The gels were left submerged in secondary antibody stain solution for 2 hours at 4 °C. The stain solution was then removed, the gels were washed twice in PBS, then submerged in PBS and placed on a rocker table for 2 hours.

After 2 hours the PBS was replaced with fresh PBS, and the gels were imaged using a confocal microscope.

## 5.3 Results

### 5.3.1 The Ability of nHDFs to Stimulate Differentiation of HUVEC Cells

Initially, the ability of nHDFs to stimulate differentiation and tube formation in HUVEC cells was tested in nHDF/HUVEC 3D co-culture (Figure 5.2).
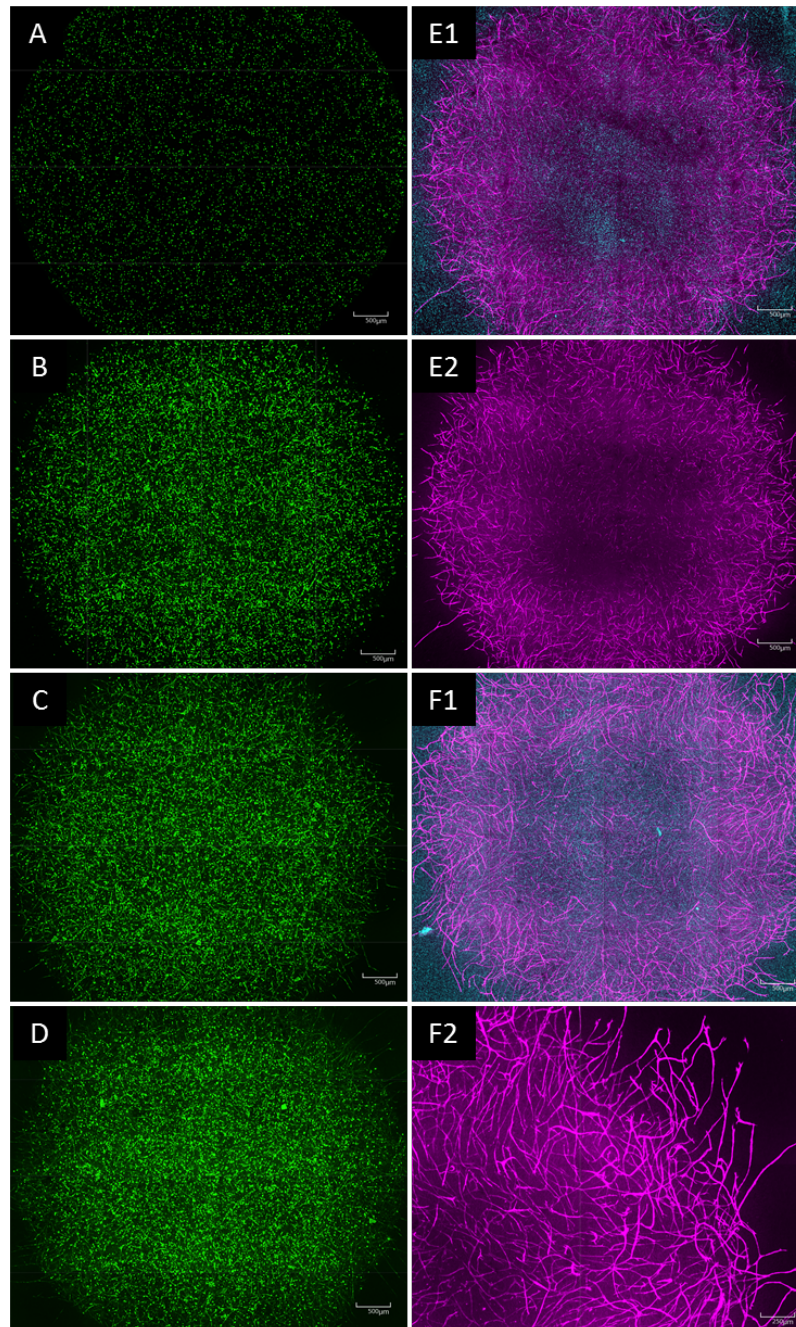


**Figure 5.2 – Fluorescence images of nHDF/HUVEC 3D co-culture at a 2:1 ratio in fibrin hydrogel.** Cells were stained with CellTracker Green(TM) Green at (A) day 0, (B) day 4, (C) day 8, (D) day 12, and CD31 immunostain counterstained with Hoescht at (E1) day 7 and (F1) day 14, and CD31 only at (E2) day 7 and (F2) day 14.

The results show that nHDFs were successful in stimulating differentiation of HUVEC cells in co-culture, as evidenced by the elongation and tube formation seen in the CellTracker Green™/CD31 stained HUVEC cells.

CellTracker Green™ staining demonstrated the elongation of HUVEC cells from arounded morphology at day 0, becoming progressively more elongated and forming networks as time in culture increased.  Complex capillary networks were seen by the day 7 timepoint with CD31 staining, and though the capillary networks were slightly more dense by day 14, the majority was achieved by day 7.

Nuclei staining with Hoescht also allowed visualisation of the nHDFs, from which it could be seen that the nHDFs were able to migrate outside of the hydrogel and onto the surface of the Petri dish due to the presence of Hoescht staining but no CD31.

### 5.3.2  The Ability of nHDFs to Stimulate Differentiation in PC12 Cells

The ability of nHDFs to stimulate differentiation and neurite outgrowth in PC12 cells was then assessed in 3D co-culture (Figure 5.3).
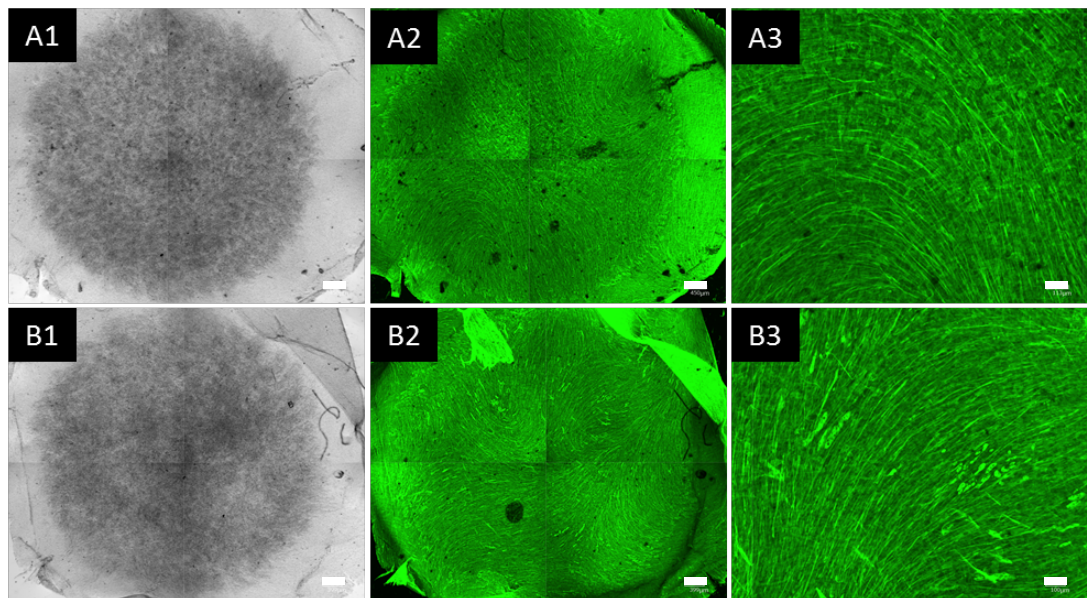


**Figure 5.3 – Brightfield and immunofluorescent images of nHDF/PC12 3D co-culture.** Cells were cultured at a 1:1 ratio of nHDF:PC12 (A1) brightfield imaging and (A2, A3) fluorescence imaging of β-III tubulin immunostain, and at a 2:1 ratio of nHDF:PC12 using (B1) brightfield imaging and (B2, B3) fluorescence imaging of β-III tubulin immunostain. Cells were cultured in 3D in fibrin hydrogel. Images taken at day 14. *(Scale bars – A1, B1, B2 = 400 µm, A2 = 450 µm, A3 = 110 µm, B3 = 100 µm)*

The results of the nHDF/PC12 co-culture showed that nHDFs were also capable of stimulating differentiation and neurite outgrowth in PC12 cells. This is evidenced by the presence of neurites from cell bodies that stain with β-III tubulin.

Though negative control gels containing PC12 cells only were also set-up, the PC12 only culture caused the fibrin hydrogels to disintegrate so rapidly that they were not able to be imaged at the day 7 timepoint.

### 5.3.3 The Ability of nHDF to stimulate differentiation in PC12 and HUVEC Cells in Co-Culture

The ability of nHDFs to stimulate differentiation of PC12 and HUVEC cells simultaneously was then tested in a co-culture of all three cell types at a range of relative cell ratios (Figure 5.4).
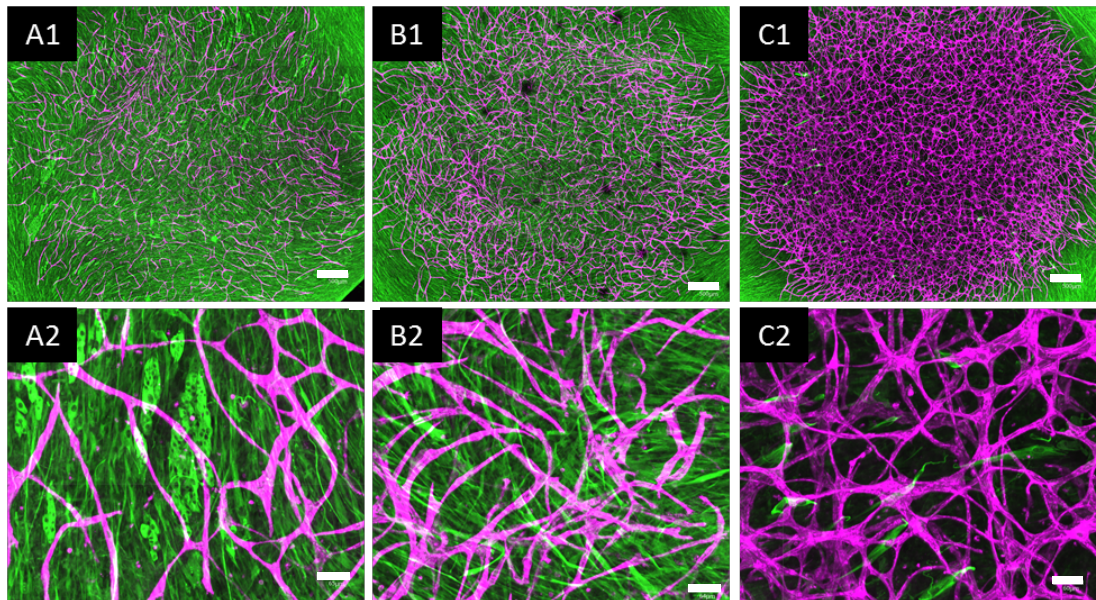


**Figure 5.4 – Immunofluorescence images of nHDF/HUVEC/PC12 3D co-culture in fibrin hydrogels.** Cells were cultured at a (A) 2:1:2 ratio of nHDF:HUVEC:PC12, (B) 2:1:1 ratio of nHDF:HUVEC:PC12, and (C) 2:1:0.2 ratio of nHDF:HUVEC: PC12, stained with CD31 (purple) and β-III tubulin (green) immunostain. Images taken at day 14. *(Scale bar – A1, B1, C1 = 500 μm, A2, B2 = 65 μm, C2 = 60 μm)*

The results show that the nHDF cells were capable of simultaneously stimulating differentiation and neurite extension/tube formation in both PC12 and HUVEC cells, respectively. The results also show that the HUVEC cells formed tighter, more intricate capillary networks with decreasing PC12 ratio. The PC12 cells, however, appear to be equally capable of differentiating and forming large amounts of neurites at both 2:1:2 and 2:1:1 nHDF:HUVEC:PC12 ratios, but not at the 2:1:0.2 ratio. At the lowest ratio of

PC12s, few PC12s were visible in the centre of the gel, and those that were visible did not achieve the same level of differentiation and neurite outgrowth as those in the higher PC12 ratio gels. The PC12s that were able to migrate outside of the gel, however, did still seem to be able to extend neurites, similar to those PC12s that migrate outside the gel in the higher PC12 ratio experimental groups.

As well as the experimental groups, positive and negative controls were also used to ensure that the PC12 and HUVEC differentiation would not happen in the absence of nHDF cells, and to ensure that background and/or non-specific staining was not significant. Positive and negative controls for β-III tubulin staining are shown in Figure 5.5.
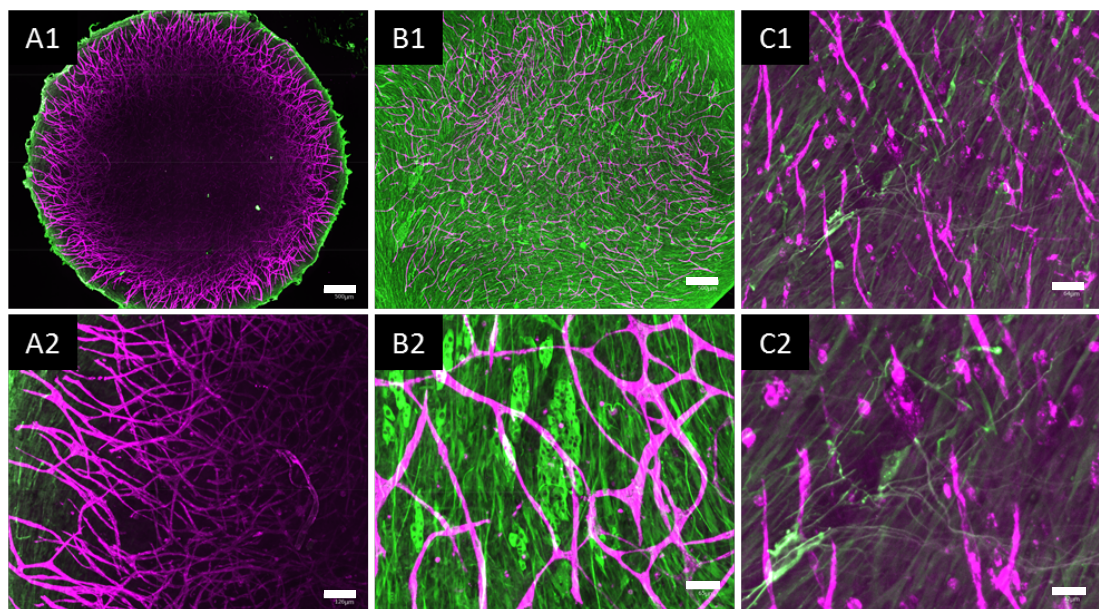


**Figure 5.5 – Immunofluorescence images of nHDF/HUVEC 3D co-cultures.** Cells were cultured at a (A) 2:1 ratio, and nHDF/HUVEC/PC12 3D co-culture in fibrin hydrogel at 2:1:2 ratio of nHDF:HUVEC:PC12 (B) without supplementation with NGF and (C) with supplementation with 100 ng/ml NGF. All images are confocal images of cells in fibrin hydrogels stained with CD31 (purple) and β-III tubulin (green) immunostain. Images taken at day 14. *(Scale bar – A1, B1 = 500 µm, C1, B2 = 65 µm, A2 = 125 µm, C2 = 32 µm)*

The negative control for the β-III tubulin stain (Figure 5.5A), which consisted of staining fibrin gels containing nHDF and HUVEC cells only with both CD31 and β-III tubulin immunostain, shows a small amount of background staining at the edges of the gel, giving the gel a 'halo' of non-specific stain. When this negative control is compared to the experimental groups it is clear to see that the non-specific staining in the negative control is not significant

in comparison to the staining of experimental gels, confirming that the β-III tubulin does in fact stain the PC12 cells. From the positive control, in which 100 µg/ml NGF was added to the nHDF/HUVEC/PC12 co-culture, it can be seen that the PC12 cells form more branched neurites in comparison to the experimental gels. It can also be seen that the HUVEC cells are less able to differentiate and form tubes and networks when compared to a co-culture of the same ratio of nHDF/HUVEC/PC12 cells at the same ratio and timepoint without supplementation with NGF.

A further negative control consisting of a co-culture of PC12 and HUVEC cells only was also used (Figure 5.6).
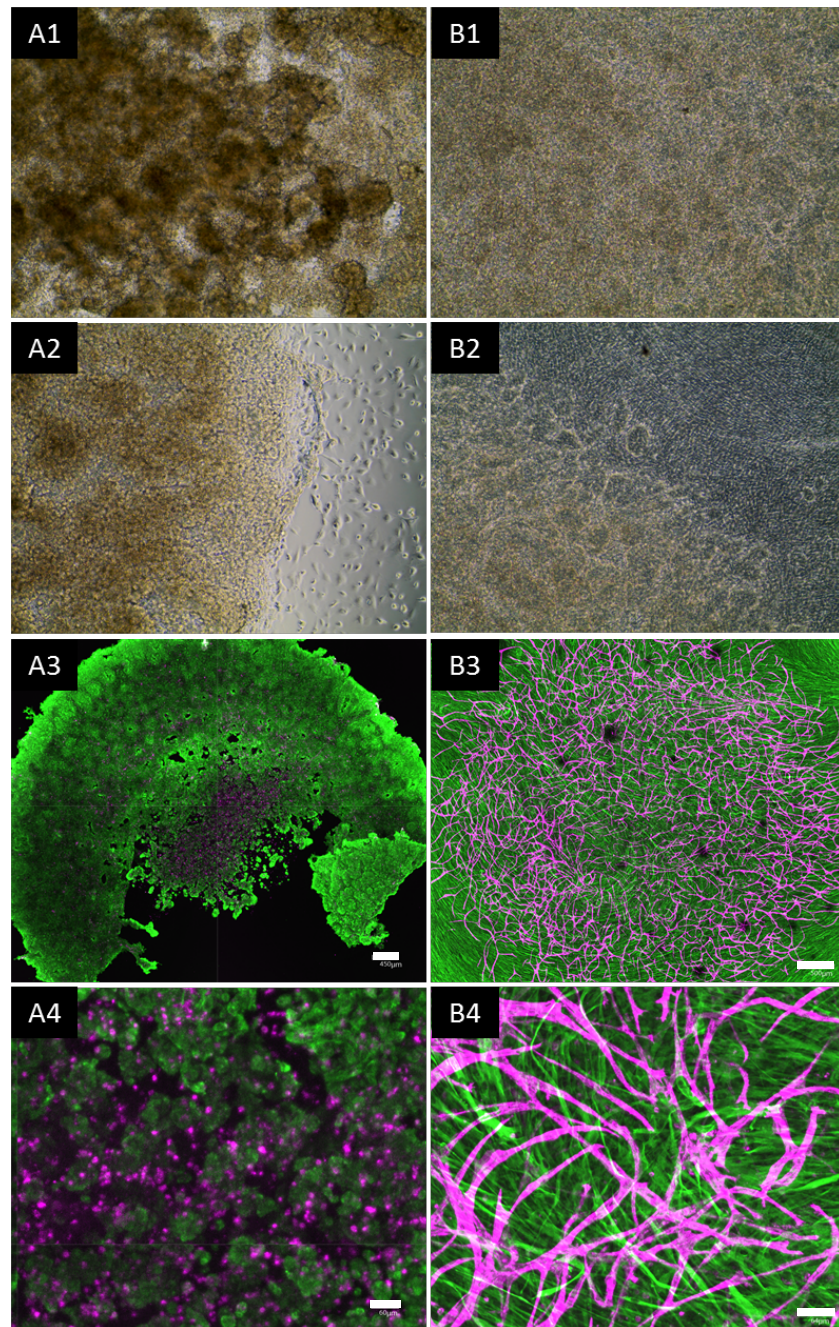
**Figure 5.6 – 3D co-culture in fibrin hydrogels using varying nHDF, HUVEC and PC12 ratios.** (A) HUVEC and PC12 cells at a 1:1 ratio and (B) nHDF/HUVEC/PC12 cells at 2:1:1 ratio, showing brightfield images of (A1, B1) the centre of the gels and (A2, B2) the edges of the gels, and confocal images of cells stained with CD31 (purple) and β-III tubulin (green) immunostain in (A3, B3) the whole gel, and (A4, B4) the centre of the gel. Images taken at day 14. *(Scale bar – A3 = 450 μm, B3 = 500 μm, A4 = 60 μm, B4 = 65 μm)*

A comparison of the brightfield images of the negative control and experimental gels show that the nHDF absent gels see a loss in homogeneity in the centre of the gel, with dark clumps forming in the gel and a loss of structure. At the edges of the gel it can also be seen that although

some cells were capable of migrating outside of the gel in the negative control, there are very few and did not form a 'sheet' as they did in the nHDF present gels.

The confocal images show that the HUVEC and PC12 cells in the negative control gel do not differentiate, as evidenced by the maintenance of their rounded morphology. There is also evidence of the gel disintegrating in the absence of nHDF cells.

## 5.4   Discussion

The results of the nHDF/PC12 co-culture experiment showed significant neurite outgrowth at both of the nHDF:PC12 ratios tested. To date, the differentiation of PC12s via co-culture with nHDFs has not been seen in the literature.

Although there are other examples of nHDF/PC12 co-culture in the literature, in these cases the nHDF cells were not specifically used to differentiate the PC12 cells. The co-culture described by Noh and colleagues (Noh *et al.*, 2020) used both nHDF and PC12 cells in a similar fibrin hydrogel, but instead cultured the PC12s in 100 ng/ml NGF for differentiation (as in the positive control used in this chapter) and compared the behaviour of the PC12s on their own against those cultured with nHDFs in terms of neurite alignment and the behaviour of the fibrin hydrogel scaffold. Interestingly, they observed that culture with increasing concentrations of nHDFs increased neurite alignment due to the contractile forces exerted on the gel by the nHDFs. Though the construct used by Noh was created using direct-write printing between two pegs to allow alignment of the contractile forces, the hydrogel used in this chapter was simply 'printed' as a single drop and not designed for alignment.

Despite the simpler shape, the contractile forces exerted by the nHDFs in this hydrogel drop will still have a significant impact on the construct. This is immediately obvious in that, similarly to that observed by Noh and coleagues, 'higher concentrations of PC12 cells exhibited severe structural degradation during culture' (Noh *et al.*, 2020). The negative controls used in this chapter which consisted of PC12 cells only and no other cell type disintegrated rapidly in culture. Severe degradation was also seen in PC12/HUVEC co-culture, in which the hydrogels likely only survived due to the reduced concentration of PC12 cells rather than the presence of the HUVECs. It can also be seen in the difference in Noh's SEM images of the fibrin structure with and without nHDFs, which closely mirror the brightfield microscope images shown in Figure 5.6. Both the HUVEC and PC12 cells also maintained rounded morphologies and did not differentiate in the negative control gels, cultured without nHDF cells, identifying the activity of the nHDF cells as being the key cause of differentiation.

Though the contractile forces are not aligned in the hydrogel 'drop' used in this chapter, the nHDFs will still create these forces, and the presence of these forces is evidenced by the different hydrogel structure with and without

nHDFs present (Figure 5.6). Because the bottom surface of the gel is stuck to the culture surface and unable to deform, the nHDFs will create stresses across the bottom of the gel, which will be perceivable by the PC12s in the same way as the aligned stresses created by Noh (Noh *et al.*, 2020). Despite being encapsulated in 3D, the PC12s cultured in these hydrogels only appear to have grown neurites in 2D at the bottom of the gel (data not shown), where the gel interfaces with the Petri dish surface, and also outside the gel in the surrounding cell sheet. Neurons are known to prefer growing along 2D surfaces with higher stiffness and topographical cues (Chua *et al.*, 2014), and thus it may be possible that the presence of PC12s at the bottom and outside of the gel is as a result of migration towards the stiffer surface before or during differentiation. The ability of the gels to allow cell migration to the Petri dish interface and outside of the gel is also demonstrated by the nHDF cells, which migrate outside of the gel during time in culture. Alternatively, the cells may have sunk to the bottom of the construct during gel curing, as the gel is still not solid enough to move for 5 minutes after pipetting and is left for a further 55 minutes to fully solidify. The HUVEC cells, however, create true 3D capillary networks in both the HUVEC/nHDF and HUVEC/nHDF/PC12 co-cultures, and thus the explanation of cells sinking to the bottom of the gel is less likely if it is just the PC12s and nHDFs that sink, but not the HUVECs. CellTracker Green™ was not used for PC12 cells due to the fact that morphological changes to PC12s in the form of neurite outgrowth would not have been picked up by the CellTracker Green™, which stains intracellular components, whilst neurites are extra-cellular protrusions. Had CellTracker Green™ been used, this would have been a potentially useful way of observing any cell migration during time in culture.

The ability of the HUVECs to remain in 3D above the 2D layer of PC12 cells at the bottom of the hydrogel means that the neuronal 'network' and the capillary network formed in the PC12/HUVEC/nHDF co-culture did not actually overlap, but do still exist in the same gel. The quality of both the capillary and neuronal networks formed by co-culture were also highly dependent on the ratios of the cells tested. Initial co-culture testing of the nHDF/HUVEC cells followed the ratio described by Naka and colleagues (Naka *et al.*, 2020) of 2:1, and in the nHDF/HUVEC/PC12 co-cultures, the highest quality capillary networks were formed at the lowest PC12 ratios, which meant that the nHDF:HUVEC ratios were closest to 2:1. In this case, the term 'quality' refers to the intricacy and connectedness of the capillary networks. The loss of quality of capillary networks can be explained by

considering the absolute cell numbers, as when seeded at a consistent overall density of 5 million cells/ml HUVECs are 33%/1.6 million of the cells in the 1:0.5:0.1 nHDF:HUVEC:PC12 group, but only 20%/1 million in the 1-0.5-1 group.

Similarly, though there is little observable difference in the neuronal differentiation of the PC12s at the two highest PC12 concentrations tested, at the lowest PC12 concentration the centre of the gel is almost completely absent of differentiated PC12s. Though there is a small number of PC12 cells observable through β-III tubulin immunostaining, these cells have not sprouted neurites and appear to be in an undifferentiated state. The PC12s that have migrated into the 2D cell layer outside the gel with the nHDFs, however, do appear to be in a differentiated state. This suggests that the PC12 cells need to be at a high enough density in comparison to the HUVECs in order to be able to differentiate in the centre of the hydrogel, and possibly that the higher density of HUVEC cells leave less availability of the factors secreted by the nHDFs that stimulate differentiation.

When the PC12s that have been differentiated via the action of the nHDFs alone are compared to those in the positive control group, which were cultured with nHDFs but also supplemented with NGF, there are some differences to note. The most significant difference is the presence of more branched neurites in the positive control group, with a larger proportion of the PC12 cells forming multiple neurites which also have branches, but in the experimental groups the neurites formed by the PC12s are generally longer but are not branched. This difference is likely due to the different methods used to stimulate differentiation.

It has previously been shown that neurite outgrowth stimulated by both NGF and bFGF is potentiated by a number of the same synergistic compounds (Ho and Raw, 1992), suggesting that neurite outgrowth by both NGF and bFGF share common intracellular events. This is supported by work from Shimosaka and Bhawal (Shimosaka and Bhawal, 2013) that suggests that bFGF acts to stimulate neurite outgrowth through the NGF receptor protein in PC12 cells. Interestingly though, morphological differences are seen in the work by Wu and colleagues (Wu *et al.*, 2018) when differentiation using bFGF and NGF are compared directly, with the PC12s differentiated by bFGF forming less connected networks, with more cells standing alone, than those differentiated using NGF. This is likely reflected in the work seen in this chapter, in that the PC12s differentiated by bFGF alone extend longer neurites because they do not stop extending when they meet other cells.

The work by Wu also demonstrated the combination of bFGF and NGF delivered to PC12s at the same time acted to promote proliferation rather than differentiation and neurite outgrowth when compared to bFGF or NGF alone. Due to the differences in bFGF and NGF mediated PC12 differentiation, and the well-established use of bFGF to stimulate differentiation in PC12 cells, the use of NGF as the positive control may be a weakness in the methodology used in this chapter. Due to the intention to use a bFGF dependent method, that causes HUVEC differentiation in co-culture with nHDFs, to stimulate differentiation in PC12s, it may have been more appropriate to use bFGF as the positive control.

The use of NGF in the positive control also had an impact on the HUVEC cells in the co-culture, with HUVEC cells in the positive control group less able to form tubules. This is unexpected, as previous studies have shown that HUVEC cells have NGF receptors and can be stimulated to form tubules using NGF alone at concentrations under 50 ng/ml, suggesting that NGF may play a key role in CNS blood vessel formation (Cantarella *et al.*, 2002). For this reason it was expected that the presence of NGF would have either a negligible impact or a positive impact on HUVEC differentiation. There is however no previous literature showing stimulation of HUVECs with NGF at the same time as the bFGF and VEGF that is released from the nHDFs to stimulate tubule formation, and thus there is no relevant comparison to make. The observed reduced capillary network in groups stimulated with NGF was consistent across experimental repeats and the only other possibility is that the effect observed is due to an interference with the CD31 immunostaining process rather than a true action of the HUVEC cells in these groups, but there is no evidence for this.

It is possible that, again, NGF and bFGF/VEGF act to stimulate differentiation through different cell-signalling pathways. Though bFGF and VEGF have also been shown to stimulate HUVECs through different cell-signalling pathways (Yoshida, Anand-apte and Zetter, 2009), these have been shown to be complementary and thus the combination of these two factors is effective in stimulating capillary formation. The inhibitory effect of NGF on HUVEC differentiation in combination with bFGF and VEGF, despite the 'potent' angiogenic effect NGF has been shown to have alone (Cantarella *et al.*, 2002), suggests that NGF does not work in a complementary manner to bFGF and VEGF, and instead activates a different cell-signalling pathway that is destructive to the pathways activated by bFGF and/or VEGF. Further work would be needed to confirm this

through systematic comparison of HUVECs stimulated with each of these three factors.

As well as the previously described novelty of PC12s differentiated by nHDFS in 3D co-culture, the formation of capillary and neuronal networks inside the same hydrogel construct is also novel, and could be used as the basis for simple BBB models for applications such as drug testing. Further work to build on this three cell type co-culture for BBB applications may take the form of further optimisation of the HUVEC:PC12 cell ratios between those used in this chapter, to find the ratio with best balance of neuronal network to capillary network. Further work may then start to add glial cells such as astrocytes and oligodendrocytes to better replicate other key aspects of CNS biology. Further, the experiments described in this chapter have shown that nHDFs are capable of stimulating PC12 to differentiate and grow neurites. Though the mechanism through which this is achieved is thought to be through secretion of the same factors as cause differentiation in HUVEC cells, namely bFGF, this is was not specifically experimentally confirmed and thus further work may use, for example, the addition of bFGF inhibitors to test this theory.

## 5.5  Conclusions

The key conclusion from this chapter is that co-culture with nHDFs can be used to stimulate differentiation in PC12 cells, and this co-culture format will be taken through to the final chapter for use with the GNR hybrid hydrogels. Also key is the cell ratios, with a 2:1 ratio of nHDF:PC12 cells being the chosen ratio to take forward.

Further than this, the experiments in this chapter also demonstrated that nHDFs can be used to simultaneously stimulate differentiation in both PC12 and HUVEC cells simultaneously, with potential applications in modelling of systems where neurons meet blood vessels, such as at the BBB.

# Chapter 6
# 3D Co-Culture in GelNOR/GNR Hybrid Hydrogels

## 6.1  Introduction and Aims

As previously described, electrically conductive scaffolds have been identified as having potential for use in tissue engineering applications for SCI repair (Shu *et al.*, 2019). To this end, previous chapters have focused on the development of an electrically conductive hydrogel, by first optimising the crosslinkers in a GelNOR hydrogel, and then incorporating GNRs into the GelNOR hydrogel to increase electrical conductivity. Further to this, the role of cells in tissue engineering strategies, and more specifically in directing the biological response to SCI, has also been discussed. To this end, a co-culture system consisting of nHDFs and PC12s was also developed in a fibrin hydrogel, with the intention that this would then be replicated in the previously developed GNR/GelNOR hybrid hydrogel. Though gold nanospheres have previously been shown to enhance extension of neurites from PC12 cells in the presence of electrical stimulation in 2D (Park *et al.*, 2009), nothing was seen in the literature analysing the effect of gold nanoparticles on the behaviour of PC12s in 3D culture.

Though the previously developed nHDF/PC12 co-culture is a potentially useful model for *in-vitro* culture, as PC12 is a well-established neuronal model cell, the use of nHDFs to stimulate PC12 differentiation relies on a specific aspect of PC12 biology, their ability to grow neurites when stimulated with bFGF (Rydel and Greene, 1987). Though the use of bFGF has been shown to promote survival and proliferation of some types of primary neurons *in-vitro* (Ray *et al.*, 1993), and some fibroblast growth factors have been identified as being beneficial in animal models of SCI treatment (Y. Zhou *et al.*, 2018), nHDFs are unlikely to have use in cell therapies for SCI treatment. This is due to the role that fibroblasts play in wound healing and fibrotic scarring. Fibroblasts are one of the principle generators of ECM, and though their presence in the CNS under normal *in-vivo* conditions is limited, SCI can induce fibroblasts to generate matrix components which may inhibit neural regeneration and prolong tissue remodelling (Bradbury and Burnside, 2019). This identifies nHDFs as poor candidates for SCI cell therapy.

As previously discussed, DPSCs have been identified as a cell type with potential for use in SCI therapy. This is due to their having numerous distinct

capabilities that are desirable in SCI repair, including immunomodulation (Yamagata *et al.*, 2013), the ability to differentiate down neuronal (J.-H. Lee *et al.*, 2014) and glial (Askari *et al.*, 2015) lineages, and the ability to create a permissive environment for neurite outgrowth (Sakai *et al.*, 2012). Due to the complex and multi-faceted nature of SCI, a successful cell therapy or tissue engineering response will likely also need to be multi-faceted, and thus the ability of DPSCs to have positive effect through numerous mechanisms identifies them as an attractive for SCI repair.

One of the mechanisms through which DPSCs are potentially capable of inducing anabolic repair after SCI is through the release of neurotrophic factors such as NGF and BDNF (Leong *et al.*, 2012). The ability of DPSCs to release these factors not only identifies them as being capable of stimulating regrowth of damaged neural tissue *in-vivo*, but also identifies them as having potential for use in *in-vitro* model co-cultures similar to the nHDF/PC12 co-culture developed in the previous chapter. To this end, previous studies have used co-culture with DPSCs and/or DPSC conditioned media to stimulate neuronal differentiation in model neuronal cells such as SH-SY5Y (N. E. M. B. Ahmed *et al.*, 2016), and more recently in PC12 (Sultan *et al.*, 2021), though as of yet this has not been demonstrated in 3D hydrogel culture.

The ability of DPSCs to stimulate neuronal differentiation of model cells in *in-vitro* co-culture identifies them as being a suitable cell source to use instead of the nHDFs used in previous chapters, with the added advantage that the DPSCs are more favourable for *in-vivo* applications. This chapter describes comparison of DPSCs and nHDFs for differentiation of PC12 cells, and the effect of GNR incorporation into the hydrogel scaffold on PC12 neurite outgrowth.

The aim of this chapter is to biologically test the GNR/GelNOR hybrid hydrogel developed in previous chapters. This will be achieved through the following objectives:

1. Compare the behaviour of DPSCs and nHDFs encapsulated in GelNOR hydrogels, and their reaction to the presence of GNRs in the GelNOR hydrogel.
2. Transfer the nHDF/PC12 co-culture in fibrin hydrogels developed in the previous chapter into GelNOR hydrogel
3. Compare the effect of nHDF and DPSC on the behaviour of co-cultured PC12 cells

4. Compare the effect of GNRs on PC12 behaviour, both when co-cultured with nHDFs and DPSCs

## 6.2   Methods

### 6.2.1  Preparation of Hydrogel Solutions

GNRs were synthesised and stored as described in section 2.2.3.

On the day of the experiment, GelNOR macromer was dissolved in PBS, heated to 37 °C , at 20 wt%. At the same time, an appropriate amount of GNR stock solution for to give a final hydrogel GNR concentration of 0.5 mg/ml was transferred to an Eppendorf tube and spun at 12,000 rpm for 10 minutes in an ultra-centrifuge, temperature controlled at 20 °C, and the supernatant discarded. The GNR pellet was then re-suspended in the GelNOR solution and mixed thoroughly by pipetting and vortexing. The GelNOR/GNR solution was then sonicated for 10 minutes at 37 °C in a sonic bath and vortexed thoroughly again to homogenise GNR dispersion within the hydrogel solution.

An amount of GelNOR solution was also kept aside for use in the negative control, which consisted of the native GelNOR hydrogel without GNRs.

### 6.2.2  Encapsulation of DPSCs

DPSCs were trypsinised and counted as described in section 2.2.4.3, and an appropriate amount to give a seeding density of 5 million cells/ml were then re-centrifuged at 1,200 rpm for 5 minutes and the supernatant discarded. The cell pellet was then re-suspended in either the GelNOR/GNR solution or the plain GelNOR solution described in section 3.2.2 so give a final seeding density of 5 million cells/ml.

To the cell suspension, 6.45 µl of 0.5 M DTT was added and the solution was mixed by pipetting for 5 seconds. Once vortexed, 3 µl of 0.5 M SPS was added to the very bottom of the Eppendorf tube, with care taken not to mix the SPS into the hydrogel solution, followed by the addition of 3 µl of 0.05 M Ruthenium to the very surface of the solution, once again being careful not to mix during addition. The whole solution was then mixed by pipetting for 10 seconds and immediately aliquoted into 30 µl disc moulds, and the moulds were covered with a microscope coverslip to maintain sterility during curing.

Hydrogel discs were cured using an Omnicure S1000 visible light unit, providing 30 mW/cm$^2$ light at wavelength 400-450 nm. Samples were

irradiated for 5 minutes before being turned over and irradiated for a further 5 minutes.

Gels were then removed from the mould and each was submerged in 1 ml of complete α-MEM, as described in section 2.2.4.4.

### 6.2.3  Encapsulation of nHDFs

nHDFs were trypsinised and counted as described in section 2.2.4.3, and an appropriate amount to give a seeding density of 5 million cells/ml were then re-centrifuged at 1,200 rpm for 5 minutes and the supernatant discarded. The cell pellet was then re-suspended in either the GelNOR/GNR solution or the plain GelNOR solution described in section 3.2.2 to give a final seeding density of 5 million cells/ml.

To the cell suspension, 6.45 µl of 0.5 M DTT was added and the solution was mixed by pipetting for 5 seconds. Once vortexed, 3 µl of 0.5 M SPS was added to the very bottom of the Eppendorf tube, with care taken not to mix the SPS into the hydrogel solution, followed by the addition of 3 µl of 0.05 M Ruthenium to the very surface of the solution, once again being careful not to mix during addition. The whole solution was then mixed by pipetting for 10 seconds and immediately aliquoted into 30 µl disc moulds, and the moulds were covered with a microscope coverslip to maintain sterility during curing.

Hydrogel discs were cured using an Omnicure S1000 visible light unit, providing 30 mW/cm$^2$ light at wavelength 400-450 nm. Samples were irradiated for 5 minutes before being turned over and irradiated for a further 5 minutes.

Gels were then removed from the mould and each was submerged in 1 ml of complete DMEM, as described in section 2.2.4.5.

### 6.2.4  Encapsulation of DPSC/PC12 Co-Culture

Both DPSCs and PC12s were trypsinised and counted as described in sections 2.2.4.3 and 2.2.4.8 respectively, and an appropriate volume of each cell suspension to give a final seeding density of 3.67 million DPSCs/ml and 1.33 million PC12s/ml were then combined and re-centrifuged at 1,200 rpm for 5 minutes and the supernatant discarded. The cell pellet was then re-suspended in either the GelNOR/GNR solution or the plain GelNOR solution described in section 3.2.2 to give a final seeding density of 5 million cells/ml.

To the cell suspension, 6.45 µl of 0.5 M DTT was added and the solution was mixed by pipetting for 5 seconds. Once vortexed, 3 µl of 0.5 M SPS was added to the very bottom of the Eppendorf tube, with care taken not to mix

the SPS into the hydrogel solution, followed by the addition of 3 µl of 0.05 M Ruthenium to the very surface of the solution, once again being careful not to mix during addition. The whole solution was then mixed by pipetting for 10 seconds and immediately aliquoted into 30 µl disc moulds, and the moulds were covered with a microscope coverslip to maintain sterility during curing.

Hydrogel discs were cured using an Omnicure S1000 visible light unit, providing 30 mW/cm$^2$ light at wavelength 400-450 nm. Samples were irradiated for 5 minutes before being turned over and irradiated for a further 5 minutes.

Gels were then removed from the mould and each was submerged in 1 ml of culture media, which consisted of 50% (v/v) complete α-MEM and 50% (v/v) complete RPMI, as described in sections 2.2.4.4 and 2.2.4.8 respectively.

## 6.2.5 Encapsulation of DPSC/PC12 Co-Culture

Both nHDFs and PC12s were trypsinised and counted as described in sections 2.2.4.3 and 2.2.4.8 respectively, and an appropriate volume of each cell suspension to give a final seeding density of 3.67 million DPSCs/ml and 1.33 million PC12s/ml were then combined and re-centrifuged at 1,200 rpm for 5 minutes and the supernatant discarded. The cell pellet was then re-suspended in either the GelNOR/GNR solution or the plain GelNOR solution described in section 3.2.2 to give a final seeding density of 5 million cells/ml.

To the cell suspension, 6.45 µl of 0.5 M DTT was added and the solution was mixed by pipetting for 5 seconds. Once vortexed, 3 µl of 0.5 M SPS was added to the very bottom of the Eppendorf tube, with care taken not to mix the SPS into the hydrogel solution, followed by the addition of 3 µl of 0.05 M Ruthenium to the very surface of the solution, once again being careful not to mix during addition. The whole solution was then mixed by pipetting for 10 seconds and immediately aliquoted into 30 µl disc moulds, and the moulds were covered with a microscope coverslip to maintain sterility during curing.

Hydrogel discs were cured using an Omnicure S1000 visible light unit, providing 30 mW/cm$^2$ light at wavelength 400-450 nm. Samples were irradiated for 5 minutes before being turned over and irradiated for a further 5 minutes.

Gels were then removed from the mould and each was submerged in 1 ml of culture media, which consisted of 50% (v/v) complete DMEM and 50% (v/v) complete RPMI, as described in sections 2.2.4.5 and 2.2.4.8 respectively.

### 6.2.6  Analysis of Cell Viability

#### 6.2.6.1  LIVE/DEAD Assay

Viability of nHDFs and DPSCs in single cell culture was analysed using LIVE/DEAD assay as described in section 2.2.5.1.

#### 6.2.6.2  Alamar Blue Assay

Viability of nHDFs and DPSCs in single cell culture was analysed using Alamar Blue assay as described in section 2.2.5.2.

### 6.2.7  Analysis of Cellular Behaviour

#### 6.2.7.1  β-III Tubulin Staining

PC12 cells in co-culture were analysed through immunostaining of β-III tubulin, as described in section 5.2.8, and observation through confocal microscopy.

#### 6.2.7.2  ImageJ Analysis

The confocal microscope images were analysed using ImageJ. Two characteristics were analysed, neurite outgrowth and particle size.

Cell morphology in single cell culture was analysed by using ImageJ to determine the average circularity of the cells in each image, which was then taken as a measure of the extent to which cells had elongated or remained rounded.

In co-culture, PC12s were analysed using the same automated software process as above to determine the mean area of the particles in each confocal image.

Neurite outgrowth was analysed manually in ImageJ and measured the length of the longest neurite of each cell that had spouted a neurite.

Taken together, neurite outgrowth and mean area were used as a measure of the extent to which PC12s had proliferated and differentiated in co-culture.

### 6.2.8  Statistical Analysis

All statistical analysis was performed using the 'rstats' package in RStudio, and used one-way ANOVA or Welch's t-test as described.

All data is presented as mean ± standard deviation. Repeats are presented as (n = x, y) where x is the number of replicates performed within an experiment, and y is the number of times the experiment was performed.

## 6.3  Results

### 6.3.1  Behaviour of nHDFs and DPSCs in Single Cell Culture

The effect of GNR incorporation on cellular behaviour when encapsulated in GelNOR hydrogels was initially tested using cultures of single cell types, encapsulated in GelNOR with and without GNRs. Both nHDFs and DPSCs were used in these single cell cultures, allowing comparison of their behaviour when encapsulated in GelNOR, and of their responses to the presence of GNRs. The results are shown in Figure 6.1.
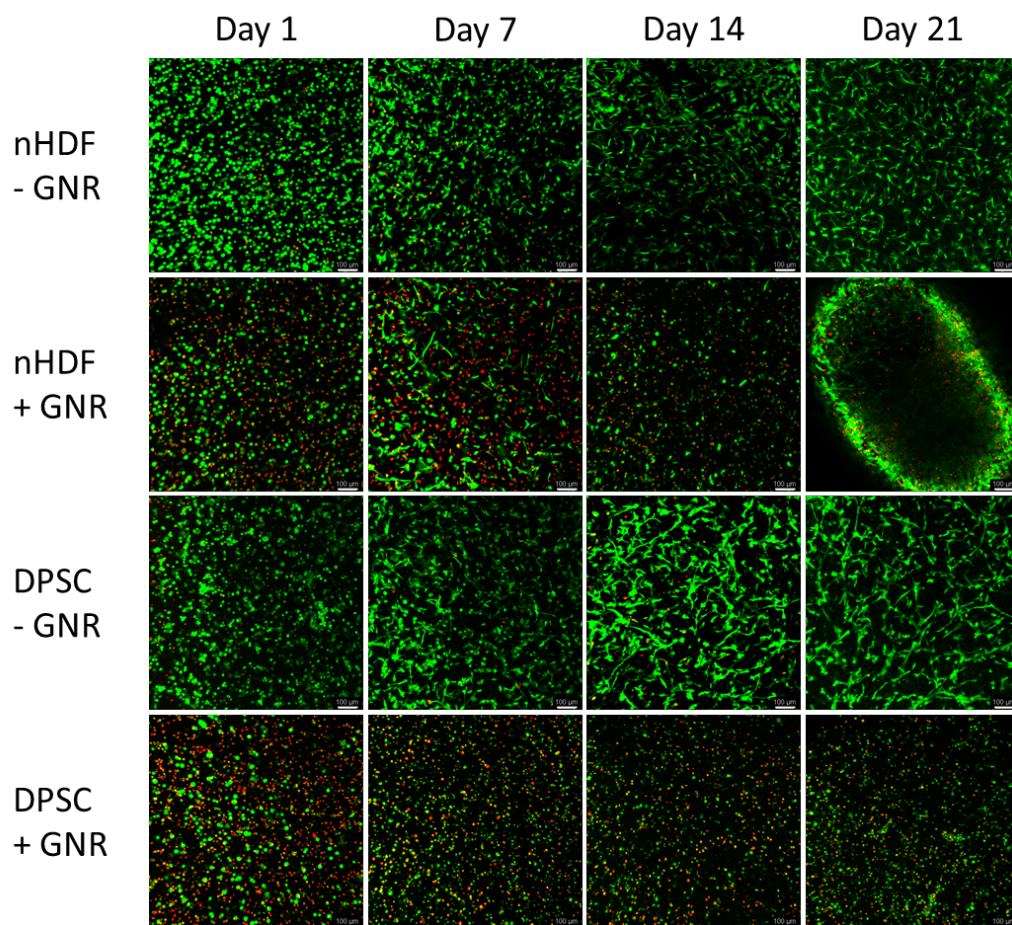


**Figure 6.1 – Confocal microscope images of nHDFs and DPSCs encapsulated in GelNOR hydrogels, with and without GNRs.** Cells were stained using the LIVE/DEAD assay stain. Scale bar = 100 μm.

The LIVE/DEAD images were processed using ImageJ software to determine cell viability. The results are shown in Figure 6.2.
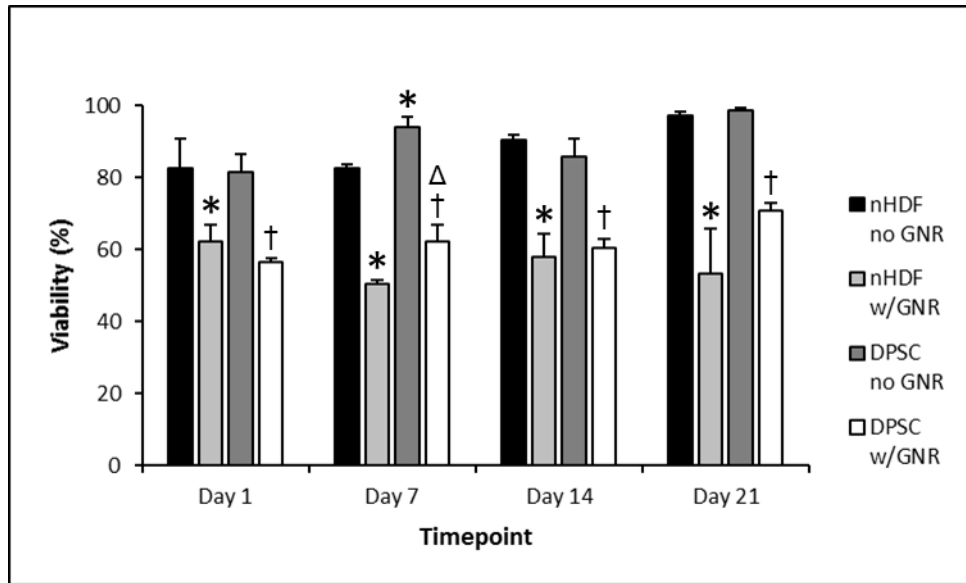
**Figure 6.2 – Viability of nHDFs and DPSCs encapsulated in GelNOR hydrogels with and without GNRs, over 21 days.** Cells were stained using a LIVE/DEAD assay and percentage viability was calculated using ImageJ analysis. Significance levels * $p<0.05$ vs. nHDF no GNR, † $p<0.05$ vs. DPSC no GNR, Δ $p<0.05$ vs. nHDF w/GNR (n=3, 2).

The results of the LIVE/DEAD assay show that encapsulation with GNRs had a significant impact on cell viability of both nHDFs and DPSCs ($p<0.001$ for both, one-way ANOVA with post-hoc Tukey test).

Though initially both DPSCs and nHDFs retained relatively high viability at >80% in the native gels, this dropped to 62% for nHDFs and 57% for DPSCs in the GNR hybrid gels. Further, as viability increased over time in culture for nHDFs and DPSCs in the native gels, the low initial viability of the cells in GNR hybrid gels did not recover and instead stayed chronically low. Though the DPSCs in GNR gels were more viable at day 21, achieving 71% viability, the hybrid hydrogel containing the nHDFs had almost completely disintegrated at the final timepoint, and both cell types were still significantly less viable in the GNR hybrid gels than in the native GelNOR ($p<0.001$ for both, one-way ANOVA with post-hoc Tukey test).

Image analysis with ImageJ was also used to assess cell morphology. This was performed by scoring the circularity of the cells between in order to determine the extent to which cells had elongated or remained rounded. The results are shown in Figure 6.3.
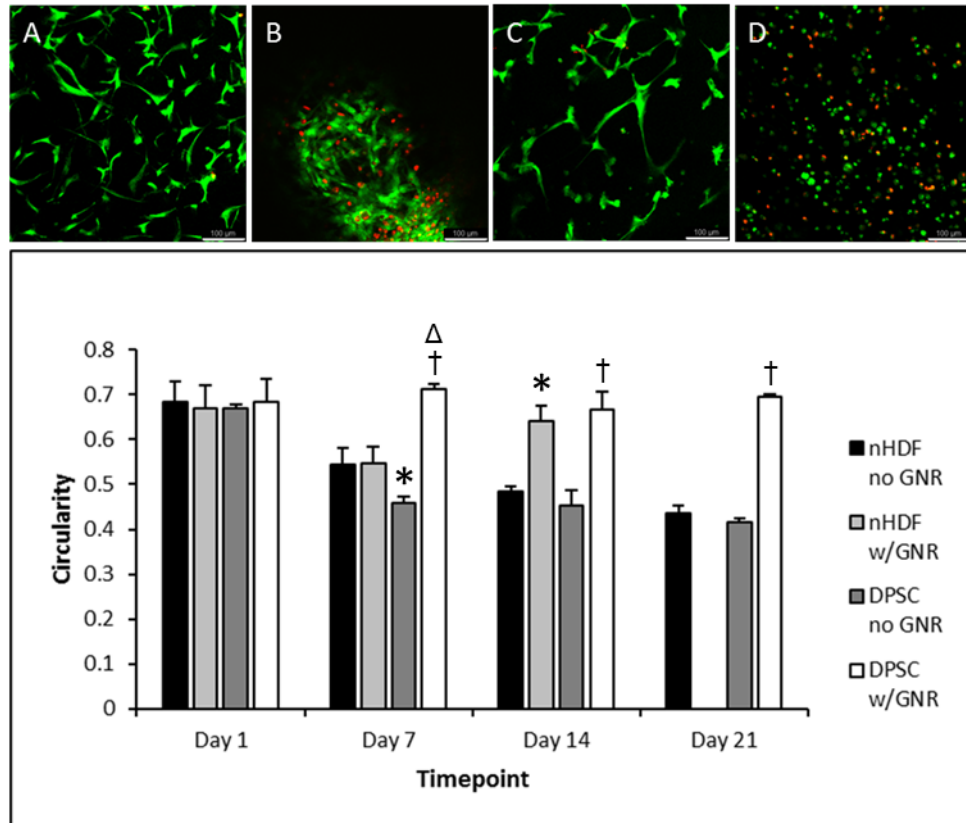
**Figure 6.3 – Morphological and quantitative characterisation of the circularity of nHDFs and DPSCs encapsulated in both GelNOR only and hybrid GNR hydrogels.** Representative images of cell morphology at day 21 for (A) nHDFs encapsulated without GNRs, (B) nHDFs encapsulated with GNRs, (C) DPSCs encapsulated without GNRs, and (D) DPSCs encapsulated with GNRs. Scale bar = 100 µm. Significance levels * $p<0.05$ vs. nHDF no GNR, † $p<0.05$ vs. DPSC no GNR, Δ $p<0.05$ vs. nHDF w/GNR (n=3, 2).

There were initially no significant differences in morphology between any of the cell types in any of the gels, however there was a rapid and statistically significant drop in circularity score (indicating cell elongation) at day 7 for both nHDFs and DPSCs in the native GelNOR gels ($p<0.01$ and $p<0.0001$ respectively, one-way ANOVA with post-hoc Tukey test). There was also a drop in circularity score for the nHDFs in the GNR hybrid gel, however this was not significant in comparison to the nHDFs in the GNR hybrid gel at day 1. The only group that did not decrease in circularity to day 7 was the DPSCs encapsulated in GNR hybrid gels, which were significantly more rounded than all other experimental groups at day 7 (one-way ANOVA with post-hoc Tukey test).

For both the DPSCs and nHDFs encapsulated in native gels, after the described rapid elongation between day 1 and 7, there were no further significant changes in circularity score after this time point.

The nHDFs encapsulated in GNR hybrid gels then unexpectedly had increased circularity score to day 14, however the difference in scores between day 1 and day 7 and between day 7 and day 14 were not significant. The hydrogels in this experimental group had disintegrated significantly at day 21, such that they were still able to be imaged but were too compromised to perform meaningful analysis for cell morphology, and thus the day 21 scores were not included in the analysis (this is shown further in Figure 6.8). The DPSCs encapsulated in the hybrid hydrogels remained rounded throughout their time in culture, with no statistically significant differences observed between the scores at any timepoint.

As well as assessing cell viability through LIVE/DEAD assay, an Alamar Blue assay was also used to determine the effect of encapsulation with GNRs on cellular metabolism. The results are shown in Figure 6.4.
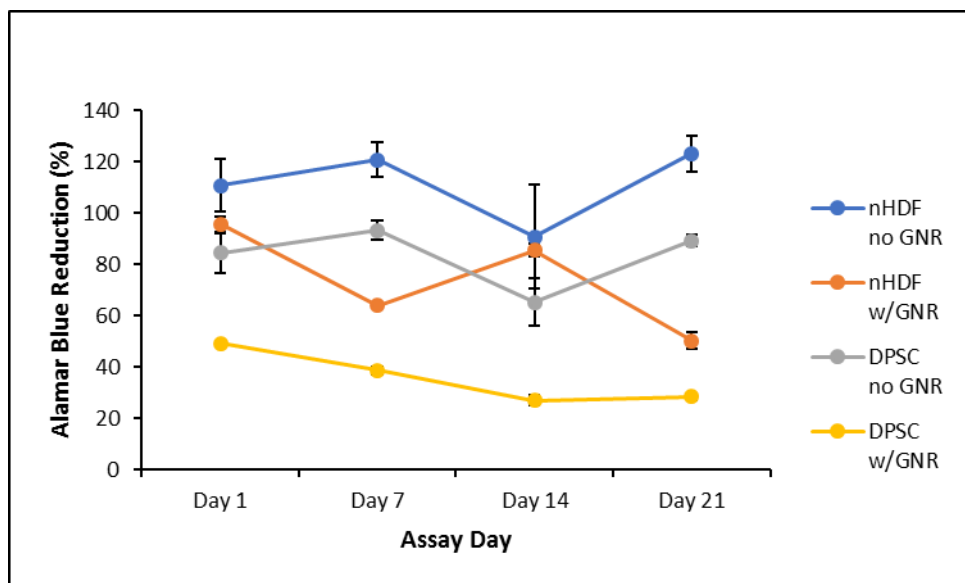


**Figure 6.4 – Cell viability of nHDFs and DPSCs encapsulated in GelNOR only and GNR hybrid hydrogels.** Cell viability was assessed using the Alamar Blue assay (n=3, 2).

Initially, the nHDFs achieved a higher rate of alamar blue reduction than the DPSCs, both with and without GNRs ($p<0.001$ and $p<0.05$ respectively, one-way ANOVA with post-hoc Tukey test). There was also initially no significant difference in alamar blue reduction for nHDFs when cultured with or without GNRs; however, for DPSCs there was a significant drop in alamar blue reduction for cells cultured with GNRs compared to those cultured without ($p<0.01$, one-way ANOVA with post-hoc Tukey test).

The alamar blue reduction for both DPSCs and nHDFs cultured in native gels remains approximately constant, with a slight increase from the day 1 to day 21 alamar blue reduction scores which was not statistically significant for either cell type. There were no significant differences observed between any timepoints for nHDFs, though the DPSCs saw a statistically significant drop from day 7 to day 14 and a concurrent statistically significant rise back up from day 14 to day 21, suggesting that the day 14 timepoint may have been an unusually low alamar blue reduction score, causing type II errors in the statistical analysis.

For both nHDFs and DPSCs cultured with GNRs, the general trend was for decreasing levels of alamar blue reduction over time in culture, representing a decreasing rate of respiration in the cell population. This was confirmed by statistically significant drops between in alamar blue reduction between day 1 and 21 in culture for both nHDFs and DPSCs ($p < 0.0001$ and $p < 0.001$ respectively, one-way ANOVA with post-hoc Tukey test).

## 6.3.2 Behaviour of PC12s in Co-Culture with nHDFs or DPSCs

As well as single cell cultures, comparison between the hybrid GNR hydrogels and the native GelNOR hydrogels was also performed using co-cultures of nHDFs and PC12s or DPSCs and PC12s. Confocal images of the co-cultures are shown in Figure 6.5.
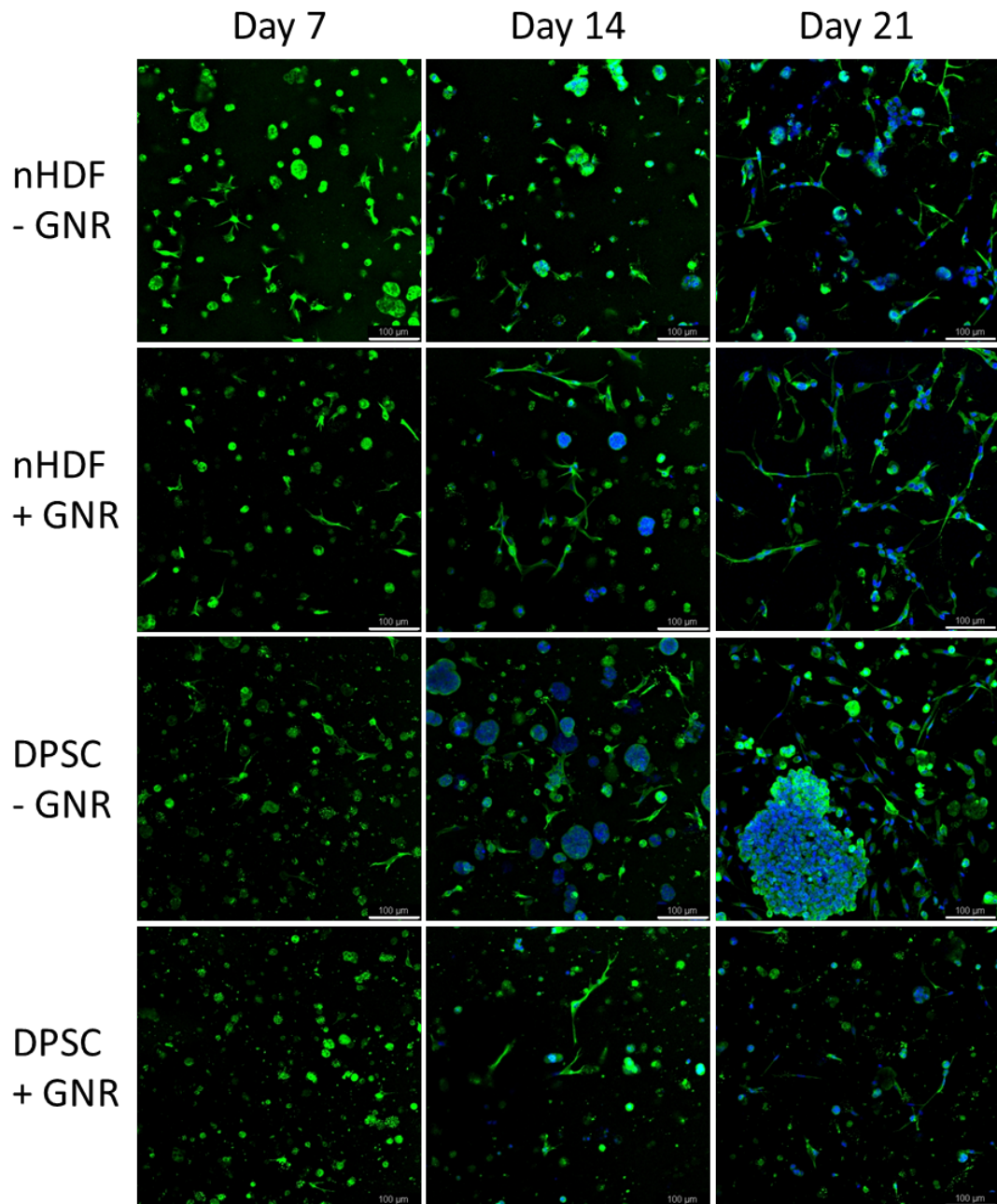


**Figure 6.5 – Confocal microscope images of nHDF/PC12 and DPSC/PC12 co-cultures, encapsulated in GelNOR hydrogels with and without GNRs.** Visible cells are PC12s, stained with β-III tubulin (green) and DAPI nuclear stain (blue). Scale bar = 100 µm**.**

The confocal images of the co-cultures were also processed using ImageJ. This was used to determine neurite outgrowth length, as a measure of PC12 differentiation, and particle size, as a measure of PC12 proliferation. The results of the ImageJ analysis are shown in Figure 6.6.
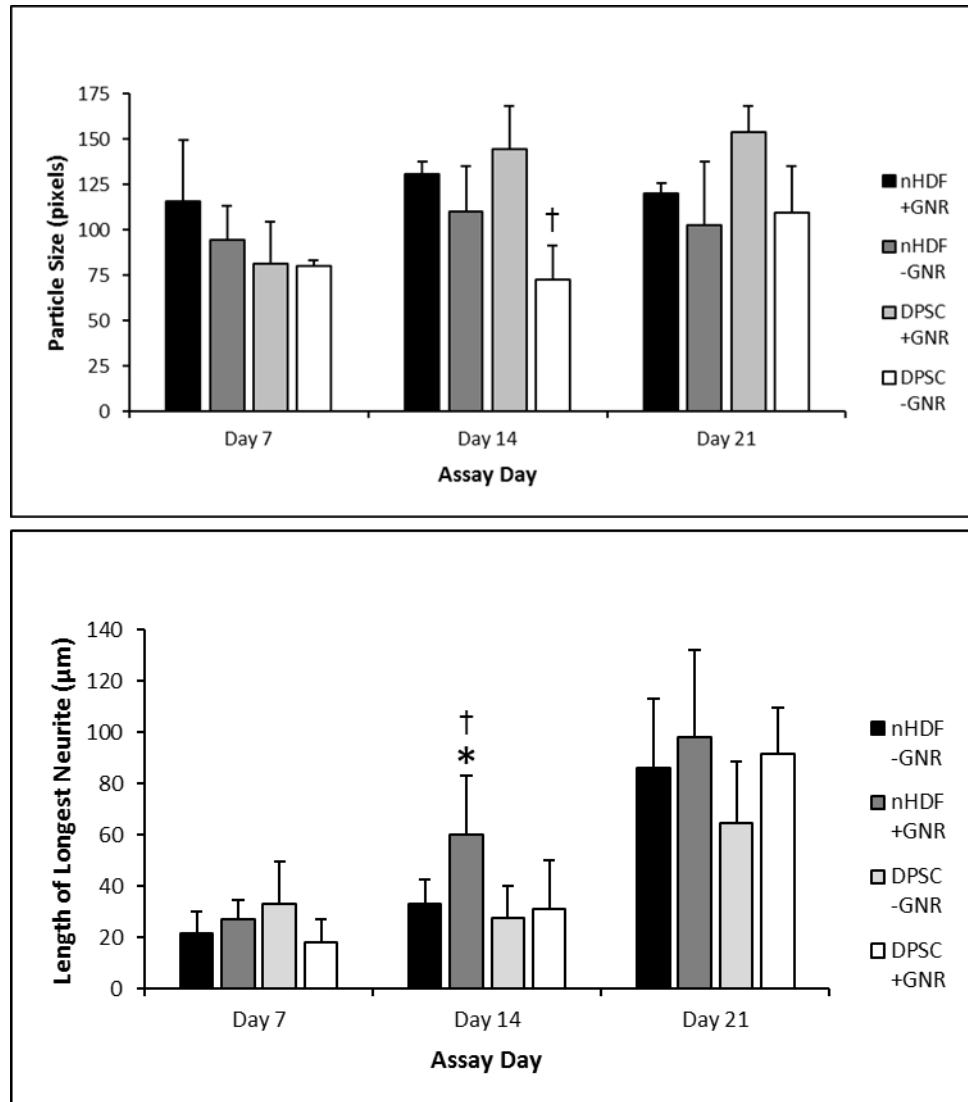


**Figure 6.6 – Effect of GNRs on nHDF and DPSC cell size and neurite outgrowth.** Significance levels * $p<0.05$ vs. nHDF no GNR, † $p<0.05$ vs. DPSC with GNR (n=3, 2).

The analysis of the confocal images showed that particle size remained approximately constant throughout the culture period for the nHDFs encapsulated in both types of gels. For DPSCs, however, though the average cell aggregate is smaller than for the nHDFs in both types of gel at day 7, there is a significant increase in the size of cell aggregates between period 7 to the day 14 timepoint ($p<0.05$, one-way ANOVA with post-hoc Tukey test) for the DPSCs encapsulated in native GelNOR. After day 14, the

average size rises again but not statistically significantly. For DSPCs encapsulated in GNR hybrid gels, the average size remains approximately constant between day 7 and 14, before rising by approximately 34% to day 21, though this increase is not statistically significant.

PC12 neurite outgrowth analysis determined that although outgrowth was greatest in the native GelNOR DPSC co-culture, there were no significant differences between the groups at day 7. At day 14 the PC12s cultured in GNR hybrid gels with nHDFs had achieved a significant increase in neurite outgrowth length compared to day 7 ($p < 0.05$, one-way ANOVA with post-hoc Tukey test). This meant that these PC12s had the longest neurite outgrowth of all the test groups, such that they were significantly longer on average than those of the PC12s cultured in the native gels with nHDFs and the hybrid gels with DPSCs ($p < 0.05$ for both, one-way ANOVA with post-hoc Tukey test). The PC12s cultured in GNR hybrid gels with nHDFs then once again achieved a significant increase in neurite outgrowth length between day 7 and day 21 ($p < 0.05$, one-way ANOVA with post-hoc Tukey test) such that they were again the test group with the longest neurite outgrowth. However, the PC12s cultured with DPSCs in both gel types also achieved statistically significant increases in neurite length from day 14 to 21 ($p < 0.001$ for both, one-way ANOVA with post-hoc Tukey test) and the PC12s cultured with nHDFs in native GelNOR also saw a large but non-significant increase, such that there was no significant difference in neurite length between the groups at day 21. Though the PC12s cultured with nHDFs in native GelNOR did not see a statistically significant increase in neurite length between day 14 and day 21, the increase across the full culture period, from day 7 to 21, was significant ($p < 0.0001$, one-way ANOVA with post-hoc Tukey test).

To ensure that the β-III tubulin stain was visualising the PC12s, as intended, and was not significantly staining the nHDFs and DPSCs, a negative control was used to the staining process, in which GelNOR hydrogels containing nHDFs or DPSCs only were stained using the same protocol. Images of this negative control are shown in Figure 6.7.
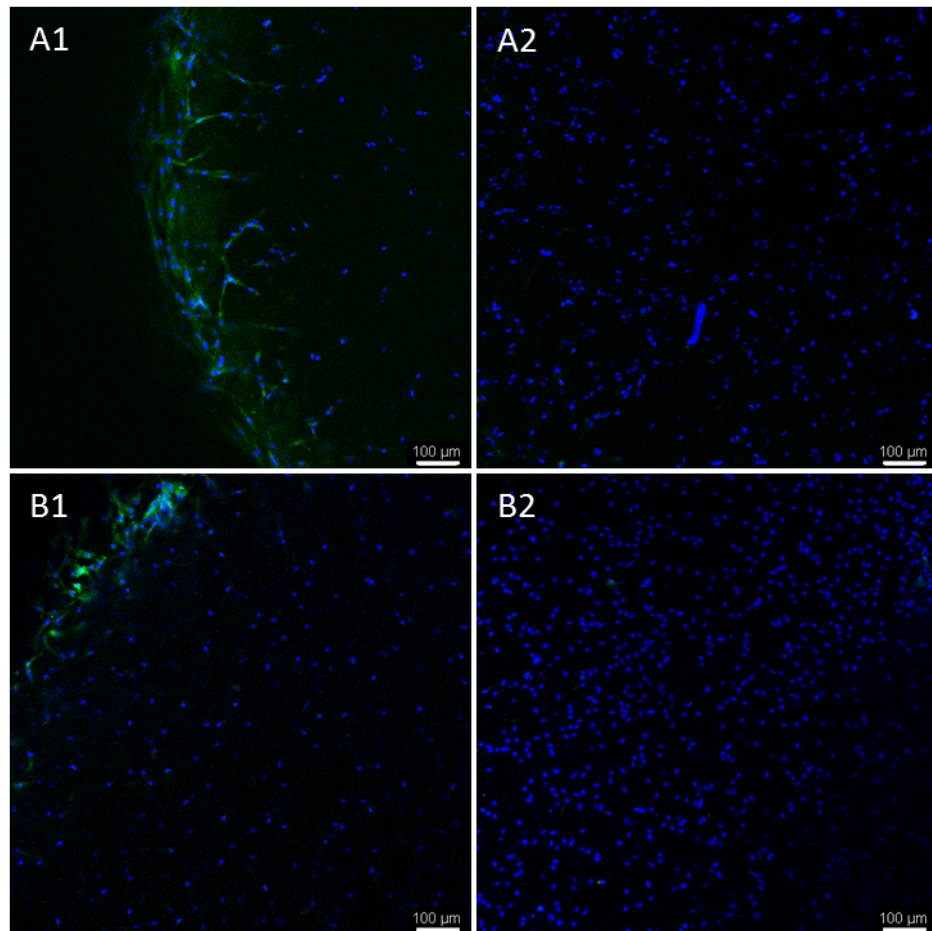
**Figure 6.7 – Confirmation of the specificity of β-III tubulin staining in nHDFs or DPSCs encapsulated in GelNOR hydrogels.** Representative images of (A1, A2) DPSC only or (B1, B2) nHDF only, gels stained with β-III tubulin (green) and DAPI nuclear stain (blue). Scale bar = 100 μm.

From the images of the negative control it can be seen that a small amount of background staining is observed at the edge of the hydrogel, and that the DPSCs may be more prone to picking up the stain than the nHDFs. The images do also show, however, that this staining is not significant.

It was also observed during single cell culture that the hybrid GNR hydrogels disintegrated more rapidly over time in culture than the native GelNOR hydrogels alone. During the co-culture testing this problem was not observed, and both the native and hybrid gels survived to the final timepoint equally well, as shown in Figure 6.8.
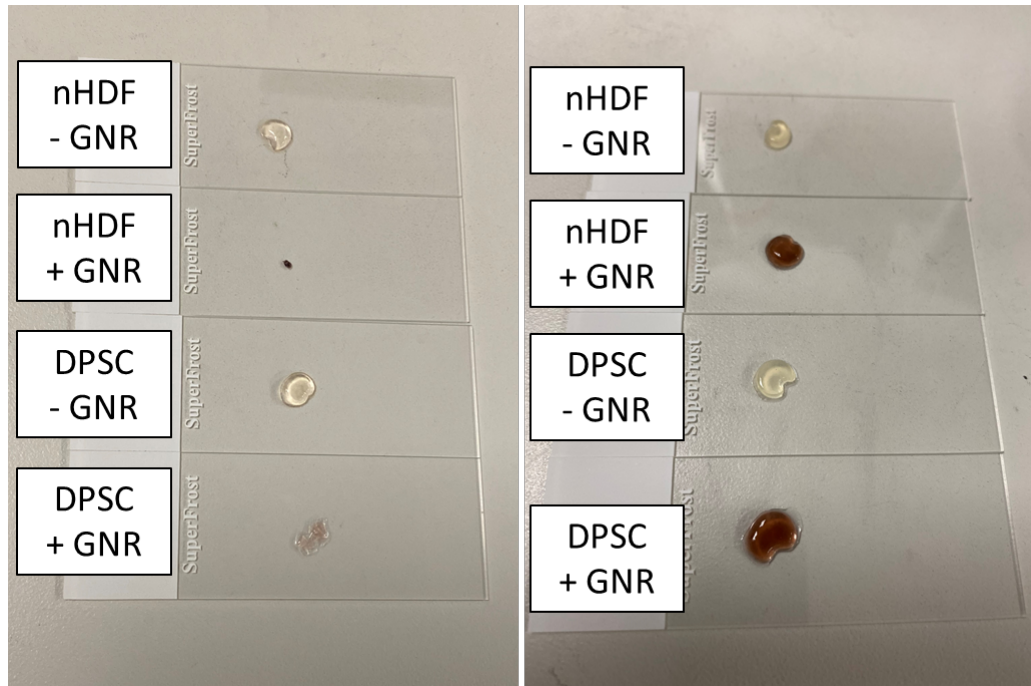
**Figure 6.8 – Gross evaluation of GelNOR hydrogels with and without GNRs after 21 days of culture.** Representative photographs of hydrogels cultured with (left) single cell only and (right) co-culture with PC12 cells.

## 6.4 Discussion

### 6.4.1 Comparison of DPSC and nHDF behaviour when encapsulated in GelNOR hydrogels and their response to the presence of GNRs

Both nHDFs and DPSCs encapsulated in 10 wt% GelNOR hydrogels were able to take an elongated morphology after just 7 days in culture and the two cell types were comparable in this respect, both achieving statistically significant drops in circularity score between day 1 and 7, but not being significantly different to each other at day 7. Further to this, despite the elongated light irradiation time used in this chapter (due to the need to overcome the light absorbance of the GNRs) the native gels achieved cell viability above 80% for both cell types. This is a particular advantage of the Ruthenium/SPS visible light initiation system used in this project in that the elongated irradiation times still allowed for good levels of cell viability at encapsulation. It would be expected that an exposure of this duration and intensity to UV light, for example when using an i2959 initiation system, would have a more significant impact on cell viability than the visible light used here (Lim *et al.*, 2016). This identifies the GelNOR hydrogel and Ruthenium/SPS initiation system as being equally suitable for culture of DPSCs as nHDFs.

The addition of GNRs to the encapsulating hydrogel, however, significantly reduced the viability of encapsulated cells for both nHDF and DPSCs, but again to a comparable level. There was no significant difference in viability between DPSCs and nHDFs in the native gels and no significant difference between the two in the hybrid hydrogels, but both cell types had a statistically significant reduction in viability when the native gels were compared to the hybrid gels. A reduction in viability was expected as previous studies have shown CTAB capped GNRs to be cytotoxic (Alkilany *et al.*, 2009), however, other studies have shown that CTAB capped GNR loaded gelatin hydrogels are still suitable for 3D cell culture in tissue engineering applications at the concentrations used in this project (Navaei *et al.*, 2016).

The reduction in viability of both cell types to approximately 60% at day 1 shows that the GNRs had a significant impact on cell health, however, the alamar blue assay showed that despite the drop in viability as measured by LIVE/DEAD assay, cell metabolism in the nHDFs was not significantly affected. This is potentially unexpected as such a significant drop in viability

would be expected to bring a corresponding drop in the overall metabolic activity of the cell population, but the nHDFs encapsulated with GNRs do not have a significantly lower metabolism than those encapsulated without, and even show higher metabolic activity than the DPSCs in the native gel. This unexpected result may be explained upon closer inspection of the confocal images of the LIVE/DEAD assay, which show significant dual labelling of the nHDFs. This means that the cells were damaged to an extent that they became permeable to the dead stain, which should be excluded from live cells with in-tact cell membranes, but are still alive and respiring to the extent that they turn the Calcein to fluorescent Calcein AM (Neri *et al.*, 2001). This explains the whole population metabolic activity not being significantly different for nHDFs encapsulated with and without GNRs despite the difference in measured viability. Despite initially not having significant difference in metabolic activity, as time in culture progresses the metabolic activity of the nHDFs in the GNR loaded gels trends downwards, whilst metabolic activity of those in the native gels remains approximately constant or trends slightly upwards, such that at day 21 there is a statistically significant difference of over 70% alamar blue reduction relative to the reference between these two test groups. Though alamar blue is generally less reliable as time in culture progresses, due to the fact that it does not account for metabolic activity per cell but rather metabolic activity of the whole population and is thus vulnerable to unequal changes in population size, this result certainly suggests a chronic effect of exposure to GNRs as the comparison is between the same group at different timepoints, and not different groups at the same timepoint. This is also reflected in the viability scores from the LIVE/DEAD assay, which do not recover after day 1 and instead stay low throughout the culture period.

For DPSCs encapsulated with GNRs, there is similarly extensive dual labelling in the LIVE/DEAD assay. Unlike the nHDFs, however, this also corresponds to a significant drop in metabolic activity as measured by the alamar blue assay at day 1, suggesting that the DPSCs are more adversely impacted by the GNRs than the nHDFs. The drop in metabolic activity then continues throughout the time in culture for DPSCs cultured in GNR loaded gels in a similar fashion to the nHDFs cultured in the GNR loaded gels. The more significant detrimental impact of the GNRs on the DPSCs can also be seen in the inability of DPSCs cultured in GNR loaded gels to elongate, instead remaining rounded throughout the full 21 days in culture despite all other test groups having significant reductions in circularity score between day 1 and 7.

Previous studies into GNR cytotoxicity have shown that it is generally driven by attached chemical side chains and other surface chemistries rather than physical elements such as the GNR size and aspect ratio (Wan *et al.*, 2015). Studies that have specifically investigated CTAB capped GNRs, such as the ones synthesised in this project, have suggested cytotoxicity in CTAB capped GNRs is largely driven by free CTAB in solution rather than the CTAB layer that is statically bound to the GNRs (Connor *et al.*, 2005) and these studies that have found CTAB to be cytotoxic have generally assessed viability over relatively short periods of time such as the 4 days used by Alkilany and colleagues (Alkilany *et al.*, 2009). For this reason it was predicted that the cytotoxic effect would reduce over time in culture as any free CTAB initially added during encapsulation was removed during media changes etc, and the only the CTAB capping the GNRs would remain. This would have resulted in poor initial cell viability at day 1, which would have then recovered over time in culture. This prediction was shown to be incorrect and the GNRs instead had a chronic effect on cell viability and metabolism. The most likely explanation is that despite the multiple centrifugation steps to reduce CTAB in the GNR storage solution to a minimal level, in line with the centrifugation described by (Takahashi *et al.*, 2005), enough CTAB is still transferred into cell culture with the GNRs to cause irreversible damage that the cell population cannot recover from even over 21 days in culture. There is also some disagreement in the literature, with others describing the CTAB 'capping' itself as still being cytotoxic without further modification (Wan *et al.*, 2015), so this is also a possibility.

Though the decrease in viability and metabolic activity for cells encapsulated in the GNR hybrid gels is significant over time in culture, it was decided that the achieved scores of approximately 60% viability were not a barrier to taking these gels forward into co-culture testing.

### 6.4.2 Comparison of PC12 behaviour when co-cultured with DPSCs or nHDFs and their response to the presence of GNRs

During the final experiments of this project, the co-culture system developed in the previous chapter was replicated in the hybrid GNR/GelNOR hydrogels developed in chapters 3 and 4. As an addition, because DPSCs are a more attractive cell type for use in tissue engineering approaches to treat SCI for the reasons previously described, a comparison between DPSCs and nHDFs was made during co-culture with PC12s, as well as during the single cell culture previously described in this chapter.

When comparing the behaviour of PC12s cultured in native GelNOR with nHDFs against those cultured with DPSCs, the most immediately obvious difference when viewing the images qualitatively is the presence of a much greater number of PC12 cell aggregates that are larger in size in the DPSC co-culture than in the nHDF. This is reflected in the semi-quantitative ImageJ analysis, in which the measured average particle size for the native GelNOR DPSC co-culture is the largest of all the test groups, though this is not statistically significant except against the DPSC/PC12 co-culture in the GNR hybrid gel. Again at day 21 the PC12s cultured with DPSCs in native GelNOR form aggregates that are much larger than those in the other test groups, but the result is not statistically significant. Particle size was taken as an indirect measurement of proliferation, with PC12s cells generally forming large aggregates in non-adherent culture unless they are differentiating (Wiatrak *et al.*, 2020), and this result suggests that DPSCs acted to drive proliferation in PC12s rather than differentiation, which is again reflected in the lower measured neurite outgrowth for PC12s culture with DPSCs than nHDFs. The significantly lower particle size in the PC12s cultured with DPSCs in GNR loaded gels compared to native GelNOR is likely reflective of the significantly impacted viability and metabolism of DPSCs in GNR loaded gels as shown in the single cell culture, meaning the DPSCs in the GNR loaded gels are unable to drive PC12 proliferation to the same extent as those in the native GelNOR. Though co-culture with DPSCs appears to drive proliferation rather than differentiation, PC12s cultured with DPSCs do still see significantly greater neurite extension between day 14 and 21 in both the GNR and non-GNR hydrogels, but still have lower neurite lengths than nHDFs in each of the gel types tested.

The consistently longer neurite extension after day 14 in PC12s cultured with nHDFs than those cultured with DPSCs suggests that nHDFs drive

differentiation in PC12 cells to a greater extent than DPSCs, and this is also reflected in the smaller average particle sizes.

DPSCs have previously been used to differentiate other neuronal cell lines through the secretion of neurotrophic factors including NGF (N. Ahmed *et al.*, 2016), and thus it was expected that DPSCs would stimulate PC12s to differentiate in a similar manner due to the well-established method of differentiating PC12s through addition of NGF (Greene and Tischler, 1976). Though the nHDFs do appear to have stimulated PC12 differentiation to a greater extent than DPSCs in this chapter, PC12 neurite length did still increase significantly in both native GelNOR and GNR hybrid gels when cultured with DPSCs. There is unfortunately no negative control to compare this neurite outgrowth to, due to the tendency of PC12 cells to rapidly degrade the GelNOR gels in single cell culture.

When the PC12 behaviour is compared in the native GelNOR and GNR hybrid hydrogels, though there is no significant difference at any time point for those cultured with DPSCs, the PC12s cultured with nHDFs sprouted statistically significantly longer neurites by day 14. At the final timepoint of day 21, the average longest neurite length of PC12s cultured with both nHDFs and DPSCs is greater in GNR hybrid hydrogels than for those cultured in native GelNOR, though neither comparison is statistically significant.

Comparing to the available literature, a number of previous studies have studied the impact of electrical conductivity on PC12 neurite outgrowth on both 2D surfaces (Park *et al.*, 2009) and in 3D hydrogels (Shi *et al.*, 2014). All currently available literature in this area, however, appears to study the effect of increased electrical conductivity in combination with electrical stimulation and there is no available comparison of tissue engineering scaffolds of various electrical conductivity in the absence of electrical stimulation, as was performed in this chapter. A recognised advantage of PC12s as a model neuronal cell is that they are themselves electrically active in differentiated state (Wang *et al.*, 2015), with a recently published study by Zhao and colleagues finding that PC12s demonstrated similar capacitance gradients across their cell bodies to primary neurons (Zhao *et al.*, 2019), and this may explain the ability of increased electrical conductivity in the surrounding hydrogel to have an impact on neurite outgrowth even in the absence of electrical stimulation. This should however be considered in the context of mixed results in statistical testing indicating a relatively low strength of evidence.

Further, because of the cytotoxicity of the GNRs in single cell culture with nHDFs and DPSCs, it is difficult to discern what impact this has in the co-culture, and may be considered a confounding variable in this final analysis. As an example, though the metabolic activity of the nHDFs was not as significantly impacted as that of the DPSCs, it is difficult to say for sure what impact the reduced metabolism and viability of the DPSCs had on the production of factors that drove the behaviour of the PC12s in co-culture.

Further to the impact on the DPSCs and nHDFs, the direct impact on the health of the PC12s themselves should be considered. From the results it does not seem that the GNRs themselves are a barrier to PC12 proliferation and differentiation, as shown by the PC12s encapsulated with nHDFs in GNR hybrid hydrogels, but the response of the PC12s to the GNRs in terms of viability and metabolism was not specifically analysed in this study. Although there has been previous analysis of GNR cytotoxicity on PC12s in the literature (Marzouni *et al.*, 2018), that study used a different method of GNR synthesis, meaning that the GNRs would not have been CTAB capped which is the likely driver of cytotoxicity in this project. Therefore it is difficult to know exactly what detrimental impact the GNRs may or may not have had on the PC12s, and in turn what effect this may have had on neurite outgrowth and cell aggregate size as key measures of PC12 behaviour in the final analysis.

A final consideration is the accuracy of the semi-quantitative image processing methods used in this chapter to generate quantitative data from qualitative images. Though automated methods such as the NeuronJ plugin for ImageJ have previously been described in the literature (Meijering *et al.*, 2004), the decision was taken in this project to use manual assessment methods in ImageJ to measure neurite outgrowth. Though the use of manual methods has been shown to be similarly accurate to automated (Meijering *et al.*, 2004), with the main advantage of automation being saving of labour intensity, manual methods are unavoidably subjective and thus may bring reduced reliability. Many of the automated image processing methods for neurite measurement perform well on 2D neurites with low spatial density and high neurite length but are not well equipped for analysis of images with many overlapping cells such as those typically obtained from confocal imaging of 3D hydrogels. This was the primary reason for using manual methods rather than automation, as well as the relative ease and low impact on accuracy of manual judgement of where a cell body ends and a neurite begins. The most significant identified weakness of this length of longest

neurite method is that it doesn't take into account that the proportion of cells in an image that are sprouting neurites and instead just represents an average of the cells that are. In this way, the measured average neurite lengths may be approximately similar between two test groups without showing that one test group may have a significantly smaller proportion of the cells actually sprouting neurites, and thus lower true levels of neurogenic differentiation may be represented as equal to higher levels of neurogenic differentiation based on neurite length alone.

## 6.5  Conclusions

The results of this chapter demonstrate the GelNOR hydrogel and visible light initiation system developed in this project to be suitable for DPSC culture. Further, it was also demonstrated that co-culture with DPSCs and nHDFs have different effects on PC12 cells, with nHDF co-culture favouring differentiation and neurite extension, and culture with DPSCs promoting proliferation ahead of differentiation. The addition of GNRs to make the GelNOR hydrogel more electrically conductive may increase neurite outgrowth length from differentiating PC12 cells, but further study is needed to confirm this.

# Chapter 7
# General Discussion and Future Work

This project was set out with two key aims; to develop an electrically conductive hydrogel scaffold and to biologically test the scaffold with both neural cells and DPSCs, with a long-term view to use in tissue engineering approaches for the treatment of SCI.

Within these two key aims were a number of objectives. Initially these objectives took the form of the development and optimisation of a hydrogel and initiation system, the synthesis and addition of electrically conductive nanoparticles to form an electrically conductive hydrogel, and the physical characterisation of this hydrogel. The project then moved on to develop a CNS model co-culture system, using nHDF and PC12 cells, and to test the effect of the electrically conductive scaffold on the co-culture model, as well as on DPSCs as a target cell type for tissue engineering applications.

As discussed in Chapter 1, electrically conductive hydrogels have recently been investigated for SCI treatment and have had success in stimulating axonal growth and NSC recruitment *in vivo* (L. Zhou *et al.*, 2018b). Despite this success, however, few of the previous studies have sought to use the hydrogel as a vehicle to deliver cells in a combined tissue engineering approach, instead opting to test the material with cells *in vitro* and deliver the hydrogel as an a-cellular biomaterial *in vivo* (Xu *et al.*, 2021). The attractiveness of DPSCs' ability to respond to SCI in a multi-faceted way identifies them as a promising cell type for tissue engineering approaches (Yamamoto *et al.*, 2014), and this is why they were chosen as the final cell type for testing with the developed electrically conductive scaffold, alongside the model neural cells.

During the first results chapter, a previously described visible light system, developed for use in chain-growth GelMA hydrogels (Lim *et al.*, 2016), was tested in a step-growth GelNOR system. The results demonstrated that the visible light system was successfully adapted for polymerisation of GelNOR. Unexpectedly, mass loss and swelling testing showed that even the lowest irradiation time of 15 seconds enabled optimum crosslinking to take place, with the soluble fraction not being significantly different to that at the highest timepoint (Figure 3.3). This is in disagreement with the findings of Munoz and colleagues (Mũnoz *et al.*, 2014), who found that although gelation is observed within 12 seconds, complete gelation was not achieved until 300 seconds. Though Munoz used a UV light initiation system, this only changes

the way in which the free radical for initiation is generated and should not have any impact on the chemical reaction that results in crosslinking. It was hypothesised that once the free radical is generated the gelation reaction is self-sustaining and thus will continue post-irradiation (Section 3.4.1). This would be advantageous in-vivo since it is difficult to light irradiate a hydrogel inside the body without the use of invasive surgery to access the area to be irradiated. This poses an interesting aspect of further work which combines the approach taken in this project of a light exposure time sweep and the approach taken by Munoz of time-sweeping rheological properties during constant irradiation. This may take the form of constant rheological measurement over the space of 10 minutes, with only a short irradiation time at the beginning of the test (e.g. 30 seconds), to allow analysis of changing rheological properties in the gel after light irradiation has ceased.

The visible light system produced good fibroblast viability in the native GelNOR gels, both at 3 minute irradiation (Chapter 3) and at 10 minute irradiation (Chapter 6). There was a difference in viability between the approximately 93% seen for HFFs irradiated for 3 minutes in Chapter 3 and the 83% seen in nHDFs irradiated for 10 minutes in Chapter 6, but both data sets had large error bars and HFFs are a juvenile type of nHDFs so the comparison may not be a fair one. Though the high viabilities achieved at long irradiation times highlights the benefit of the visible light system, these benefits could have been demonstrated more strongly through comparison to UV-light initiation systems that have previously been used to initiate gelation in GelNOR such as LAP or i2959 (Tigner *et al.*, 2020).

One problem with the use of a light-based initiation system, as used in this project, was the addition of GNRs which have an impact on the ability of light to pass through the hydrogels and are highly light absorptive, even if less so in the 400-450 nm wavelength used with this initiation system (Scarabelli *et al.*, 2015). The impact of this light absorption is to limit the GNR concentration able to be used at a set thickness, with the trade-off being that the thicker the gel, the lower the GNR concentration that can be achieved whilst maintaining an equal level of gel curing and vice-versa. Other researchers using GNR loaded hydrogels and light based initiation systems have sought to use thin films of approximately 150 μm to avoid the problem with light having difficulty passing through the construct (Navaei *et al.*, 2016). This in turn, however, presents issues associated with the use of thin films, including limitations on the types of physical characterisation available and special preparation of samples that these techniques require. For example,

surface based techniques, such as AFM, are required to characterise materials at this thickness (Ma *et al.*, 2016) rather than techniques that measure bulk properties of the construct such as the uni-axial compressive and rheological testing used in this project, which may be more relevant to future in-vivo applications.

This trade-off between hydrogel thickness and GNR concentration was not considered a limiting factor in this project due to the significant increase in electrical conductivity at the lowest GNR concentration used (0.5 mg/ml) thus the impact of increased electrical conductivity on the behaviour of cultured cells could still be investigated.

A more significant consideration than the reduced light absorbance is the significant cytotoxicity caused by the GNRs even at low concentrations, indicating that higher GNR concentrations may have performed poorly in cell-culture. Though the use of multiple centrifugation steps in DIW to remove excess CTAB was initially explored, in line with Navaei and colleagues (Navaei *et al.*, 2016), the results of UV-visible spectrophotometry and TEM analysis into GNR encapsulations showed that this approach was not feasible due to poor GNR dispersion in the hybrid hydrogel. Subsequently, low CTAB concentrations (0.0001M) were used as previous literature suggested at least some surfactant would be needed to prevent aggregation (Scarabelli *et al.*, 2015).

The development of the co-culture system, in which nHDFs are used to differentiate PC12s, described in this project is possibly novel as nothing was found in the literature that previously demonstrated this co-culture for this purpose. Interestingly, the co-culture seemed to perform differently between the fibrin hydrogels used in Chapter 5 and the GelNOR gels used in Chapter 6. In Chapter 5 the PC12s seemed to only form a layer in 2D at the bottom of the gel and move outside the gel and onto the 2D culture surface, rather than remain in true 3D culture. In the GelNOR gels this movement was not seen, and the PC12s differentiated in 3D throughout the height of the gels. In the discussion in Chapter 5 it was hypothesised that the movement to the bottom surface of the gel was due to the contractile forces created at the bottom of the gel due to the gel/culture surface interface. In the fibrin hydrogels the gel remained attached to the culture surface during long term culture and this will create contractile forces along the interface as demonstrated by Noh and colleagues who deliberately used pins to align these forces (Noh *et al.*, 2020). The fact that the PC12s remained in 3D throughout the height of GelNOR gels, which were separated from the mould

immediately after curing and were cultured in a 'free-floating' manner, would seem to support this hypothesis. Similarly in the GelNOR gels, nHDFs and PC12s were not able to migrate outside of the gels, as they were when cultured in fibrin hydrogels. This is likely due to the lack of attached gel/culture surface interface, which has been shown to have a significant impact on migration and behaviour of cells in 3D hydrogels due to the creation of stiffness gradients at the stiffened support interface (Rao *et al.*, 2012).

Although the co-culture of PC12 cells in hybrid hydrogels still performed well with nHDFs in terms of PC12 differentiation and neurite outgrowth, allowing investigations into the effect of electrical conductivity on neurite outgrowth, the PC12 co-cultures performed less well with DPSCs. Future work specifically aimed at the use of DPSCs with GNR-loaded scaffolds may look to initially explore the use of methods to reduce CTAB toxicity. Approaches to minimise GNR cytotoxicity whilst maintaining electrical conductivity may include re-capping of the GNRs after synthesis in CTAB (Mehtala *et al.*, 2014), addition of inerting groups to the CTAB to minimise GNR cytotoxicity from surface chemistry (Wan *et al.*, 2015), or using an alternative synthesis approach resulting in GNRs capped with alternate chemicals such as citrate (Jana, Gearheart and Murphy, 2001) at the expense of production volume. Further, an investigation into lower GNR concentrations may systematically reduce the GNR concentration from the 0.5 mg/ml used in Chapter 6, and determine at which point the hybrid hydrogel stops being statistically significantly more electrically conductive than the native GelNOR.

Electrical activity is a key aspect of neural biology, and although PC12 cells do not form real synapses with each other, they are capable of generating action potentials (Hu *et al.*, 2018). In this project  neurite outgrowth was observed following culture of PC12 cells with nHDFs and DPSCs (Chapter 6). However, whether these cells were functional and generated action potentials was not evaluated. Further work to support the morphological data could employ techniques like patch clamping or electrode arrays to evaluate the functional activity of the PC12 cells; however, though there is some use of use of these techniques in 3D hydrogels in the literature (Kruskal *et al.*, 2015), it is limited. Further work could also use molecular biology approaches to elucidate the mechanism though which nHDFs and DPSCs are directing the behaviour of PC12s in this study. Previous research has shown that nHDFs and DPSCs release numerous factors which are known to contribute to the differentiation of PC12 cells (Nishiguchi *et al.*, 2014;

Sultan *et al.*, 2021), and a good starting point may be to use inhibitors of these previously identified factors and observe the effects on PC12 behaviour. Further, techniques to measure changes in gene expression such as PCR and changes in protein secretion such as gel electrophoresis could have been used to identify exactly what parts of the nHDF and DPSC secretome are having significant effects on the PC12s.

There is also the question of whether the use of native GelNOR as a negative control to the GNR loaded GelNOR is appropriate to demonstrate the effect of increased electrical conductivity alone. This may disregard the effect of nanoparticles in general, some of which have been shown affect cell viability based on shape alone (Bahadar *et al.*, 2016), and it is possible that a more appropriate negative control to isolate the effect of electrical conductivity alone would have been to use GelNOR loaded with another type of non-conductive nanoparticle, such as silica nanoparticles (Park and Park, 2009).

There may be other weaknesses present in the recurring methods used throughout this project, with the use of the alamar blue assay to measure cellular metabolism and of ImageJ to generate quantitative data from qualitative images being two possible areas.

Alamar blue is a well-accepted method of testing cell metabolism and viability, being one of the most highly referenced substances for cytotoxicity and viability assays on PubMed (Rampersad, 2012). Despite its well accepted use, alamar blue measures metabolic activity across a whole cell population and thus is weak to the confounding variable of differing cell population growth rates across test groups. As a result of this, the tendency of alamar blue to overestimate cell proliferation by combining it with cell metabolism is recognised in the literature (Quent *et al.*, 2010). Though the particular weaknesses of alamar blue were taken into account in the discussion of each chapter it was used in, and the fact that it did not provide a per cell metabolic activity measurement was emphasised, stronger data may have been obtained by combining the alamar blue assay with a DNA quantification assay such as Pico Green in order to control for cell population size.

The use of ImageJ to semi-quantitatively generate numerical data from images is also a possible weakness. In order to minimise the subjective input from an operator, images measuring cell size, viability, and circularity were analysed using an automated routine that was applied equally across all images. Though this removed operator error from the image processing,

the images themselves were taken by a manual operator, on gels that contained different cell types, often behaving differently from each other, and thus the images themselves contained natural variations. The natural variations in images meant that not all images were processed equally accurately because no one automated routine would work equally well for all of them. This is a possible weakness in the use of ImageJ to quantify aspects such as cell viability, which could possibly be done by alternate methods such as LDH assay (Kaja *et al.*, 2017), but for aspects such as circularity and size there is little option other than image processing, and the technique is consistent with the literature (Mũnoz *et al.*, 2014).

There are a number of possible avenues for further work continuing from the results achieved in this project, some of which have already been discussed. The most significant of these potential avenues is the addition of aligned mechanical forces and electrical stimulation. These are important for tissue engineering approaches to the spinal cord because they both stimulate cell alignment (Zhang *et al.*, 2018; Noh *et al.*, 2020). Though the hydrogel scaffold in this project was electrically conductive, no external electrical or mechanical cues were added to stimulate alignment. The spinal cord, conversely, is highly aligned and contains complex architectures in which cells are highly organised with neurons bundled into tracts in ascending and descending pathways (O'Shea, Burda and Sofroniew, 2017). Thus, the addition of external forces to stimulate alignment would be a logical next step in the development of this culture system. A possible set-up to achieve cellular alignment within hydrogels is detailed in Figure 7.1.

## 1. Assemble Electrical Stimulation Chamber
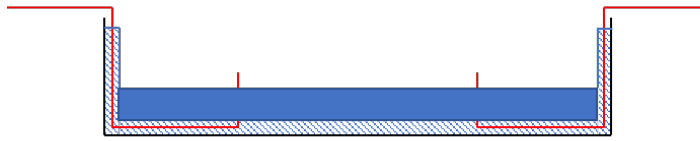
## 2. Add Mould and Hydrogel Solution
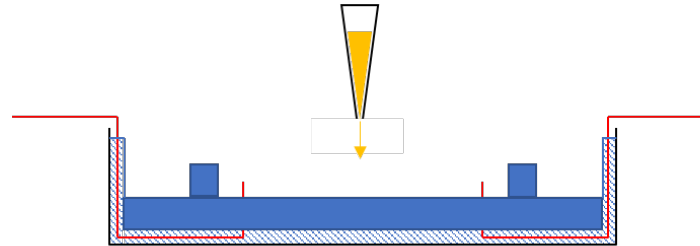
## 3. Cure Hydrogel with Light-Irradiation
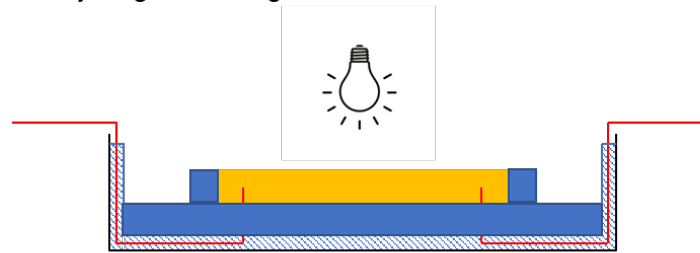
## 4. Remove Mould and Add Culture Media

| | | | |
|---|---|---|---|
| — | Platinum wire electrode | ▨ | Silicone Filler |
| — | Petri dish | ■ | Hydrogel |
| ■ | Silicone Sheet | ▨ | Cell culture media |

**Figure 7.1 – Possible equipment and process set-up for future work, allowing addition of electrical stimulation and aligned contractile forces.**

The set-up described in Figure 7.1 would use platinum wires, insulated by silicone, connected to a power supply in cell culture, to stimulate the cells encapsulated within a GNR hybrid hydrogel , such as the model co-culture developed in Chapters 5 and 6. These platinum wires would serve two functions: firstly, the electrodes allow electrical stimulation of the cells. Previous studies have typically used alternating current at a potential of

approximately 250 mV for short periods each day over multiple days in culture to successfully stimulate increased neurite outgrowth in PC12s in 2D (Park *et al.*, 2009). Although this research applied electrical stimulation to cells in 2D, this could be adapted for use in 3D. Further, other studies have also used electrical stimulation to enhance neurite outgrowth from other cell types in 3D, such as the dorsal root ganglia used by Koppes and colleagues (Koppes *et al.*, 2016). Koppes' study, however, used direct rather than alternating current, which has previously been shown to result in poor viability when used with PC12s (Park *et al.*, 2009), and used 50 mV stimulation for an extended period of 8 hours in a one-time exposure. In short, the literature is far from in agreement on the best electrical stimulation protocols to elicit improved neurite extension from neural cells, and any future protocol may combine aspects from many different sources.

The second function of the platinum wires would be to act as 'pins' for the construct. By pinning the construct at set distances, when the cells remodel the matrix and cause the hydrogel to contract, this will align those contractile forces along the axis of the pins (Noh *et al.*, 2020). This alignment of contractile forces has been shown to produce alignment in the encapsulated cells and is a well-used technique not only in neural tissue engineering, but also in other tissues where alignment is important, such as muscle (Sharples *et al.*, 2012).

Further to that already discussed, replacement of PC12s with primary cells such as primary cortical neurons may be a logical next step as they have been shown to respond well to electrical stimulation (Zhang *et al.*, 2018). The movement from cell line to primary cells is a progression of the work to higher physiological relevance, due to the tendency of primary cells to be more representative of the *in vivo* tissue.

The final development worth mentioning at this point is the movement to a hydrogel initiation system capable of initiation in the dark, or at least being capable of delivery through injection. If the developed biomaterial is to be used in *in vivo* applications this is likely to be important as the use of a light initiated system would theoretically require open spinal surgery to expose the hydrogel to light for curing.

In summary, this project provided novel data on a number of areas within the scientific literature. Firstly, the ruthenium and SPS visible light initiation system had not been used previously in step-growth hydrogels, and this demonstration of its capability identifies it as a viable solution across a range of hydrogels where other norish type II visible light systems have previously

been outperformed by norish type I photo-cleaved initiators that rely on UV-light (Lin, Ki and Shih, 2015). Further, the project demonstrated crosslinking of GelNOR using a wider range of crosslinkers and NOR:SH ratios, most notably PEG-8SH, which had not previously been demonstrated for crosslinking of GelNOR in the literature. Though PEG-8 was not suitable for use in this project, it will undoubtedly be of use as a crosslinker for GelNOR hydrogels in applications requiring higher modulus gels such as osteochondral tissue engineering (Hung *et al.*, 2004). The project also demonstrated increased electrical conductivity in GNR loaded GelNOR hydrogels, a new hybrid hydrogel type which had not previously been described, and used these gels to support a 3D co-culture in which nHDFs were used to stimulate differentiation in PC12 cells.

# Chapter 8
# General Conclusions

After matching the key conclusions from this project with the previously described aims and objectives from each chapter, they are as follows:

- The visible light initiation system using Ruthenium and SPS is suitable for gelation of step-growth hydrogels of the thiol-norbornene 'click' type used in this project with a range of crosslinkers.
- The physical properties of GelNOR hydrogels are highly tuneable through selection of wt%, crosslinker, and crosslinker ratio across a larger range of crosslinkers and ratios than previously described in the literature.
- The combination of the GelNOR hydrogel and Ruthenium/SPS visible-light initiation system is highly cytocompatible with both nHDFs/HFFs and DPSCs.
- The addition of GNRs to GelNOR increases its electrical conductivity, but above a concentration of approximately 1.0 mg/ml GNR addition causes GelNOR to lose its structure when cured using a visible light initiation system.
- nHDFs are capable of stimulating differentiation and neurite outgrowth of PC12 cells in co-culture.
- CTAB capped GNRs have a significant cytotoxic effect on both nHDFs and DPSCs.
- DPSCs acted to increase proliferation of PC12 cells in co-culture.
- There is evidence that the increased electrical conductivity of the GNR/GelNOR hybrid scaffold improved neurite outgrowth in PC12s, but due to mixed results in statistical analysis and potential confounding variables the strength of evidence is weak and further study is required.

# List of References

AANS/CNS (2002) 'Pharmacological therapy after acute cervical spinal cord injury.', *Neurosurgery*, 50(3 Suppl), pp. S63-72. Available at: http://www.ncbi.nlm.nih.gov/pubmed/12431289 (Accessed: 4 July 2017).

Abematsu, M. *et al.* (2010) 'Neurons derived from transplanted neural stem cells restore disrupted neuronal circuitry in a mouse model of spinal cord injury.', *The Journal of clinical investigation*, 120(9), pp. 3255–66. doi: 10.1172/JCI42957.

Ahmed, E. M. (2015) 'Hydrogel: Preparation, characterization, and applications: A review', *Journal of Advanced Research*, 6, pp. 105–121. doi: 10.1016/j.jare.2013.07.006.

Ahmed, N. *et al.* (2016) 'The effects of hypoxia on the stemness properties of human dental pulp stem cells (DPSCs).', *Scientific reports*, 6, p. 35476. doi: 10.1038/srep35476.

Ahmed, N. E. M. B. *et al.* (2016) 'Therapeutic Potential of Dental Pulp Stem Cell Secretome for Alzheimer's Disease Treatment: An in Vitro Study', *Stem Cells International*, 2016. doi: 10.1155/2016/8102478.

Ahmed, T. A. E., Dare, E. V. and Hincke, M. (2008) 'Fibrin: A Versatile Scaffold for Tissue Engineering Applications', *https://home.liebertpub.com/teb*, 14(2), pp. 199–215. doi: 10.1089/TEN.TEB.2007.0435.

Alkilany, A. M. *et al.* (2009) 'Cellular Uptake and Cytotoxicity of Gold Nanorods: Molecular Origin of Cytotoxicity and Surface Effects', *Small*, 5(6), pp. 701–708. doi: 10.1002/smll.200801546.

de Almeida, F. M. *et al.* (2011) 'Human Dental Pulp Cells: A New Source of Cell Therapy in a Mouse Model of Compressive Spinal Cord Injury', *Journal of Neurotrauma*, 28(9), pp. 1939–1949. doi: 10.1089/neu.2010.1317.

Alper, J. (2009) 'Geron gets green light for human trial of ES cell–derived product', *Nature Biotechnology*, 27(3), pp. 213–214. doi: 10.1038/nbt0309-213a.

Alvarez-Buylla, A. and García-Verdugo, J. M. (2002) 'Neurogenesis in Adult Subventricular Zone', *Journal of Neuroscience*, 22(3), pp. 629–634. doi: 10.1523/JNEUROSCI.22-03-00629.2002.

Anderson, K. D. (2004) 'Targeting Recovery: Priorities of the Spinal Cord-Injured Population', *Journal of Neurotrauma*, 21(10), pp. 1371–1383. doi: 10.1089/neu.2004.21.1371.

Arnold, S. A. and Hagg, T. (2011) 'Anti-Inflammatory Treatments during the Chronic Phase of Spinal Cord Injury Improve Locomotor Function in Adult Mice', *Journal of Neurotrauma*, 28(9), pp. 1995–2002. doi: 10.1089/neu.2011.1888.

Arthur, A. *et al.* (2008) 'Adult Human Dental Pulp Stem Cells Differentiate Toward Functionally Active Neurons Under Appropriate Environmental Cues', *Stem Cells*, 26(7), pp. 1787–1795. doi: 10.1634/stemcells.2007-0979.

Askari, N. *et al.* (2015) 'Human Dental Pulp Stem Cells Differentiate into Oligodendrocyte Progenitors Using the Expression of Olig2 Transcription Factor', *Cells Tissues Organs*, 200(2), pp. 93–103. doi: 10.1159/000381668.

Ates, O. *et al.* (2007) 'Comparative neuroprotective effect of sodium channel blockers after experimental spinal cord injury', *Journal of Clinical Neuroscience*, 14(7), pp. 658–665. doi: 10.1016/j.jocn.2006.03.023.

Athukorala, S. S. *et al.* (2021) '3D Printable Electrically Conductive Hydrogel Scaffolds for Biomedical Applications: A Review', *Polymers*, 13(3), pp. 1–21. doi: 10.3390/POLYM13030474.

Bae, K. S. *et al.* (2011) 'Neuron-like differentiation of bone marrow-derived mesenchymal stem cells.', *Yonsei medical journal*, 52(3), pp. 401–12. doi: 10.3349/ymj.2011.52.3.401.

Bahadar, H. *et al.* (2016) 'Toxicity of Nanoparticles and an Overview of Current Experimental Models', *Iranian Biomedical Journal*, 20(1), p. 1. doi: 10.7508/IBJ.2016.01.001.

Bak, L. K. and Walls, A. B. (2018) 'Rebuttal from Lasse K. Bak and Anne B. Walls', *Journal of Physiology*, 596(3). doi: 10.1113/JP275507.

Balint, R., Cassidy, N. J. and Cartmell, S. H. (2014) 'Conductive polymers: Towards a smart biomaterial for tissue engineering', *Acta Biomaterialia*, 10(6), pp. 2341–2353. doi: 10.1016/J.ACTBIO.2014.02.015.

Bao, F. *et al.* (2004) 'Early anti-inflammatory treatment reduces lipid peroxidation and protein nitration after spinal cord injury in rats', *Journal of Neurochemistry*, 88(6), pp. 1335–1344. doi: 10.1046/j.1471-4159.2003.02240.x.

Bartlett, R. D., Choi, D. and Phillips, J. B. (2016) 'Biomechanical properties of the spinal cord: Implications for tissue engineering and clinical translation', *Regenerative Medicine*. doi: 10.2217/rme-2016-0065.

Baumann, N. and Pham-Dinh, D. (2001) 'Biology of oligodendrocyte and myelin in the mammalian central nervous system', *Physiological Reviews*. doi: 10.1152/physrev.2001.81.2.871.

Bermúdez-Jiménez, C. *et al.* (2019) 'Hydrogel-embedded gold nanorods activated by plasmonic photothermy with potent antimicrobial activity', *Nanomedicine: Nanotechnology, Biology, and Medicine*, 22. doi: 10.1016/j.nano.2019.102093.

Bhardwaj, N. and Kundu, S. C. (2010) 'Electrospinning: A fascinating fiber fabrication technique', *Biotechnology Advances*, 28(3), pp. 325–347. doi: 10.1016/J.BIOTECHADV.2010.01.004.

Del Bigio, M. R. (2010) 'Ependymal cells: Biology and pathology', *Acta Neuropathologica*. doi: 10.1007/s00401-009-0624-y.

Billiet, L., Fournier, D. and Du Prez, F. (2009) 'Step-growth polymerization and "click" chemistry: The oldest polymers rejuvenated', *Polymer*. doi: 10.1016/j.polymer.2009.06.034.

Boido, M. *et al.* (2009) 'Embryonic and adult stem cells promote raphespinal axon outgrowth and improve functional outcome following spinal hemisection in mice', *European Journal of Neuroscience*, 30(5), pp. 833–846. doi:

10.1111/j.1460-9568.2009.06879.x.

Borgens, R. B. (1999) 'Electrically mediated regeneration and guidance of adult mammalian spinal axons into polymeric channels', *Neuroscience*, 91(1), pp. 251–264. doi: 10.1016/S0306-4522(98)00584-3.

Bracken, M. B. *et al.* (1990) 'A Randomized, Controlled Trial of Methylprednisolone or Naloxone in the Treatment of Acute Spinal-Cord Injury', *New England Journal of Medicine*, 322(20), pp. 1405–1411. doi: 10.1056/NEJM199005173222001.

Bradbury, E. J. and Burnside, E. R. (2019) 'Moving beyond the glial scar for spinal cord repair', *Nature Communications 2019 10:1*, 10(1), pp. 1–15. doi: 10.1038/s41467-019-11707-7.

Bradbury, E. J. and Carter, L. M. (2011) 'Manipulating the glial scar: Chondroitinase ABC as a therapy for spinal cord injury', *Brain Research Bulletin*, 84(4–5), pp. 306–316. doi: 10.1016/j.brainresbull.2010.06.015.

Bretzner, F. *et al.* (2011) 'Target Populations for First-In-Human Embryonic Stem Cell Research in Spinal Cord Injury', *Cell Stem Cell*, 8(5), pp. 468–475. doi: 10.1016/j.stem.2011.04.012.

Brunette, D. D. and Rockswold, G. L. (1987) 'Neurologic recovery following rapid spinal realignment for complete cervical spinal cord injury.', *The Journal of trauma*, 27(4), pp. 445–7. Available at: http://www.ncbi.nlm.nih.gov/pubmed/3573096 (Accessed: 4 July 2017).

Burnside, E. R. and Bradbury, E. J. (2014) 'Review: Manipulating the extracellular matrix and its role in brain and spinal cord plasticity and repair', *Neuropathology and Applied Neurobiology*. doi: 10.1111/nan.12114.

Burrows, N. D. *et al.* (2016) 'Surface Chemistry of Gold Nanorods', *Langmuir*, 32(39), pp. 9905–9921. doi: 10.1021/ACS.LANGMUIR.6B02706.

Byrnes, K. R. *et al.* (2007) 'Cell cycle activation contributes to post-mitotic cell death and secondary damage after spinal cord injury', *Brain*, 130(11), pp. 2977–2992. doi: 10.1093/brain/awm179.

Cantarella, G. *et al.* (2002) 'Nerve growth factor-endothelial cell interaction leads to angiogenesis in vitro and in vivo.', *The FASEB journal : official publication of the Federation of American Societies for Experimental Biology*, 16(10), pp. 1307–1309. doi: 10.1096/fj.01-1000fje.

Cao, J., Sun, T. and Grattan, K. T. V (2014) 'Gold nanorod-based localized surface plasmon resonance biosensors: A review', *Sensors & Actuators: B. Chemical*, 195, pp. 332–351. doi: 10.1016/j.snb.2014.01.056.

Carnicer-Lombarte, A. *et al.* (2019) 'Mechanical matching of implant to host minimises foreign body reaction', *bioRxiv*, p. 829648. doi: 10.1101/829648.

Cha, C. *et al.* (2011) 'Tuning the dependency between stiffness and permeability of a cell encapsulating hydrogel with hydrophilic pendant chains', *Acta Biomaterialia*, 7(10), pp. 3719–3728. doi: 10.1016/j.actbio.2011.06.017.

Chua, J. S. *et al.* (2014) 'Extending neurites sense the depth of the underlying topography during neuronal differentiation and contact guidance', *Biomaterials*, 35(27), pp. 7750–7761. doi:

10.1016/J.BIOMATERIALS.2014.06.008.

Connor, E. E. *et al.* (2005) 'Gold Nanoparticles Are Taken Up by Human Cells but Do Not Cause Acute Cytotoxicity', *Small*, 1(3), pp. 325–327. doi: 10.1002/SMLL.200400093.

Costa-Almeida, R. *et al.* (2015) 'Fibroblast-Endothelial Partners for Vascularization Strategies in Tissue Engineering', *Tissue Engineering. Part A*, 21(5–6), p. 1055. doi: 10.1089/TEN.TEA.2014.0443.

Cramer, G. D. and Darby, S. A. (2013) *Clinical Anatomy of the Spine, Spinal Cord, and ANS*, *Clinical Anatomy of the Spine, Spinal Cord, and ANS*. doi: 10.1016/C2009-0-42801-0.

Dahle, J. *et al.* (2005) 'Bystander effects may modulate ultraviolet A and B radiation-induced delayed mutagenesis', *Radiation Research*, 163(3), pp. 289–295. doi: 10.1667/RR3305.

Dahle, J., Kvam, E. and Stokke, T. (2005) 'Bystander effects in UV-induced genomic instability: Antioxidants inhibit delayed mutagenesis induced by ultraviolet A and B radiation', *Journal of Carcinogenesis*, 4. doi: 10.1186/1477-3163-4-11.

Danner, S. M. *et al.* (2015) 'Human spinal locomotor control is based on flexibly organized burst generators', *Brain*, 138(3), pp. 577–588. doi: 10.1093/brain/awu372.

Das, S. *et al.* (2015a) 'In vivo studies of silk based gold nano-composite conduits for functional peripheral nerve regeneration', *Biomaterials*, 62, pp. 66–75. doi: 10.1016/j.biomaterials.2015.04.047.

Das, S. *et al.* (2015b) 'In vivo studies of silk based gold nano-composite conduits for functional peripheral nerve regeneration.', *Biomaterials*, 62, pp. 66–75. doi: 10.1016/j.biomaterials.2015.04.047.

David Willets (2013) *Eight great technologies - https://www.gov.uk/government/speeches/eight-great-technologies*, *2013*. Available at: https://www.gov.uk/government/speeches/eight-great-technologies (Accessed: 13 July 2017).

Deiber, J. A. *et al.* (2009) 'Characterization of cross-linked polyampholytic gelatin hydrogels through the rubber elasticity and thermodynamic swelling theories', *Polymer*, 50(25), pp. 6065–6075. doi: 10.1016/j.polymer.2009.10.046.

Dergham, P. *et al.* (2002) 'Rho Signaling Pathway Targeted to Promote Spinal Cord Repair', *Journal of Neuroscience*, 22(15). Available at: http://www.jneurosci.org/content/22/15/6570.short (Accessed: 4 July 2017).

Donnelly, D. J. and Popovich, P. G. (2008) 'Inflammation and its role in neuroprotection, axonal regeneration and functional recovery after spinal cord injury', *Experimental Neurology*, 209(2), pp. 378–388. doi: 10.1016/j.expneurol.2007.06.009.

Dumont, C. M. *et al.* (2019) 'Aligned hydrogel tubes guide regeneration following spinal cord injury', *Acta Biomaterialia*, 86, pp. 312–322. doi: 10.1016/J.ACTBIO.2018.12.052.

Evaniew, N. *et al.* (2016) 'Methylprednisolone for the Treatment of Patients

with Acute Spinal Cord Injuries: A Systematic Review and Meta-Analysis', *Journal of Neurotrauma*, 33(5), pp. 468–481. doi: 10.1089/neu.2015.4192.

Fairbanks, B. D., Schwartz, M. P., Halevi, A. E., *et al.* (2009) 'A versatile synthetic extracellular matrix mimic via thiol-norbornene photopolymerization', *Advanced Materials*, 21(48), pp. 5005–5010. doi: 10.1002/adma.200901808.

Fairbanks, B. D., Schwartz, M. P., Bowman, C. N., *et al.* (2009) 'Photoinitiated polymerization of PEG-diacrylate with lithium phenyl-2,4,6-trimethylbenzoylphosphinate: polymerization rate and cytocompatibility', *Biomaterials*, 30(35), pp. 6702–6707. doi: 10.1016/j.biomaterials.2009.08.055.

Fan, Z. *et al.* (2020) 'Heterophase fcc-2H-fcc gold nanorods', *Nature Communications*, 11(1), pp. 1–8. doi: 10.1038/s41467-020-17068-w.

Fehlings, M. *et al.* (2020) 'Novel innovations in cell and gene therapies for spinal cord injury', *F1000Research*. doi: 10.12688/f1000research.21989.1.

Fehlings, M. G. *et al.* (2011) 'A Phase I/IIa Clinical Trial of a Recombinant Rho Protein Antagonist in Acute Spinal Cord Injury', *Journal of Neurotrauma*, 28(5), pp. 787–796. doi: 10.1089/neu.2011.1765.

Fehlings, M. G. and Perrin, R. G. (2005) 'The role and timing of early decompression for cervical spinal cord injury: Update with a review of recent clinical evidence', *Injury*, 36(2), pp. S13–S26. doi: 10.1016/j.injury.2005.06.011.

Feron, F. *et al.* (2005) 'Autologous olfactory ensheathing cell transplantation in human spinal cord injury', *Brain*, 128(12), pp. 2951–2960. doi: 10.1093/brain/awh657.

Filbin, M. T. (2003) 'Myelin-associated inhibitors of axonal regeneration in the adult mammalian CNS', *Nature Reviews Neuroscience*, 4(9), pp. 703–713. doi: 10.1038/nrn1195.

Forgione, N. and Fehlings, M. G. (2014) 'Rho-ROCK Inhibition in the Treatment of Spinal Cord Injury', *World Neurosurgery*, 82(3–4), pp. e535–e539. doi: 10.1016/j.wneu.2013.01.009.

Fu, Q., Hue, J. and Li, S. (2007) 'Nonsteroidal Anti-Inflammatory Drugs Promote Axon Regeneration via RhoA Inhibition', *Journal of Neuroscience*, 27(15), pp. 4154–4164. doi: 10.1523/JNEUROSCI.4353-06.2007.

Führmann, T. *et al.* (2016) 'Injectable hydrogel promotes early survival of induced pluripotent stem cell-derived oligodendrocytes and attenuates longterm teratoma formation in a spinal cord injury model', *Biomaterials*, 83, pp. 23–36. doi: 10.1016/J.BIOMATERIALS.2015.12.032.

Garaschuk, O. and Verkhratsky, A. (2019) 'Physiology of Microglia', in *Methods in Molecular Biology*. doi: 10.1007/978-1-4939-9658-2_3.

Garber, K. (2015) 'RIKEN suspends first clinical trial involving induced pluripotent stem cells', *Nature Biotechnology*, 33(9), pp. 890–892. Available at: http://go.galegroup.com/ps/anonymous?id=GALE%7CA428998641&sid=googleScholar&v=2.1&it=r&linkaccess=fulltext&issn=10870156&p=AONE&sw=

w&authCount=1&isAnonymousEntry=true (Accessed: 13 July 2017).

Garcia-Alias, G. *et al.* (2015) 'Plasticity of subcortical pathways promote recovery of skilled hand function in rats after corticospinal and rubrospinal tract injuries', *Experimental Neurology*, 266, pp. 112–119. doi: 10.1016/j.expneurol.2015.01.009.

Geisler, F. H. *et al.* (2001) 'The Sygen multicenter acute spinal cord injury study.', *Spine*, 26(24 Suppl), pp. S87-98. Available at: http://www.ncbi.nlm.nih.gov/pubmed/11805614 (Accessed: 4 July 2017).

Gelain, F. *et al.* (2010) 'Transplantation of Nanostructured Composite Scaffolds Results in the Regeneration of Chronically Injured Spinal Cords', *ACS Nano*, 5(1), pp. 227–236. doi: 10.1021/NN102461W.

Gieni, R. and Hendzel, M. (2008) 'Mechanotransduction from the ECM to the genome: are the pieces now in place?', *Journal of cellular biochemistry*, 104(6), pp. 1964–1987. doi: 10.1002/JCB.21364.

Gordon, J., Amini, S. and White, M. K. (2013) 'General overview of neuronal cell culture', *Methods in molecular biology (Clifton, N.J.)*, 1078, p. 1. doi: 10.1007/978-1-62703-640-5_1.

Greene, L. A. and Tischler, A. S. (1976) 'Establishment of a noradrenergic clonal line of rat adrenal pheochromocytoma cells which respond to nerve growth factor', *Proceedings of the National Academy of Sciences*, 73(7), pp. 2424–2428. doi: 10.1073/PNAS.73.7.2424.

Greene, T. and Lin, C.-C. (2015) 'Modular Cross-Linking of Gelatin-Based Thiol–Norbornene Hydrogels for *in Vitro* 3D Culture of Hepatocellular Carcinoma Cells', *ACS Biomaterials Science & Engineering*, 1(12), pp. 1314–1323. doi: 10.1021/acsbiomaterials.5b00436.

Grenier, J. *et al.* (2019) ' Mechanisms of pore formation in hydrogel scaffolds textured by freeze-drying', *Acta Biomaterialia*, 94, pp. 195–203. doi: 10.1016/j.actbio.2019.05.070.

Grossman, R. G. *et al.* (2014) 'A prospective, multicenter, phase I matched-comparison group trial of safety, pharmacokinetics, and preliminary efficacy of riluzole in patients with traumatic spinal cord injury.', *Journal of neurotrauma*, 31(3), pp. 239–55. doi: 10.1089/neu.2013.2969.

Gundimeda, U. *et al.* (2015) 'Polyphenols from green tea prevent antineuritogenic action of Nogo-A via 67-kDa laminin receptor and hydrogen peroxide', *Journal of Neurochemistry*, 132(1), pp. 70–84. doi: 10.1111/jnc.12964.

Han, S. *et al.* (2020) 'Gas-assisted transformation of gold from fcc to the metastable 4H phase', *Nature Communications*, 11(1), pp. 1–9. doi: 10.1038/s41467-019-14212-z.

Henson, B. B. C. *et al.* (2018) 'Synthesis of Gold Nanorods : Avoiding Common Pitfalls Six Common Pitfalls in Gold Nanorod Synthesis', *Material Matters*, 12(2), pp. 1–8.

Hicks, A. L. *et al.* (2005) 'Long-term body-weight-supported treadmill training and subsequent follow-up in persons with chronic SCI: effects on functional walking ability and measures of subjective well-being', *Spinal Cord*, 43(5),

pp. 291–298. doi: 10.1038/sj.sc.3101710.

Hlavac, N., Kasper, M. and Schmidt, C. E. (2020) 'Progress toward finding the perfect match: hydrogels for treatment of central nervous system injury', *Materials Today Advances*, 6, p. 100039. doi: 10.1016/J.MTADV.2019.100039.

Ho, P. L. and Raw, I. (1992) 'Cyclic AMP potentiates bFGF-induced neurite outgrowth in PC12 cells', *Journal of Cellular Physiology*, 150(3), pp. 647–656. doi: 10.1002/JCP.1041500326.

Hofstetter, C. P. *et al.* (2002) 'Marrow stromal cells form guiding strands in the injured spinal cord and promote recovery', *Proceedings of the National Academy of Sciences*, 99(4), pp. 2199–2204. doi: 10.1073/pnas.042678299.

Hofstetter, C. P. *et al.* (2005) 'Allodynia limits the usefulness of intraspinal neural stem cell grafts; directed differentiation improves outcome', *Nature Neuroscience*, 8(3), pp. 346–353. doi: 10.1038/nn1405.

Hong, L. T. A. *et al.* (2017) 'An injectable hydrogel enhances tissue repair after spinal cord injury by promoting extracellular matrix remodeling', *Nature Communications 2017 8:1*, 8(1), pp. 1–14. doi: 10.1038/s41467-017-00583-8.

Hu, R. *et al.* (2018) 'A novel method of neural differentiation of PC12 cells by using Opti-MEM as a basic induction medium', *International Journal of Molecular Medicine*, 41(1), p. 195. doi: 10.3892/IJMM.2017.3195.

Huangfu, D. *et al.* (2008) 'Induction of pluripotent stem cells from primary human fibroblasts with only Oct4 and Sox2', *Nature Biotechnology*, 26(11), pp. 1269–1275. doi: 10.1038/nbt.1502.

Huff, T. B. *et al.* (2007) 'Controlling the cellular uptake of gold nanorods', *Langmuir*, 23(4), pp. 1596–1599. doi: 10.1021/la062642r.

Hulsebosch, C. E. (2002) 'Recent advances in pathophysiology and treatment of spinal cord injury.', *Advances in physiology education*, 26(1–4), pp. 238–55. doi: 10.1152/advan.00039.2002.

Hung, C. T. *et al.* (2004) 'A Paradigm for Functional Tissue Engineering of Articular Cartilage via Applied Physiologic Deformational Loading', *Annals of Biomedical Engineering 2004 32:1*, 32(1), pp. 35–49. doi: 10.1023/B:ABME.0000007789.99565.42.

Iadecola, C. and Nedergaard, M. (2007) 'Glial regulation of the cerebral microvasculature', *Nature Neuroscience*. doi: 10.1038/nn2003.

Ichiyama, R. M. *et al.* (2005) 'Hindlimb stepping movements in complete spinal rats induced by epidural spinal cord stimulation', *Neuroscience Letters*, 383(3), pp. 339–344. doi: 10.1016/j.neulet.2005.04.049.

Ichiyama, R. M. *et al.* (2008) 'Dose dependence of the 5-HT agonist quipazine in facilitating spinal stepping in the rat with epidural stimulation', *Neuroscience Letters*, 438(3), pp. 281–285. doi: 10.1016/j.neulet.2008.04.080.

Ikada, Y. (1994) 'Surface modification of polymers for medical applications', *Biomaterials*, 15(10), pp. 725–736. doi: 10.1016/0142-9612(94)90025-6.

de Isla, N. *et al.* (2010) 'Introduction to tissue engineering and application for

cartilage engineering', *Bio-medical materials and engineering*, 20(3), pp. 127–133. doi: 10.3233/BME-2010-0624.

Iwai, H. *et al.* (2015) 'Allogeneic Neural Stem/Progenitor Cells Derived From Embryonic Stem Cells Promote Functional Recovery After Transplantation Into Injured Spinal Cord of Nonhuman Primates', *STEM CELLS Translational Medicine*, 4(7), pp. 708–719. doi: 10.5966/sctm.2014-0215.

Iwanami, A. *et al.* (2005) 'Transplantation of human neural stem cells for spinal cord injury in primates', *Journal of Neuroscience Research*, 80(2), pp. 182–190. doi: 10.1002/jnr.20436.

Jacob, J. *et al.* (2018) 'Piezoelectric smart biomaterials for bone and cartilage tissue engineering', *Inflammation and Regeneration*. BioMed Central Ltd., pp. 1–11. doi: 10.1186/s41232-018-0059-8.

Jana, N. R., Gearheart, L. and Murphy, C. J. (2001) 'Seed-Mediated Growth Approach for Shape-Controlled Synthesis of Spheroidal and Rod-like Gold Nanoparticles Using a Surfactant Template', *Advanced Materials*, 13(18), pp. 1389–1393. doi: 10.1002/1521-4095(200109)13:18<1389::AID-ADMA1389>3.0.CO;2-F.

Jeong, H. J. *et al.* (2021) 'Biomaterials and strategies for repairing spinal cord lesions', *Neurochemistry International*, 144, p. 104973. doi: 10.1016/J.NEUINT.2021.104973.

Jiang, J.-P. *et al.* (2020) 'Three-dimensional bioprinting collagen/silk fibroin scaffold combined with neural stem cells promotes nerve regeneration after spinal cord injury', *Neural Regeneration Research*, 15(5), p. 959. doi: 10.4103/1673-5374.268974.

Kaja, S. *et al.* (2017) 'Quantification of lactate dehydrogenase for cell viability testing using cell lines and primary cultured astrocytes', *Current protocols in toxicology*, 72, p. 2.26.1. doi: 10.1002/CPTX.21.

Kaklamani, G. *et al.* (2018) 'On the electrical conductivity of alginate hydrogels', *Regenerative Biomaterials*, 5(5), pp. 293–301. doi: 10.1093/rb/rby019.

Kang, H. W., Tabata, Y. and Ikada, Y. (1999) 'Fabrication of porous gelatin scaffolds for tissue engineering', *Biomaterials*, 20(14), pp. 1339–1344. doi: 10.1016/S0142-9612(99)00036-8.

Kanno, H. *et al.* (2014) 'Combination of Engineered Schwann Cell Grafts to Secrete Neurotrophin and Chondroitinase Promotes Axonal Regeneration and Locomotion after Spinal Cord Injury', *Journal of Neuroscience*, 34(5), pp. 1838–1855. doi: 10.1523/JNEUROSCI.2661-13.2014.

Karimi, A., Shojaei, A. and Tehrani, P. (2017) 'Mechanical properties of the human spinal cord under the compressive loading', *Journal of Chemical Neuroanatomy*, 86, pp. 15–18. doi: 10.1016/j.jchemneu.2017.07.004.

Kawabata, S. *et al.* (2016) 'Grafted Human iPS Cell-Derived Oligodendrocyte Precursor Cells Contribute to Robust Remyelination of Demyelinated Axons after Spinal Cord Injury', *Stem Cell Reports*, 6(1), pp. 1–8. doi: 10.1016/j.stemcr.2015.11.013.

Keirstead, H. S. *et al.* (2005) 'Human Embryonic Stem Cell-Derived

Oligodendrocyte Progenitor Cell Transplants Remyelinate and Restore Locomotion after Spinal Cord Injury', *Journal of Neuroscience*, 25(19). Available at: http://www.jneurosci.org/content/25/19/4694.short (Accessed: 13 July 2017).

Kendall, R. T. and Feghali-Bostwick, C. A. (2014) 'Fibroblasts in fibrosis: novel roles and mediators', *Frontiers in Pharmacology*, 0, p. 123. doi: 10.3389/FPHAR.2014.00123.

Khanal, B. P. and Zubarev, E. R. (2008) 'Purification of high aspect ratio gold nanorods: Complete removal of platelets', *Journal of the American Chemical Society*, 130(38), pp. 12634–12635. doi: 10.1021/ja806043p.

Kigerl, K. A. *et al.* (2009) 'Identification of Two Distinct Macrophage Subsets with Divergent Effects Causing either Neurotoxicity or Regeneration in the Injured Mouse Spinal Cord', *Journal of Neuroscience*, 29(43). Available at: http://www.jneurosci.org/content/29/43/13435.short (Accessed: 12 July 2017).

Kim, B. G. *et al.* (2007) 'Stem Cell-Based Cell Therapy for Spinal Cord Injury', *Cell Transplantation*, 16(4), pp. 355–364. doi: 10.3727/000000007783464885.

Klotz, B. J. *et al.* (2016) 'Gelatin-Methacryloyl Hydrogels: Towards Biofabrication-Based Tissue Repair', *Trends in Biotechnology*, 34(5), pp. 394–407. doi: 10.1016/j.tibtech.2016.01.002.

Klusman, I. and Schwab, M. E. (1997) 'Effects of pro-inflammatory cytokines in experimental spinal cord injury.', *Brain research*, 762(1–2), pp. 173–84. Available at: http://www.ncbi.nlm.nih.gov/pubmed/9262171 (Accessed: 29 June 2017).

Kobayashi, Y. *et al.* (2012) 'Pre-Evaluated Safe Human iPSC-Derived Neural Stem Cells Promote Functional Recovery after Spinal Cord Injury in Common Marmoset without Tumorigenicity', *PLoS ONE*. Edited by K. Hashimoto, 7(12), p. e52787. doi: 10.1371/journal.pone.0052787.

Konigsberg, W. (1972) '[13] Reduction of disulfide bonds in proteins with dithiothreitol', *Methods in Enzymology*, 25(C), pp. 185–188. doi: 10.1016/S0076-6879(72)25015-7.

Koppes, A. N. *et al.* (2016) 'Robust neurite extension following exogenous electrical stimulation within single walled carbon nanotube-composite hydrogels', *Acta Biomaterialia*, 39, pp. 34–43. doi: 10.1016/J.ACTBIO.2016.05.014.

Kruskal, P. B. *et al.* (2015) 'Beyond the Patch Clamp: Nanotechnologies for Intracellular Recording', *Neuron*, 86(1), pp. 21–24. doi: 10.1016/J.NEURON.2015.01.004.

Kwok, J. C. F. *et al.* (2011) 'Extracellular matrix and perineuronal nets in CNS repair', *Developmental Neurobiology*, 71(11). doi: 10.1002/dneu.20974.

Kwon, B. K. *et al.* (2011) 'A systematic review of non-invasive pharmacologic neuroprotective treatments for acute spinal cord injury.', *Journal of neurotrauma*, 28(8), pp. 1545–88. doi: 10.1089/neu.2009.1149.

Lai, J.-Y. and Li, Y.-T. (2010) 'Functional Assessment of Cross-Linked

Porous Gelatin Hydrogels for Bioengineered Cell Sheet Carriers', *Biomacromolecules*, 11(5), pp. 1387–1397. doi: 10.1021/BM100213F.

Lammertse, D. P. *et al.* (2012) 'Autologous incubated macrophage therapy in acute, complete spinal cord injury: results of the phase 2 randomized controlled multicenter trial', *Spinal Cord*, 50(9), pp. 661–671. doi: 10.1038/sc.2012.39.

Lau, L. W. *et al.* (2013) 'Pathophysiology of the brain extracellular matrix: A new target for remyelination', *Nature Reviews Neuroscience*. doi: 10.1038/nrn3550.

Lee, B. B. *et al.* (2014) 'The global map for traumatic spinal cord injury epidemiology: update 2011, global incidence rate', *Spinal Cord*, 52(2), pp. 110–116. doi: 10.1038/sc.2012.158.

Lee, J.-H. *et al.* (2014) 'Neurogenic differentiation of human dental stem cells *in vitro*', *Journal of the Korean Association of Oral and Maxillofacial Surgeons*, 40(4), p. 173. doi: 10.5125/jkaoms.2014.40.4.173.

Leong, W. K. *et al.* (2012) 'Human adult dental pulp stem cells enhance poststroke functional recovery through non-neural replacement mechanisms.', *Stem cells translational medicine*, 1(3), pp. 177–87. doi: 10.5966/sctm.2011-0039.

Li, N. and Leung, G. K. K. (2015) 'Oligodendrocyte Precursor Cells in Spinal Cord Injury: A Review and Update', *BioMed Research International*, 2015, pp. 1–20. doi: 10.1155/2015/235195.

Lim, K. S. *et al.* (2016) 'New Visible-Light Photoinitiating System for Improved Print Fidelity in Gelatin-Based Bioinks', *ACS Biomaterials Science & Engineering*, 2(10), pp. 1752–1762. doi: 10.1021/acsbiomaterials.6b00149.

Lin, C.-C., Ki, C. S. and Shih, H. (2015) 'Thiol-norbornene photoclick hydrogels for tissue engineering applications', *Journal of Applied Polymer Science*, 132(8), p. n/a-n/a. doi: 10.1002/app.41563.

Lin, C. C., Raza, A. and Shih, H. (2011) 'PEG hydrogels formed by thiol-ene photo-click chemistry and their effect on the formation and recovery of insulin-secreting cell spheroids', *Biomaterials*, 32(36), pp. 9685–9695. doi: 10.1016/j.biomaterials.2011.08.083.

Lin, C. C., Sawicki, S. M. and Metters, A. T. (2008) 'Free-radical-mediated protein inactivation and recovery during protein photoencapsulation', *Biomacromolecules*, 9(1), pp. 75–83. doi: 10.1021/bm700782c.

Liu, J.-M. *et al.* (2016) 'Is Urgent Decompression Superior to Delayed Surgery for Traumatic Spinal Cord Injury? A Meta-Analysis', *World Neurosurgery*, 87, pp. 124–131. doi: 10.1016/j.wneu.2015.11.098.

Liu, S. *et al.* (2000) 'Embryonic stem cells differentiate into oligodendrocytes and myelinate in culture and after spinal cord transplantation.', *Proceedings of the National Academy of Sciences of the United States of America*, 97(11), pp. 6126–31. doi: 10.1073/PNAS.97.11.6126.

Lu, S. *et al.* (2021) 'Crystal Phase Control of Gold Nanomaterials by Wet-Chemical Synthesis', *Acc. Chem. Res*, 2020, p. 33. doi:

10.1021/acs.accounts.0c00487.

Lück, J. and Latz, A. (2019) 'The electrochemical double layer and its impedance behavior in lithium-ion batteries', *Physical Chemistry Chemical Physics*, 21(27), pp. 14753–14765. doi: 10.1039/c9cp01320b.

Lukovic, D. *et al.* (2014) 'Perspectives and Future Directions of Human Pluripotent Stem Cell-Based Therapies: Lessons from Geron's Clinical Trial for Spinal Cord Injury', *Stem Cells and Development*, 23(1), pp. 1–4. doi: 10.1089/scd.2013.0266.

Lulevich, V. *et al.* (2009) 'Cell tracing dyes significantly change single cell mechanics', *Journal of Physical Chemistry B*, 113(18), pp. 6511–6519. doi: 10.1021/jp8103358.

Ma, C. *et al.* (2016) 'Measuring stiffness and residual stress of thin films by contact resonance atomic force microscopy', *Applied Physics Express*, 9(11), p. 116601. doi: 10.7567/APEX.9.116601.

Ma, S. *et al.* (2014) 'Immunobiology of mesenchymal stem cells.', *Cell death and differentiation*, 21(2), pp. 216–25. doi: 10.1038/cdd.2013.158.

Mabon, P. J., Weaver, L. C. and Dekaban, G. A. (2000) 'Inhibition of Monocyte/Macrophage Migration to a Spinal Cord Injury Site by an Antibody to the Integrin ?D: A Potential New Anti-inflammatory Treatment', *Experimental Neurology*, 166(1), pp. 52–64. doi: 10.1006/exnr.2000.7488.

Mackay-Sim, A. *et al.* (2008) 'Autologous olfactory ensheathing cell transplantation in human paraplegia: a 3-year clinical trial.', *Brain : a journal of neurology*, 131(Pt 9), pp. 2376–86. doi: 10.1093/brain/awn173.

Martens, W. *et al.* (2014) 'Human dental pulp stem cells can differentiate into Schwann cells and promote and guide neurite outgrowth in an aligned tissue-engineered collagen construct in vitro.', *FASEB journal : official publication of the Federation of American Societies for Experimental Biology*, 28(4), pp. 1634–43. doi: 10.1096/fj.13-243980.

Martinez-Lopez, A. L. *et al.* (2011) 'The Peroxidase/H2O2 System as a Free Radical-Generating Agent for Gelling Maize Bran Arabinoxylans: Rheological and Structural Properties', *Molecules*, 16(12), pp. 8410–8418. doi: 10.3390/molecules16108410.

Marzouni, H. Z. *et al.* (2018) 'Cytotoxic Effects of Coated Gold Nanoparticles on PC12 Cancer Cell', *Galen Medical Journal*, 7, p. e1110. doi: 10.22086/GMJ.V0I0.1110.

McCall, J. D. and Anseth, K. S. (2012) 'Thiol-ene photopolymerizations provide a facile method to encapsulate proteins and maintain their bioactivity', *Biomacromolecules*, 13(8), pp. 2410–2417. doi: 10.1021/bm300671s.

McDonald, J. W. *et al.* (1999) 'Transplanted embryonic stem cells survive, differentiate and promote recovery in injured rat spinal cord.', *Nature Medicine*, 5(12), pp. 1410–1412. doi: 10.1038/70986.

McKeon, R. J., Jurynec, M. J. and Buck, C. R. (1999) 'The Chondroitin Sulfate Proteoglycans Neurocan and Phosphacan Are Expressed by Reactive Astrocytes in the Chronic CNS Glial Scar', *Journal of*

*Neuroscience*, 19(24). Available at: http://www.jneurosci.org/content/19/24/10778.short (Accessed: 1 July 2017).

Mehtala, J. G. *et al.* (2014) 'Citrate-stabilized gold nanorods', *Langmuir*, 30(46), pp. 13727–13730. doi: 10.1021/la5029542.

Meijering, E. *et al.* (2004) 'Design and validation of a tool for neurite tracing and analysis in fluorescence microscopy images', *Cytometry. Part A : the journal of the International Society for Analytical Cytology*, 58(2), pp. 167–176. doi: 10.1002/CYTO.A.20022.

Merten, O. W. (2015) 'Advances in cell culture: Anchorage dependence', *Philosophical Transactions of the Royal Society B: Biological Sciences.* Royal Society of London, p. 20140040. doi: 10.1098/rstb.2014.0040.

Min, J. H., Patel, M. and Koh, W. G. (2018a) 'Incorporation of conductive materials into hydrogels for tissue engineering applications', *Polymers*. MDPI AG. doi: 10.3390/polym10101078.

Min, J. H., Patel, M. and Koh, W. G. (2018b) 'Incorporation of conductive materials into hydrogels for tissue engineering applications', *Polymers*. MDPI AG. doi: 10.3390/polym10101078.

Monnier, P. P. *et al.* (2003) 'The Rho/ROCK pathway mediates neurite growth-inhibitory activity associated with the chondroitin sulfate proteoglycans of the CNS glial scar', *Molecular and Cellular Neuroscience*, 22(3), pp. 319–330. doi: 10.1016/S1044-7431(02)00035-0.

Mosesson, M. W. (2005) 'Fibrinogen and fibrin structure and functions', *Journal of Thrombosis and Haemostasis*, 3(8), pp. 1894–1904. doi: 10.1111/j.1538-7836.2005.01365.x.

Mũnoz, Z. *et al.* (2014) 'Gelatin hydrogels formed by orthogonal thiol–norbornene photochemistry for cell encapsulation', *Biomaterials Science*, 2(8), p. 1063. doi: 10.1039/c4bm00070f.

Mwangi, J. W. and Ofner, C. M. (2004) 'Crosslinked gelatin matrices: release of a random coil macromolecular solute', *International Journal of Pharmaceutics*, 278(2), pp. 319–327. doi: 10.1016/j.ijpharm.2004.03.024.

Naka, Y. *et al.* (2020) 'Wholly vascularized millimeter-sized engineered tissues by cell-sized microscaffolds', *Materials Today Bio*, 6, p. 100054. doi: 10.1016/j.mtbio.2020.100054.

Navaei, A. *et al.* (2016) 'Gold nanorod-incorporated gelatin-based conductive hydrogels for engineering cardiac tissue constructs', *Acta Biomaterialia*, 41, pp. 133–146. doi: 10.1016/J.ACTBIO.2016.05.027.

Navaei, A. *et al.* (2017) 'Electrically conductive hydrogel-based micro-topographies for the development of organized cardiac tissues †'. doi: 10.1039/c6ra26279a.

Nejati, K. *et al.* (2020) 'GDNF gene-engineered adipose-derived stem cells seeded Emu oil-loaded electrospun nanofibers for axonal regeneration following spinal cord injury', *Journal of Drug Delivery Science and Technology*, 60, p. 102095. doi: 10.1016/J.JDDST.2020.102095.

Neri, S. *et al.* (2001) 'Calcein-acetyoxymethyl cytotoxicity assay: Standardization of a method allowing additional analyses on recovered

effector cells and supernatants', *Clinical and Diagnostic Laboratory Immunology*, 8(6), pp. 1131–1135. doi: 10.1128/CDLI.8.6.1131-1135.2001.

Nicola, F. C. *et al.* (2016) 'Human dental pulp stem cells transplantation combined with treadmill training in rats after traumatic spinal cord injury', *Brazilian Journal of Medical and Biological Research*, 49(9), p. e5319. doi: 10.1590/1414-431X20165319.

Nikoobakht, B. and El-Sayed*, M. A. (2003) 'Preparation and Growth Mechanism of Gold Nanorods (NRs) Using Seed-Mediated Growth Method'. doi: 10.1021/CM020732L.

Nishiguchi, A. *et al.* (2014) 'Effects of angiogenic factors and 3D-microenvironments on vascularization within sandwich cultures', *Biomaterials*, 35(17), pp. 4739–4748. doi: 10.1016/J.BIOMATERIALS.2014.01.079.

Noh, S. *et al.* (2020) 'Direct-write printing for producing biomimetic patterns with self-aligned neurites', *Additive Manufacturing*, 32, p. 101072. doi: 10.1016/j.addma.2020.101072.

O'Brien, F. J. *et al.* (2004) 'Influence of freezing rate on pore structure in freeze-dried collagen-GAG scaffolds', *Biomaterials*, 25(6), pp. 1077–1086. doi: 10.1016/S0142-9612(03)00630-6.

O'Shea, T. M., Burda, J. E. and Sofroniew, M. V. (2017) 'Cell biology of spinal cord injury and repair', *The Journal of Clinical Investigation*, 127(9), pp. 3259–3270. doi: 10.1172/JCI90608.

Occhetta, P. *et al.* (2015) 'VA-086 methacrylate gelatine photopolymerizable hydrogels: A parametric study for highly biocompatible 3D cell embedding', *Journal of Biomedical Materials Research Part A*, 103(6), pp. 2109–2117. doi: 10.1002/jbm.a.35346.

Okano, H. *et al.* (2003) 'Transplantation of neural stem cells into the spinal cord after injury', *Seminars in Cell & Developmental Biology*, 14(3), pp. 191–198. doi: 10.1016/S1084-9521(03)00011-9.

Osathanon, T. *et al.* (2014) 'Neurogenic differentiation of human dental pulp stem cells using different induction protocols', *Oral Diseases*, 20(4), pp. 352–358. doi: 10.1111/odi.12119.

Oudega, M. and Xu, X.-M. (2006) 'Schwann Cell Transplantation for Repair of the Adult Spinal Cord', *Journal of Neurotrauma*, 23(3–4), pp. 453–467. doi: 10.1089/neu.2006.23.453.

Pabari, A. *et al.* (2014) 'Nerve conduits for peripheral nerve surgery', *Plastic and reconstructive surgery*, 133(6), pp. 1420–1430. doi: 10.1097/PRS.0000000000000226.

Pan, S. *et al.* (2019) 'Graphene oxide-PLGA hybrid nanofibres for the local delivery of IGF-1 and BDNF in spinal cord repair', *https://doi.org/10.1080/21691401.2019.1575843*, 47(1), pp. 651–664. doi: 10.1080/21691401.2019.1575843.

Parakalan, R. *et al.* (2012) 'Transcriptome analysis of amoeboid and ramified microglia isolated from the corpus callosum of rat brain', *BMC Neuroscience*, 13(1). doi: 10.1186/1471-2202-13-64.

Park, E. and Park, K. (2009) 'Oxidative stress and pro-inflammatory responses induced by silica nanoparticles in vivo and in vitro', *Toxicology letters*, 184(1), pp. 18–25. doi: 10.1016/J.TOXLET.2008.10.012.

Park, E., Velumian, A. A. and Fehlings, M. G. (2004) 'The Role of Excitotoxicity in Secondary Mechanisms of Spinal Cord Injury: A Review with an Emphasis on the Implications for White Matter Degeneration', *Journal of Neurotrauma*, 21(6), pp. 754–774. doi: 10.1089/0897715041269641.

Park, J. S. *et al.* (2009) 'Electrical pulsed stimulation of surfaces homogeneously coated with gold nanoparticles to induce neurite outgrowth of PC12 cells', *Langmuir*, 25(1), pp. 451–457. doi: 10.1021/la8025683.

Park, K., Koerner, H. and Vaia, R. A. (2010) 'Depletion-induced shape and size selection of gold nanoparticles', *Nano Letters*, 10(4), pp. 1433–1439. doi: 10.1021/nl100345u.

Peehl, D. M. and Stanbridge, E. J. (1981) 'Anchorage-independent growth of normal human fibroblasts.', *Proceedings of the National Academy of Sciences of the United States of America*, 78(5), pp. 3053–3057. doi: 10.1073/pnas.78.5.3053.

Perale, G. *et al.* (2011) 'Hydrogels in spinal cord injury repair strategies.', *ACS chemical neuroscience*, 2(7), pp. 336–45. doi: 10.1021/cn200030w.

Petersen, O. W. *et al.* (1992) 'Interaction with basement membrane serves to rapidly distinguish growth and differentiation pattern of normal and malignant human breast epithelial cells.', *Proceedings of the National Academy of Sciences of the United States of America*, 89(19), p. 9064. doi: 10.1073/PNAS.89.19.9064.

Philips, T. and Rothstein, J. D. (2017) 'Oligodendroglia: Metabolic supporters of neurons', *Journal of Clinical Investigation*. doi: 10.1172/JCI90610.

Phillips, J. B. *et al.* (2005) 'Neural Tissue Engineering: A Self-Organizing Collagen Guidance Conduit', *Tissue Engineering*, 11(9–10), pp. 1611–1617. doi: 10.1089/ten.2005.11.1611.

PITTS, L. H. *et al.* (1995) 'Treatment with Thyrotropin-Releasing Hormone (TRH) in Patients with Traumatic Spinal Cord Injuries', *Journal of Neurotrauma*, 12(3), pp. 235–243. doi: 10.1089/neu.1995.12.235.

Popovich, P. G. *et al.* (1999) 'Depletion of Hematogenous Macrophages Promotes Partial Hindlimb Recovery and Neuroanatomical Repair after Experimental Spinal Cord Injury', *Experimental Neurology*, 158(2), pp. 351–365. doi: 10.1006/exnr.1999.7118.

Quent, V. M. *et al.* (2010) 'Discrepancies between metabolic activity and DNA content as tool to assess cell proliferation in cancer research', *Journal of Cellular and Molecular Medicine*, 14(4), p. 1003. doi: 10.1111/J.1582-4934.2010.01013.X.

Rampersad, S. N. (2012) 'Multiple applications of alamar blue as an indicator of metabolic function and cellular health in cell viability bioassays', *Sensors (Switzerland)*, 12(9), pp. 12347–12360. doi: 10.3390/s120912347.

Rao, S. S. *et al.* (2012) 'Inherent Interfacial Mechanical Gradients in 3D Hydrogels Influence Tumor Cell Behaviors', *PLOS ONE*, 7(4), p. e35852.

doi: 10.1371/JOURNAL.PONE.0035852.

Rashidi, H. *et al.* (2010) 'Simvastatin release from poly(lactide-co-glycolide) membrane scaffolds', *Polymers*, 2(4), pp. 709–718. doi: 10.3390/POLYM2040709.

Ray, J. *et al.* (1993) 'Proliferation, differentiation, and long-term culture of primary hippocampal neurons.', *Proceedings of the National Academy of Sciences of the United States of America*, 90(8), p. 3602. doi: 10.1073/PNAS.90.8.3602.

Rossignol, S. *et al.* (1999) 'Locomotor performance and adaptation after partial or complete spinal cord lesions in the cat.', *Progress in brain research*, 123, pp. 349–65. Available at: http://www.ncbi.nlm.nih.gov/pubmed/10635730 (Accessed: 4 July 2017).

Rossignol, S. (2000) 'Locomotion and its recovery after spinal injury', *Current Opinion in Neurobiology*, 10(6), pp. 708–716. doi: 10.1016/S0959-4388(00)00151-3.

Rydel, R. and Greene, L. (1987) 'Acidic and basic fibroblast growth factors promote stable neurite outgrowth and neuronal differentiation in cultures of PC12 cells', *Journal of Neuroscience*, 7(11), pp. 3639–3653. doi: 10.1523/JNEUROSCI.07-11-03639.1987.

Sabelstrom, H. *et al.* (2013) 'Resident Neural Stem Cells Restrict Tissue Damage and Neuronal Loss After Spinal Cord Injury in Mice', *Science*, 342(6158), pp. 637–640. doi: 10.1126/science.1242576.

Sagner, A. and Briscoe, J. (2019) 'Establishing neuronal diversity in the spinal cord: A time and a place', *Development (Cambridge)*. doi: 10.1242/dev.182154.

Sakai, K. *et al.* (2012) 'Human dental pulp-derived stem cells promote locomotor recovery after complete transection of the rat spinal cord by multiple neuro-regenerative mechanisms.', *The Journal of clinical investigation*, 122(1), pp. 80–90. doi: 10.1172/JCI59251.

Salzer, J. L. and Zalc, B. (2016) 'Myelination', *Current Biology*. doi: 10.1016/j.cub.2016.07.074.

Sanfilippo, S. *et al.* (2011) 'Viability assessment of fresh and frozen/thawed isolated human follicles: Reliability of two methods (Trypan blue and Calcein AM/ethidium homodimer-1)', *Journal of Assisted Reproduction and Genetics*, 28(12), pp. 1151–1156. doi: 10.1007/s10815-011-9649-y.

Sarrazin, S., Lamanna, W. C. and Esko, J. D. (2011) 'Heparan sulfate proteoglycans', *Cold Spring Harbor Perspectives in Biology*, 3(7). doi: 10.1101/cshperspect.a004952.

Sayed, N., Liu, C. and Wu, J. C. (2016) 'Translation of Human-Induced Pluripotent Stem Cells: From Clinical Trial in a Dish to Precision Medicine.', *Journal of the American College of Cardiology*, 67(18), pp. 2161–76. doi: 10.1016/j.jacc.2016.01.083.

Sayılır, S., Ersöz, M. and Yalçın, S. (2013) 'Comparison of urodynamic findings in patients with upper and lower cervical spinal cord injury.', *Spinal cord*, 51(10), pp. 780–3. doi: 10.1038/sc.2013.83.

Scarabelli, L. *et al.* (2015) 'A "Tips and Tricks" Practical Guide to the Synthesis of Gold Nanorods', *The Journal of Physical Chemistry Letters*, 6(21), pp. 4270–4279. doi: 10.1021/acs.jpclett.5b02123.

Schaub, N. *et al.* (2016) 'Electrospun Fibers for Spinal Cord Injury Research and Regeneration', *https://home.liebertpub.com/neu*, 33(15), pp. 1405–1415. doi: 10.1089/NEU.2015.4165.

Schawe, J. E. K., Possart, W. and Krogh, L. (2016) 'Solid state rheology of polymer films and layers: Influence of the thickness on mechanical properties of a PU-adhesive between metallic substrate', *AIP Conference Proceedings*, 1713, p. 80004. doi: 10.1063/1.4942293.

Scuteri, A. *et al.* (2011) 'Mesenchymal stem cells neuronal differentiation ability: a real perspective for nervous system repair?', *Current stem cell research & therapy*, 6(2), pp. 82–92. Available at: http://www.ncbi.nlm.nih.gov/pubmed/21190538 (Accessed: 13 July 2017).

Sebastián, V. *et al.* (2012) 'One-step continuous synthesis of biocompatible gold nanorods for optical coherence tomography', *Chemical Communications*, 48(53), pp. 6654–6656. doi: 10.1039/C2CC32969G.

Serwanski, D. R., Jukkola, P. and Nishiyama, A. (2017) 'Heterogeneity of astrocyte and NG2 cell insertion at the node of ranvier', *Journal of Comparative Neurology*, 525(3). doi: 10.1002/cne.24083.

Sharma, V., Park, K. and Srinivasarao, M. (2009) *Shape separation of gold nanorods using centrifugation*, *PNAS*. Available at: www.pnas.orgcgidoi10.1073pnas.0800599106.

Sharples, A. P. *et al.* (2012) 'Modelling in vivo skeletal muscle ageing in vitro using three-dimensional bioengineered constructs', *Aging Cell*, 11(6), pp. 986–995. doi: 10.1111/J.1474-9726.2012.00869.X.

Shechter, R. *et al.* (2009) 'Infiltrating Blood-Derived Macrophages Are Vital Cells Playing an Anti-inflammatory Role in Recovery from Spinal Cord Injury in Mice', *PLoS Medicine*. Edited by M. B. Graeber, 6(7), p. e1000113. doi: 10.1371/journal.pmed.1000113.

Shi, L. *et al.* (2013) 'The Improved Biological Performance of a Novel Low Elastic Modulus Implant', *PLoS ONE*, 8(2). doi: 10.1371/journal.pone.0055015.

Shi, Z. *et al.* (2014) 'In Situ Synthesis of Robust Conductive Cellulose/Polypyrrole Composite Aerogels and Their Potential Application in Nerve Regeneration', *Angewandte Chemie*, 126(21), pp. 5484–5488. doi: 10.1002/ange.201402751.

Shih, H. and Lin, C. C. (2012) 'Cross-linking and degradation of step-growth hydrogels formed by thiol-ene photoclick chemistry', *Biomacromolecules*, 13(7), pp. 2003–2012. doi: 10.1021/bm300752j.

Shih, H. and Lin, C. C. (2013) 'Visible-light-mediated thiol-ene hydrogelation using eosin-Y as the only photoinitiator', *Macromolecular Rapid Communications*, 34(3), pp. 269–273. doi: 10.1002/marc.201200605.

Shimosaka, M. and Bhawal, U. K. (2013) 'bFGF Upregulates the Expression of NGFR in PC12 Cells', *Journal of Hard Tissue Biology*, 22(1), pp. 19–24.

doi: 10.2485/JHTB.22.19.

Shin, S. R. *et al.* (2013) 'Carbon-nanotube-embedded hydrogel sheets for engineering cardiac constructs and bioactuators', *ACS Nano*, 7(3), pp. 2369–2380. doi: 10.1021/nn305559j.

Shirwaiker, R. A., Purser, M. F. and Wysk, R. A. (2014) 'Scaffolding hydrogels for rapid prototyping based tissue engineering', *Rapid Prototyping of Biomaterials: Principles and Applications*, pp. 176–200. doi: 10.1533/9780857097217.176.

Shu, B. *et al.* (2019) 'Restoring electrical connection using a conductive biomaterial provides a new therapeutic strategy for rats with spinal cord injury', *Neuroscience Letters*, 692, pp. 33–40. doi: 10.1016/j.neulet.2018.10.031.

Siddall, P. J. *et al.* (2003) 'A longitudinal study of the prevalence and characteristics of pain in the first 5 years following spinal cord injury.', *Pain*, 103(3), pp. 249–57. Available at: http://www.ncbi.nlm.nih.gov/pubmed/12791431 (Accessed: 30 June 2017).

Sierra, A. *et al.* (2010) 'Microglia shape adult hippocampal neurogenesis through apoptosis-coupled phagocytosis', *Cell Stem Cell*, 7(4). doi: 10.1016/j.stem.2010.08.014.

Silva, N. A. *et al.* (2014) 'From basics to clinical: A comprehensive review on spinal cord injury', *Progress in Neurobiology*, 114, pp. 25–57. doi: 10.1016/j.pneurobio.2013.11.002.

Silver, J. and Miller, J. H. (2004) 'Regeneration beyond the glial scar', *Nature Reviews Neuroscience*, 5(2), pp. 146–156. doi: 10.1038/nrn1326.

Simard, M. *et al.* (2003) 'Signaling at the gliovascular interface', *Journal of Neuroscience*, 23(27). doi: 10.1523/jneurosci.23-27-09254.2003.

Sloka, J. S. and Stefanelli, M. (2005) 'The mechanism of action of methylprednisolone in the treatment of multiple sclerosis', *Multiple Sclerosis Journal*, 11(4), pp. 425–432. doi: 10.1191/1352458505ms1190oa.

Snow, D. M. *et al.* (1990) 'Sulfated proteoglycans in astroglial barriers inhibit neurite outgrowth in vitro.', *Experimental neurology*, 109(1), pp. 111–30. Available at: http://www.ncbi.nlm.nih.gov/pubmed/2141574 (Accessed: 4 July 2017).

Sofroniew, M. V. and Vinters, H. V. (2010) 'Astrocytes: Biology and pathology', *Acta Neuropathologica*. doi: 10.1007/s00401-009-0619-8.

Song, Y. H. *et al.* (2019) 'Recent advances in nanotherapeutic strategies for spinal cord injury repair', *Advanced Drug Delivery Reviews*, 148, pp. 38–59. doi: 10.1016/J.ADDR.2018.12.011.

Sood, A. and Panchagnula, R. (2003) 'Design of controlled release delivery systems using a modified pharmacokinetic approach: a case study for drugs having a short elimination half-life and a narrow therapeutic index', *International journal of pharmaceutics*, 261(1–2), pp. 27–41. doi: 10.1016/S0378-5173(03)00267-9.

Van den Steen, P. *et al.* (2002) 'Biochemistry and molecular biology of gelatinase B or matrix metalloproteinase-9 (MMP-9)', *Critical reviews in*

*biochemistry and molecular biology*, 37(6), pp. 375–536. doi: 10.1080/10409230290771546.

Stifani, N. (2014) 'Motor neurons and the generation of spinal motor neuron diversity', *Frontiers in Cellular Neuroscience*. doi: 10.3389/fncel.2014.00293.

Straley, K. S., Foo, C. W. P. and Heilshorn, S. C. (2010) 'Biomaterial design strategies for the treatment of spinal cord injuries.', *Journal of neurotrauma*, 27(1), pp. 1–19. doi: 10.1089/neu.2009.0948.

Sultan, N. *et al.* (2021) 'Dental pulp stem cells stimulate neuronal differentiation of PC12 cells', *Neural Regeneration Research*, 16(9), p. 1821. doi: 10.4103/1673-5374.306089.

Sun, X. *et al.* (2019) 'Devising micro/nano-architectures in multi-channel nerve conduits towards a pro-regenerative matrix for the repair of spinal cord injury', *Acta Biomaterialia*, 86, pp. 194–206. doi: 10.1016/J.ACTBIO.2018.12.032.

Tabakow, P. *et al.* (2013) 'Transplantation of Autologous Olfactory Ensheathing Cells in Complete Human Spinal Cord Injury', *Cell Transplantation*, 22(9), pp. 1591–1612. doi: 10.3727/096368912X663532.

Tabakow, P. *et al.* (2014) 'Functional Regeneration of Supraspinal Connections in a Patient with Transected Spinal Cord following Transplantation of Bulbar Olfactory Ensheathing Cells with Peripheral Nerve Bridging', *Cell Transplantation*, 23(12), pp. 1631–1655. doi: 10.3727/096368914X685131.

Taghipour, Z. *et al.* (2012) 'Transplantation of Undifferentiated and Induced Human Exfoliated Deciduous Teeth-Derived Stem Cells Promote Functional Recovery of Rat Spinal Cord Contusion Injury Model', *Stem Cells and Development*, 21(10), pp. 1794–1802. doi: 10.1089/scd.2011.0408.

Takahashi, H. *et al.* (2005) 'Modification of Gold Nanorods Using Phosphatidylcholine to Reduce Cytotoxicity', *Langmuir*, 22(1), pp. 2–5. doi: 10.1021/LA0520029.

Takahashi, K. and Yamanaka, S. (2006) 'Induction of Pluripotent Stem Cells from Mouse Embryonic and Adult Fibroblast Cultures by Defined Factors', *Cell*, 126(4), pp. 663–676. doi: 10.1016/j.cell.2006.07.024.

Takakusaki, K. *et al.* (2016) 'Brainstem control of locomotion and muscle tone with special reference to the role of the mesopontine tegmentum and medullary reticulospinal systems.', *Journal of neural transmission (Vienna, Austria : 1996)*, 123(7), pp. 695–729. doi: 10.1007/s00702-015-1475-4.

Takami, T. *et al.* (2002) 'Schwann cell but not olfactory ensheathing glia transplants improve hindlimb locomotor performance in the moderately contused adult rat thoracic spinal cord.', *The Journal of neuroscience : the official journal of the Society for Neuroscience*, 22(15), pp. 6670–81. doi: 20026636.

Tararam, R. *et al.* (2017) 'Atomic Force Microscopy: A Powerful Tool for Electrical Characterization', in *Nanocharacterization Techniques*. Elsevier Inc., pp. 37–64. doi: 10.1016/B978-0-323-49778-7.00002-3.

Telano, L. N. and Baker, S. (2018) *Physiology, Cerebral Spinal Fluid (CSF)*,

*StatPearls*.

Tester, N. J. and Howland, D. R. (2008) 'Chondroitinase ABC improves basic and skilled locomotion in spinal cord injured cats', *Experimental Neurology*, 209(2), pp. 483–496. doi: 10.1016/j.expneurol.2007.07.019.

Tigner, T. J. *et al.* (2020) 'Comparison of Photo Cross Linkable Gelatin Derivatives and Initiators for Three-Dimensional Extrusion Bioprinting', *Biomacromolecules*, 21(2), pp. 454–463. doi: 10.1021/acs.biomac.9b01204.

Tortora, G. J. and Derrickson, B. (2014) *Tortora Principles of Anatomy and Physiology 14th Edition*, *Physiology*.

Tracy, J. A. (2015) 'Spinal Cord Anatomy', in *Mayo Clinic Neurology Board Review*. doi: 10.1093/med/9780190214883.003.0007.

Tremblay, M. È. *et al.* (2011) 'The role of microglia in the healthy brain', *Journal of Neuroscience*, 31(45). doi: 10.1523/JNEUROSCI.4158-11.2011.

Tropel, P. *et al.* (2006) 'Functional Neuronal Differentiation of Bone Marrow-Derived Mesenchymal Stem Cells', *Stem Cells*, 24(12), pp. 2868–2876. doi: 10.1634/stemcells.2005-0636.

Trounson, A. and McDonald, C. (2015) 'Stem Cell Therapies in Clinical Trials: Progress and Challenges', *Cell Stem Cell*, 17(1), pp. 11–22. doi: 10.1016/j.stem.2015.06.007.

Truong, V. X. *et al.* (2016) 'In situ-forming click-crosslinked gelatin based hydrogels for 3D culture of thymic epithelial cells', *Biomater. Sci.*, 4(7), pp. 1123–1131. doi: 10.1039/C6BM00254D.

Turner, J. G., Og, J. H. and Murphy, C. J. (2020) 'Gold nanorod impact on mechanical properties of stretchable hydrogels', *Soft Matter*, 16(28), pp. 6582–6590. doi: 10.1039/d0sm00737d.

Ueno, M. *et al.* (2016) 'Silencing spinal interneurons inhibits immune suppressive autonomic reflexes caused by spinal cord injury.', *Nature neuroscience*, 19(6), pp. 784–7. doi: 10.1038/nn.4289.

UK, S. R. (no date) *Spinal Research UK | Research for spinal cord injury*. Available at: http://www.spinal-research.org/.

Vismara, I. *et al.* (2017) 'Current Options for Cell Therapy in Spinal Cord Injury', *Trends in Molecular Medicine*, 23(9), pp. 831–849. doi: 10.1016/J.MOLMED.2017.07.005.

Wan, J. *et al.* (2015) 'Surface chemistry but not aspect ratio mediates the biological toxicity of gold nanorods in vitro and in vivo', *Scientific Reports*, 5(1), pp. 1–16. doi: 10.1038/srep11398.

Wang, K. C. *et al.* (2002) 'p75 interacts with the Nogo receptor as a co-receptor for Nogo, MAG and OMgp', *Nature*, 420(6911), pp. 74–78. doi: 10.1038/nature01176.

Wang, W.-L. *et al.* (2015) 'Current Situation of PC12 Cell Use in Neuronal Injury Study', *International Journal of Biotechnology for Wellness Industries*, 4(2), pp. 61–66. doi: 10.6000/1927-3037.2015.04.02.3.

Wang, X. *et al.* (2009) 'Ibuprofen enhances recovery from spinal cord injury by limiting tissue loss and stimulating axonal growth.', *Journal of*

*neurotrauma*, 26(1), pp. 81–95. doi: 10.1089/neu.2007.0464.

Watson, C. and Kayalioglu, G. (2009) 'The Organization of the Spinal Cord', in *The Spinal Cord*. doi: 10.1016/B978-0-12-374247-6.50005-5.

Watzlawick, R. *et al.* (2016) 'Olfactory Ensheathing Cell Transplantation in Experimental Spinal Cord Injury: Effect size and Reporting Bias of 62 Experimental Treatments: A Systematic Review and Meta-Analysis', *PLOS Biology*. Edited by L. Bero, 14(5), p. e1002468. doi: 10.1371/journal.pbio.1002468.

Wei, W., Bai, F. and Fan, H. (2019) 'Oriented Gold Nanorod Arrays: Self-Assembly and Optoelectronic Applications', *Angewandte Chemie - International Edition*. Wiley-VCH Verlag, pp. 11956–11966. doi: 10.1002/anie.201902620.

WHO (2013) 'Spinal cord injury - World Health Organization Fact sheet N°384', *WHO*.

Wiatrak, B. *et al.* (2020) 'PC12 Cell Line: Cell Types, Coating of Culture Vessels, Differentiation and Other Culture Conditions', *Cells*, 9(4). doi: 10.3390/CELLS9040958.

Wickramasinghe, S. *et al.* (2020) 'Photoactivated Gold Nanorod Hydrogel Composite Containing d -Amino Acids for the Complete Eradication of Bacterial Biofilms on Metal Alloy Implant Materials', *ACS Applied Nano Materials*, 3(6), pp. 5862–5873. doi: 10.1021/acsanm.0c01018.

Wu, Y. *et al.* (2018) 'Dual Delivery of bFGF- and NGF-Binding Coacervate Confers Neuroprotection by Promoting Neuronal Proliferation', *Cellular Physiology and Biochemistry*, 47(3), pp. 948–956. doi: 10.1159/000490139.

Xu, C. *et al.* (2021) 'Two-Dimensional-Germanium Phosphide-Reinforced Conductive and Biodegradable Hydrogel Scaffolds Enhance Spinal Cord Injury Repair', *Advanced Functional Materials*, p. 2104440. doi: 10.1002/ADFM.202104440.

Xu, C. Y. *et al.* (2004) 'Aligned biodegradable nanofibrous structure: a potential scaffold for blood vessel engineering', *Biomaterials*, 25(5), pp. 877–886. doi: 10.1016/S0142-9612(03)00593-3.

Xu, Y. *et al.* (2020) 'Overcoming the intestinal barrier: A look into targeting approaches for improved oral drug delivery systems', *Journal of Controlled Release*, 322, pp. 486–508. doi: 10.1016/J.JCONREL.2020.04.006.

Yamagata, M. *et al.* (2013) 'Human Dental Pulp-Derived Stem Cells Protect Against Hypoxic-Ischemic Brain Injury in Neonatal Mice', *Stroke*, 44(2), pp. 551–554. doi: 10.1161/STROKEAHA.112.676759.

Yamagata, T. *et al.* (1968) 'Purification and properties of bacterial chondroitinases and chondrosulfatases.', *The Journal of biological chemistry*, 243(7), pp. 1523–35. Available at: http://www.ncbi.nlm.nih.gov/pubmed/5647268 (Accessed: 4 July 2017).

Yamamoto, A. *et al.* (2014) 'Multifaceted neuro-regenerative activities of human dental pulp stem cells for functional recovery after spinal cord injury', *Neuroscience Research*, 78, pp. 16–20. doi: 10.1016/j.neures.2013.10.010.

Yoo, L. *et al.* (2014) 'Atomic force microscopy determination of Young's

modulus of bovine extra-ocular tendon fiber bundles', *Journal of Biomechanics*, 47(8), pp. 1899–1903. doi: 10.1016/j.jbiomech.2014.02.011.

Yoshida, A., Anand-apte, B. and Zetter, B. R. (2009) 'Differential Endothelial Migration and Proliferation to Basic Fibroblast Growth Factor and Vascular Endothelial Growth Factor', *https://doi.org/10.3109/08977199609034566*, 13(1–2), pp. 57–64. doi: 10.3109/08977199609034566.

Yoshida, A. and Toshima, N. (2014) 'Gold Nanoparticle and Gold Nanorod Embedded PEDOT:PSS Thin Films as Organic Thermoelectric Materials', *Journal of Electronic Materials*, 43(6), pp. 1492–1497. doi: 10.1007/s11664-013-2745-2.

Young, F. I. *et al.* (2016) 'Clonal Heterogeneity in the Neuronal and Glial Differentiation of Dental Pulp Stem/Progenitor Cells', *Stem Cells International*, 2016, pp. 1–10. doi: 10.1155/2016/1290561.

Zhang, C. *et al.* (2016) 'Treatment of multiple sclerosis by transplantation of neural stem cells derived from induced pluripotent stem cells', *Science China Life Sciences 2016 59:9*, 59(9), pp. 950–957. doi: 10.1007/S11427-016-0114-9.

Zhang, K. *et al.* (2020) 'Injectable, anti-inflammatory and conductive hydrogels based on graphene oxide and diacerein-terminated four-armed polyethylene glycol for spinal cord injury repair', *Materials and Design*, 196, p. 109092. doi: 10.1016/j.matdes.2020.109092.

Zhang, N. *et al.* (2012) 'Inflammation &amp; apoptosis in spinal cord injury.', *The Indian journal of medical research*, 135(3), pp. 287–96. Available at: http://www.ncbi.nlm.nih.gov/pubmed/22561613 (Accessed: 30 June 2017).

Zhang, Q. *et al.* (2018) 'Electrical Stimulation with a Conductive Polymer Promotes Neurite Outgrowth and Synaptogenesis in Primary Cortical Neurons in 3D', *Scientific Reports 2018 8:1*, 8(1), pp. 1–10. doi: 10.1038/s41598-018-27784-5.

Zhang, Y. and Rutledge, G. C. (2012) 'Electrical Conductivity of Electrospun Polyaniline and Polyaniline-Blend Fibers and Mats', *Macromolecules*, 45(10), pp. 4238–4246. doi: 10.1021/MA3005982.

Zhao, J. *et al.* (2014) 'Green tea polyphenols protect spinal cord neurons against hydrogen peroxide-induced oxidative stress.', *Neural regeneration research*, 9(14), pp. 1379–85. doi: 10.4103/1673-5374.137591.

Zhao, W. *et al.* (2019) 'Direct study of the electrical properties of PC12 cells and hippocampal neurons by EFM and KPFM', *Nanoscale Advances*, 1(2), pp. 537–545. doi: 10.1039/c8na00202a.

Zhou, L. *et al.* (2018a) 'Soft Conducting Polymer Hydrogels Cross-Linked and Doped by Tannic Acid for Spinal Cord Injury Repair', *ACS Nano*, 12(11), pp. 10957–10967. doi: 10.1021/acsnano.8b04609.

Zhou, L. *et al.* (2018b) 'Soft Conducting Polymer Hydrogels Cross-Linked and Doped by Tannic Acid for Spinal Cord Injury Repair', *ACS Nano*, 12(11), pp. 10957–10967. doi: 10.1021/ACSNANO.8B04609.

Zhou, Y. *et al.* (2018) 'Fibroblast growth factors in the management of spinal cord injury', *Journal of cellular and molecular medicine*, 22(1), pp. 25–37.

doi: 10.1111/JCMM.13353.

Zhu, J. and Marchant, R. E. (2014) 'Design properties of hydrogel tissue-engineering scaffolds', *http://dx.doi.org/10.1586/erd.11.27*, 8(5), pp. 607–626. doi: 10.1586/ERD.11.27.

# List of Abbreviations

| | |
|---|---|
| AANS | American Association of Neurological Surgeons |
| AgNO3 | Silver Nitrate |
| CNS | Central Nervous System |
| CSPG | Chondroitin sulphate proteoglycan |
| CTAB | Hexadecyltrimethylammonium Bromide |
| DPSC | Dental Pulp Stem Cell |
| DTT | Di-thiothreitol |
| EIS | Electrical Impedance Spectroscopy |
| ESC | Embryonic stem cell |
| GelNOR | Gelatin-Norbornene |
| HAuCl4 | Gold (III) Chloride Trihydrate |
| HFF | Human Foreskin Fibroblast |
| iPSC | Induced pluripotent stem cell |
| LEMAS | Leeds Electron Microscopy and Spectroscopy Centre |
| MAG | Myelin Associated Glycoprotein |
| MP | Methylprednisolone |
| MSC | Mesenchymal Stem Cells |
| NaBH4 | Sodium Bromide |
| NOR | Norbornene |
| NSAID | Non-steroidal anti-inflammatory drug |
| NSC | Neural stem cell |
| OEC | Olfactory ensheathing cell |
| PEG | Poly-ethylene glycol |
| PSC | Pluripotent stem cell |
| ROCK | Rho-associated kinase |
| SC | Schwann cell |
| SCI | Spinal Cord Injury |
| SEM | Scanning Electron Microscopy |
| SH | Thiol |
| TEM | Transmission Electron Microscopy |
| UV | Ultra-violet |
| wt% | Percentage by weight |
| w/v | weight per volume |
| v/v | volume per volume |